Honda R&D

Technical Review



October 2007

©2007 Honda Motor Co., Ltd. (All rights reserved)

ISSN 1881-6223

Published by:
Honda Motor Co., Ltd.
2-1-1, Minami-Aoyama, Minato-ku,
Tokyo 107-8556, Japan

Edited by:
Honda R&D Co., Ltd.
Honda R&D Technical Paper Committee

Distributor:
SAE International
400 Commonwealth Drive
Warrendale, PA 15096-0001
www.sae.org

Contact:
SAE Customer Service:
1-724-776-4970 phone
1-724-776-0790 fax
CustomerService@sae.org
SAE ISBN: 978-01-7680-1972-8

Printed:
Sep. 1, 2007





Technical Review

October 2007

Honda R&D

CONTENTS

Introduction of new technologies

Style and Design for CROSSROAD ..... Yosuke TOKORO, Takehiro ISHIBASHI 1

Styling Design of New MONPAL ML200 ..... Masahiko YAMAGISHI 7

Waza (Skilled Craftsmanship) that Produced "Honda Music": Creation of RA272 Exhaust Pipe
..... Koji UEDA, Ryuichi TAKAHASHI, Osamu KONNO 12

Presentation of 2006 Model RC211V ..... Kyoichi YOSHII, Koichi TSUTSUMI
..... Nobuo SHIGEMIZU, Shin SATO 20

Development of V8 Engine for American Le Mans Series
..... Trevor Knowles, Yasuhide Sakamoto, Tom Nickols 26

Electrical System Development for American Le Mans Racing
..... Manminder Hayre, Marcelo Martinelli, Yasuhide Sakamoto 32

Low Noise and Lightweight Technology of Inverter Generator EU6500is
..... Yoshio TANAKA, Kaku OKABE
Taiyo ONODERA, Takashi ITO 37

Development of Electric Power Steering System for ATV
..... Tomokazu SAKAMOTO, Megumu OKADA, Kazushiro INOUE 45

Technology for Updating Digital Map Using Differential Data
..... Masayuki ARAI, Keizo YAMANAKA, Toshihide YOFU 50

Development of Heat-resistant Nickel-based Super Alloy for Exhaust Valve
..... Katsuhiko TOMINAGA, Tetsuya SHIMIZU, Shigeki UETA
Seiji KURATA, Akihiro TOJI 56

Development of Low Volatile Organic Compound Dust Sealing Material ..... Naoki TSURUTA 62

Interior Sound Enhancement of Vehicle Acceleration for New Model ACCORD
– Transfer Path Analysis Using Principal Component Regression Method –
..... Atsushi SAKAMOTO, Mutsuru OZAKI 67

Development of High Performance Floor Insulation Structure of 2008 Model Year ACCORD
..... Yoshihiro NOGUCHI, Kenji TANAKA, Hiroko TADA
Fumihiko IDE, Kazuhito MISAJI 72

Technical papers

Development of Aluminum Liner in Die-cast Cylinder Block for High-power and High-displacement V6 Engine
..... Takashi KOMATSUDA, Masayuki TAKAHASHI, Katsuhisa YASUKAWA
Junichi OHMURA, Noriyuki NAMBA 76

Study on Estimation Method of Anti-oxidation Performance for Engine Oil Deterioration Monitoring System
..... Yosuke OKUYAMA, Koichiro AIKAWA
Wataru HOSHIKAWA, Masashi MARUYAMA 86

Development of Cylinder Pressure Measurement System Using Adaptive Calculation
..... Yuji YAMAMOTO, Shusuke AKAZAKI
Masanori OHARA, Takahide MIZUNO 93

Dynamic Simulation of Oil Pump Chain Using Link-by-link Method
..... Hiroshi TAKAGISHI, Atsushi NAGAKUBO
Kazuto MUGURUMA, Nobuharu TAKAHASHI 100

Prediction of Mesh Misalignment of External Gear for Transmission
..... Yoshikazu TATENO, Yoshiomi FURUI, Kazuhiro NORITA 109

Simulation of Stress on Elements of Metal Pushing V-belt for CVT under Transient Operating Conditions
..... Toshihiro SAITO 116

Establishment of Evaluation Method for Riding Comfort of Motorcycle Seats
..... Mitsue KOYANO, Tsutomu TAKEUCHI
Takeshi OHARA, Motoharu YOKOI 123

Image Fusion for Night-time Pedestrian Recognition Assistance
..... Junji EGUCHI, Izumi KONDO, Hiroyuki KOIKE 129

Research of High Fatigue Strength for Powder-forged Connecting Rods
..... Kentaro TAKADA, Ryosuke KOGURE, Teruo KOBAYASHI 136

Development and Application for Identification of Sound Source Using Inverse Method for Road Noise
..... Fumihiko IDE, Hiroko TADA, Kazuhito MISAJI
Theophane Courtois, Claudio Bertolini 145

Calibration of Tooth Profile Measurement and Uncertainty Analysis Based on Ball Artifact Method
..... Kenta UMETSU, Wataru ISHIDO, Kinya FUJIWARA 152

Development of Moment Assist and System Weight Compensation Control for Wearable Walking Assist System
..... Yasushi IKEUCHI 164

Style and Design for CROSSROAD

Yosuke TOKORO* Takehiro ISHIBASHI*

ABSTRACT

The CROSSROAD was developed based on the concept of “Active Life Navigator.” It combines a compact body with the ruggedness of a 3-row, 7-seater SUV to accommodate new driver lifestyles.

Based on the idea of “small but tough,” the vehicle’s individual design stands out even in the city. CROSSROAD expresses a tough image through its solid, angular lines and prominent fender.

Every corner of the CROSSROAD’s interior has been refined with the concept of “Exhilarating and Brawny,” complimenting the vehicle’s angular body, while its sturdy frame and modern, robust interior were created to provide passengers with a sense of security and safety.

With the CROSSROAD’s tough exterior and modern interior, we hope to provide vehicle owners with new value in their automobiles.

1. Introduction

The CROSSROAD was developed for the Japanese market to bring our customers new value. The market is overflowing with cars for every type of customer preference. One user trend in particular caught our eye. A new indication that has emerged with the changing times is that people who enjoy virtual activities, such as surfing the Internet and video games, are wanting to get out, move their bodies, and enjoy their five senses. Their interests have moved inward; they seek to better themselves while having fun, and continue to value the expansion of their worlds.

More and more people also want to share these experiences with their families, friends, lovers, and others around them.

Taking this into account, the development team wondered if they couldn’t make a vehicle that matches the driver’s lifestyle in a size that fits effortlessly into their full lives. They wanted to give the vehicle three rows of seats that could hold several people for everyday life, while asserting its style as an SUV. The team wanted drivers to feel eager to get out and do something.

The designers aimed for a vehicle that stands out in the city, one with a compact design that is unique. Balancing an exterior with presence with an interior space full of possibility, the design team strove to realize a vehicle that would leave the owners satisfied for years to come.

To realize these goals, the design team started by developing what was to become the CROSSROAD under the new concept “Active Life Navigator,” seeking to create a vehicle that is both tough and cool, and expands its owner’s life with its limitless possibilities (Fig. 1).

Figure 2 shows the final design mock-up.



Fig. 1 Concept of Crossroad



Fig. 2 Final design mock-up

* Automobile R&D Center

2. Package layout

Figure 3 shows the package layout. The package combines two key concepts: "3-row seating everyone can enjoy" and a "convenient size," making it easy to use in day-to-day life. The overall body size has been cut by 100 mm from the first-generation CR-V, which proved popular in the Japanese market, while also being given three rows of seats—enough room for 7 adults. The first and second seat rows are AM95%, a measurement indicating that they accommodate dummies that cover the space requirements of 95% of American males, meaning that four adults can quite comfortably sit in the cabin. We approached the third row with the idea that people of smaller stature would have no problem sitting there, and therefore chose JM50% measurements, which accommodate a dummy representing the space requirements of 50% of Japanese males.

Using our own technique, developed for use in the STREAM, to lower the platform, and by removing the spare tire, the design team was able to lower the CROSSROAD's overall height and include three rows of seats accommodating seven adults. Also, by giving the CROSSROAD a square design, the team was able to laterally expand the headroom in line with the STEPWGN, creating a cabin that feels larger than it actually is. Overall, the new CROSSROAD is 60 mm wider than the STREAM. Together with bigger wheels, the design team has realized a CROSSROAD that is as tough and sturdy as an SUV.

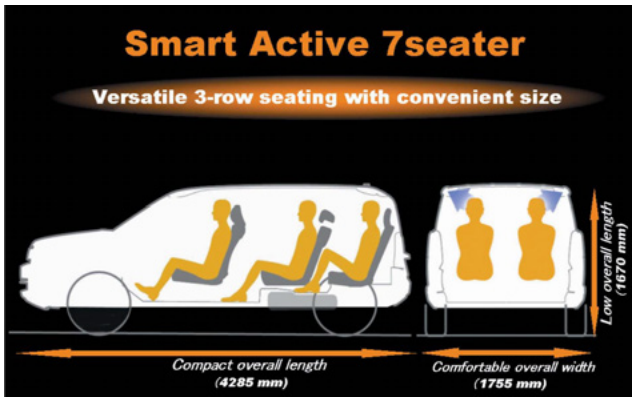


Fig. 3 Concept of package layout

3. Exterior Design

The concept for the exterior of the new CROSSROAD is "Small" but "Tough." A major question in the design was whether the CROSSROAD could be made into a size that would be easy to use in day-to-day life, while at the same time having the presence of an SUV. There are many vehicles of every style available on the market. To create a new market, however, the team felt it necessary to develop a unique design that would be instantly recognizable.

Usually, designers use clay to create their vehicle's design, shaping and molding it to create a clay model. But for this vehicle, we avoided getting caught up in the details at first, instead focusing on the overall proportions to create an impression that the whole vehicle had been chiseled out of one solid piece of metal.

Our motif was the power of a sculptor who, after envisioning the final product while studying the raw material, then sculpts the piece in one go. We named this concept "Sculptural Tough Form" (Fig. 4).

In the actual package layout, we complimented the advantageous square layout with a prominent fender and wider body, focusing on the CROSSROAD's SUV qualities.

The side panels have been refined, from the front to the rear, and from the roof to the tires. The designers also gave the surface a more intense trim [Figs. 5(a), (b)].

From the side, the large tires that support the CROSSROAD's compact body give the lower body a look of sturdiness, while the higher beltline makes the windows appear longer. All of this serves to make the CROSSROAD appear larger than it actually is. By insetting the windows, the designers have brought out the thickness of the paneling, creating an impression of toughness (Fig. 6).

Aiming to create an intrepid-looking wide front view, the designers used a two-step bumper and side panels with better balance.

For the back, the design team used vertical taillights and a beveled rear window, making the D-pillar appear narrow and hiding the fact that the CROSSROAD actually has three rows of seats.

Image not displayed for copyright reasons.

Fig. 4 Concept of exterior

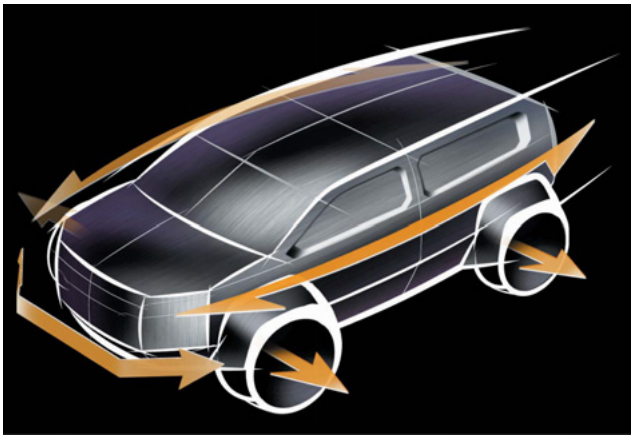


Fig. 5(a) Beveled side panel and pendent fender



Fig. 5(b) Beveled rear-end



Fig. 6 Underbody concept and deep beveled window frame

4. Interior Design

The concept for the interior of the new CROSSROAD is “Exhilarating X Brawny.”

For the interior, the design team attempted to fuse two values: A spacious, invigorating space that is comfortable for the passengers and a solid, brawny space that creates a sense of safety, one of the defining characteristics of an SUV (Fig. 7).

To realize the invigorating cabin space, the design team paid particular attention to bringing the quality of the exterior’s square form into the interior. The designers expanded the space by squaring every inch of the cabin, bringing out the “squareness” to create the unique invigorating cabin space of the CROSSROAD.

To bring about a secure feeling that the cabin is protected, the designers used the image of an architectural “pillar.” We created that sense of security in the cabin by designing it based on the bare pillars and beams used to ensure strength that you sometimes see in buildings.

The basic construction of the prominent instrument panel, meanwhile, has a horizontal design, which evokes a backbone that supports the entire square space. And with the square beefed-up design in every inch of the cabin, from the pillars to the floor, the designers have realized an “Exhilarating X Brawny” interior for the new CROSSROAD (Fig. 8).

The detail design was developed along the lines of strength and refinement, or “Tough Modern.” The



Fig. 7 Final design of instrument panel

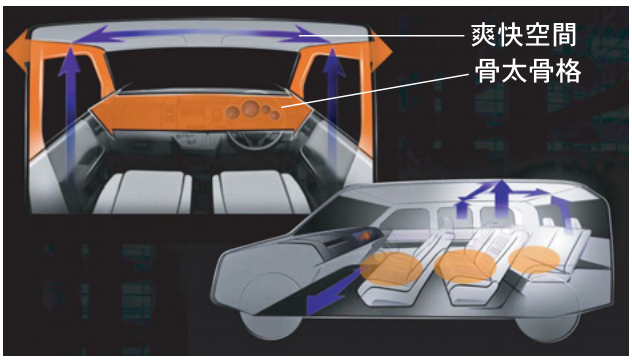


Fig. 8 Tough modern interior

systems around the instrument panel have an intuitive visibility, and their functionality gives the appearance of strength. In particular, the air conditioning is controlled using three simple, easy-to-understand dials. The size of the dials was taken into consideration, allowing drivers and passengers to instantly identify their functions based on that size (Fig. 9).

With a cockpit design centered on 4-unique shaped gauges, whose size and placement make them easy to see, the new CROSSROAD provides the elation of handling an SUV (Fig. 9).

The design team aimed to create continuity through the entire vehicle by incorporating concepts from the exterior into the interior. The designers concentrated their efforts on incorporating the shaping of "Sculptural Tough Form" into every part of the interior by carving parts as if they came from one piece of metal, thereby succeeding in creating a tough-looking CROSSROAD (Fig. 10).

Special attention has also been paid to the functional features of the comfortable seats, which have been designed for simple, one-touch operation.



Fig. 9 Tough modern cockpit



Fig. 10 Convenient functionality that carved from solid block of metal

5. Color Design

5.1. Exterior Color

To realize the tough solidness of the exterior design, the design team searched for a refined, urban color with the coolness of metal and the transparency of a building covered in windows.

Mixing coarse aluminum flakes with a transparent blue-green hue, we have created Atlantic Blue-Gray Metallic, a new color that accentuates the new CROSSROAD's solidness and bulk, and in particular, gives a rich feel to the side panels.

Other colors center on existing palletes, as well as chromatic colors, such as sparkling black, which contains larger than normal metallic particles, and a modern-looking pearl white, giving the vehicle a range of expressions (Fig. 11).

5.2. Interior Color

With the interior color concept "Tough Modern," the designers sought to create a sophisticated cabin space that is both strong and refined. The new CROSSROAD is available in two interiors, a dark interior of virile Black, and a lighter interior of clean Titan Ivory (Fig. 12). Though the dark interior is based on black, the designers used a fabric that gives off a hint of blue, creating a richly textured space (Fig. 13).

The bright Titan Ivory fittings provide a refreshing and sophisticated cabin space, a result of its contrast with black. The parts of the interior with which people come in contact are in the soft, bright color, while areas such as the luggage compartment are black, making dirt less noticeable. This color scheme gives the CROSSROAD the ruggedness and functionality of an SUV. Also, by including highly reflective metallic decorations on the three-dimensional sculptures, the team accentuated the CROSSROAD's strength, while evoking a cabin space incorporating quality and opulence (Fig. 14).



Fig. 11 Concept of exterior color

5.3. Fabric

For the fabric, too, the designers of the new CROSSROAD sought to develop a comfortable "Tough Modern" fabric that was refined and strong. The strength of the vehicle is expressed through a heavily textured fabric, while the striped pattern serves to create a unified design throughout the vehicle's interior and make the seats appear wider. The pattern was designed so that no lines bisect the vertical or horizontal lines. It has an efficient design in which the vertical and horizontal lines are not bisected, rendering even slightly slanted lines unnoticeable (Fig. 15).

The material's texture was created by applying heat embossing to a thick laminate. An additional low-density 10 mm-thick laminate was added to the front seat, resulting in a tough fabric that is comfortable and soft to the touch. (Fig. 16)

The Utility Package includes a water-repellant finish, taking into consideration the CROSSROAD's active uses as an SUV.

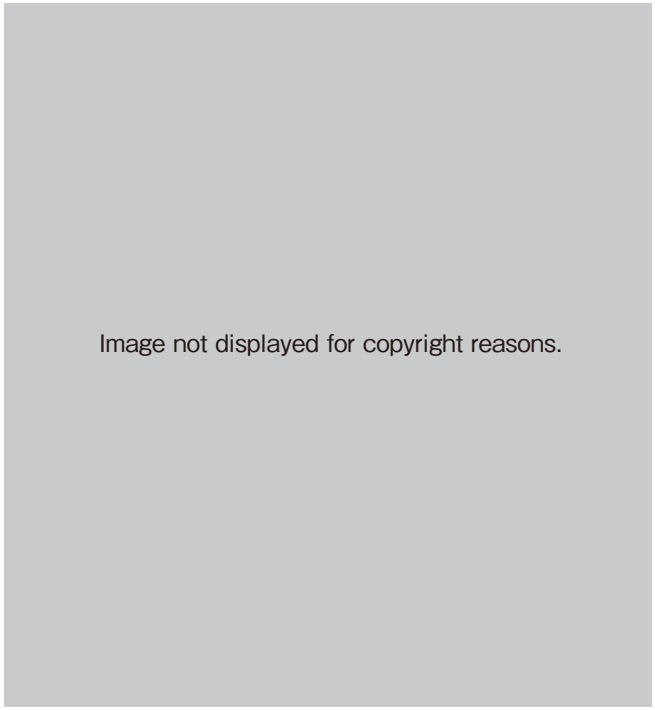


Fig. 12 Concept of interior color

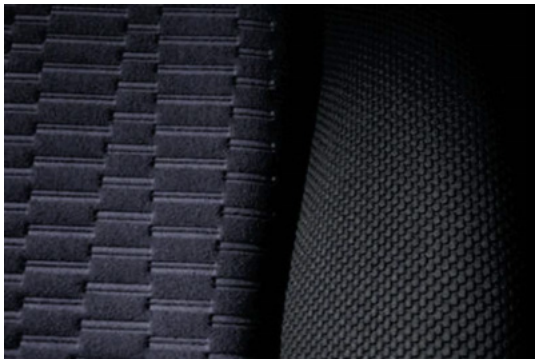


Fig. 13 Fabric with bluish coloring



Fig. 14 Metallic decoration

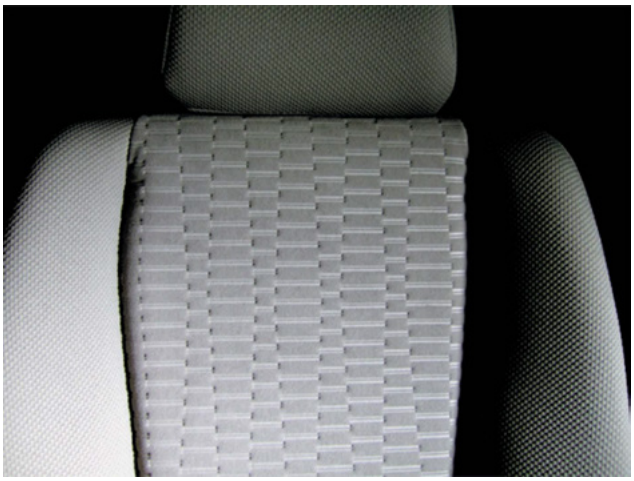


Fig. 15 Striped pattern



Fig. 16 Cube representation raminating and embossing

With its softness and texture, the designers have created an expression of comfortable safety. The urethane layer (laminate layer) of the front seat is twice as thick as that of the STREAM's 5 mm, making it soft to the touch while giving it a secure hold when the driver sinks into the soft seat. Special attention has also been paid to the functional features of the comfortable seats, which have been designed for simple, one-touch operation.

6. Logo Type

The name CROSSROAD has nine letters. As it is challenging to perceive each letter individually, the designers have made it one solid icon.

The "C" at the beginning of the name represents the moon, while each of the remaining letters represents a building, creating an image of a moon rising over a city skyline.

Like that image, the C is round like the moon, differentiating it from the remaining eight letters, which are square, giving the overall logo its own distinct image (Fig. 17).



Fig. 17 Logo design of Crossroad

7. Conclusion

What sort of configuration can satisfy a driver while still being compact?

The new CROSSROAD was proposed as a vehicle with a cool and tough exterior designed with a cube motif. We succeeded in realizing a new car with a relaxing, secure-feeling interior that seats seven. We debated constantly over how to highlight the characteristics of this car, a new type of vehicle designed under the Active Life Navigator concept.

The idea of effortlessly expanding one's world helped channel our focus. The CROSSROAD is not a car for showing off size or wealth.

Amid the trend of rounded-off SUVs, we imagined the CROSSROAD pulling away from such stereotypes.

Furthermore, in the proposal stage, we imagined the image and stories of our drivers and where they might take the CROSSROAD. This has also had an effect on our advertising as well.

We believe the new CROSSROAD's design, functional cabin space, convenient size, and ride will capture our customers' hearts. Those who buy one for themselves will come to understand intimately the fun of the vehicle and will want to share it with others. We hope the new CROSSROAD will become a partner in the new lifestyles of our customers.

■ Author ■



Yosuke TOKORO



Takehiro ISHIBASHI

Styling Design of New MONPAL ML200

Masahiko YAMAGISHI*

ABSTRACT

Looking towards the advent of an aged society, the new Monpal ML200 four-wheel scooter was developed to increase the quality of life of a greater number of users.

Taking into consideration of using the vehicle in the city and suburbs, the basic framework is that of a "smart package" no wider than a bicycle. Visibility has been increased by the use, for the first time in a commercial vehicle, of the ASV-3 LONG technology employed in Honda's Advanced Safety Vehicle.

The vehicle's affection-inspiring front "face" and the trapezoidal form that provides users with a sense of stability were designed, based on the concept of offering a new style of mobility that is also firmly within the Honda tradition.

1. Introduction

"An outstanding engineer today should be both a superb engineer and a fine artist, combining the knowledge of a scientist and the sensitivity of an artist".

With these words, Honda's founder, Soichiro Honda, stated his belief that form is an important aspect of manufactured objects, and that if the form is right, then the content, for example the structure or function of an engine, will follow[(1)]. As these words indicate, designers, like engineers, should constantly aim towards the creation of appealing products based on designs that are also superbly functional. The issue is to realize superb designs within the given constraints (hardware, cost, etc.), while avoiding extravagance. However, even if the design is superb, if it is not highly functional, the product is unfinished. When a scooter is designed for elderly users, the product should not only have an attractive color and form, but should also be useful. The design of the new model Monpal ML200 four-wheel scooter incorporated methods used in the vehicle design process in order to realize a design that would give the vehicle a strong presence, even when compared to an automobile.

2. Design Goals

During the development of the new Monpal ML200, elderly users of a suburban senior citizens' center were interviewed to determine their thoughts regarding the design of four-wheel scooters. "They shouldn't be too conspicuous;" "They should be small enough not to bother pedestrians;" "I prefer ones with larger baskets." As such responses indicate, the interviewees did not express particularly "positive" opinions regarding electric cart design. A simple design without a strong sense of presence was certainly viable, but the possibility of adopting the opposite orientation and producing a striking design was also considered, as the elderly, who may be seen on busy city streets, and active senior citizens, such as those who participated in the interviews, are fashionable and tend to wear highly colorful clothes. Designing a four-wheel scooter to be more noticeable would also contribute to increased visibility, making it easier for pedestrians and drivers to recognize the vehicle.

The design concept established for the new Monpal ML200 was that of "a new style of mobility that simultaneously fits firmly within the Honda tradition," which meant that the design for the new Monpal ML200 would not be tailored exclusively for elderly customers. Four-wheel scooters are not only purchased by the actual users; the scenario of the vehicle being given to the user as a birthday present by children or grandchildren was also considered. It was assumed that potential purchasers see Honda cars and motorcycles on a daily basis, and would use similar criteria of judgment when choosing a four-wheel scooter for an elderly person. The Monpal ML200 is a Honda power product, and in this category, a design that fits within the Honda tradition indicates a design orientation in which there is no "generation gap" in the products.

* Power Products R&D Center



Fig. 1 Design concept

Figure 1 shows the design concept for the Monpal ML200. With "Quality Life" as the keyword, the focus was the creation of a vehicle that would make its users' daily lives more fulfilling.

(1) Stylish design for "Smart Riding."
(2) High level of visibility for "Safety Riding."
(3) Smart package for "Easy Riding."

3. Image Catalogue

The first stage of the design process was to formulate an image catalogue in advance of the actual design work, to clarify the design concept. The purpose of this image catalogue was to communicate to the sales and manufacturing departments, in addition to the development team, the fact that an entirely new product, rather than a full model change, was being proposed in order to realize a "new style of mobility that simultaneously fits firmly within the Honda tradition." It would also function as a shared tool indicating the design orientation of the product. The projected target users in the formulation of the image catalogue were an elderly married couple leading a stylish lifestyle in a resort in northern Europe. The wife had formerly been an interior designer, and the couple preferred high-quality and tasteful items. This scenario was considered as symbolic of the "Quality Life" focused on in the design concept. (Fig. 2)



Fig. 2 Image catalogue

4. Features of the Design

4.1. A Design that Accentuates the "Smart Package"

The goal in developing the new Monpal ML200 was to create a vehicle that would be suited not only to users in hilly regions, which represents the largest market for the vehicle, but also to users in suburban areas. The realization of a "smart package" was therefore made the design focus. The width of the vehicle has been reduced by 85 mm against that of the previous ML100 to 595 mm, equivalent to the width of a bicycle[(2)]. This compact body helps ensure that the vehicle does not bother pedestrians, even when used on a sidewalk. The design aimed to display this "smart package" more effectively. One aspect of this was the front "cycle" fender. Separating the fender from the front of the body has made the body appear slimmer. The front fender also makes it easy for the user to see the angle of the front tires from their seat. Day by day, an electric cart will often be used on sidewalks with numerous obstructions and on the edge of roads with drainage channels, and the ability to judge the position of the front tires will contribute to preventing collisions and preventing the tires from leaving the road or sidewalk. (Fig. 3).

A "two-tone" color scheme has also been used to make the body look even more compact. This design idea originated in the desire to make the body frame, a structural part, into an aspect of the exterior of the vehicle. It was found that a two-tone color scheme made the design of the vehicle appear slimmer and more compact than a monotone color scheme. In addition, even if users select a dark color as the main body color, there is no change in the color of the side covers, and this bright silver (or bright grey) surrounding the entire body should make the vehicle more noticeable to pedestrians and drivers (Fig. 4).

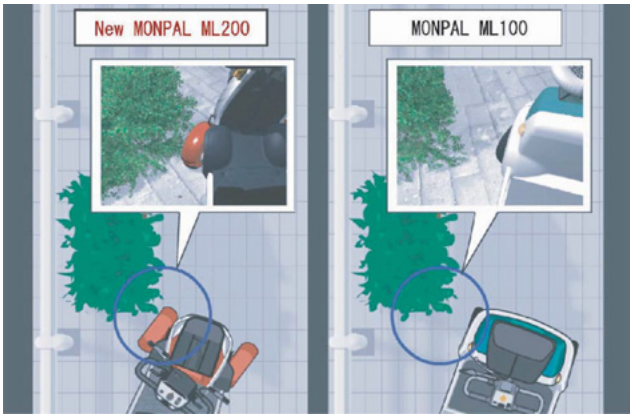


Fig. 3 Front fender

4.2. A Lovable Front "Face" Design

The majority of modern four-wheel scooters use a single headlight. The vehicles are sometimes not recommended for nighttime use; in Japan, a standard for the lights has not been clearly specified. In order to increase visibility, and due to the designers' commitment to giving the vehicle a front "face," two headlights (two "eyes") have been employed in the ML200. The design concept was the creation of "a lovable front face." It was felt that the realization of a design using human and animal faces as a motif would inspire a sense of "affinity" with the vehicle.

The use of two "eyes" on a four-wheel framework (which is similar to four legs), gives a sense that the vehicle looks like a living creature. Vehicles are products that inspire a greater sense of affection in their users than other manufactured products, such as white goods, etc. Some car owners even give nicknames to their cars. In addition, the anthropomorphization of motor vehicles is increasingly popular today, as seen in Disney movies. The use of the twin headlamp configuration gives the vehicle an affection-inspiring "expression" (Fig. 5).

4.3. Trapezoidal Form for a Sporty Feel and a Sense of Stability

In the first stage of the development process, the key sketch selected for the new Monpal ML200 did not give the impression of a vehicle with a top speed of 6 km/h, but rather of a vehicle giving a greater sense of speed. This was a result of the concept that the design should give the sense that the scooter was capable of sporty performance, a characteristic that is representative of Honda vehicles.

In addition, the use of front and rear suspension as a chassis technology to absorb impact and vibration and provide a more comfortable ride provided static and dynamic stability, despite the narrow width of the vehicle[3]. A form that gave an impression of stability was also sought. Specifically, the "wide stance" trapezoidal form used in automobile design was the design target here. The four tires firmly grip the ground, while the upper section is tapered to produce a lower center of gravity and sense of stability (Fig. 6). In addition, in the Monpal ML200, the design team succeeded in making the center of gravity appear lower by increasing the width of the upper surface of the rear fender that covers the rear tires.

4.4. Honda ASV-3 LONG Design

The new Monpal ML200 incorporates the LONG technology employed in the advanced safety research vehicle, the Honda ASV-3. Specifically, this means that reflectors have been placed on the wheel cover (in the deluxe version) or low on the side cover (in the standard version).

LONG (Longitudinal Oriented Normative temporal Gap compensate) design attempts to make it easier for drivers and pedestrians to perceive the distance to the vehicle by employing lights (reflectors) positioned low on



Fig. 5 Front face design

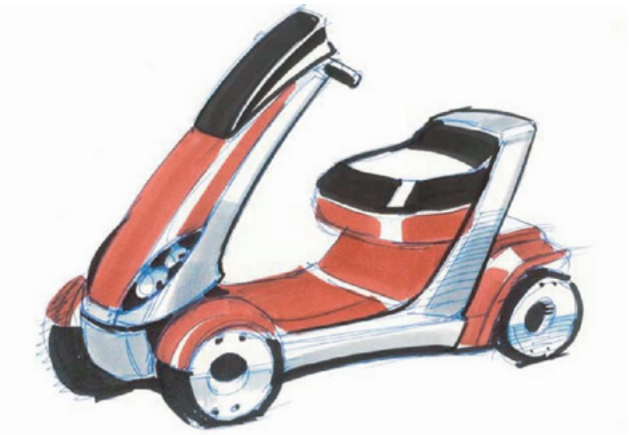


Fig. 4 Conceptual sketch of two-tone body color



Fig. 6 Honda CIVIC (1983) Low centre of gravity.

its body. By emphasizing the points of connection with the ground, it increases visibility at twilight and night[4].

Figure 7 shows the effect of the law of perspective; the greater the vertical distance from the horizon of the target object within the line of sight, the closer it appears. On the left side of Fig. 7, when a > b, object A appears to be closer than object B. On the right side of Fig. 7, the distance to scooter A, provided with lights closer to the ground, can be judged more accurately than the distance to scooter B, that uses a light positioned further from the ground.

In addition, increasing the number of lights and positioning them higher on the scooter increases the rate of recognition of the vehicle, by car drivers, etc.

4.5. Control Panel Design

The control system used in the new Monpal ML200 is a more evolved version of the ML100 system. At the conceptual stage, the idea of using a horizontal bar handle like a bicycle was considered, but loop handles and lever operation for going forward and stopping are standard in four-wheel scooters, and it was judged that the employment of this type of system would enable users to feel comfortable and familiar with the controls when changing to a new scooter. The advancements made in the new control panel include the use of larger letters and different colors to increase the visibility of the display panel and make it easier for users to read. Messages such as “Park brake on” and “Charge battery” are displayed only when necessary, making the display simple and easy to understand. In addition, changes over time have been considered, and the speed setting dial and forward/reverse switch do not have printed indications but use double molding, ensuring that they are not only functional, but will maintain the attractiveness of their design over the long term (Fig. 8).

4.6. Seat Design

The basic framework of the seat employed in the Monpal ML100 was used as the base in designing a seat for the new model, and sought a design that provided increased user comfort (Fig. 9). The height of the backrest was increased by approximately 30 mm against that of the ML100, increasing the degree of support provided to the user. The materials used in the urethane cushion, as well as the thickness of the cushion, were modified to make sitting more comfortable. A covering offering a sense of luxury has been employed on a base color of black. A constantly flashing LED lamp (in the deluxe version) or a reflector (in the standard version) has been employed in the seat back, while reflectors and blinkers have been employed at the side of the scooter, in order to increase visibility from the side and the rear. The deluxe version also features a swivel seat that increases the ease of getting on and off the scooter, in addition to an armrest that can be lowered into position.

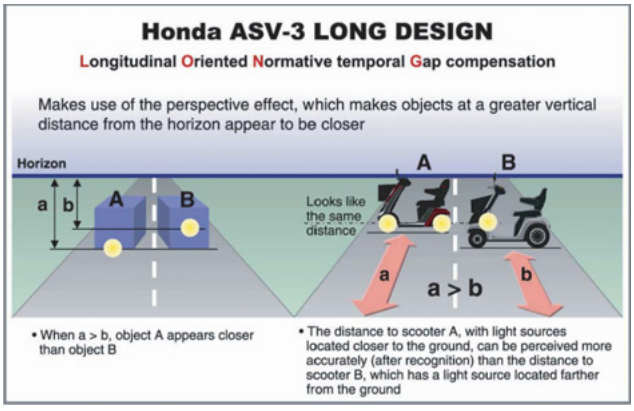


Fig. 7 Honda ASV-3 LONG design



Fig. 8 Design sketch of control panel



Fig. 9 Design sketch of seat

5. Conclusion

The new Monpal ML200 (Fig. 10) has been extremely well-received by the design world. In addition to receiving a Good Design Gold Prize in the Good Design Award 2006 held by the Ministry of Economy, Trade and Industry, it was selected for Vol. 8 of the Design Museum Selection of the Japan Industrial Designers’ Association (JIDA). The evaluation of the Good Design Award judging committee was as follows:

Motorized carts in the field of assistive carts and senior mobility have tended to emphasize function over form. Finally there’s a vehicle that bespeaks a commitment to



Fig. 10 External view of new MONPAL ML200

design quality and appeals to our senses. In short, the designers have succeeded in creating a smartly appointed cart while upholding a development concept of setting a new standard in mobility in the Honda tradition. The Monpal's refinements ensure that it easily meets expectations as a member of the Honda line. With a body as narrow as a bicycle, a low rear fender imparting stability, an attractive visage, and universal-design-inspired features, including highly visible wheels and indicators, this four wheeled scooter promises to be popular in many contexts, not only for active seniors but also as a new form of neighborhood transportation[(5)].

This is the type of praise that the new Monpal ML200 has received from the design world since its introduction. But the vehicle has also been evaluated highly for its characteristics as a "product," the superior functions and basic framework that provide satisfaction to its users. Looking towards the advent of an aged society, Honda will continue to develop products that meet the company's high standards, based on its mottos "Fun for Everyone" and "Safety for Everyone," in an attempt to spread happiness by offering products that benefit their users.

References

(1) Honda, S.: Honda Soichiro Yume wo Chikarani Watashi no Rirekisho, Nikkei Inc, p. 218 (2001) (in Japanese)
(2) Hosaka, J., Inui, T., Maesaka, K.: Development of a 4-wheel electric wheelchair-MonPal ML100, HONDA R&D Technical Review, Vol. 12, No. 1, p. 21-26
(3) Ichikawa, K., Hirose, Y., Yamamoto, T., Yamagishi, Y., Ishikawa, T.: Development of Monpal ML200 4-Wheel Scooter, Honda R&D Technical Review, Vol. 18, No. 2, p. 28-35
(4) Kushida, K., Katayama, M., Tsutsumi, Y., Maruyama, K., Kamata, Y., Murata, Y.: Introduction of Honda ASV-3 (Motorcycles), Honda R&D Technical Review, Vol. 18, No. 2, p. 13-20
(5) Japan Industrial Design Promotion Organization: "Japan Design" GOOD DESIGN AWARD YEAR BOOK 2006-2007, p. 18-21

Author



Masahiko YAMAGISHI

Waza (Skilled Craftsmanship) that Produced “Honda Music”: Creation of RA272 Exhaust Pipe

Koji UEDA* Ryuichi TAKAHASHI* Osamu KONNO*

ABSTRACT

In the 1960s, when Honda won its first Formula 1 race, the Japanese automotive industry entered a new era. This study attempted to accurately reproduce and analyze the process of formation of the exhaust pipe of the winning RA272 engine, using the *waza* (skills) employed in its fashioning, which have been handed down by its makers. This analysis showed that the manual bending method, used to create the RA272 exhaust pipe, which was filled with sand and bent while being flame-heated, enabled the achievement of a continuous curve with a high bending limit, without the use of figures or molds, and was superior to the mechanical bending method of that time, from the standpoint of the degree of freedom of the layout, as well as that of speed of production. Study of the skills employed by sheet metal specialists at the moment of pipe bending has provided information on the bending temperature and point at which bending is initiated, which is important in elucidating the pipe production technique. The fact that the pipe displays lower residual stress from bending and that the microstructure of the material remains stable, even at exhaust temperatures of 700 °C to 900 °C, has also provided useful information on the pipe’s shape stability and mechanical strength.

1. Introduction

Participating in Formula 1 and other races is part of Honda’s culture, and Honda engineers have honed their *waza* (skills) under the limit conditions represented by racing. In 1965, in Honda’s first term of racing, the 1.5 L V12 RA272[(1)] (Fig. 1) won the Mexico Grand Prix. From the early days of the company’s involvement in racing, Honda’s prototype engineers have worked to create and supply engines and parts that meet the demands of racing vehicle design and satisfy the requirements of racing drivers. In order to keep the techniques that went into the creation of the RA272 alive, engineers are now attempting to accurately reproduce the vehicle using the *waza* that were originally employed in its creation. The design of the RA272 exhaust pipe to fit a predetermined layout earned the accolade “pipe art”[(2)]. This was a functional component that determined the power characteristic of the racing engine, and the term “Honda music” came to be applied to its particular dry, high-frequency exhaust note[(3)].

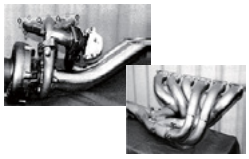
Amid today’s quest for increasingly advanced manufacturing techniques using CAD, CAM, and CAE, it is not an easy issue to decide how to transmit and pass on *waza* and the value of those skills. In the process of seeking a method of transmitting to coming generations the *waza* employed in the *tsukuri* (fashioning) of this exhaust pipe to which the appellations “art” and “music” had been applied, interest was generated in using contemporary measurement technologies to conduct a



Fig. 1 RA272

* Automobile R&D Center

Table 1 Manufacturing methods for Formula 1 vehicle exhaust pipes

	First term 1963-1968	Second term 1984-1992	Third term 1999-
Material	Steel pipe (STKM)	Stainless steel, inconel	Stainless steel, inconel
Manufacturing method	Manual bending	Mechanical bending, welding	Mechanical bending, welding, press forming
Engine type	V8, V12	V6, V10, V12	V10, V8
Photograph			

value analysis on the pipe. Introducing the *waza* that went into the creation of the "Honda music" that was part of this exhaust pipe is one method of attempting to ensure this *waza* is passed on. This paper attempts to introduce these *waza* to a large number of people and to pass them on to coming generations.

The term *waza* used in this paper refers to superior skills, unique to Japan, employed in the fashioning of objects. The tempering techniques used in the creation of Japanese swords, and the manufacture of the composite structure of the swords, which do not break despite their hardness, may be taken as an example. These were born from *waza* and a traditional mind-set that produced sword fabrication methods that have no equal elsewhere, resulting in a beauty that gives the swords a high value as art objects. The manual dexterity inherited from their ancestors and the traditional ethos of crafting displayed by the Japanese people have enabled *waza* to be passed down and to be continuously developed in unique ways, despite the nation's lack of natural resources. These *waza* form the foundation of the Japanese automotive industry.

After confirming the validity of the instinctive decisions made on the basis of *waza* by the sheet metal specialist who recreated the RA272 exhaust pipe (Fig. 2), a value analysis was attempted by using a concrete evaluation method to compare the manual bending techniques used with the mechanical bending method that was the rival method available at the time when the pipe was originally manufactured. This paper will introduce the *waza* employed in the fashioning of this exhaust pipe employed in Honda's first term of involvement in racing, and present the findings resulting from this study.

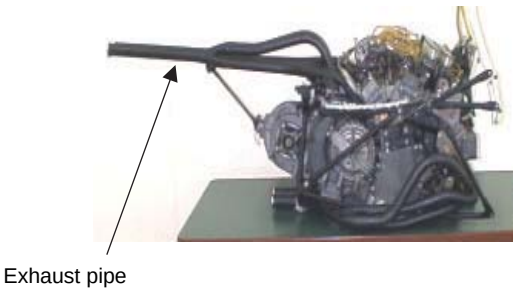


Fig. 2 RA272 engine and exhaust pipe

2. The Exhaust Pipe

2.1. Change in Method of Manufacturing Exhaust Pipes for Racing Vehicles

Table 1[4] shows the exhaust pipe materials and manufacturing methods, and the engine types employed, from Honda's first to third terms of involvement in racing. During the first and second terms, the exhaust pipes were bent; in the third term there was a transition to press forming. This was because the quest for compactness made it necessary to employ a layout that exceeded the bending limit of the pipe, and formation using bending techniques thus became a challenge. A change in the materials used from steel to high-strength and high heat-resistance stainless steel and inconel was another reason for the change in manufacturing method. Today, also, modifications are made day by day, as engineers seek a compact structure that balances heat resistance with lower weight.

2.2. Exhaust Pipe Configuration

To enable the employment of a comparatively high-order exhaust pulsation[2] in the high-speed, high-power (12 000 rpm, 230 ps) engine used in the 1965 RA272, the exhaust system employed four tail pipes, each of which was formed by three pipes converging into a single pipe (this configuration will be termed a "3-to-1 convergence" below) (Fig. 3). Table 2 shows the teams participating in races at the time and the engines that they used.

The exhaust pipe commenced from the flange connected to the engine exhaust head, and was made up

Table 2 Team and engine type

Team	Ferrari	BRM	Honda
Engine type	Dino 158 V8 1489 cc 210 ps 11000 rpm	B.R.M. 56 V8 1498 cc 220 ps 11500 rpm	RA 272 V12 1500 cc 230 ps 12000 rpm

of primary, collector, and tail pipes (Fig. 4). The system featured the greatest number of pipes of the systems used by any of the racing teams, but also employed the most compact layout. To minimize exhaust interference as much as possible, 12 pipes of equal length were employed, producing a 3-to-1 convergence that was easily mounted in the vehicle. Arranged compactly around the engine, the primary pipes were 12 pipes of different shapes, but of identical length, in a twining layout, leading to the application of the term “pipe art.”

2.3. Reproduction of the Exhaust Pipe

This section will discuss the main points that had to be observed in the reproduction of the exhaust pipe. As Fig. 5 shows, the mouth of the pipe that is connected to the flange is expanded and connected to the primary pipe. To attempt to ensure that there is no unevenness, the external diameter of the pipe should be uniformly expanded from 32 to 35 mm.

Figure 6 shows the primary pipe, displaying a continuous curve without joins from the first bend to the fourth bend. No diagrams or bending dies are used in the procedure. The pipe is filled with sand and bent, relying on feel, while being heated over a gas burner. This method of pipe manufacture uses a bending technique that necessitates highly developed *waza*.

To create a 3-to-1 convergence from the primary pipe, the pipe is cut in the shape shown in Fig. 7(a). The pipe is then clamped in a jig, and the sections are welded together while using a shield gas to attempt to prevent oxidation [Fig. 7(b)]. The optimum join is judged to have been achieved when scaly beads appear at the background of welding. Considerable experience in welding on ultra-thin sheets using tungsten inert gas welding is necessary. The welded areas of the 3-to-1 convergence are effective in controlling drag of exhaust gas, and thus become a concealed “tuning” mechanism, resulting in the pure high

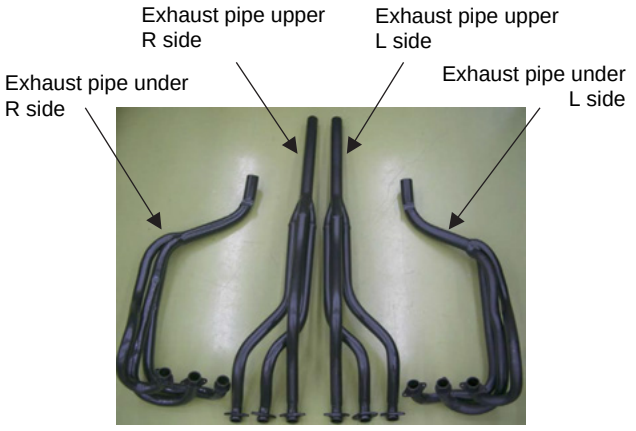


Fig. 3 RA272 exhaust pipe

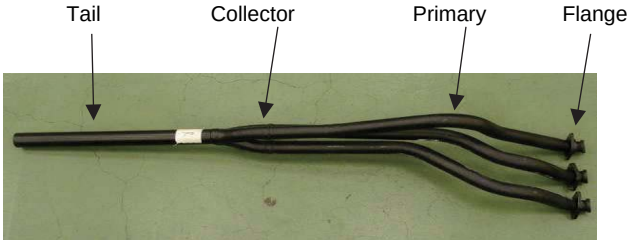


Fig. 4 Configuration of exhaust pipe

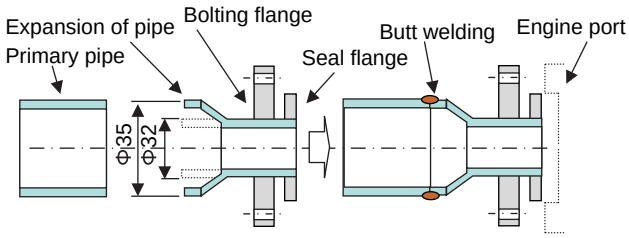


Fig. 5 Method of manufacture of flange

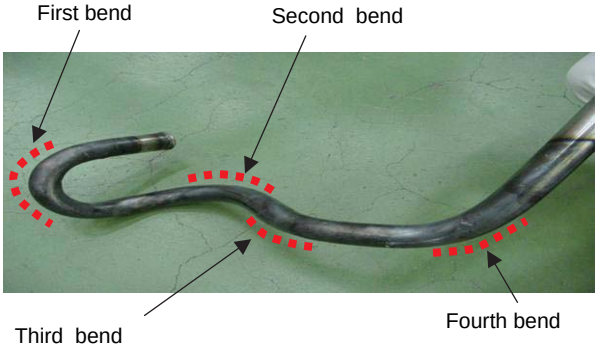


Fig. 6 Technique of bending primary pipe

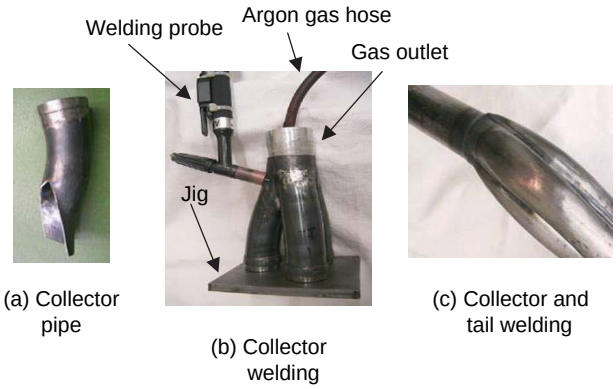


Fig. 7 Method of manufacture of collector

notes of "Honda music." When the collector pipe in which the three pipes converge into one is joined with the tail pipe, as shown in Fig. 7(c), the pipe is completed. Having defined the various points to be observed in the reproduction of the "pipe art" of the RA272 exhaust pipe, as introduced in Section 2.2., the pipe has been recreated by Honda's contemporary Racing Division using the *waza* of a sheet metal specialist.

3. The *Waza* of the Sheet Metal Specialist

Bending a pipe in the conventional manner results in wrinkles of the type shown in Fig. 8. In order to investigate the *waza* involved in producing the continuous curve in the primary pipe discussed in Section 2.3, the project studied the instinctive decisions of a sheet metal specialist, to whom the techniques of fabrication employed in the period of original manufacture of the pipe had been passed down (Fig. 9).

3.1. The Moment of Bending

The sheet metal specialist indicated that while watching the burnt color of the surface of the pipe, he would judge the moment to bend the pipe (Fig. 10) as the moment when his hands gripping the pipe felt that the pipe had lost rigidity. The project therefore examined the burnt color watched for by the sheet metal specialist and the moment of bending.

Figure 11(a)-(d) shows the results of measurements of the temperature of the pipe during flame heating, at the moment of bending, immediately after bending, and following natural cooling. The results indicated that the burnt color watched for by the sheet metal specialist occurred at around 820 °C. The bending operation commenced when the 820 °C area had expanded and covered approximately one-third of the surface of the pipe. At this point in time, the pipe lost its feeling of rigidity, and the sheet metal specialist judged that the moment was right for bending. Up to this point, it had been conjectured that the magnitude of the angle of bending was adjusted with a focus on the outside of the leading edge of the bend, where the material was stretched to the greatest degree. However, as the arrow in Fig. 11(c) shows, the section of the pipe with the highest surface temperature becomes the point of commencement of bending, and a bending radius is formed. The magnitude of the bending angle is adjusted by increasing or reducing the area at the bending temperature, centering on the point of origin of bending.



Fig. 8 Conventional bending



Fig. 9 Sheet metal specialist

3.2. Correction of Bending

Immediately after the pipe is bent, flat sections are bent back a little against the direction of the original bending to bring them closer to a perfect circle. If this process leaves wrinkles on the pipe, the sheet metal specialist stops the flame and immediately flattens out the wrinkles using an iron hammer (Fig. 12).

A comparison of the external appearance and cross-section of a pipe before and after hammering is shown in



Fig. 10 Manual bending by specialist

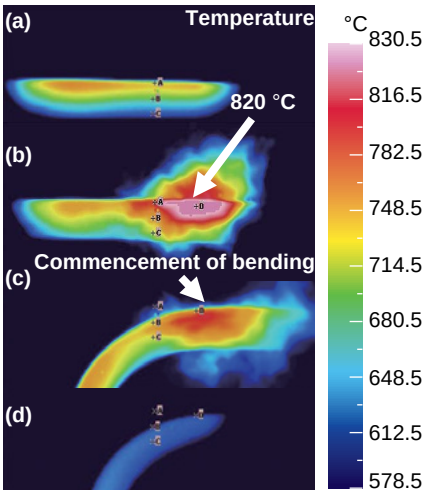


Fig. 11 Results of temperature measurement

Fig. 13. After hammering, the wrinkles have disappeared, and there are no flat areas. Following this, even if wrinkles occur in the radius section at the bending limit, hammering maintains a uniform pipe diameter, and the bend is connected to the next bend, completing the continuous curve of the primary pipe. This *waza* is a technique offering a higher degree of freedom in curvature, enabling a pipe to be bent with no joins to fit a tight layout. The origin of the primary pipe that played "Honda music" was the refined *waza* of the sheet metal specialist, using a hammer to flatten out any wrinkles.

3.3. Speed of Production

In the second term of Honda involvement in racing, mechanical bending was employed, and the materials were changed to high heat-resistance stainless steel and inconel. These methods were responses to the use of two racing teams and involvement in an increased number of races. However, due to the limitations of the bending machine and the bending limit of the pipe, a continuous bending could not be achieved, and this meant that pipes of different bending radii had to be connected, necessitating increased expense for benders and bending dies and resulting in increased production times.

The main reason for the use of manual bending during



Fig. 12 Correction with hammer

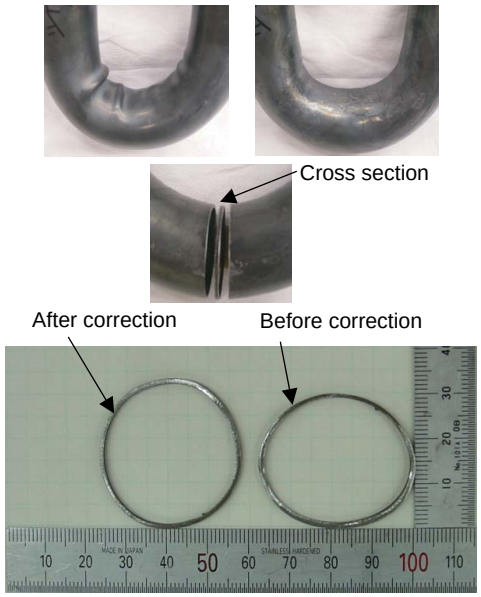
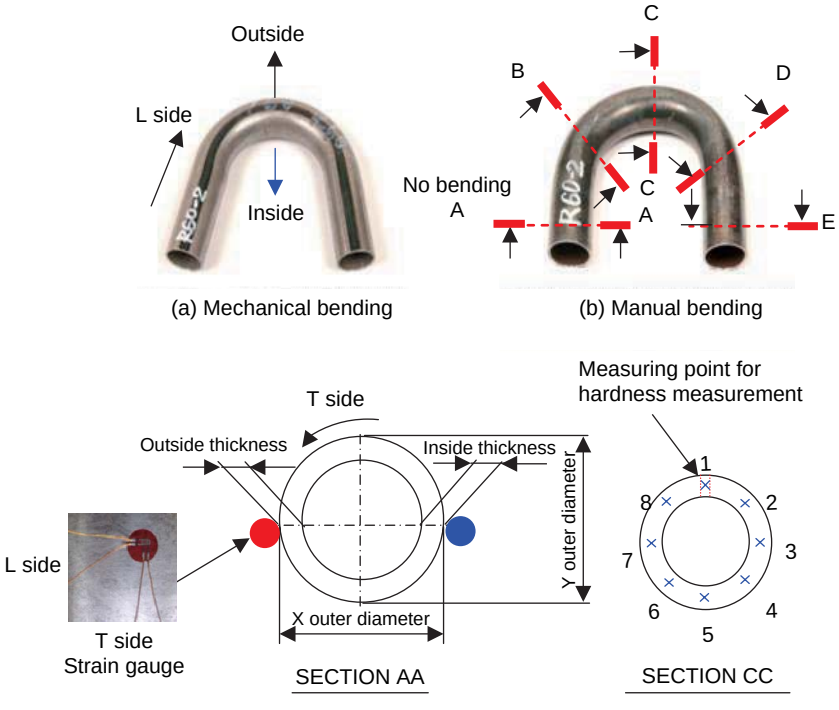


Fig. 13 Comparison of correction with hammer

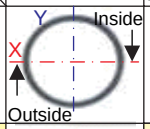
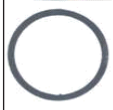
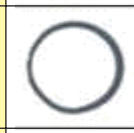
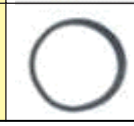


(a) Mechanical bending (b) Manual bending

(c) Section AA (d) Section CC

Fig. 14 Comparison of mechanical and manual bending

Table 3 Rate of change table of outer diameter and thickness

	Mechanical bending					Manual bending				
	Form	X outer diameter	Y outer diameter	Outside thickness	Inside thickness	Form	X outer diameter	Y outer diameter	Outside thickness	Inside thickness
Section A		34.14 mm	34.14 mm	2.21 mm	2.13 mm		33.49 mm	34.16 mm	2.10 mm	2.19 mm
		Rate of change					Rate of change			
B		–4.3 %	0 %	–23.5 %	23.0 %		–3.3 %	–1.0 %	–16.2 %	13.2 %
C		–6.2 %	–0.2 %	–18.6 %	22.1 %		–9.0 %	–1.2 %	–17.1 %	14.2 %
D		–5.0 %	–0.7 %	–22.6 %	23.5 %		–5.5 %	–0.1 %	–15.2 %	13.2 %

the first term of Honda racing involvement can be conjectured to be the fact that it enabled exhaust pipes with complex continuous curves to be manufactured in a very short period (within a single day) without the use of diagrams or bending dies.

From the qualifying sessions to the final race, races are completed within two or three days. Assuming that exhaust pipes could be manufactured at the race track, if a heat source was available and it was only a matter of producing two or three pipes, manual bending would enable production in time for the test laps. Exploiting the speed of this *waza*, the race teams of the first term of Honda racing chose a method of fashioning that enabled production right up to the moment of the final race.

4. Special Characteristics of the Manually Bent Exhaust Pipe

Section 3.3. above indicated that manual bending was superior to mechanical bending from the perspective of the manufacturing speed of the exhaust pipe. This section will present the results of a comparison of the quality and the performance of pipes manufactured using manual and mechanical bending techniques.

4.1. Change in External Diameter and Thickness

The effectiveness of the two bending techniques in the manufacture of a 180° U-shaped test piece with a radius of 60 mm was compared using 2.3 mm thick STKM with an external diameter of 34 mm [Fig. 14(a), (b)]. Due to the structure of the machine and the position of the bending mandrel, the shape of the test piece manufactured using the bending machine was slightly open, while manual bending enabled the achievement of a complete 180° curve.

The external diameter of the test pieces was measured in two directions (X and Y), and their thickness was measured at the inner and outer surfaces of the bend [Fig. 14(c)]. Table 3 shows the rate of thickness change of cross-sections B, C, and D against cross-section A, which had not undergone bending. In terms of change in external diameter, little difference can be observed between mechanical and manual bending, with reductions in diameter of only a few percent displayed by each. However, the rate of change of thickness at the inner and outer surfaces of the bend was lower in the case of manual bending at 31.3% against a maximum of 46.6% for that in mechanical bending. This demonstrates the superiority of manual bending in terms of bending marginal performance. In addition, the mechanically bent test piece displayed a higher rate of reduction of thickness at the outer surface of the bend in the cross-section from B to D, the origin and termination points of the bend, indicating that the highest degree of stretching of the material occurred at the outer surface of the bend.

4.2. Residual Stress caused by Bending

Residual stress was measured at the inner and outer surfaces of the test pieces using a strain gauge, as shown in the cross-section in Fig. 14(c). The results are shown in Fig. 15. As Fig. 15(a) shows, the test piece manufactured using mechanical bending displayed a higher level of strain due to residual stress on the inner surface at point B, close to the point of origin of the bend, and in addition, displayed higher strain than the test piece manufactured using manual bending at all measurement points. It can be predicted that the residual stress in the mechanically bent test piece would cause deformation as stress was released at the exhaust temperatures that occur during actual operation. By contrast, as shown in Fig.

15(b), manual bending is effective in minimizing variations in residual stress, resulting in a more stable shape.

4.3. Microstructure and Hardness

Measurements were taken at a cross-section of the leading edge of the bend in order to study the microstructure and hardness of the bent section [Fig. 14(d)]. The results of hardness measurements for the test pieces produced by mechanical and manual bending are shown in Fig. 16. Despite the fact that the hardness of the material declines because of heating during the manual bending process, the hardness is uniform and there is therefore minimal deformation of the toroidal shape.

In the mechanical bending process, the microstructure of the pipe becomes finer during work hardening, immediately following bending. Because of this, the product displays an excellent static strength characteristic from room temperature to around 700 °C, but the grain growth due to heating and deformation resulting from creep are both concerns. Grain growth and a coarsening of the microstructure due to flame heating can be observed in the case of the test piece manufactured using manual bending (Fig. 17). However, in tests from 700 °C to 900 °C, the predicted increase in exhaust temperature, the test piece produced using manual bending did not display the changes displayed by the mechanically bent test piece, indicating that its mechanical strength would remain stable under actual operating conditions.

5. Conclusion

The study discussed in this paper accurately reproduced the method of manufacture of the RA272 exhaust pipe, and compared the results with the results achieved using the mechanical bending method that was also available at the time of the original manufacture of the exhaust pipe. The study produced the following conclusions:

(1) The moment for bending the pipe in the manual bending process was reached when the temperature of the surface of the pipe was around 820 °C, and the magnitude of the bending angle was adjusted by increasing or decreasing the area of the pipe at this bending temperature, centering on the point of origin of the bend.

(2) While mechanical bending was unable to produce a continuous bending and necessitated the use of benders and bending dies, manual bending enabled a pipe to be manufactured in a short period (within a day) without the use of diagrams or bending dies.

(3) The maximum rate of change in the thickness of the inner and outer surfaces of the bend of a manually bent test piece was 31.3%, against 46.6% for a mechanically bent test piece, demonstrating the superiority of manual bending in terms of bending marginal performance.

(4) The manually bent pipe displayed minimal residual

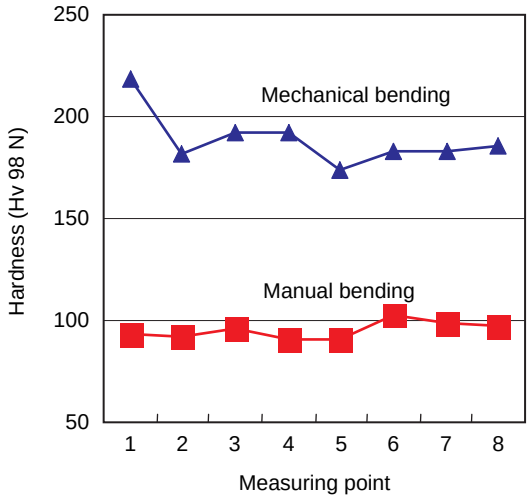


Fig. 16 Results of hardness measurements

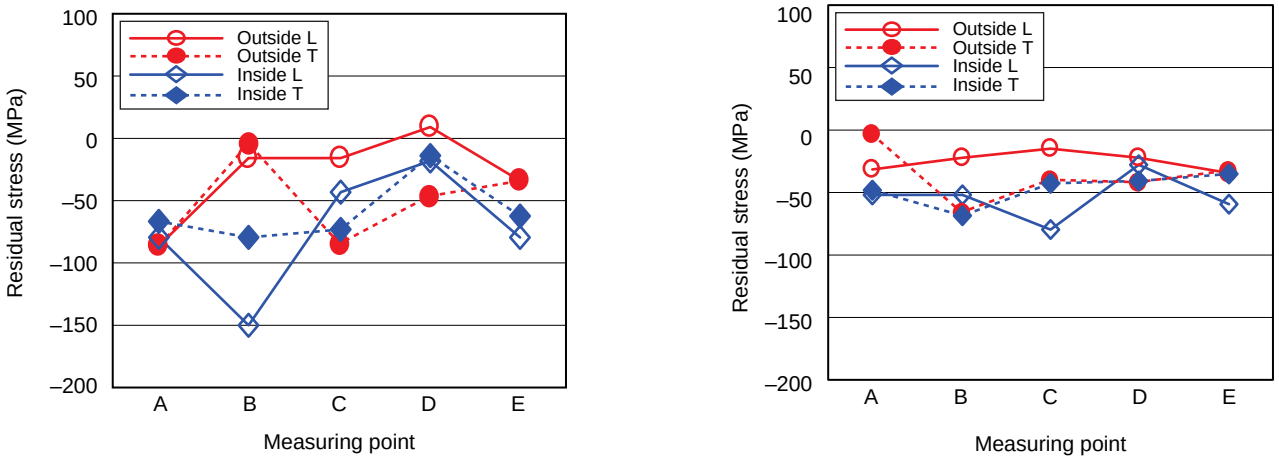


Fig. 15 Results of residual stress measurements

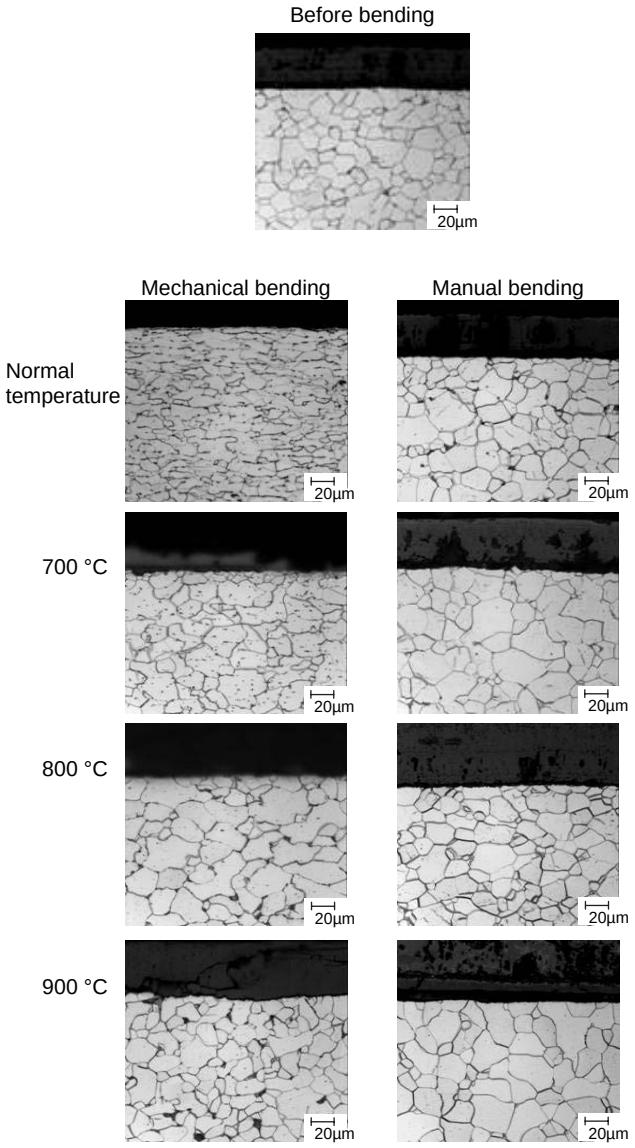


Fig. 17 Microstructure from normal temperature to 900 °C

stress. In addition, despite a decline in hardness, hardness was uniform, and there was minimal change in the toroidal shape. In tests simulating the increase in exhaust temperature, the microstructure of a test piece manufactured using manual bending did not display the magnitude of change of that of a mechanically bent test piece, indicating that its mechanical strength would be stable under actual operating conditions.

The *waza* that produced the RA272 exhaust pipe increased the degree of freedom of the layout, and was able to respond immediately to race requirements. The exhaust pipe also demonstrated its superiority in the fact that it displayed minimal residual stress, and would maintain its stability of shape and mechanical strength at exhaust temperatures.

6. Afterword

The study discussed here emerged from an interest in investigating “pipe art” and “Honda music” that was generated by the process of seeking a method of passing on *waza* to coming generations. The results achieved by the study indicated that the RA272 exhaust pipe displayed a higher level of performance than had at first been conjectured. The *waza* employed to reproduce the RA272 exhaust pipe as it was originally manufactured have been passed down by involvement in racing, and their considerable value, as indicated in this paper, is still an aspect of the manufacture of certain prototype production technology. The scientific measurements and analyses employed in this study have clarified the value of these *waza*. They have demonstrated that the methods used to fashion engine components represented an important element in Honda’s first race victory achieved in the Mexico Grand Prix. In addition, they have provided hints as to how to attempt to ensure that these *waza* are passed on from this point.

Honda’s early racing teams used their *waza* to create the world’s most sophisticated parts, competed in races and won, and in doing so passed on a dream to later generations. The purpose of this paper has been fulfilled if it has succeeded in introducing some part of those historical *waza*.

References

(1) http://www.honda.co.jp/collection-hall/episodes_old/motor/ra272/,2007/3/2
(2) Nakamura, Y., Kanda, S.: HONDA F1 1964-1968, CAR GRAPHIC, NIGENSHA, p. 260 (1984) (in Japanese)
(3) Nakamura, Y.: Reishingu Enjin no Kako Genzai Mirai, GURANPULI SHUPPAN, p. 231 (1981) (in Japanese)
(4) Ando, Y., Ueda, K., Takahashi, R., Nakajima, K., Yamagami, T., Fukushima, Y.: Development of Exhaust System for F-1 Engine, HONDA R&D Technical Review, F-1 Special, p. 143-146

■ Author ■


Koji UEDA


Ryuichi TAKAHASHI


Osamu KONNO

Presentation of 2006 Model RC211V

Kyoichi YOSHII* Koichi TSUTSUMI*
Nobuo SHIGEMIZU* Shin SATO*

ABSTRACT

A full model change of the RC211V was performed, in order to achieve highly controllable handling and enhanced cornering performance. The engine used in the new model is based on the light, compact, and high output V-type five-cylinder engine, which is the backbone of the RC211V, and has been made more compact and lighter. The entire completed machine has been re-designed for greater mass concentration, and the frame and suspension dimensions have been modified, enabling the moment of inertia of the overall machine to be reduced. In addition, the adoption of the Honda Intelligent Throttle Control System II (HITCS II), which electronically controls the fuel supply system for only two of the five cylinders, has enhanced maximum output and increased fuel economy and throttle controllability. In addition, the side area of the fairing has been reduced, resulting in greater handling performance.

Based on these results, a stable racing machine with high potential performance has been developed.

1. Introduction

The RC211V[(1)], which entered the Moto-GP race in 2002 and held the title for two consecutive years until 2003, lost the title for two consecutive years in 2004 and 2005. A study was performed to acquire the title once again. In the case where evolution due to only detailed changes in the machines that raced until 2005 was considered, it was believed that although the various kinds of electrical control could be evolved, the potential performance was not able to be enhanced. For this reason, it was decided to simultaneously develop a model in which the dimensions of the body were changed. The 2006 race was fought with two kinds of RC211V, an enhanced version (original) of the 2005 model and a new generation model that had undergone a full model change. Set out below is a description of the technology that is applicable to the new generation RC211V.

2. Development Concept

A Moto-GP class machine consists of a 148 kg machine fitted with an engine of a maximum output exceeding 180 kW.

Even if the maximum output of the engine is high, unless it has usable controllability, it will not have potential performance. The 2005 model RC211V was reliable in respect of total performance and had basic potential performance, however, it had insufficient stability during deceleration compared to rival machines, and because of this there were issues concerning cornering speed enhancement, and there were races in which the rider's skill could not be adequately utilized.

Based on these issues, it was decided to focus on highly controllable handling and enhanced cornering for the 2006 model. The development concept employed was the enhancement of total performance, which was intended to further controllability of the completed machine. The main three items of this concept were as follows.

* Enhanced deceleration performance
* Enhanced cornering performance
* Enhanced traction performance

In order to realize these performance factors, it was necessary to newly design both the engine and the chassis, so a new generation machine was developed (Fig. 1).

* Motorcycle R&D Center

Table 1 Major specifications

Item		Specifications
Overall length (mm)		2 050
Overall width (mm)		645
Overall height (mm)		1 130
Wheel base (mm)		1 440
Vehicle dry mass (kg)		Over 148
Engine type		Liquid cooled 4-stroke DOHC V-5 cylinder
Valve train		DOHC 4-valve
Engine displacement (cm^3)		990
Max. power (kw/r/min)		Over 180
Fuel supply system		PGM-FI
Ignition system		Digital CDI
Transmission		6-speed constant mesh
Clutch type		Dry multi-plate type (hydraulic)
Fuel tank capacity(Liter)		22
Frame type		Aluminum twin tube
Tire size	Front	16.5
	Rear	16.5
Suspension	Front	Telescopic
	Rear	Unit pro-link

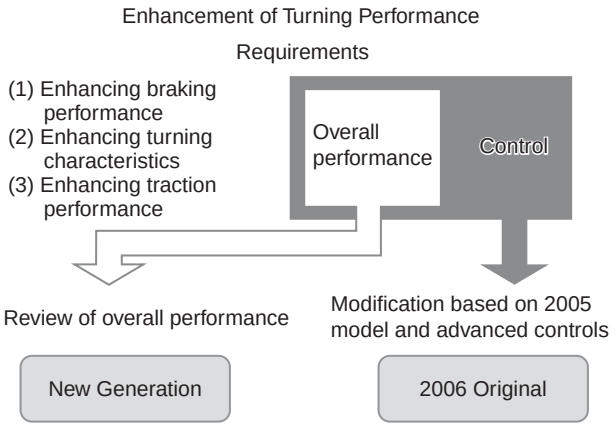


Fig. 1 Development concept

3. Model Outline

Table 1 shows the main specifications of the RC211V and Fig. 2 shows the exterior.

In order to enhance the deceleration performance, cornering performance, and traction performance, it is necessary to reduce the moment of inertia of the completed machine. To this end, it is necessary to concentrate the mass and change the frame and suspension dimensions. The most effective way of achieving this, while keeping the wheel base within that of the 2005 model, was to redesign the engine, which is the heaviest part of the machine and is located at the center of the chassis. This was an important point concerning the performance of the completed machine.



Fig. 2 2006 RC211V external view

4. Engine

The engine was not based on the models of the RC211V up to 2005. Rather, all of the parts, including the crankcase, were newly designed for making a light, compact engine. Figure 3 shows a comparison of the size of the 2005 and 2006 model engines.

By redesigning the engine details, the distance between the crankshaft and the transmission countershaft was reduced by 27 mm, the front cylinder was inclined 6∞ to the rear, and the length of the connecting rod was reduced by 4 mm, as well as the height of the cylinder head by 6 mm, each cylinder pitch by 5 mm, and the crankshaft width by 21 mm.

As a result, the length of the engine in the front-rear direction has been reduced by 60 mm and its width by 30 mm, compared to the existing V5 engine, which is highly appraised for its potential performance, without increasing the height of the engine. Weight was reduced by 7%, which contributes to the performance of the completed machine, and friction at each part was also reduced, enhancing the maximum output and torque. The resulting engine characteristics enabled the acceleration performance to be further increased. Figure 4 shows a comparison of the output characteristics of the 2006 model and that of the 2005 model.

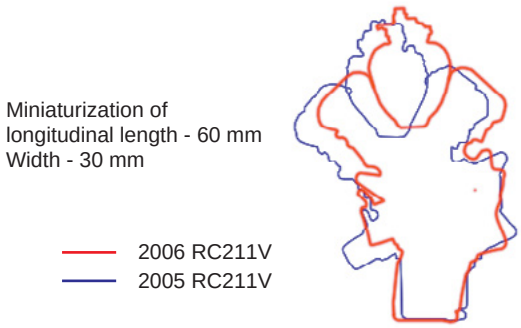


Fig. 3 Comparison of engine size

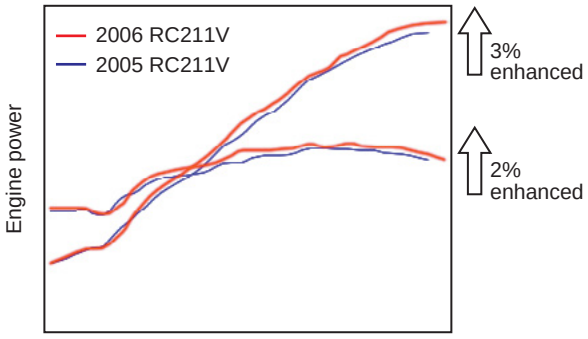


Fig. 4 Engine performance curve

5. Fuel Supply System

Fuel economy and throttle controllability are important items, and efforts were made to enhance both features. In order to achieve higher throttle controllability, it is necessary to perform finer throttle control.

In contrast to the uniform control of all cylinders (variable relaxation control) employed in conventional models, the Honda Intelligent Throttle Control System II (HITCS II), which controls the throttle of the front and rear banks independently, was newly adopted. In order to independently control the front bank, the HITCS II controls the three cylinders of the front bank by conventional throttle control (variable relaxation control), and controls the two cylinders of the rear bank by full electric control (motor drive). Compared to uniform throttle control of all five cylinders (variable relaxation control), control that conforms to the demands of the rider in situations where fine throttle control is required at the commencement of the opening of the throttle can now be performed, for example.

As a result, even though the maximum output of the engine was enhanced, the fuel economy was the same as that of the 2005 RC211V. The structure of HITCS II is shown in Fig. 5, and the throttle control of the front bank and rear bank is shown in Fig.6. In the region where the engine speed in 1st to 3rd gears is lower, the throttle opening of the rear bank is limited. Figure 7 shows the operating situation of the throttle opening and the increase in speed of the wheels. It indicates that by controlling the front and rear banks separately, the rotational speed of the rear wheel increases smoothly.

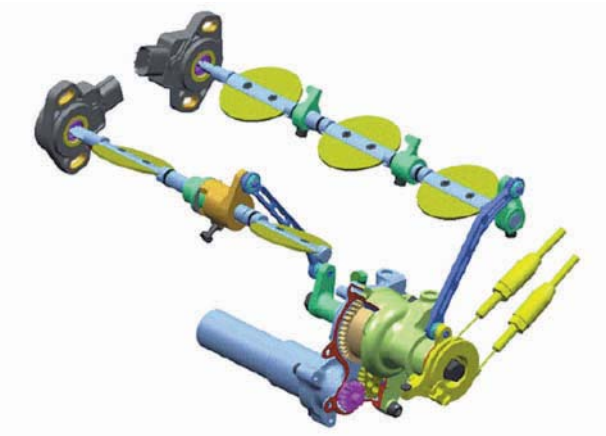


Fig. 5 Structure of HITCS II

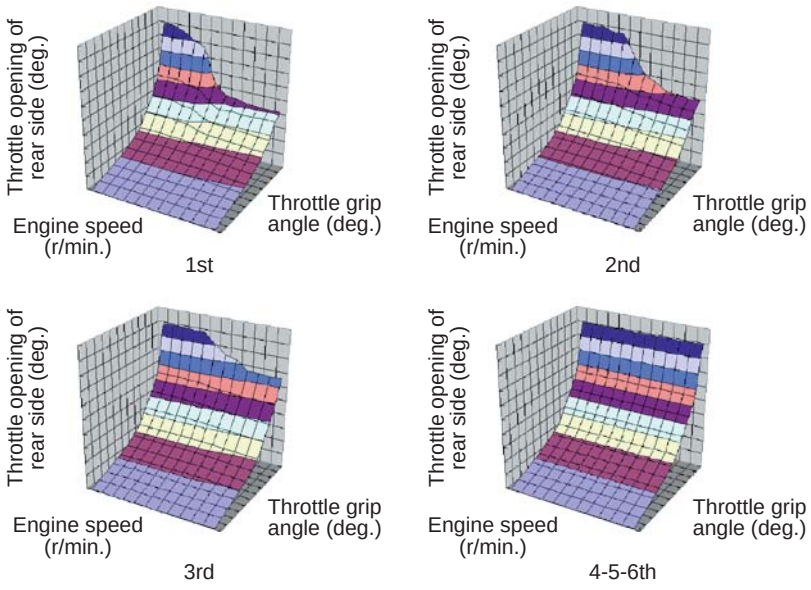


Fig. 6 Maps of front and rear throttle valve control

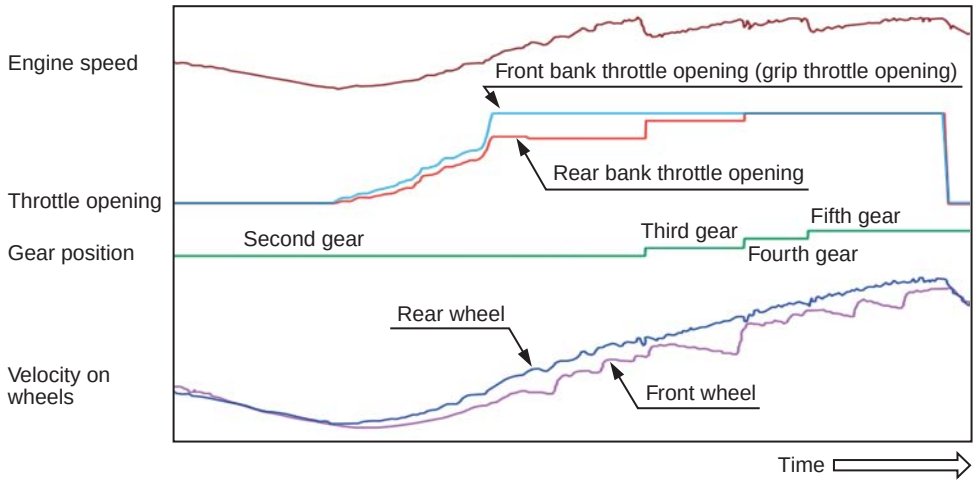


Fig. 7 Controlled throttle opening and wheel rotations

6. Frame

The compact, lightweight engine is mounted on a newly designed frame.

The dimensions of the frame were determined with the objective of enhancing the traction performance from deceleration to acceleration while enhancing the stability during deceleration. The greatest feature of the frame is the long swing arm fitted inside the wheel base, which is the same as that of the 2005 RC211V.

In general, when the wheel base is longer, the traction is enhanced, but the cornering performance decreases. When the wheel base is shorter, the cornering performance increases, but the traction performance decreases. In order to obtain dimensions that satisfy both of these characteristics, the reduced engine size was effectively utilized in the body design. Figure 8 shows a schematic diagram of the overall body.

Like the compact engine, the main frame was also made compact. At the same time, stiffness analysis using CAE was performed in order to clarify the parts of the frame that affected steering stability, and actual running tests were performed to determine the optimum stiffness balance. Figure 9 shows a comparison of the frame layout, and a comparison of stiffness between the 2006 and 2005 models.

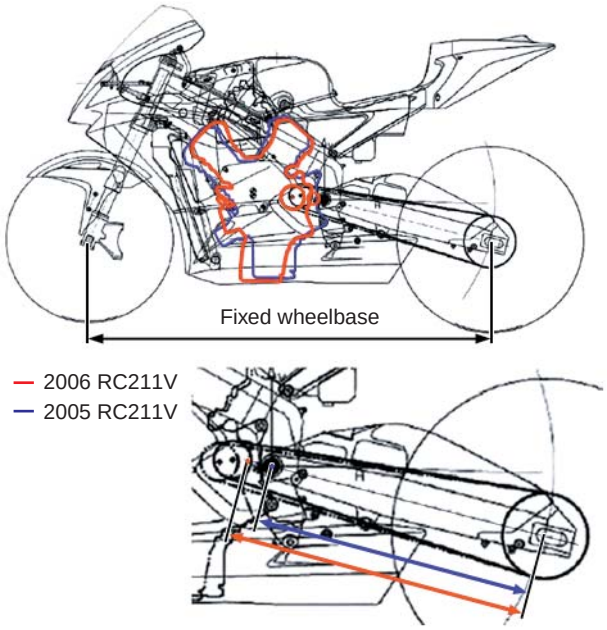


Fig. 8 Engine position and swing arm length

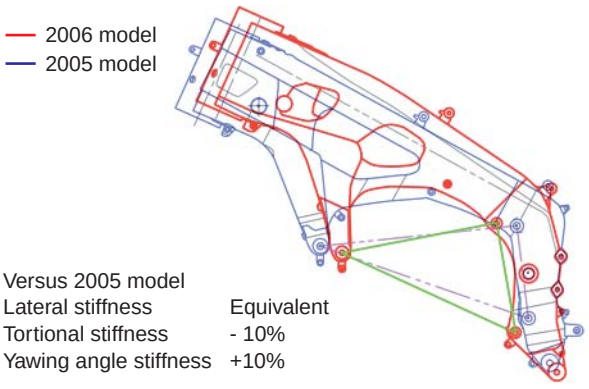


Fig. 9 Frame body

7. Suspension

In order to transmit the drive force from the engine to the ground, and enhance the cornering performance, the rear suspension and the swing arm were also newly designed. The objectives of this were to increase the stability when the machine was decelerating due to reduction of friction, and to enhance traction performance.

The rear cushion was located in the downward direction of the body, and the installation point at the top

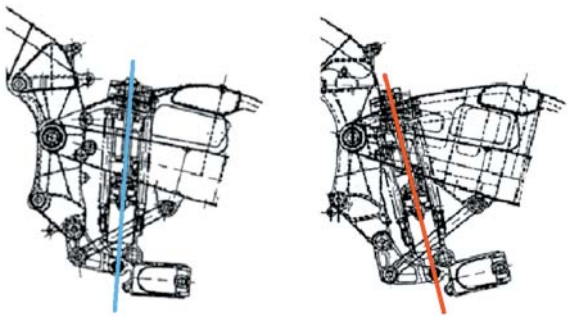


Fig. 10 Comparison of unit pro-link

of the rear cushion was brought near the pivot. In the design, the distance between the pivot and the link mounting part was increased, and the load at the link portion was reduced by at least 10% in order to reduce friction. Figure 10 shows a comparison of the unit pro-link mechanism of the 2006 model and that of the 2005 model.

8. Aerodynamic Performance

In the 2005 model, the side face area was reduced to enhance cornering performance. In the case of the 2006 model, many wind tunnel experiments were performed with a view to optimizing the profile, and light handling, stability in crosswinds, low air resistance, and wind protection were all satisfied. As a result, enhanced handling performance was realized while the same air resistance value as those of the 2005 RC211V were attained. Figure 11 shows a comparison of the side area of the fairing.

9. Results Achieved

The moment of inertia of the entire machine was reduced by 0.9% in the roll direction, 0.5% in the yaw direction, and 3.4% in the pitch direction. Also, the stability during deceleration, cornering performance, and traction performance were enhanced (Fig. 12).

The enhanced running stability during deceleration appears in the running data as a fluctuation of the engine speed or rear wheel speed. The 2006 RC211V exhibits less fluctuation of engine speed during deceleration, compared to the 2005 RC211V. The subsequent throttle opening has also increased, and the cornering speed has increased. These results are shown in Figs. 13 and 14, which show the running measurement data.



Fig. 12 Result of moment of inertia

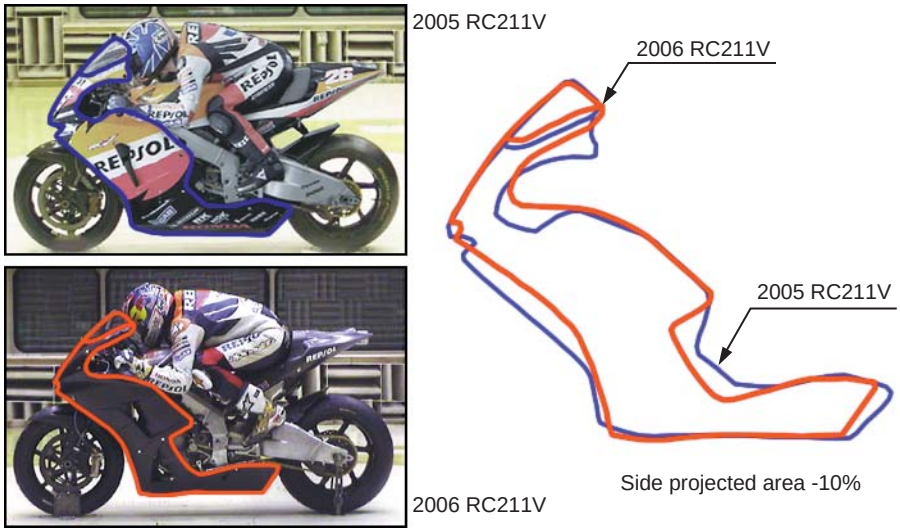


Fig. 11 Comparison of fairing

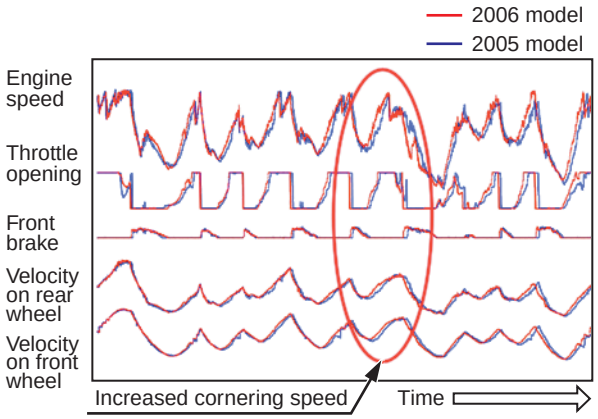


Fig. 13 Comparison of engine speed and wheel speed fluctuations in actual race

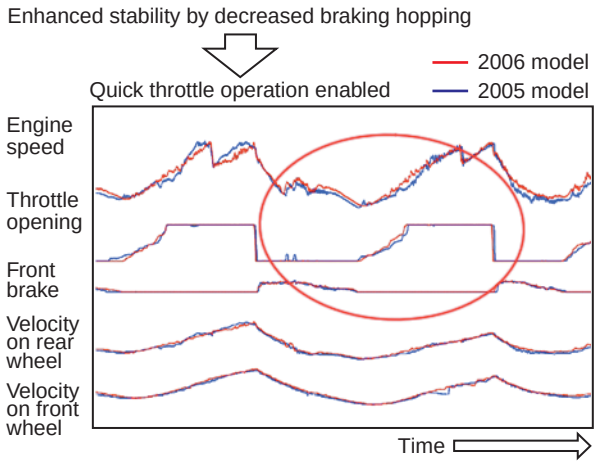


Fig. 14 Comparison of engine speed and wheel speed fluctuations in actual race (Enlarged detail)

10. Conclusion

The 2006 RC211V has achieved reduced moment of inertia of the entire machine due to the larger changes in the dimensions of the frame and suspension. The changes made to the electronic control of the fuel supply system have enhanced the maximum output, and enhanced fuel economy and throttle controllability. Also, deceleration performance, cornering performance, and traction performance, which were issues, have been enhanced in accordance with these objectives. As a result, this machine successfully regained the 2006 Moto-GP class rider's and manufacturer's titles.

Along with the change in the regulations in 2007, the RC211V will no longer be eligible to race, however the RC series will continue to take up technical challenges as an image leader of Honda super sports and as a symbol of challenging spirits.

Acknowledgements

The authors wish to sincerely thank the related persons at the cooperative manufacturers for their valuable cooperation.

Reference

(1) Kadomasu, H.: Presentation of RC211V Equipped with 4-Stroke Engine, Honda R&D Technical Review Vol. 15 No. 2, p. 17-24

Author


Kyoichi YOSHII


Koichi TSUTSUMI


Nobuo SHIGEMIZU


Shin SATO

Development of V8 Engine for American Le Mans Series

Trevor Knowles* Yasuhide Sakamoto* Tom Nickols*

ABSTRACT

A V8 engine was developed to optimize it for the Prototype 2 category (LMP2) of the American Le Mans Series (ALMS) racing. This engine was introduced at the 2007 Sebring 12 hour race.

The technical character of the performance, reliability and serviceability were all changed while keeping within the ALMS regulations such as a 44 mm inlet restrictor for the 3.4L V8 engine. The Indy Racing League (IRL) engine was utilized for the comparison reference. The effects of the significant differences between the series, such as the change from ethanol fuel to an ethanol/gasoline mix and changing from a rev limited engine running mainly on oval courses to an intake-restricted engine, running on road and street courses are discussed.

New test procedures that we created to assess engine hardware changes are discussed. Novel design features of the engine such as the valve gear detail and the combustion chamber design are reviewed.

1. Introduction

IRL rules give detailed limits on major engine dimensions including engine capacity, number of cylinders, cylinder bore, overall engine length, minimum engine weight, crankshaft dimensions, injector position, airbox dimensions and engine sensors[1]. ALMS rules are set by the organization responsible for the Le Mans 24 hours race, the Automobile Club de l'Ouest (ACO) and , in contrast, allow a variety of engine configurations and capacities[2].

Table 1 highlights the major differences in the rules between the two series and it can be seen that the ACO rules allow much more freedom of design and development over the IRL rules. While both series call for mechanical throttle control, fixed inlet lengths and



Fig. 1 General view of ALMS engine

Table 1 Comparison of IRL and ALMS rules

	IRL	ALMS
Engine configuration	3.0 liter, 90° V8	Up to 3.4 liters, 8 cylinder, N/A or Up to 6 cylinder supercharged.
Inlet manifold	Up to 2 injectors. Placed between throttle and head face. Fixed length	8 max. Vee or in-line
Power limit	10,300 rpm limiter	Inlet restrictor. Size based on engine configuration
Development constraints	Major castings, ports, combustion chamber, pumps, valve train gears	None
Fuel	100% ethanol	92% gasoline/10% ethanol
Noise limit	IRL-supplied silencer	113 dBA

* HONDA PERFORMANCE DEVELOPMENT INC.

fixed valve timing, they use different fuels and have different means of trying to limit engine power with the IRL controlling engine speed and the ALMS restricting the air intake. It was in these two areas where we focused our development.

2. Engine Specification

The priorities for the engine were reliability foremost, engine cost second and engine power third. In several cases this led us to choose the most reliable solution rather than the one that would give the greatest performance.

When we made the decision to enter the ALMS, the development engine specification was 2.8 liters. It had downward-facing injectors located just downstream of the throttle bodies with supplementary injectors located at the manifold-to-head joint. This joint face was as close to the inlet valves as possible to minimize the distance from these lower injectors to the cylinder. We did not change the main engine architecture as we wanted to use our resources to concentrate on other areas which had to change.

One such area was the airbox. The IRL airbox was flexible and leaked air where the air snorkel fitted to it and where it fitted to the head. The ALMS officials carry out a leak test at events in which the engine inlet has to maintain a 150 mbar vacuum for over half a second. The air box, made from carbon-fiber, reinforced plastic (CFRP), was stiffened by adding foam inserts to the floor and sides. The IRL specifies the latch to fix the airhorn to the airbox. These have a spring element in them. On the dynamometer, the combustion air supply pressure was sufficient to lift the airhorn off the airbox when the throttles closed. At higher speeds where the restrictor took effect, the joint closed up. This fatigued the fasteners in a few hundred miles' running. We changed to self-locking fasteners similar to those used to attach the car's body panels to the chassis.

Studying the ACO table of restrictor size against engine capacity showed that the 3.0 liter with its 44.7 mm diameter restrictor would allow the highest power output but we chose the more conservative route of having the maximum capacity with its corresponding smaller (44.0 mm) restrictor on the basis that this combination chokes at a lower engine speed. Reducing the engine speed would extend engine life.

The original IRL engine capacity was 3.5 liters, although this was reduced to 3.0 liters in 2004, so we knew that the crankcase would accommodate the longer crank throw to achieve the higher swept volume. Another change between the two series is the higher electrical load in ALMS to support the use of electric fuel pumps, electric power steering, lights, an on-board engine starter and, in our case, an electrically-operated gearshift. This meant we had to accommodate a larger alternator. This is driven off the back of the water pump, running at 0.48 engine speed. To protect them from vibration and heat, the alternator's electronics are remotely-mounted in the radiator inlet duct.

Table 2 Restrictors for normally-aspirated gasoline engines

	> 2 valves per cyl.	2 valves per cyl.
< 3000 cm³	44.7	46.2
>3000 and up to 3200 cm³	44.3	45.8
>3200 and up to 3400 cm³	44.0	45.5
Homologated engines up to 4000 cm³	44.7	46.2

3. Inlet System

Changing from ethanol to 92% gasoline and 8% ethanol fuel reduced the injector flow rate requirements. We decided to maintain the two-injector-per-cylinder layout as this allows us to modify the torque curve based on the proportion of the fuel flow through the upper injector. The lower injector near the inlet valves gives good response but little charge cooling from fuel evaporation while fuel from the upper injector cools the charge but displaces air. In an effort to reduce the cost of the engine, we tested injectors used on several Honda production cars. The 2006 IRL engine ran 10 bar fuel pressure but the production injectors would not open at such a high pressure. We reduced the fuel pressure to 5 bar to suit the injectors. Figure 2 shows power variation as injector type is changed. One can see that the alternative injectors reduced performance by almost 2% but, for this series, reliability is the most important characteristic. Rather than going for the injectors which gave the most power, we chose the Alternative injector 1

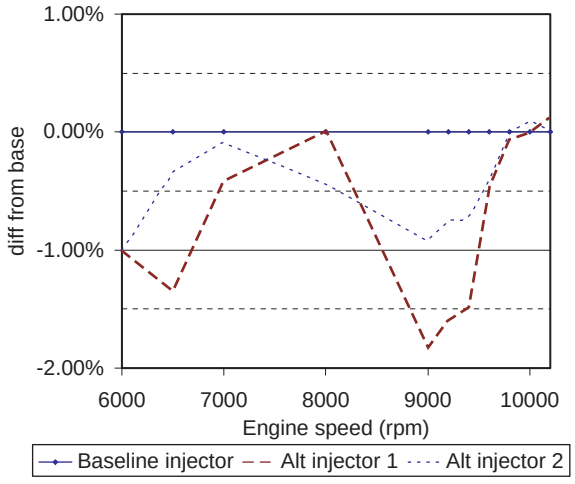


Fig. 2 Injector test results

as this design gave the most reliable starting, an important consideration for this series as the engine has to be shut off in pitstops and restarted using the on-board starter. The figure also shows that, when running in the restricted region, the injector has almost no effect on power.

The governing body caused some confusion over the restrictor size. The ACO reduced restrictor diameters for the P2 class by 5% for 2007. We set about optimizing the intake length to suit the lower choking speed this gave us. To ensure reliability, we had one-piece trumpets made of the appropriate length. At the end of the January, the International Motorsports Association (IMSA) who controls the ALMS rules enforcement announced that they would maintain the larger, 2006 restrictor sizes. This meant that our intake was too long for optimum performance but we decided to keep the one-piece trumpets for Sebring in the interests of reliability. Another late rule change was the introduction of fuel consisting of 92% 100 octane gasoline and 8% ethanol. This cost some performance and economy while needing a complete engine re-map.

4. Cylinder Head for ALMS P2

The cylinder head is a 4 valve per cylinder design with 10.4° exhaust angle and 8.5° intake angle. The poppet valves are fitted with twin coil springs, and are activated by a pair of camshafts per bank with finger followers located on a common axis.

Oil for the cylinder head is fed through the cylinder head to the camshafts. The shafts are hollow and distribute oil to the finger followers, cam bearings and spring cooling. There are two scavenge ports at either end of the spring chest core, and the core has a flat bottom to aid oil drain.

Support for the camshafts and swing arms are from twin buttresses between cylinders. This design was chosen for the space saving through the cylinder area.

The spark plug centrally located in the compact chamber passes through the spring chest core. A light weight alloy tube sandwiched between the cam cover and the head seals it from the engine oil. The ignition coils reside in these tubes and the wiring is attached to a carrier for the coils, which is covered by a CFRP cosmetic cover.

The swing arm assembly has been designed to be stiff, light weight and low cost. Originally

the shaft was designed as an interference fit to the top faces colored red in Figure 3.

The shaft could be fitted by hand and then drawn upwards to lock with the bore by tightening the bolts. This lead to a rather unsatisfactory condition where by the forces on the followers were great enough to overcome the system and lead to instability.

We redesigned the cylinder head to join adjacent pairs of buttresses together enabling a bolt through system that is now used in the race engines. Figure 4 shows how the pair of pivots are joined through the buttresses via an M8 stud and the finger followers are then retained by a special keeper. Lubrication is performed by splash via slots machined in the upper thrust faces of the arms.

An unexpected side effect from this change was that the valve train requires less power to drive. As shown in Figure 5, the new fixing method reduced the motoring power by 20% at high engine speeds.

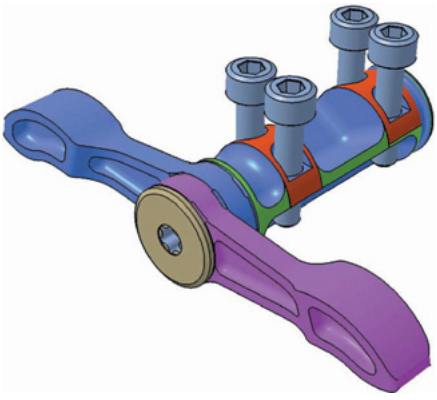


Fig. 3 Early swing arm location method

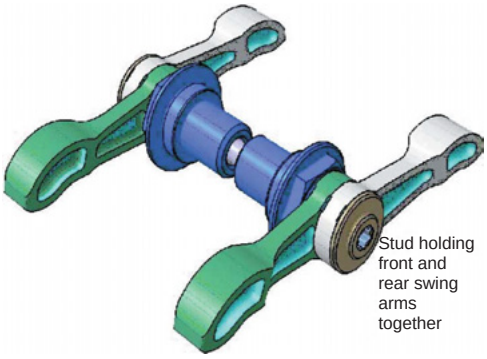


Fig. 4 Final swing arm shaft detail

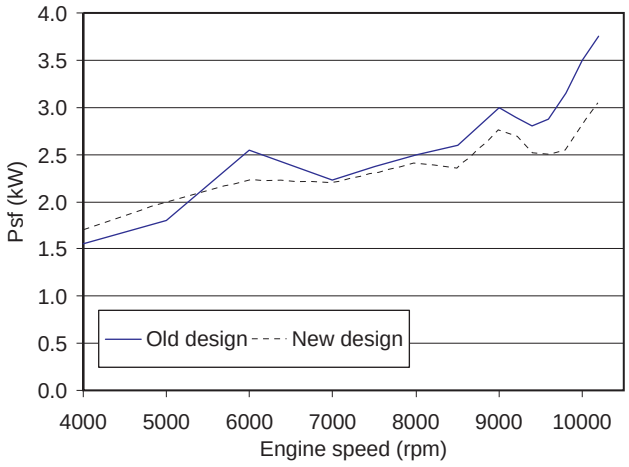


Fig. 5 Friction reduction with new design of shaft fixing

5. Durability Testing

The IRL engine target life was 600 miles. The initial target for the ALMS engine had to be at least 1400 to cover the Sebring 12 hour race. Moreover, the duty cycle between an IRL engine designed to operate mainly on oval circuits and the ALMS engine operating on road and street course would be different. At the time of the first durability test, we had no track data to use to set a durability cycle. Instead we used a simulation of a fast lap of Sebring with the power curve the engine had and the characteristics of the P2 chassis. The simulation had been developed by a consulting company for use in the IRL program so we were confident in its accuracy. In fact, when we did run at the track, the actual trace was close enough to the prediction that we made no change to the test cycle. After the Sebring race, where the combination of a tire with increased grip and the developed aerodynamic package allowed so much more wide-open throttle (WOT) running, we needed to revise the cycle. Figure 6 below shows the original and final traces.

Originally, we expected to have to include slow laps in the cycle but we soon learned that the races are run like sprint races. The drivers do not drive to conserve the car.

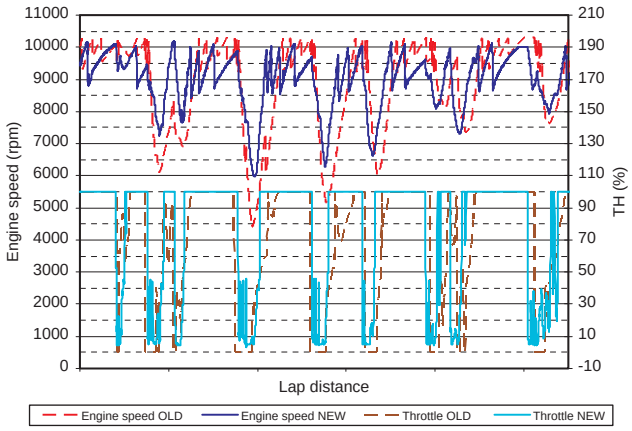


Fig. 6 Simulation speed throttle trace and final track data

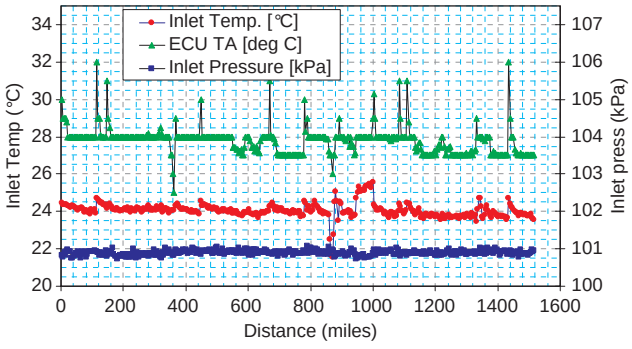


Fig. 7 Air inlet condition variation over test cycle

Durability testing ran on a test cell equipped with an alternating-current (AC) dynamometer to give fast response. The shift cut settings in the engine control unit (ECU) were tuned to match the dynamometer control to simulate shift-without-lift upshifts. The total cycle distance for a successful was equivalent to 1517 miles, based on a 3.7 mile lap of Sebring.

Initial tests ran standard atmospheric conditions but we were concerned that races as long as 12 hours take place under a variety of conditions and some may stress the engine more than others. Running at fixed conditions may miss the worst case and allow the engine to pass the test but fail on the track. Therefore, later tests used weather data taken from the 2006 race to vary humidity, temperature and barometric temperature. Figure 7 shows the inlet temperature and pressure variation over the test.

We did not take into account the charging effect due to the car moving through the air. This lead to detonation damage to car engines which we had not seen on the dynamometer engines. Following the realization of the importance of this, we vary the combustion air system pressure with simulated car speed.

6. Performance Testing

We used a technique of 1-D prediction to define the flow targets, flow-bench tests of SLA models (both inflow and outflow), prediction using these results, fine tuning of the shape and flow-bench and dynamometer testing of machined parts. Early tests showed a good correlation between the SLA models and actual cylinder heads provided the valve seat was accurate in the SLA piece although we did have some instances where the aluminum part results were different from the SLA results. This always was when the port had to change from the original design to accommodate manufacturing requirements. Port refinement was already underway as part of the IRL engine development when we changed direction. During this testing we modified the NE limit calculation to divide it by a typical volumetric efficiency factor, in this case 120%. This gave good agreement with the NE limit and the peak power engine speed.

To try to assess the effects of port design changes on drivability, we devised a transient power test using a rate of 2000 rpm/s based on acceleration rates from the 2005 St. Petersburg IRL race. 100 Hz data was smoothed by using a moving average of 7 data points. This testing confirmed that the IRL inlet port we had developed (IP26) would be too large for ALMS use. The first iteration, IP34, was created from the IP26 by adding material to the port floor. A further, later modification to improve lower injector nozzle clearance changed its designation to IP37. Another iteration, IP35, reduced the port volume further. Figure 8 compares the IP26 and IP35 ports.

Another new test, where the engine was held at WOT and 6500 rpm when the dynamometer control switched to absorb a constant 350 Nm. The time taken for the engine to accelerate to 10000 rpm was used another measure of the port's effect on engine response. Figure 9 shows an example of the results of such a response test with different sizes of inlet port.

These tests confirmed the improved response with the smaller port but also showed that we had not yet reached the lower limit. This led to the design of the smaller-diameter IP40 port. By this stage, port volume had dropped from 403 cc, for the IP26, to 320 cc for the IP40. As Figure 10 shows, this did provide a further benefit over the IP35 port at low speed and just before the restrictor went sonic but it was so small that we felt we were near the limit. Thus, rather than continuing to investigate smaller and smaller ports, we selected IP40 as the race port.

Apart from the ports being set to suit IRL racing, the camshaft design and timing also favored high-speed running. We designed several alternatives, with combinations of revised accelerations, lift version and duration as shown in Table 3.

Table 3 Development camshaft details

Camshaft spec	Intake		Exhaust	
	Lift	Duration	Lift	Duration
A400	15.34	253	12.46	236
B400	15.34	253	12.66	237
C400	14.33	254	11.65	237

The results of the camshaft changes can be seen in Figure 11.

As expected, the lower-lift intake camshafts suited the low speed nature best while the exhaust camshaft had little effect on performance.

Performance development is an on-going process in

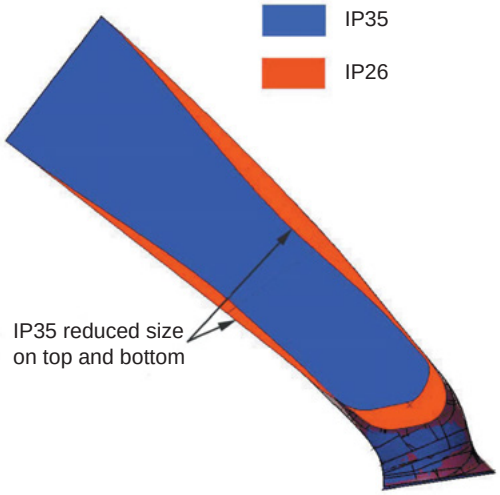


Fig. 8 Changes from IP26 to IP35 inlet port

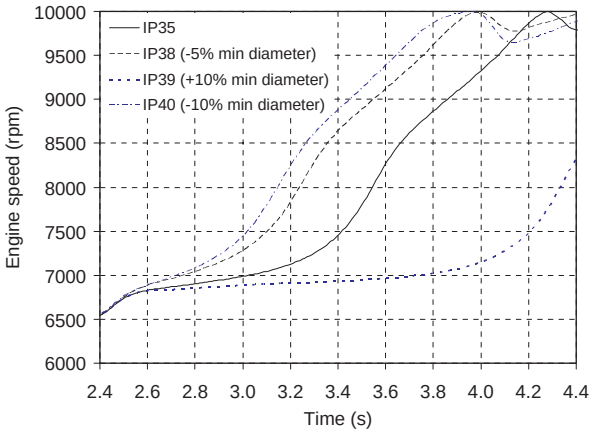


Fig. 9 Response of different inlet ports

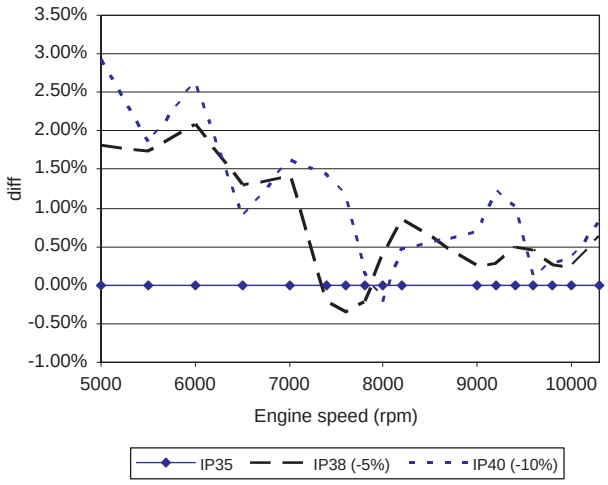


Fig. 10 Comparison of torque with different inlet ports

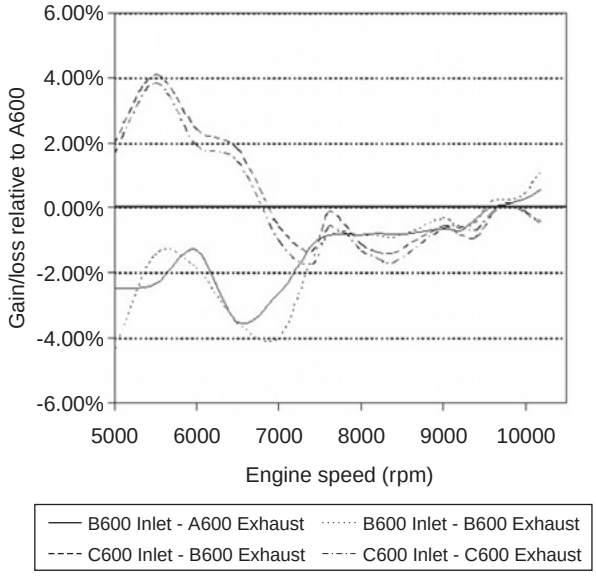


Fig. 11 Camshaft comparison

racing. We are still investigating the ideal inlet length, camshaft profile, exhaust layout, piston shape oil viscosity and pressure while trying to remove weight and cost from the engine.

7. Conclusions

We successfully have developed an ALMS LMP2 engine. Major changes from an IRL engine were focused on the airbox, fuel injector and alternator.

Despite using a conservative approach to ensure reliability, we were able to make performance improvements.

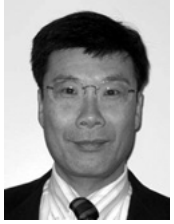
Using a knock-control system together with piston crown geometry changes allowed us to use as high a compression ratio with 92% gasoline / 8% ethanol mix as we had been using with 100% ethanol fuel.

Reference

(1) 2006 Indycar® Series Rule Book, p.147-155
(2) Regelement Technique ACO – ACO Technical Regulations 2007 Prototype “LM”P1 & “LM”P2, p.25

■ Author ■


Trevor Knowles


Yasuhide Sakamoto


Tom Nickols

Electrical System Development for American Le Mans Racing

Manminder Hayre* Marcelo Martinelli* Yasuhide Sakamoto*

ABSTRACT

The electrical system developed for the American Le Mans Series (ALMS) racing car, used a modular approach for both the engine control unit complete with associated satellite components and the interface and management of 3rd party devices. The basis of the system applied the modular approach by expanding the base engine control system; while still allowing continual development of the engine including different injectors and sensors, with optimized peripheral units for the different engine hardware.

Within the control system a shift to model-based code and simulation for software test and validation was developed and implemented. This resulted in the ability to provide strategies at an average of three times the rate compared with the previous system, and ultimately providing the higher efficiency of overall system application to changing targets.

1. Introduction

The designs of previous systems were very engine-specific with algorithms closely coupled to the specific hardware used on the engine. Additionally, the PC tools for the control system were specific products that all users had to be familiar with.

To economize on the resources used to produce and support a new generation of control systems and provide a more efficient development structure allowing multiple applications, a completely new approach was required.

The key points to be addressed with the new system were:

(1) The main component of the system i.e. Engine Control Unit (ECU), to have a life exceeding five years. Allowing the latest technologies to be applied without this system core being outdated.
(2) Provide enough expansion for not only engine control but also driveline control.
(3) Reduce the time from concept to track application for system operation and control algorithm development.
(4) Develop as close to ECU independent control algorithms as possible.
(5) The ability to apply the system to different or changing engine and vehicle specifications without the need for completely new hardware or software.

With the original system assumptions of driveline control and diversity in control applications, the correct steps to fulfilling the requirements for the first race application to be implemented with the Le Mans Prototype 2 (LMP2) project were in place. Figure 1 shows the Acura LMP2 car during initial testing of the new engine and control system.



Fig. 1 Acura LMP2 car

* HONDA PERFORMANCE DEVELOPMENT INC.

2. Engine Control Unit (ECU)

The design of the ECU incorporated very powerful Power PCs, using floating point computation and operating at clock speeds of up to 1.2 GHz, providing digital signal processing (DSP) and parallel processing with the potential of 600+ Million Instructions Per Second (MIPS). This would provide over 10x greater processing than the outgoing control system and the ability to easily implement auto-coding. Added to this was one of the latest Field Programmable Gate Arrays (FPGAs) for Input/ Output (I/O) processing and control. To these basics, up to 1GB of memory, multiple 400 Mbit/sec Low Voltage Differential Signaling (LVDS) high speed links and the implementation of four separate Controller Area Network links (CAN) were added allowing the addition of peripheral and 3rd party drive stages or data input units to the control system. In comparison to any previous system used for a motor racing application, this system far surpassed the processing, control speed and expandability. Figure 2 shows the ECU main component design.

3. Injector Driver Unit (IDU)

The distributed approach allowed the development of a custom designed injector driver stage for the LMP2 engine injectors resulting in a LMP2 specific IDU, while provisional engine development was being carried out on the dynamometer with the standard IDU.

Through investigations on the fuel bench, testing different injectors and their responses to different injector drive stages, an evolution of the standard peak and hold design was set. To this design, the extra functionality of injector diagnostics was added. Different injector current and voltage waveforms were processed and a signature for a working or broken injector identified. This signature resulted in using a simple but effective means of providing information on the movement of the injector pintle and hence a means to identify a non-operating injector. To allow firmware up-dates, CAN communication was incorporated into the design. High Density Integrated Circuit (HDIC) technology was used to address the size and weight reduction. This resulted in a successfully designed, developed and tested injector driver unit.

4. Knock Detection Unit (KDU)

With the use of gasoline for the LMP2 engine, there was a requirement to optimize the ignition to maintain the high compression ratio under all conditions. Also, due to the inconsistency of fuels at different racing tracks and the need to run at the optimum performance for long durations, a knock detection and control system was needed.

As with the IDU development, the distributed architecture of the control system allowed engine development to proceed with the available control system components before the addition of a usable KDU and software could be developed. As with the IDU, the additional goals of reducing component size and weight led to the implementation of HDIC for the KDU as well. To provide reliable working hardware without the need for extensive research and development, the design of the KDU used an existing Knock IC. This device processed one of four broadband analogue accelerometer inputs switched by a multiplexer. Figure 3 shows the architecture of the system with the Knock IC interfacing to the ECU via an FPGA.

To select the correct frequency and optimize the

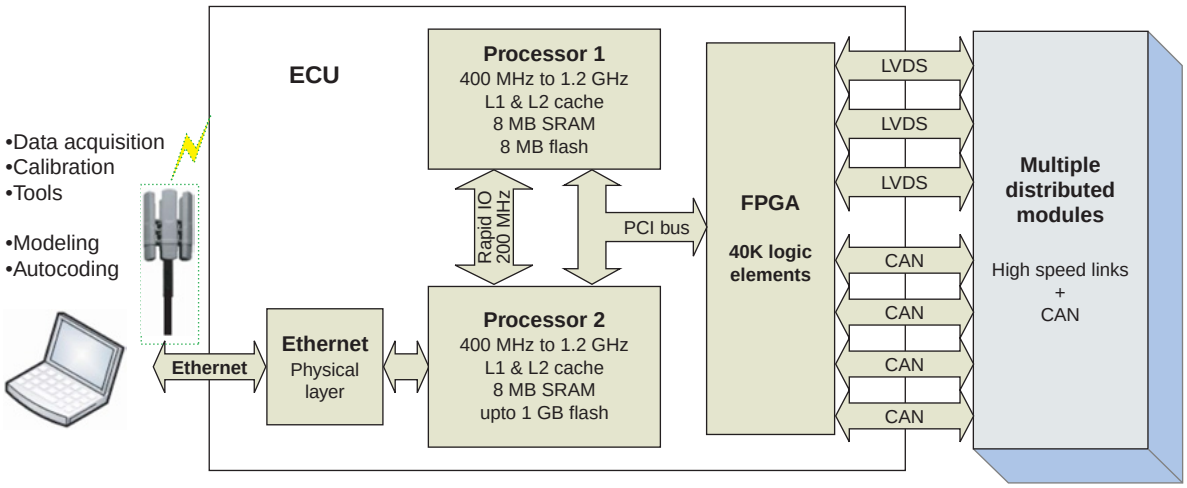


Fig. 2 ECU architecture

detection, high bandwidth knock sensor data and cylinder pressure data were gathered. The high sampling rate data was post processed using an in-house developed numerical computing model of the hardware to yield a target for the optimum filter pass frequencies and window angles. The upper filter frequency was dictated by the operating range of the sensor. The lower frequency was to encompass the 1st order frequency of knock without dropping into a high area of noise seen with lower frequencies. The band pass filter ranges where a result of an iterative process of data analysis. Figure 4 shows a plot of the minimum detectable cylinder pressure oscillations against engine speed for different data filtering ranges to determine the most suitable filter type and range. The three lines plot, Plot 1.the best signal to noise ratio with a high pass filter of >20 kHz. Plot 2. the chosen band-pass filter of 12 KHz to 20 kHz and Plot 3. the worst with a band-pass 6 kHz to 17 kHz filter. The optimum filter and frequency range, Plot 2, was chosen because it minimized the detectable cylinder pressure oscillations while also remaining within the knock sensors' operating range yielding a clear detectable knock event.

The development of the algorithm was split into an ignition open loop and a knock feedback numerical computing model both developed using a multi-domain simulation and model based design system platform. The Ignition model provided a baseline knock threshold ignition timing and integrated with the other ignition algorithms affecting the engine torque. The feedback model used two knock thresholds. One threshold caused an immediate retard with the other using a statistical means for control. The knock calibration continually evolved with data available from dynamometer and subsequent track testing. This led to the knock signal noise and probability of knock being determined through statistical analysis leading to a further evolution of the system.

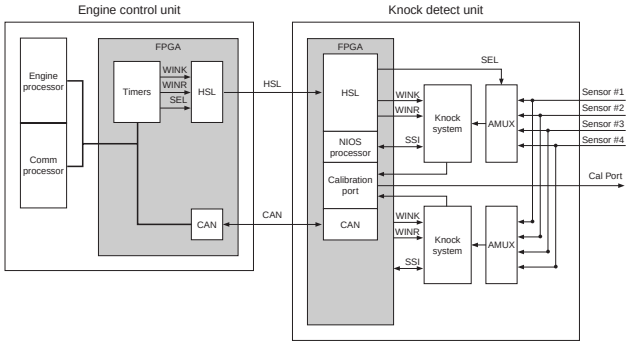


Fig. 3 KDU embedded architecture

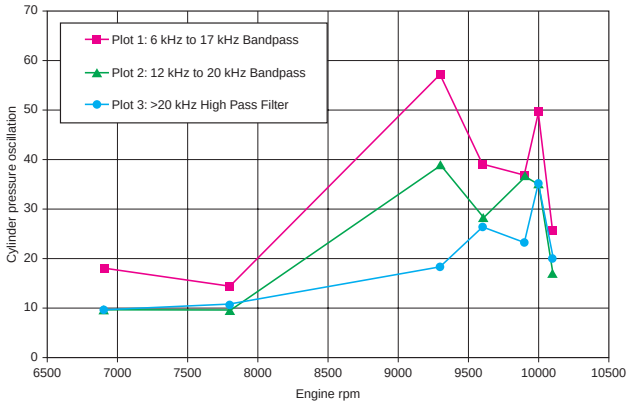


Fig. 4 Filter performance for knock data

5. System Communication Architecture

The distributed nature of the engine control system along with all 3rd party chassis electronic components required a unique communications and control architecture unlike the standard interfacing scheme previously used.

A configurable CAN interface was developed in order to meet the changing requirements for data sharing between engine ECU, chassis logger and telemetry radio. Figure 5 shows the System communication architecture. CAN buses were segregated into control and monitoring classifications in order to make the overall system more robust and fault-tolerant in the event of a link failure or link overload condition. CAN 4, blue lines, denotes monitoring only link. CAN 1, red line, denotes system control messages link. CAN 2 and 3, denotes 3rd party links with CAN 3 used for specifically for timing critical information. The use of CAN for driver/dash switches as well as expansion I/O, was a means to reduce overall wiring weight and still maintain the ability to attach additional sensors for testing and development purposes during the course of the season. Message transmission rates between the different buses varied from 10 Hz to 1 kHz.

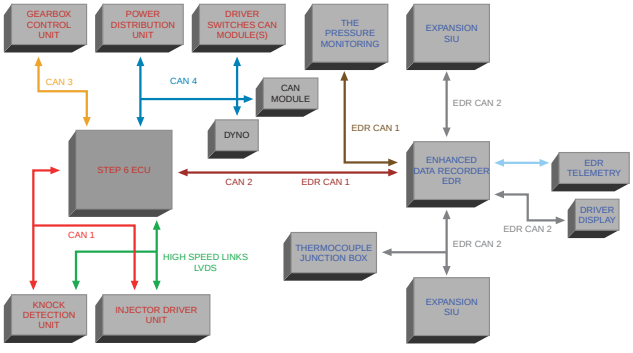


Fig. 5 System communication architecture

6. Embedded Software Structure

The embedded code was split into three layers to provide abstraction specifically for auto-coding, which was new for this system:

(1) HAL – Hardware Abstraction Layer
  (a) Lowest layer of software. Defines hardware drivers, input/output conditioning, interface to memory, register addresses, communications etc.

(2) VAL – Vehicle Abstraction Layer
  (a) Middle layer of software. Converts low level signals into engineering units.
  (b) Characterizes sensors like wheels speed, crank and cam, temperature, pressure, knock, etc. Converts calibrated injection end angle into a start angle.

(3) APP – Application Layer
  (a) Highest layer of software. Contains all high level functionality. Fuel and ignition control, pit lane speed limiter, yellow mode, idle control, shift control, knock control, engine torque control, etc.
  (b) This layer is auto-coded.

A Real Time Operating System (RTOS) was implemented for one of the processors to handle higher level controls, such as the Ethernet communications and other items. The main processor, however, required the development of bespoke drivers which provided the basics of the Hardware Application Layer (HAL). The result of this software structure together with the hardware design and firmware management was the application of a structured software code base. Figure 6 shows the flow of information organized in the different software layers. e.g. the decision on the injector angle is made in the APP layer. This decision interfaces with the VAL layer which translates the angle to a value associated with the calculation parameters i.e. the start angle. This is then translated to an actual time or/and event controlled by the ECU hardware in the HAL layer. Similarly, the raw inputs are read by the hardware specific devices. i.e. analogue to digital converters at the HAL layer. These are then translated to pulses or volts, i.e engineering units at the VAL layer then used in the algorithms for temperature, pressures or engine speed at the APP layer.

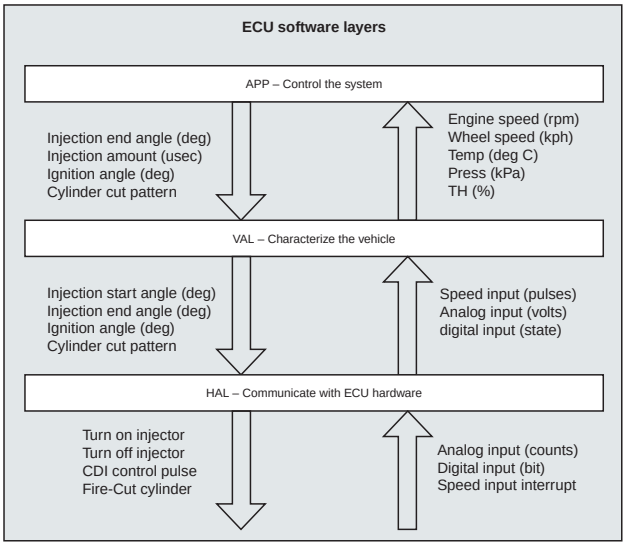


Fig. 6 Embedded software layers

As part of the software structure direction, the goal of reducing the time from concept to application code and hardware independency was realized by implementing 100% of the ECU embedded code application layer in model format.

7. Code Testing

To complete the loop for coding efficiency a custom configured Commercial Test Hardware and associated Open Source Software (CTHOSS) system was utilized to expand our testing capabilities. In conjunction with this and to compliment the ECU models we also had to develop plant models for testing and simulation. For the engine model, we started with a basic model of a V8 engine. To this, enhancements were made and then a transmission, drive shafts, uprights and basic tire model where added. The platform for the testing and implementation of the model-based environment was an industry standard numerical computing tool, multi-domain simulation and model based design platform in conjunction with the CTHOSS. The CTHOSS interface fitted in with our entire simulation and auto-coding environment. The same plant models where used offline as well as in hardware in the loop simulation. The two methods in which we used the system, connecting directly to an ECU were:

(1) Hardware in the Loop Simulation (HILS) - CTHOSS houses a plant model of engine and vehicle. ECU operates as if driving a real car.

(2) Bench tester – CTHOSS houses a model that maps buttons and dials, displayed on the screen of a PC, to ECU I/O.
  (a) User can manually exercise functionality, test hardware and check communications between different hardware modules.
  (b) User can run track accumulated or dynamometer data through the ECU.
  (c) Automated tests are run through the ECU to exercise existing functionality.
  (d) Representative signals had to be created for ECU excitation. i.e. variable reluctance cam and crank, wheel speed, knock, etc.

With the above approach, all the hardware that made up the vehicle electrical system could be connected together for bench testing prior to dynamometer or track running. i.e.

(1) ECU, gearshift controller, knock detection, injector driver, CDI, etc.

(2) Real system loads like injectors, spark plugs, shift actuator, all sensors, etc.

8. Conclusion

The development of the system provided new directions in many areas. On the controller side, the ECU used two power PCs running at speeds that are more associated with desktops. The implementation of the HDIC technology and the use of a multiplexed knock IC for the knock allowed the use of new technology with existing components but in a different environment. The use of injector movement signatures for the diagnostics again was new for the LMP project. The handling of the different component communications utilizing CAN at a much greater level than previously used, provided the ability to quickly add 3rd party components and expand the complete vehicle system but still provide diagnostic abilities through component fault interrogation and hence isolation. Figure 7 shows the extent of the electronic components required for an LMP car. On the software side, the implementation of model-based code and auto-coding the application layer was the basis of the new development environment and the goal of concept to code time reduction resulted in the release of a strategy at three times the rate as in the previous system approach. This was achieved by using the test hardware and having the ability to simulate the track environment better. Coupled with this was the development of the plant models for the engine driveline and system expansion, which provided more accurate simulations and hence the ability to provide a calibrated system for different circuits more feasible.



Fig. 7 LMP2 vehicle cockpit layout

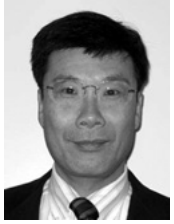
Author



Manminder Hayre



Marcelo Martinelli



Yasuhide Sakamoto

Low Noise and Lightweight Technology of Inverter Generator EU6500is

Yoshio TANAKA* Kaku OKABE*
Taiyo ONODERA* Takashi ITO*

ABSTRACT

A lightweight, portable engine generator, EU6500is, which has a rated output of between 4.5 and 5.5 kVA and a world top-level quietness was developed.

The EU6500is, which is based on the existing EM6500is open frame type inverter generator, on which an air-cooled single cylinder engine is mounted, employs a muffler cooling system with an air guide for cooling the muffler and realizes low noise and reduced weight due to the use of a highly rigid monocoque frame, and the like. As a result, the noise value L_{WA} at the rated output of 5.5 kVA was 90 dB. This is at least as low as the EU series soundproof frame type inverter generator, which has an output of about half that of the EU6500is. Also, while the noise emitted from the new generator is at least as low as that of the EX5500 portable engine generator, on which a 2-cylinder water-cooled engine of comparable output is mounted, the weight has been successfully reduced by 35% and the volume by 33%.

As a result, the new generator can cope with a wide range of needs, such as an emergency backup power source or for leisure, as the top model in the EU series.

1. Background

Portable engine generators are being demanded at many sites as emergency backup power sources for use in natural disasters, which have been occurring with increasing frequency in recent years, as power sources for electrical appliances, tools, etc., at work sites, as outdoor power sources for leisure, and the like. Also, in developing countries where power outages frequently occur due to the imbalance between supply and demand of electric power as a result of rapid economic development, many portable engine generators are being used as emergency backup power sources for electrical and electronic appliances in business and at home. As living standards rise throughout the world, the demand for electric power increases, resulting in greater needs for portable power sources. In order to cope with these various needs, higher quality electrical performance, lower noise, greater compactness, and reduced fuel consumption (reduction of CO_2) are being demanded.

An inverter generator has high quality electrical performance[1] and is also advantageous from the viewpoint of its performance, which is friendlier to the environment (low fuel consumption, low noise). By utilizing noise reduction technology in this inverter generator, a generator that meets these market needs as well can be produced.

Previously, a soundproof type generator with an inverter type generating system was mainly used for leisure activities, such as camping, so a generating system for the 3 kVA and lower class was developed. On the other hand, the market for emergency backup generators, for example, has also demanded higher output, at 5 kVA or more. Also, as a result of the widening applications of electronic appliances and the heightened interested in environmental conformity such as noise reduction, there are greater demands for higher quality electrical performance and lower noise. In order to meet these diverse needs, a system with the rated output of the generator set to 5.5 kVA was developed, focusing on noise reduction and weight reduction technology.

* Power Products R&D Center

2. Development Goal and Issues

Portable engine generators are divided into a simple, lightweight open frame type construction, and a soundproof frame type construction for reducing noise. Also, the generating systems consist of a 2-pole or 4-pole field rotating type cylinder alternator, which was the conventional system, and a combination of a multi-pole field rotary alternator and inverter unit, which has come into increasing use in recent years (Fig. 1).

In the development of the EU6500is, the noise target value was set to the same level as that of the existing EU series[1, 2] generators (EU1000i, EU2000i, EU3000is). The existing EU series used a two-tiered noise dampening system, and a load-dependent speed control function that reduces the rotational speed of the engine during light load operation, thus reducing noise in the heavily used practical use load range (hereafter called the service load range, from no load to 1/2 load) (Fig. 2). As a result, the noise target value of the EU6500is is no higher than a sound power level of L_{WA}80 to 85 dB in the service load range, and is less than 90 dB at rated load. These target values are approximately 10 dB lower than those of the EM6500is open frame type inverter generator.

When the sound power level of L_{WA}80 to 85 dB in the service load range was compared with the sound pressure level in a living area L_{PA} (Table 1), at a distance of 7 m from the generator, the noise level was roughly the same level as that of ordinary conversation (50 to 60 dB), which was recognized as an adequately low noise level, and so was set as a target.

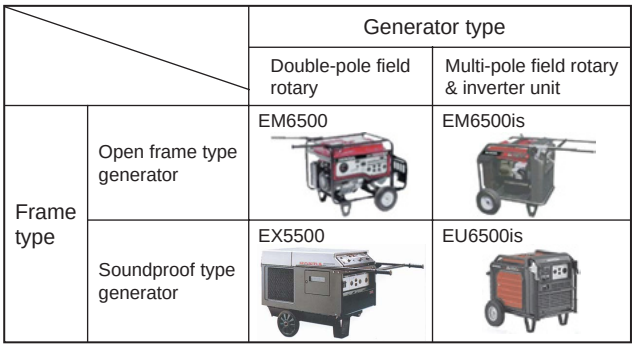


Fig. 1 Type of generator

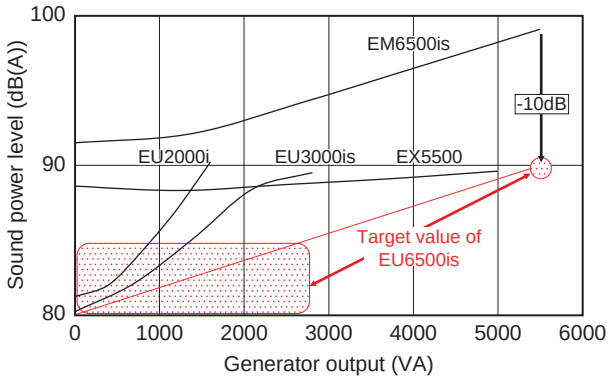


Fig. 2 EU series sound power level

Table 1 Sound pressure level in living area

Sound pressure level L_{PA} (dB)	Typical sound
100 – 110	Loud car horn
90 – 100	Noisy factory
80 – 90	Inside subway
70 – 80	Noisy office
60 – 70	Business office
50 – 60	Conversational speech
40 – 50	Living room
30 – 40	Library

Figure 3 shows the ranking in respect of weight and noise level of the open frame type generators and conventional model soundproof type generators, and the target value settings of the EU6500is. The EX5500 is a low noise generator, but it is heavy. Also, the EM6500is is light, but from a noise viewpoint, not as good as the EU series. Accordingly, it was decided to realize the abovementioned noise target in a generator of the same size and weight as those of the EM6500is.

The issues for achieving the above noise values and weight are shown below.

1. Simultaneous achievement of noise absorption and noise insulating performance, cooling performance, and compactness of the housing
2. Acquiring airtightness of the housing to keep noise leakage from happening
3. Development of low cost noise reduction technology

In order to address these issues, it was decided to develop a generator based on the lightweight and compact open frame type EM6500is inverter generator[3], which can achieve enhanced fuel economy and reduced noise by reducing the rotational speed in the service load range, using the same generating section and basic structure as

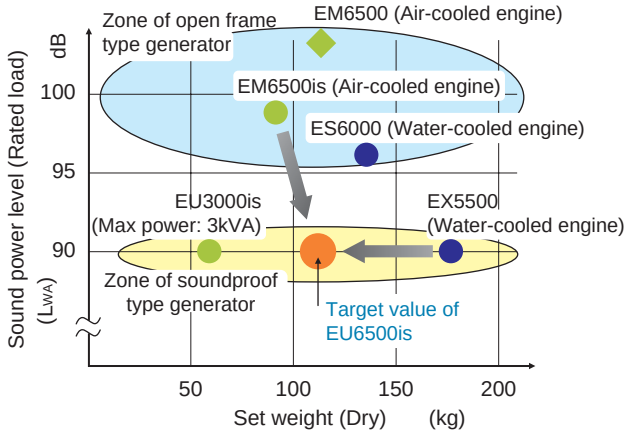


Fig. 3 Target positioning for sound power level and set weight

Table 2 Comparison of specification with EM6500is and EX5500

		EM6500is	EX5500
Engine	Displacement (cm^3)	389	359
	Speed (rpm)	∗ 2400 - 3600	3600
		☆ 3300 - 3600	
Operating noise level (L_{WA}; dB)		98	90
Generator	Type	Multi-pole field rotary	Double-pole field rotary
	AC voltage (V)	120/240	120/240
	AC frequency (Hz)	60	60
	Max. AC output	6500	5500
	Rated AC output	5500	5000
Dimensions	L × W × H (mm)	810 × 672 × 692	942 × 580 × 650
	Dry weight (kg)	97	177

∗ : Eco SW ON
☆ : Eco SW OFF



Fig. 4 External view of EM6500is and EX5500

that of the EM6500is.

Figure 4 shows the exterior of the soundproof type EX5500, which uses the conventional cylindrical type alternator, and the EM6500is base inverter generator, and Table 2 shows a comparison of the main specifications.

3. Noise Reduction Technology

The noise emitted by the EM6500is base generator was analyzed using the noise masking method. Figure 5 shows the noise contributory ratio. In order to reduce the noise emitted from the EU6500is, it was decided to reduce the noise emitted by each of the following four paths, which constitute 97% of the cause of the generator noise.

1. Path of engine radiation
2. Path of air intake system
3. Path of exhaust system
4. Path of cooling air outlet

The methods used to reduce noise in each path are shown below.

3.1. Reduction of noise from the path of engine radiation

In order to reduce radiation of mainly mechanical noise (radiation noise, due to additional vibration force of engine, valve system noise, piston noise, fan noise, and the like) emitted from the engine, it was decided to adopt a two-tiered noise dampening system consisting of a shroud and a housing outer panel covering the entire periphery of the engine. By making the space formed by the shroud and the housing outer panel a sealed space, the generator was provided with a soundproofing effect. Also, regarding the housing, leakage of noise was prevented by using a clearance seal.

As a result of the above configuration, engine radiation noise was reduced by 95%, in terms of energy level, compared to the open frame type EM6500is. Details of the lightweight and highly sealed housing structure are described in Section 4.

3.2. Reduction of Noise from the Air Intake System

Figure 6 shows the layout of the air intake system.

For this air intake system, the air intake system of the EM6500is was used, with an expansion room additionally installed mid-way between the narrow part, which is made of rubber, and the air intake path at the air intake port, in order to acquire a high transmission loss of noise so as to reduce the air intake noise, which was emitted from the EM6500is mainly between 200 and 500 Hz. The resulting change in transmission loss is shown in Fig. 7.

As a result of the change in the air intake system, the air intake noise was reduced by 70% of that of the EM6500is in terms of energy level.

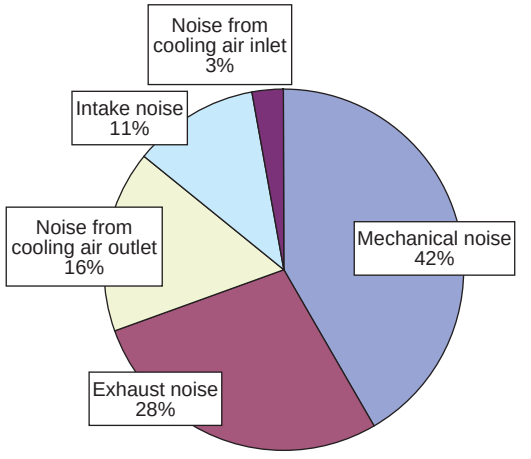


Fig. 5 Sound contribution ratio (EM6500is)

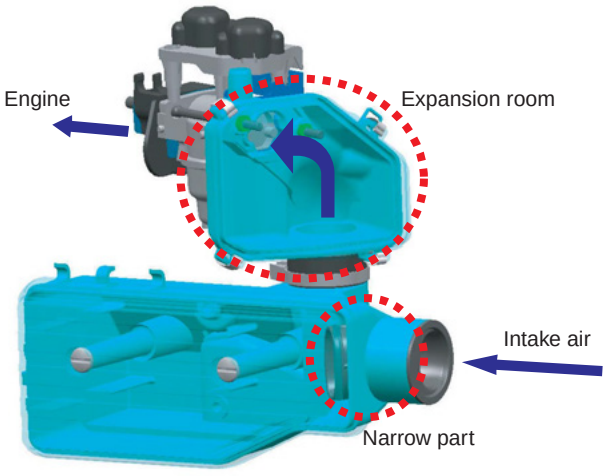


Fig. 6 Layout of intake system

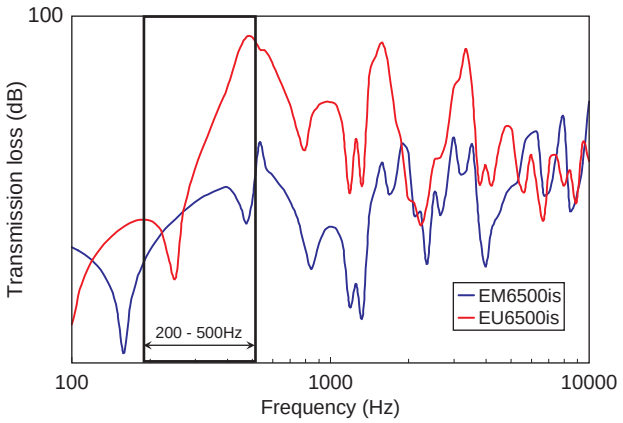


Fig. 7 Comparison of transmission loss (EU6500is, EM6500is)

3.3. Reduction of Exhaust Noise

In order to reduce the exhaust noise, a 6.4 liter big muffler structured with four chambers, with acoustic absorbent installed in part of the expansion room, was adopted. The end part of the entrance side of the internal chamber joint pipe was flared in order to reduce exhaust gas flow noise and back pressure.

As a result of the increased size of the muffler and change in the internal construction, noise from the exhaust outlet was reduced by 95% in terms of energy level.

3.4. Reduction of Cooling Air Outlet Noise

The main noise source in the cooling air outlet system is engine mechanical noise radiated from the exhaust air outlet. Although it was decided to reduce this engine mechanical noise, if an air-cooled engine is used as the motive power source there will be a risk of a change in the cooling air path, causing the cooling performance to fall. Consequently, with a focus on the cooling performance, and by changing the muffler room structure, the associated noise reduction was examined.

The development targets with respect to the EM6500is were the following three points.

(1) A reduction of the noise energy emitted from the exhaust air outlet of at least 80%
(2) A cooling performance at least as good as that of existing generators, both when the generator is running and after it has stopped
(3) Lightweight and compact structure

Figure 8 shows the cooling structure of the EM6500is for reference.

The concept of cooling in the EM6500is, both when the generator is running and after it has stopped, is as follows.

Cooling when the generator is running: Cooling is performed by forced convection generated by a cooling fan that is directly connected to the engine, in sequence from low heat generation.

Cooling after the generator has stopped: An incline is formed on the internal structure of the housing, and heat is allowed to dissipate by free convection from the exhaust air outlet at the top end.

In the case of a conventional portable engine generator, compactness is demanded, so as shown in Fig. 8 the exhaust air outlet and engine are brought close to each other, and as a result there is a tendency for the engine mechanical noise from the exhaust air outlet to increase.

Methods of reducing this mechanical noise include a method in which noise insulating material or acoustic absorbent is installed near the exhaust air outlet, and a method in which the area of the exhaust air outlet is reduced, with a silencing chamber added after the exhaust air outlet[4]. However, these methods generate issues such as exacerbating cooling performance and increased size. For this reason, all of the targets using conventional methods were not easily achieved.

In this development work, the above issues, which were in a tradeoff relationship, were addressed by installing the air guide shown in Fig. 9 between the engine and the muffler.

3.4.1. Noise reduction

The installation location of the air guide was determined so as to partition the muffler and engine for the following three reasons.

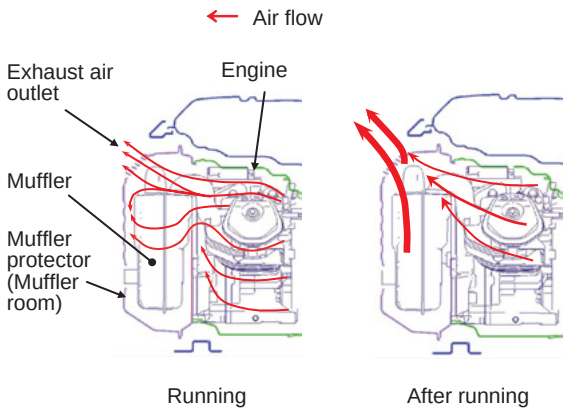


Fig. 8 Conventional cooling system (EM6500is)

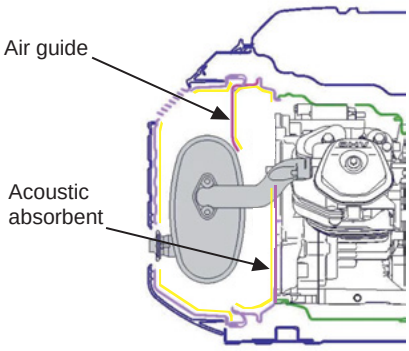


Fig. 9 Air guide

(1) The engine mechanical noise that is discharged directly from the exhaust air outlet is able to be reduced.
(2) Because the cooling air path is able to be lengthened from the engine to the exhaust air outlet without increasing the overall length, noise is able to be attenuated using a compact structure.
(3) Maintaining the cooling performance (Described in 3.4.3.)

Here, in order to increase the effect of (1), the air guide was made into a shape such that the engine could not be seen directly from the exhaust air outlet. Also, to increase the effect of (2), acoustic absorbent was installed inside the cooling air path.

As a result of measurement, it was found that by using the air guide, the noise energy reduction in the exhaust air outlet was 90%, which exceeds the target value. Also, the feeling of noise was lessened due to a reduction of unsteady noise in the high frequency range resulting from the use of acoustic absorbent.

3.4.2. Cooling performance during operation

There was apprehension that the installation of the air guide might have decreased performance of the engine and the muffler during operation as a result of reduction of the cooling air flow due to pressure loss, however the engine oil temperature and the temperature of the electrical parts during operation was of the same level as that of existing models.

Regarding the cooling performance of the muffler, the temperature of the exhaust gas inside the muffler was measured. As a result of temperature measurement, it was found that the exhaust gas temperature fell by approximately 30°C. This indicates that the air guide causes the cooling air to be rectified, enabling the surface of the muffler to be efficiently cooled. The enhanced cooling of the muffler reduces the risk of after-burn after the engine has stopped. Figure 10 shows a pattern diagram of the flow of cooling air around the muffler and the ambient cooling air flow during operation rendered visible using the tuft method.

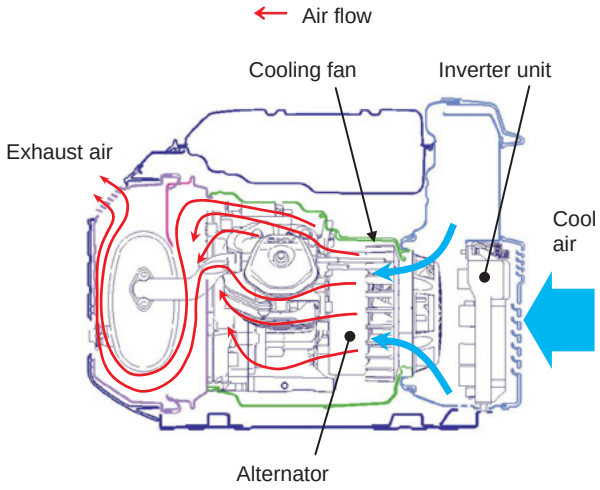


Fig. 10 Ambient airflow of muffler (Running)

3.4.3. Countermeasures for heat after the engine-stop

An important point in cooling an air-cooled soundproof type generator is the adoption of countermeasures for heat after the engine has stopped. In the case of a generator that uses an air-cooled engine, because the cooling fan is directly connected to the engine, the supply of cooling air stops as soon as the engine stops. As a result, the atmospheric temperature in the vicinity of the muffler, which is the hottest part inside the housing, rises abruptly as soon as the engine stops. If this high temperature air flows in reverse to the engine chamber or electrical chamber, the functions of the electrical and plastic parts may fall, and the restarting performance may fall due to the increase in temperature of the gasoline inside the carburetor float chamber.

In the case of the EU6500is, conventional heat dissipation due to free convection was developed in order to address the heat issue after the engine stops.

The installation location of the air guide was set at a partitioning position between the muffler and the engine. This was done so as to utilize the free convection (updraft) generated by the heat of the muffler after the engine stops, in order to actively exhaust the heat inside the housing. Figure 11 shows the flow of heat after the engine stops.

When the engine stops, the muffler atmospheric temperature (T_m) abruptly rises. As a result of this temperature rise, the gas in the vicinity of the muffler becomes an updraft, and is exhausted from the exhaust air outlet to the outside of the housing.

Also, the air guide causes the partitioned engine atmospheric temperature (T_e) to rise as well. However, as a result of the updraft in the vicinity of the muffler, the air in the engine atmosphere is drawn to the bottom of the muffler chamber. Next, it is heated by the muffler to become an updraft and is exhausted to the outside of the housing.

Because the entire engine is covered by the shroud, the cooling air path from the cooling air inlet to the exhaust air outlet has been made a closed path, hence this heat

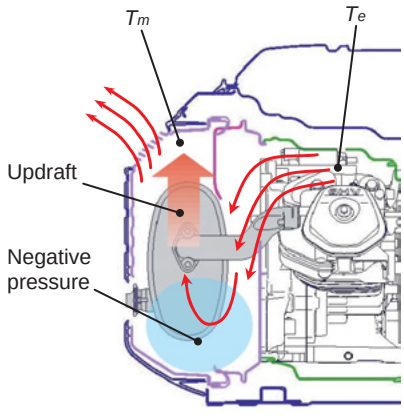


Fig. 11 Waste heat flow (After running)

flow is generated continuously immediately after the engine stops.

Figure 12 shows the relationship between the muffler atmospheric temperature (T_m) and engine atmospheric temperature (T_e) after the engine stops.

Immediately after the engine stops, the muffler atmospheric temperature rises to a maximum of 200°C, but the engine atmospheric temperature does not rise past 100°C. This indicates that the hot air near the muffler is being discharged to the outside of the housing, without flowing in the reverse direction. Also, because the heat is dissipated continuously, the temperature inside the housing falls along with the passage of time, and the result obtained was of the same level as that of existing soundproof type generators.

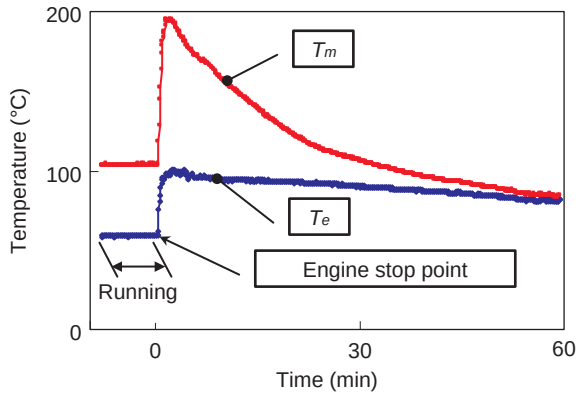


Fig. 12 Temperature of T_m, T_e

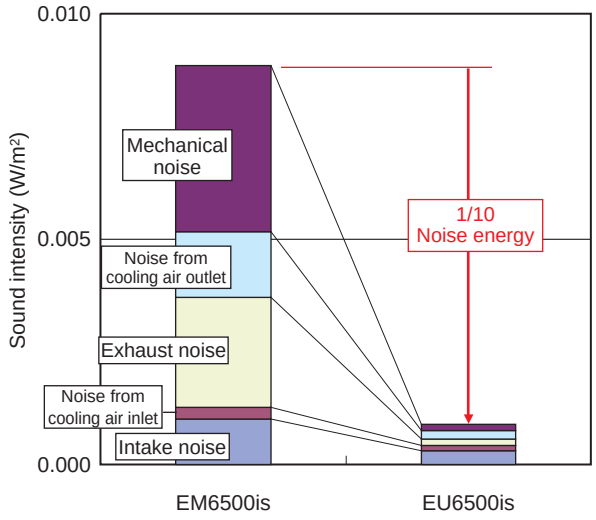


Fig. 13 Effective noise level

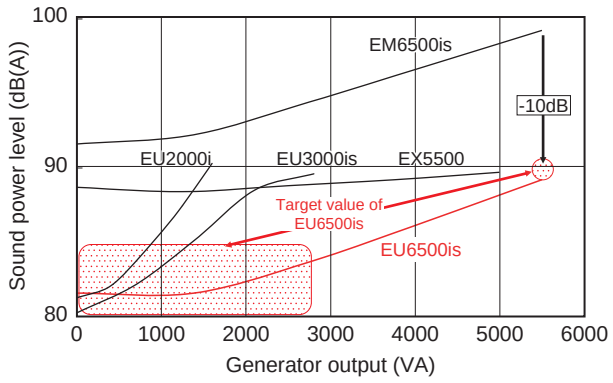


Fig. 14 Sound power level

Figure 13 shows the noise contributory ratio of each noise transmission path concerning both EU6500is, for which countermeasures have been taken in respect of the above four paths, and EM6500is, and Fig. 14 shows a noise comparison between the target value and the values for other models.

Compared to the EM6500is, the noise level in terms of noise energy has been reduced to 1/10, and a level of L_{WA} 90 dB was attained at the rated load. Also, the noise performance was at least as good as that of the existing EU series (rated output 2.8 kVA or below).

4. Lightweight Frame Technology

The EU6500is realizes a weight and volume reduction compared to the EX5500 soundproof type generator, which produces the same order of output, due to the abovementioned noise reducing technology, cooling structure, and monocoque frame structure. Details are described in this section.

Reduction of weight and cost of the frame structure of a soundproof type generator is an issue. The issues concerning a soundproof, lightweight frame are as follows.

1. In order to increase the soundproof performance, a highly sealed structure is necessary.
2. Rigidity using the outer panel alone should be able to be secured, without increasing the weight, even when a maintenance door is provided.
3. Easy assembly, without increasing the number of parts, should be able to be secured.

Figure 15 shows the basic frame structure of the conventional EX5500 and the EU6500is.

Conventional large soundproof type generators, including the EX5500, mainly use a frame structure consisting of a highly rigid ladder frame with stiffeners installed in the perpendicular direction to fix the outer panel. In this case, it is easy to replace the panel, but on the other hand, there is a tendency for the number of parts to increase, which is disadvantageous from the viewpoints of lightness and cost. Also, airtightness is not able to be easily secured by increasing the area of the mating faces of the outer panel.

Accordingly, it was decided to make the EU6500is of a simple construction in which the under-frame supporting the heavy sprung weight, such as the engine and alternator, consists of a combination of pipes and channels. The stiffeners in the perpendicular direction were integrated with the outer panels on the left and right

sides, and were then welded to the under-frame to form a monocoque frame. As a result, strength that permitted the generator to be hoisted without any need for special stiffeners in the vertical direction was obtained. The under-cover can be set so that its only function is to reduce noise, and weight reduction and low cost can be realized by using plated steel sheet.

The maintenance cover was formed simultaneously when the side panels were being pressed, and the frame was designed in such a way that there was no waste material, thus reducing the cost considerably. Also, to facilitate engine mounting, the front was opened wide, and the engine was connected to the front frames.

The monocoque frame structure provided adequate rigidity, so a structure in which the front and rear were covered by a plastic cover having a high degree of freedom was used, realizing greater weight reduction and higher sealing performance. Also, the fuel tank was made to function as an upper cover, thus contributing to additional weight reduction.

As a result, the number of main frame components was reduced from 19, as used by the conventional EX5500 model, to 8, and the weight was reduced from 81 to 27.5 kg, and in addition, the soundproofing effect was successfully increased.

The results are shown in Table 3.

Table 3 Number of frame components and weight reduction effect

Item \ Type	EX5500	EU6500is	Reduction ratio
Number of principal constitute parts for frame	19	8	–58%
Weight of principal constitute parts for frame	81.0 kg	27.5 kg	–66%

Table 4 Specification of EU6500is

		EU6500is
Engine	Displacement (cm³)	389
	Speed (rpm)	✻ 2400 - 3600
		☆3300 - 3600
Operating noise level (L_{WA}; dB)		90
Generator	Type	Multi-pole field rotary
	AC voltage (V)	120/240
	AC frequency (Hz)	60
	Max. AC output	6500
	Rated AC output	5500
Dimensions	L × W × H (mm)	850 × 672 × 699
	Dry weight (kg)	115

✻ : Eco SW ON
☆ : Eco SW OFF

5. Conclusion

The newly developed EU6500is has a noise level of approximately 10 dB less than that of the EM6500is. It achieved a value of L_{WA} 90 dB, which is the same as that of the existing EU series (EU1000i, EU2000i, EU3000is). Also, the noise level is approximately 5 dB lower than that of the EX5500 soundproof type generator in the service load range, which produces the same order of output (Fig. 14), and the weight has been reduced by 35%, as well as the volume by 33%.

The points that were enhanced in this development are as follows.

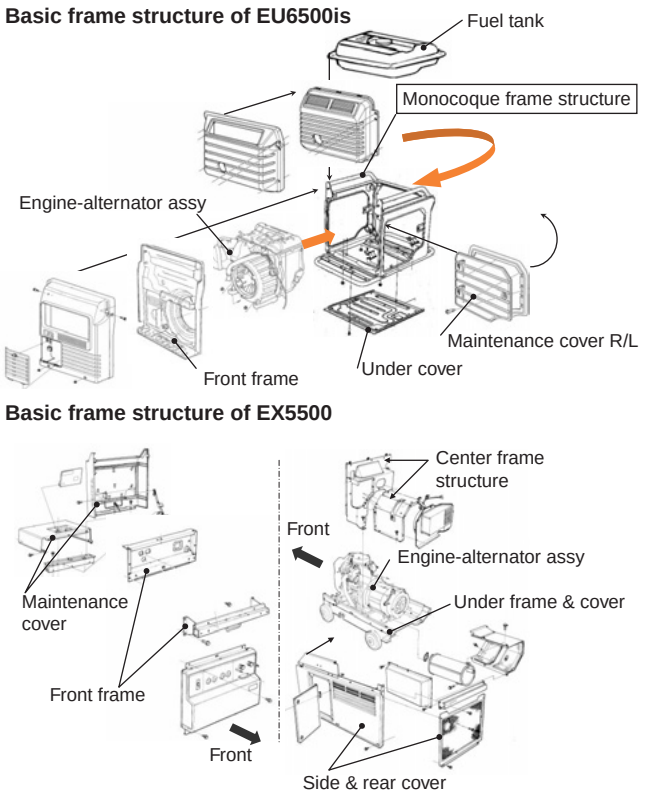


Fig. 15 Frame structure of EU6500is and EX5500



Fig. 16 External view of EU6500is

1. The noise generation and transmission paths are divided into four (engine radiation system, air intake system, exhaust system, and cooling air outlet). Countermeasures were adopted for each path, resulting in a noise reduction of approximately 10 dB, compared to the EM6500is.
2. An air guide was installed in the cooling air path, enabling noise from the cooling air outlet to be reduced and cooling performance to be maintained, without increasing the capacity of the muffler room.
3. A lightweight and compact soundproof type frame was made by using a lightweight, highly airtight, and highly rigid monocoque frame structure.

By employing these noise reduction and weight reduction technologies in the EM6500is, results could be obtained that conformed to the target, and a generator that has higher product strength has been developed.

Table 4 and Fig. 16 show the specifications and exterior of the generator.

References

(1) Kouchi, T., Ito, K., Nakamura, M.: Development of a Lightweight and Compact 1 kVA-class Potable Generator, SAE Paper, 1999-01-3304 (1999)
(2) Kouchi, T., Shimizu, M., Hirose, T., Sugimoto, Y.: Development of Lightweight, Compact Sine Wave Inverter-Equipped EU16i Generator, Honda R&D Technical Review, Vol. 13, No. 2, p. 35-42
(3) Nakamura, M., Kasagi, S., Hirose, T., Shinkawa, Y., Asai, K., Kamimura, K.: Development of EM7000is Dual-voltage Inverter Generator, Honda R&D Technical Review, Vol. 16, No. 2, p. 55-64
(4) Fukuda, T., Maruyama, K., Takemura, K., Suzuki, S.: Study of Sound Isolation Structure for Engine Generators, SAE Paper, 2005-32-0070 (2005)

Author


Yoshio TANAKA


Kaku OKABE


Taiyo ONODERA


Takashi ITO

Development of Electric Power Steering System for ATV

Tomokazu SAKAMOTO* Megumu OKADA* Kazushiro INOUE*

ABSTRACT

An electric power steering system (EPS) has been developed for an all-terrain vehicle (ATV), based on an automobile EPS system. The new EPS has been employed in the 2007 TRX500FPE FourTrax Foreman 4X4 ES. The EPS unit has been made compact to enable fitting without having to modify the vehicle configuration. Optimization of the size of the motor, the reduction ratio, and the spring rate of the torsion bar has enabled the prior ATV steering torque to be halved in both 2WD and 4WD operation, and has resulted in the achievement of a balance between reduced kickback and the maintenance of an appropriate level of feedback from the road surface. The use of a configuration that enables the EPS unit to avoid external loads (use of bearing holders, etc.) and a waterproof structure has helped ensure that the unit satisfies the requirements of ATV use.

1. Introduction

Honda has a long history in the development of power steering systems for 4-wheel all-terrain vehicles (ATVs). After the company commenced marketing 4-wheel ATVs, the development of a hydraulic power steering system for use in the vehicles was started in 1986. Engine power loss is high in hydraulic power steering systems, and at that time, low-displacement vehicles with low steering torque represented the major market trend; these factors meant that market demand for the system was not high, and unfortunately it did not enter mass production. The increased displacement of today's ATVs, in addition to the use of 4WD operation, has increased steering torque and thus also increased the demand for power steering. Mass production of the world's first light vehicle fitted with electric power steering was commenced in 1988. The electric power steering system was efficient, displaying an extremely low level of engine power loss, compared to a hydraulic system, and its use became widespread. Honda judged electric power steering as possessing potential for application in ATVs, and commenced development in 2003. This paper provides an overview of an electric power steering system developed for use in ATVs, and discusses its specific features and effects.

2. Development Goals

An ATV is designed for off-road use, and will see service on rough and rocky ground, and be driven through puddles and very shallow creeks and rivers. Consideration of this type of use environment, user-friendliness and ease of fitting in the vehicle led to the establishment of the following goals for the development of the electric power steering system:

(1) System should require no alteration of existing ATV configuration.
The EPS unit should make maximum use of components used in automobiles and should employ a compact configuration enabling multipurpose use.
(2) Each component should be configured for ATV use conditions. (Consider waterproof property, etc in off-road driving.)
(3) Reduction of steering torque by half (2WD and 4WD).
(4) Feedback of reaction force from the surface the vehicle is traveling on; reduction of kick-back.
(5) Equivalent level of steering stability to a conventional model, even if the EPS becomes non-functional.

3. System Layout

3.1. Overall Layout

Figure 1 shows an external view of the TRX500FPE FourTrax Foreman 4X4 ES, in which the developed EPS is fitted. Figure 2 shows the overall system layout. The developed EPS system was able to be fitted in the vehicle without altering the configuration of the base model, the previously-marketed TRX500FE. The EPS unit is positioned on the steering shaft. A dedicated EPS control unit is located close to the EPS unit. The sensors used in

* Motorcycle R&D Center

the base model have been used to monitor vehicle speed and engine speed in the new vehicle. In addition, an indicator lamp has been positioned inside the speedometer to warn the rider of system malfunctions.



Fig. 1 TRX500FPE FourTrax Foreman 4x4 ES

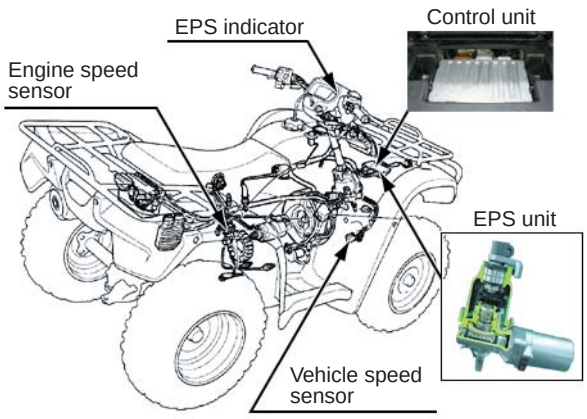


Fig. 2 EPS system layout

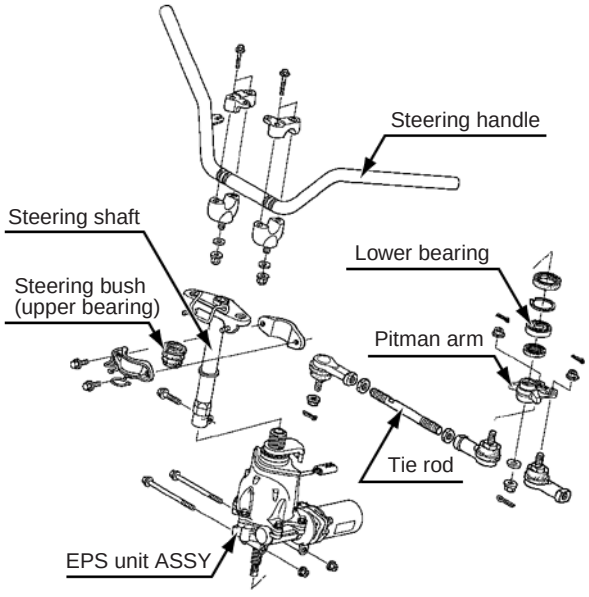


Fig. 3 Configuration of steering system

3.2. Steering System

The steering system of the ATV features a steering handle attached to the steering shaft (column), which is in turn connected to a steering arm (Pitman arm). When the EPS system was fitted, the lower half of the steering shaft was replaced with a column-type EPS unit, with no change to the overall configuration of the vehicle. As Fig. 3 shows, the EPS unit connected to the steering shaft is supported by upper and lower sets of spherical sliding bearings, a configuration that does away with the requirement for adjustment when the system is assembled, regardless of the precision of the vehicle framework, and prevents an increase in friction.

3.3. EPS Unit Configuration

Figure 4 shows the configuration of the ATV EPS unit. Figure 5 shows a cross-section of the unit.

A bearing holder is positioned above the EPS unit;

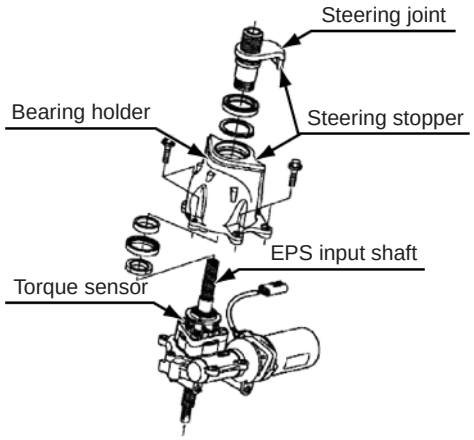


Fig. 4 Configuration of EPS unit

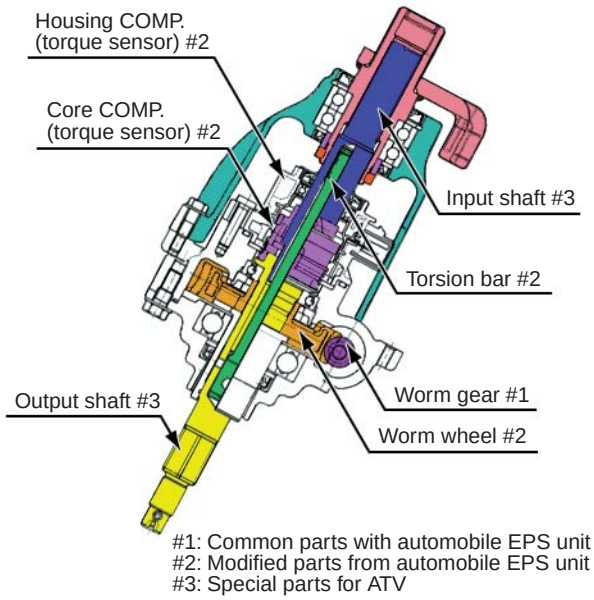


Fig. 5 Cross-section of EPS unit

above this, a steering joint is connected to the steering shaft and the steering handle. This configuration ensures that the load in the direction of inclination of the shaft is received by the bearing holder, and is not inputted to the torque sensor. The steering joint and the input shaft of the EPS unit are fitted by a spline, rather than a clamp. When a load is input from the handle in the axial direction, this spline slides to dissipate the load. In addition to the steering stopper installed on the Pitman arm, stoppers have also been fitted onto the bearing holder and the steering joint in the upper section of the EPS unit, providing a configuration that receives impact loads from the steering handle if the vehicle rolls or slides. The bearing holder also functions to help protect the torque sensor from foreign objects, such as flying stones or branches.

The basic structure of the interior that is used in an automobile EPS has been used in the ATV EPS unit. The motor used in light vehicles has been employed, and a worm gear has been used as the reduction mechanism, as in automobiles, making the unit more compact. The unit is also completely sealed, in consideration of waterproof property that is needed in the ATV use environment.

3.4. Torque Sensor

As discussed in section 3.3, the steering system of the ATV is a Pitman arm with a steering handle. Because wheel movement is directly transmitted to the handle, the transmission torque is relatively high, compared to that of an automobile. In addition, the spring rate of the torsion bar has a significant effect on the assist function and steering stiffness. Given this, it is necessary to increase the spring rate by approximately 7 times against that of an automobile. In order to do so, the external diameter of the torsion bar was increased, as shown in Fig. 5. Despite this, only a modification of the size of the internal bearings was required to enable the torque sensor housing comp from an automobile to be used.

3.5. Motor

An ATV has a higher steering torque than an automobile, and thus also requires high assist torque. The unit employs an automobile motor, but the maximum motor current was increased by approximately 7% in order to increase the maximum assist torque and satisfy this requirement. ATVs are frequently used on winding mountain roads and rough roads, and the frequency with which maximum current is transmitted to the motor is therefore correspondingly high. Because of this, the brush in the motor generates more heat than is the case in an automobile. A material that controlled this heat generation was therefore used for the brush.

3.6. Control Unit

As in the case of the EPS unit, waterproof property in the ATV use environment was considered for the control unit; waterproof connectors were used, and the interior was filled with potting material. Because of this, the configuration of the case, heat sink, circuit board, etc., was designed specifically for ATV use. The basic circuit configuration that is used in the control unit of an automobile has been used in the ATV control unit, but a circuit enabling detection of the signal from the 2WD/4WD switching mechanism has been added for ATV use.

4. EPS Control

As described below, the basic control that is used in an automobile EPS has been used in the ATV. Figure 6 shows a block diagram of the control system. The values of the controlled currents in (1)-(3) can each be varied on the basis of vehicle speed. The control elements in (4) and (5) have been modified and added for ATV use.

(1) Base current control
Sends current to the motor in response to torque sensor signal, and controls basic assist torque.

(2) Damper control
Estimates revolution speed of motor, and reduces motor current based on estimated speed, to produce a damping effect.

(3) Inertia control

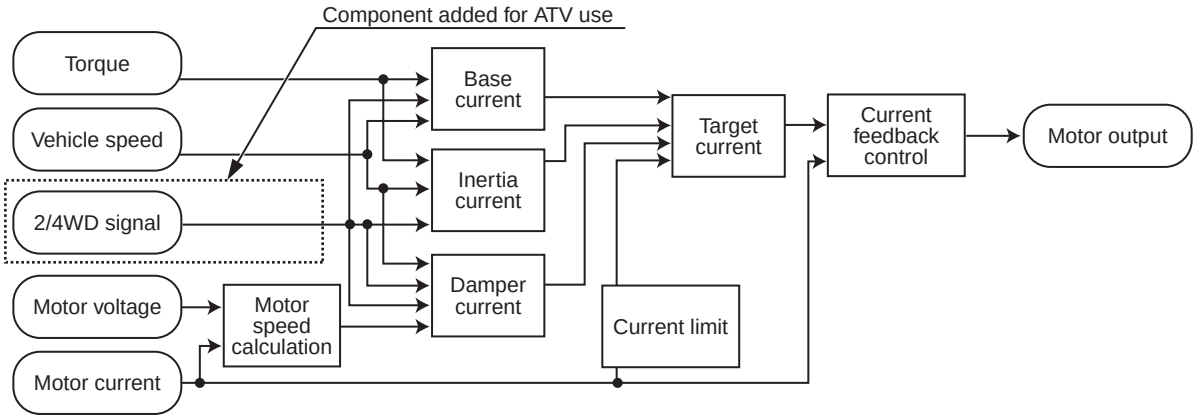


Fig. 6 Control system block diagram

Increases the motor current on the basis of the time-rate-of-change of the torque sensor signal and achieves greater assist torque responsiveness, thus enabling correction of torque for motor inertia.

(4) Targeted current limit
To help prevent the motor and control unit from overheating, if a high current continues to be provided, the unit features a mechanism for heat control, as in an automobile. The level of generated heat is estimated on the basis of the motor current, which is detected by a current sensor positioned inside the control unit. If the heat exceeds a preset figure, the upper limit for motor current is reduced. The method of estimating the level of heat generation has been modified to increase accuracy, to enable control of the increased amount of heat generated by an ATV.

(5) 2WD/4WD assist torque switching control
Steering torque is generally higher in 4WD operation than that in 2WD operation in an ATV that does not employ EPS. The new ATV has been provided with a mechanism for switching control of assist torque in response to the signal for switching between 2WD and 4WD operation, as detected by the detection circuit discussed in section 3.6, in order to enable the achievement of similar steering torque during 2WD and 4WD operation.

5. Performance

5.1. Assist / Steering Characteristic

Figure 7 shows a graph of the assist torque characteristic of the EPS against vehicle speed. As vehicle speed increases, the level of assist torque is reduced. The level of assist torque is not reduced to 0 even at high speeds (40 mph and above); the use of the damper and inertia control discussed in section 4 helps prevent phase delay caused by twisting of the torsion bar, as shown in Fig. 8, and produces a direct and responsive steering characteristic without instability.

As the graph of steering torque characteristics in Fig. 9 shows, a conventional ATV that does not employ EPS displays the following characteristics:

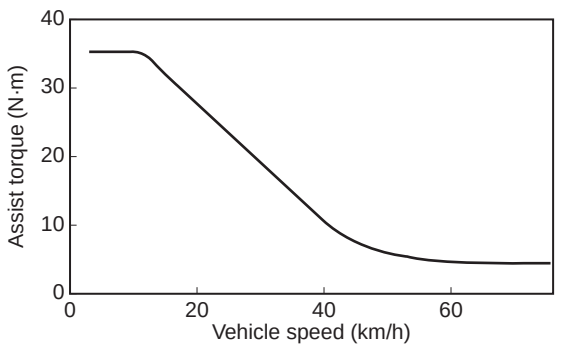


Fig. 7 Assist characteristic against on vehicle speed

2WD operation: The degree of increase of counter torque against steering angle is linear and stable, but steering becomes slightly heavy.

4WD operation: The steady state steering counter torque when the vehicle is proceeding straight or turning is stronger; the counter torque against steering angle declines in linearity, but the counter torque when the handle is turned is weaker.

Changing the assist characteristic between 2WD and 4WD operation has reduced steering torque by half while maintaining the above characteristics.

5.2. Steering Damper Performance

The reduction ratio employed and motor size were decided with consideration of the achievement of a balance with assist torque, resulting in a reduction in kickback, while feedback of the reaction force from the road surface has been maintained at an appropriate level.

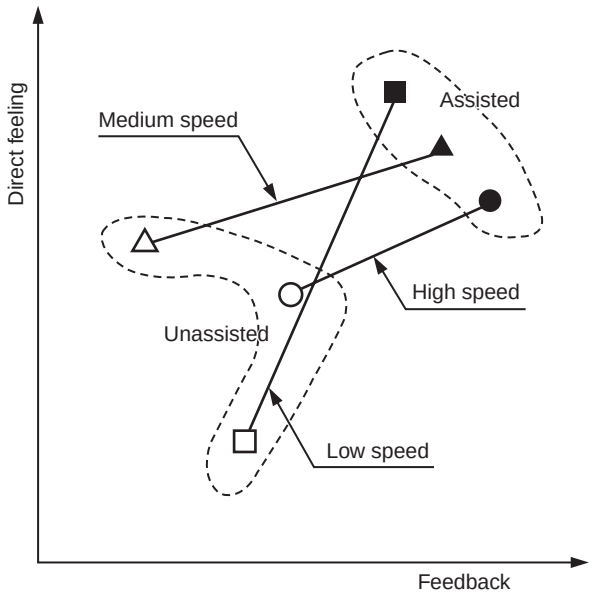


Fig. 8 Characteristic of steering feeling

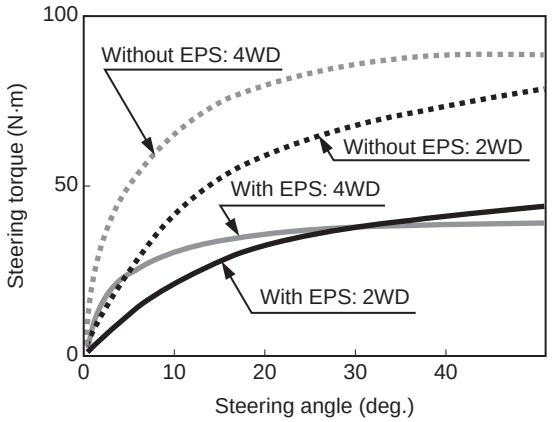


Fig. 9 Characteristic of steering torque

5.3. Steering Characteristic during Malfunction

(1) Failsafe control
The control unit conducts diagnosis in all electrical system components. If a malfunction is detected, the indicator lamp flashes, and assist is stopped.

(2) Steering characteristic during malfunction
To reduce the inertial mass of the gears and motor employed in the EPS unit, and reduce friction and increase the efficiency of the worm wheel/gear, the worm wheel teeth have been made of plastic, and the level of backlash in the worm wheel/gear has been increased above the standard level for an automobile. This has resulted in the achievement of a steering characteristic similar to that of a non-power-steering vehicle when assist is stopped during a malfunction, as discussed above.

6. Conclusion

A new electric power steering system for ATVs has been developed to increase user comfort. The salient points of this development can be summarized as follows:

(1) The EPS unit has been made more compact, and is able to be fitted without having to modify vehicle configuration.
(2) Configuration of the EPS unit to avoid external loads (use of bearing holders, etc.) and other measures including the use of a waterproof structure have helped ensure that the unit satisfies ATV use requirements.
(3) The use of 2WD/4WD assist torque switching control has enabled steering torque to be halved in both 2WD and 4WD operation.
(4) A focus on the motor, reduction ratio, and EPS control has reduced kickback while maintaining an appropriate level of reaction force feedback from the road surface.
(5) Reduction of the inertial mass of the motor and other components and reduction of gear friction has enabled the achievement of a steering characteristic equivalent to that of a conventional vehicle, even if the system malfunctions.

Acknowledgments

The authors wish to take this opportunity to thank everyone at SHOWA Corporation who generously assisted in this development project.

■ Author ■


Tomokazu SAKAMOTO


Megumu OKADA


Kazushiro INOUE

Technology for Updating Digital Map Using Differential Data

Masayuki ARAI* Keizo YAMANAKA* Toshihide YOFU*

ABSTRACT

In recent years, the increase in performance of car navigation systems has led to a corresponding increase in the size of the map data, which in turn has led to the use of a hard disk drive (HDD) as the data storage medium.

Map data should be regularly updated to include newly constructed roads, facilities, and the like. Currently, this updating procedure is facilitated through removal of the HDD; hence, the navigation system cannot be used during the process.

Now, by employing a new data storage structure, a simple, convenient, and quick method has been developed to update the data without removing the HDD.

1. Introduction

The purpose of the car navigation system is to guide the user to the destination safely and comfortably. In order to enhance this functionality, the types and amount of data has increased every year. For example, it provides city map data that shows the shapes of houses and blocks of land, and search data with the types of shops and businesses and telephone numbers so they can be found. As this data has increased, so has the storage media changed, from the initial CD-ROM to DVD-ROM format, which can hold approximately 12 times the amount of data, then to hard disk drives (HDD) that can hold several times more data and can be read from and written to at higher rates of speed, anytime. Since 2003, Honda has fitted HDDs to all navigation systems fitted in the factory for the Japanese market.

Until now, in order to update the data stored on the HDD, the dealer has removed the HDD from the navigation system and the data has been rewritten. For this reason, it has been necessary to have the dealer visit the user twice; once to have the HDD removed and again to have it reinstalled[(1)] (Fig. 1). Also, because the HDD is removed, there is the further inconvenience of being unable to use the navigation system during this time.

Incorporating a high speed communications interface, and rewriting all the data without removing the HDD was also considered; however, there was the issue wherein rewriting 13 GB or so of data takes about two hours. To reduce this rewrite time, the database was completely revised with the adoption of a new file structure. The result was that by receiving a DVD-ROM from the dealer, the data rewrite could not only be performed while driving the vehicle, but the downtime of the navigation system could be reduced to 20 to 30 minutes. The technology adopted to achieve this is described below.

2. Navigation System Data Structure

Digital map data, used by the navigation system and comprised of data for display, and road data that shows the orientation and location of the vehicle, is defined by points (nodes) and their joining lines (links) that make up each individual road. This data, along with data showing the connecting relations where two or more roads intersect, is stored in the database (Fig. 2).

In addition to the data used to display the map on the screen, there are various types of data, optimized according to function, such as destination search data and route calculation network data, which determines the guide route.

The search data performs searches based on names or

* Automobile R&D Center

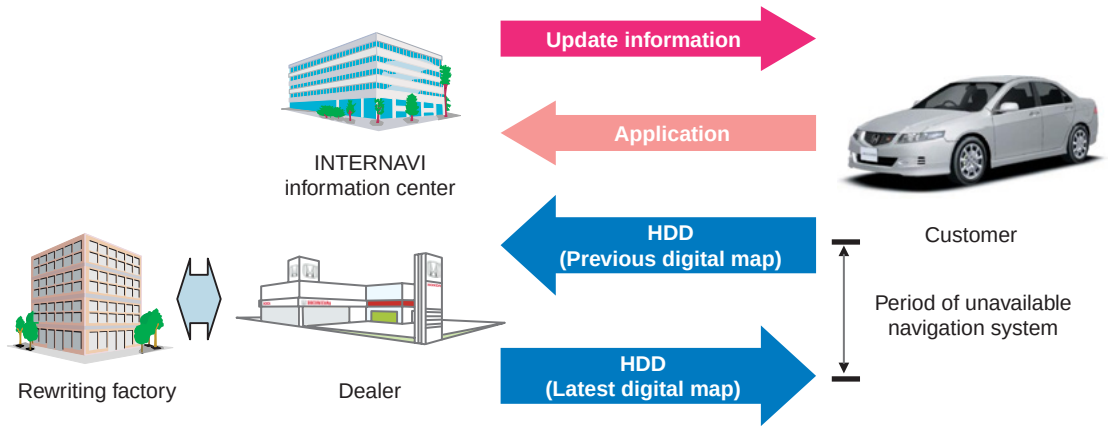


Fig. 1 Previous renewal service of digital map data

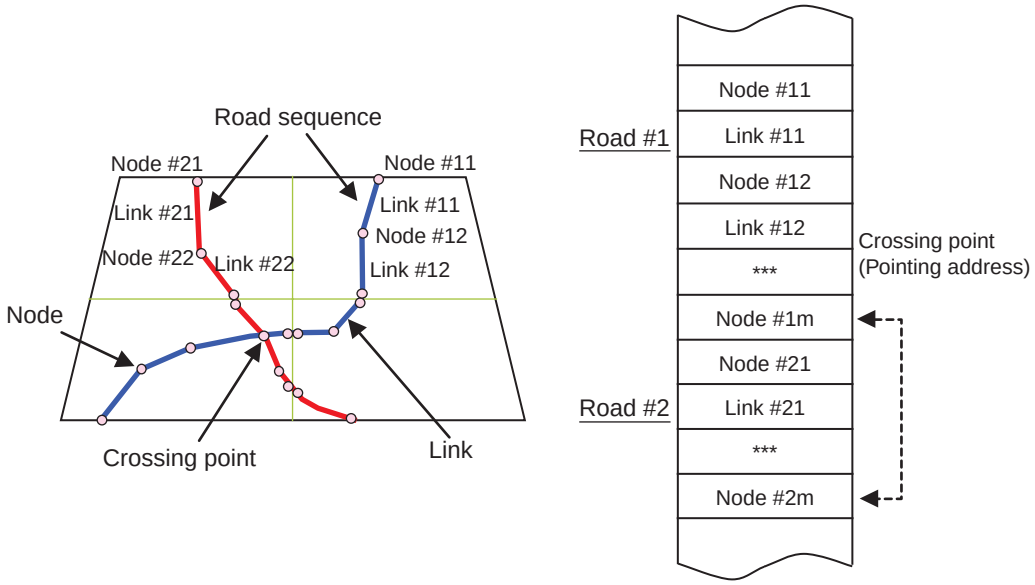


Fig. 2 Digital map data structure (road data)

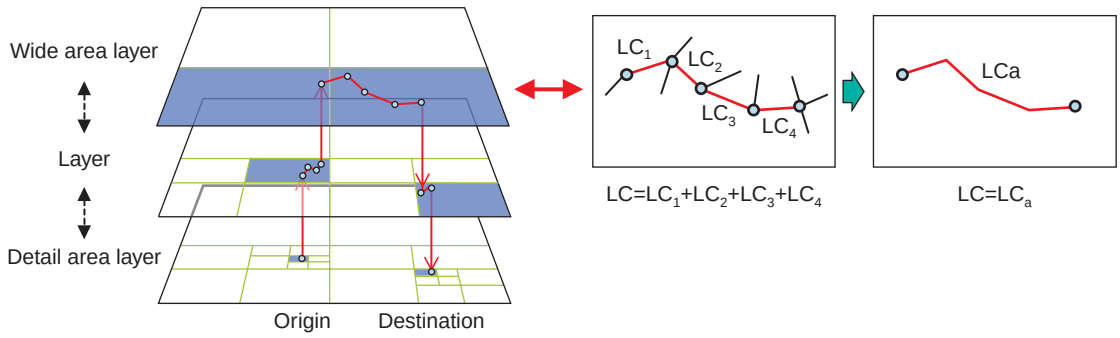


Fig. 3 Digital map data structure (route calculated data)

telephone numbers to specify a building location as the destination. The number of possible buildings throughout the whole of Japan can be as many as 10 000 000. For example, when entering a name, one character at a time, during a destination search by Japanese KANA character, processing takes a considerable amount of time, as a search is made for matching data as each character is entered. For this reason, the data is structured to enable quick processing in response to the user interface.

Route calculation network data has route weighting information (link cost) applied at each junction. When the route calculations start after setting the destination, this data is used to determine the shortest route from the current position to the destination using the Dijkstra method[2], or other calculation methods, to calculate the route. The data is layered and processing using data obtained by pre-calculation of intermediate routes for each area also takes place. It has the ability to calculate the route with a small amount of processing (Fig. 3).

3. Map Update Issues

A characteristic of the previous map data for the navigation system described above is that it has a structure that comprises groups of combined data, ranging in size from tens to hundreds of megabytes. Location information is determined from the actual data's relative address information[3, 4] (Fig. 4).

Display of navigation information is made possible by taking the node and link connection information for the displayed road and looking at each of the various pieces of data, indicated by the relative address information, one at a time, and reconstructing the data as connected roads.

Figure 5 shows an example in which a road (Road #2) branching off a highway (Road #1) has ceased to exist and a new road (Road #3) has been added.

First, the data forming the branch road (Road #2) is deleted. Then the data forming the new branch road (Road #3) is added, and a new intersection (Node #7) is added to the highway (Road #1). With the previous data structure, this would be inconvenient because simply inserting, adding, or deleting data would result in misalignment of the address information of the data sequence, introducing data reading inconsistencies.

Furthermore, as this map data structure was a single large data mass, change to even one part would necessitate rewriting the entire data, and the navigation system could not be used until this rewriting had finished.

4. Data Structure for Differential Data Update

Unlike previous map data that employs the method of using a relative address for relevant actual data, this time, as shown in Fig. 6, finely divided file data for elements of the map structure, such as scale (level) and region (mesh), is accessed.

With the previous map data, even if the update only changed one part of the map data, it was necessary to

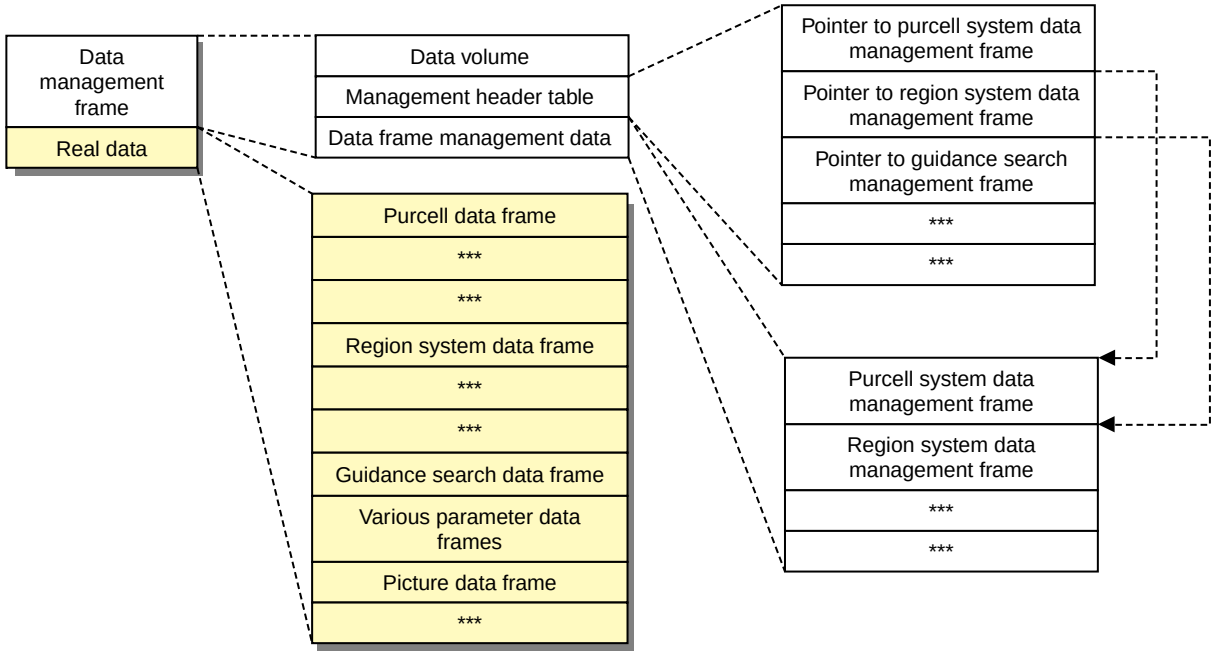


Fig. 4 Data structure of whole digital map data

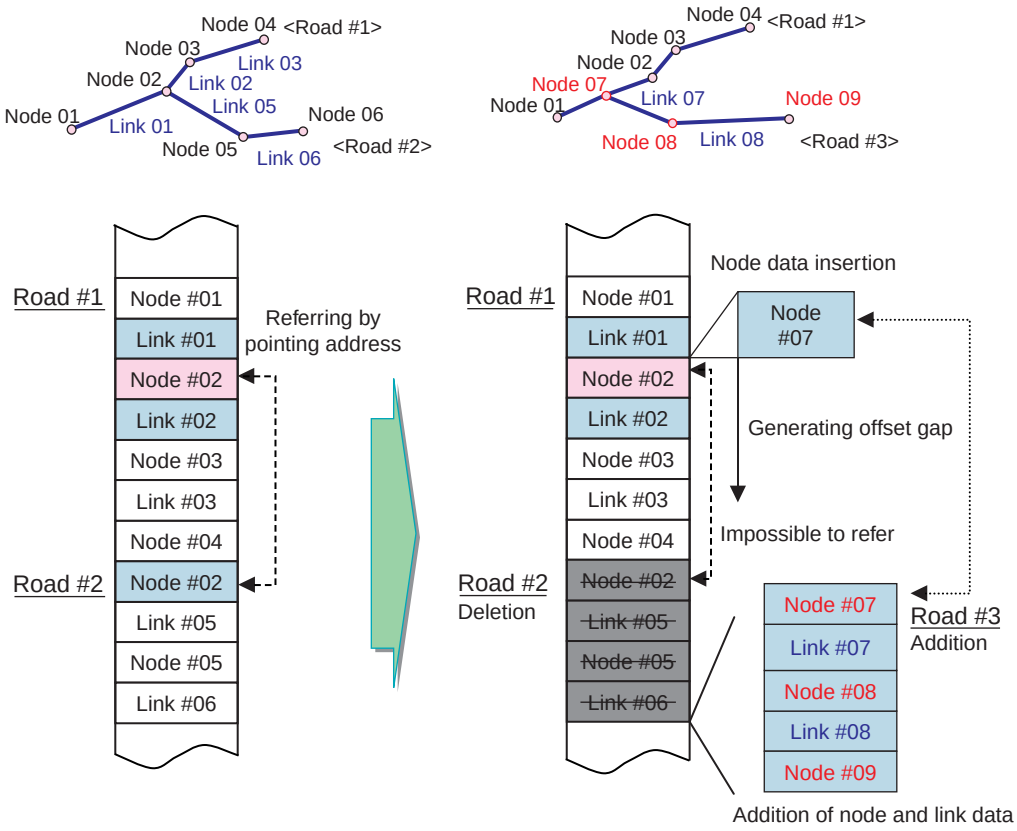


Fig. 5 Present digital map data structure issues

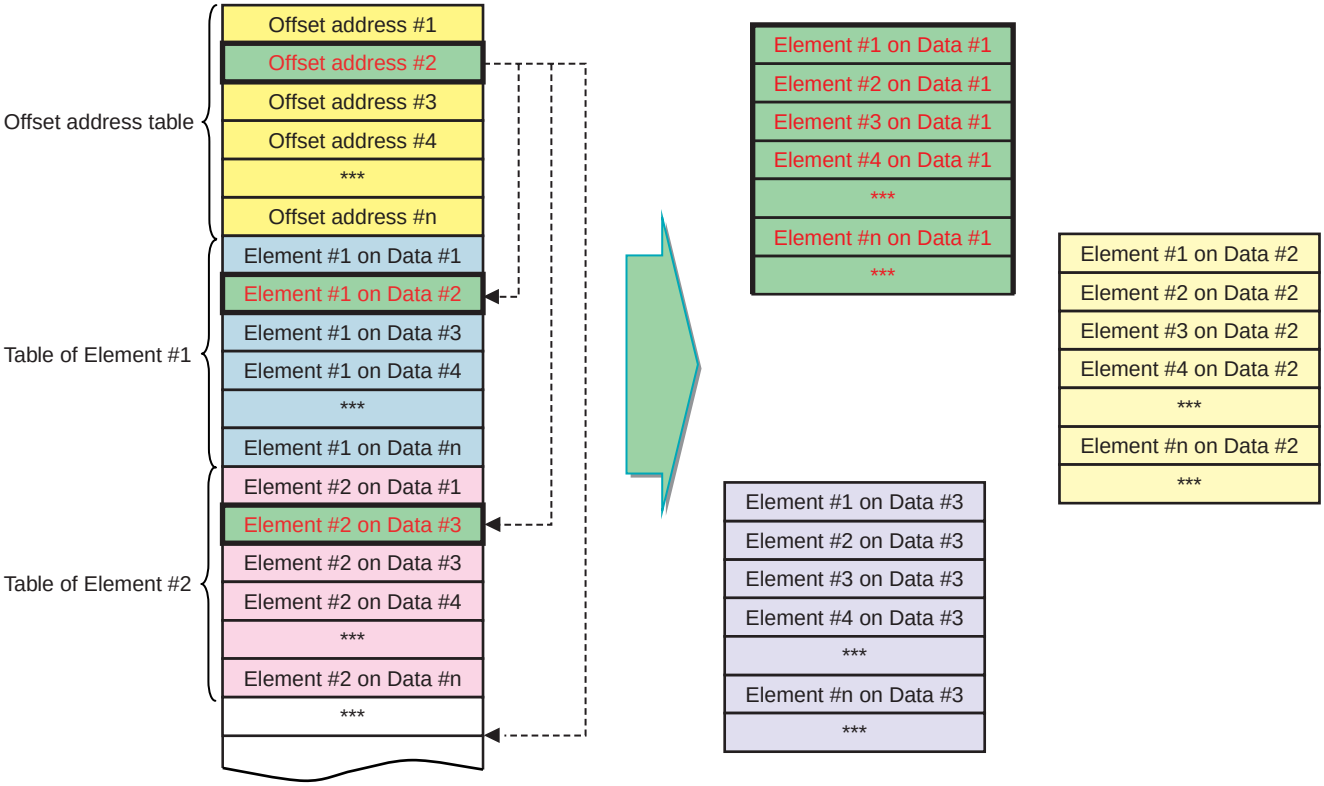


Fig. 6 File composition of differential digital map data

update the entire data. By finely dividing the files, only the file that has changed needs to be updated and the size of the data necessary to perform an update is also reduced.

5. Data Update

The process of updating after receipt of differential data will be described with reference to Fig. 7.

The map provider's server compares the same map data version as that of the navigation system with the latest version of map data to determine the differential data. This data is then brought to the navigation system by cell phone communication or by physical media, such as CD-ROM or DVD-ROM. The navigation system then uses this differential data to perform the updating process on the map data.

The map data is finely divided up into multiple files, one for each level or mesh.

As shown in Fig. 8, when updating, each file that makes up the map data is checked to see if it needs to be updated and the rewriting process is performed based on the differential data information.

Even in the case of the file being updated, the process is performed so that for the elements within the file structure that do not require updating the data is used as is, and only the elements that need updating are rewritten (Fig. 9).

By these means, it has become feasible to rewrite using only a small amount of differential data.

With the previous map data structure, data could not be used until all the files, ranging in size from tens to hundreds of megabytes, had been rewritten. By making full use of the advantages of fine file division, the updating process can be performed as a background task while the navigation system is in use. In other words, it has now become feasible to firstly update higher priority map data, such as the data for the vicinity of the current location, and then update other files as necessary, when the processing load is lighter.

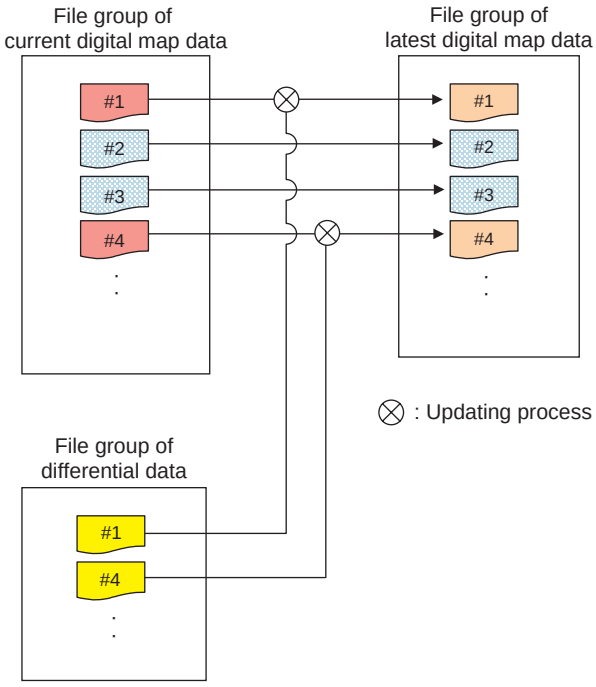


Fig. 8 Updating operation by differential digital map data

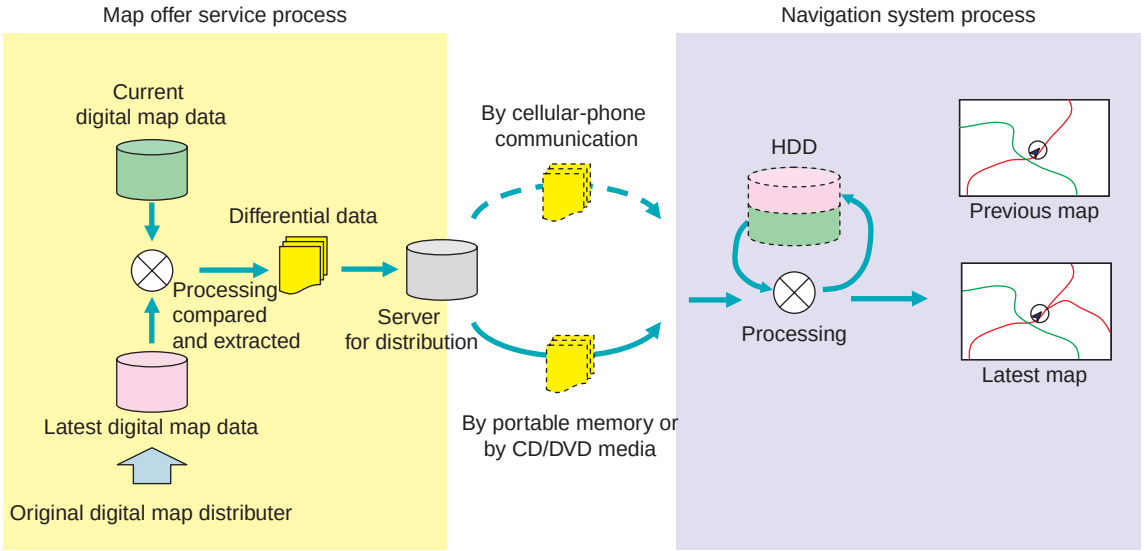


Fig. 7 Updating system by differential digital map data

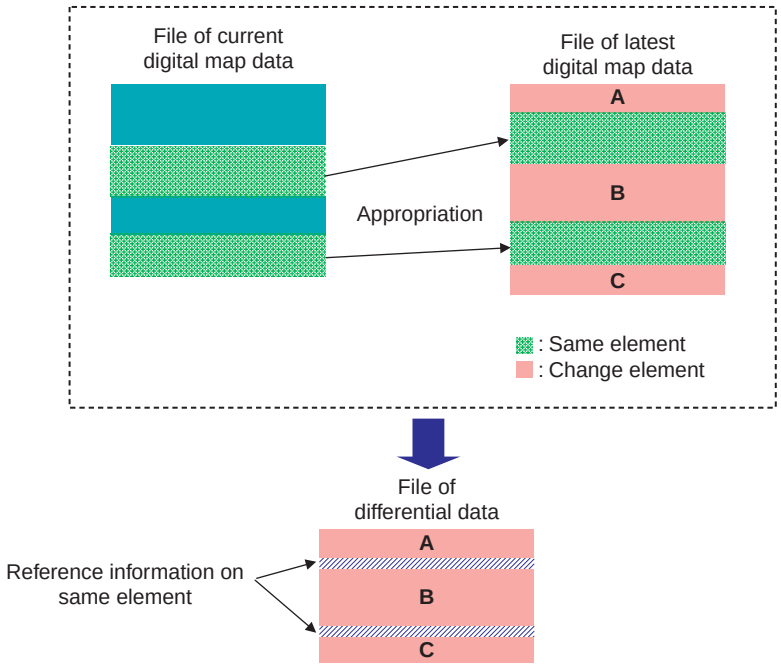


Fig. 9 Structure of differential digital map data

6. Conclusions

Map data updating has been made more convenient by introducing the following technical enhancements:

(1) Fine division of map data
The amount of differential data provided for update has been reduced by finely dividing the previous data structure, which comprised data of the order of several hundred megabytes, into files ranging in size from between several hundred kilobytes to several megabytes. On the other hand, as the increase in the number of files also results in a corresponding increase in the memory requirements of the navigation application, the optimum number was set to make the overall system easy to handle.

(2) Differential data structure
The differential file for map update does not simply rewrite the file, but is also designed so that elements within the file structure that are unchanged are used as they are, further reducing the size of the differential file provided.

(3) Update process prioritization
By setting application process prioritization, it has become feasible to perform the updating process as a background task. This was achieved as a synergistic effect resulting from the fine division of the differential file. As a result of these developments, a system has been achieved that allows the user to easily rewrite the latest map by simply obtaining a CD-ROM or DVD-ROM without the need to repeatedly visit the dealer. Furthermore, the navigation system downtime has been kept to within around 20 to 30 minutes.

References

(1) http://www.premium-club.jp/service/service1.html
(2) Dijkstra, E. W.: A note on two problems in connection with graphs, Numerische Mathematik 1 (1959)
(3) Road vehicles - Map Data Physical Storage Format for Car Navigation Systems, JIS D0810
(4) Kakumoto, S., Takahata, S., Mimori, T., Nishiyama, S., Kakuta, S., Kudo, Y., Maruyama, H., Ozaki, N., Fujimoto, H., Hamada, T., Fukumizu, T., Ohki, H., Sueyoshi, N.: Car Navigation System Open Data Structure “KIWI” and Its Usage, KYORITSU SHUPPAN CO., LTD, p. 25 (2003)

■ Author ■


Masayuki ARAI


Keizo YAMANAKA


Toshihide YOFU

Development of Heat-resistant Nickel-based Super Alloy for Exhaust Valve

Katsuhiko TOMINAGA* Tetsuya SHIMIZU** Shigeki UETA**
Seiji KURATA** Akihiro TOJI***

ABSTRACT

A heat-resistant super alloy, NCF5015, which has lower nickel content than a conventional high nickel heat-resistant alloy, was developed for use in a highly heat-resistant valve. This alloy has reliable high-temperature strength, abrasion resistance, and phase stability after long-term heating.

These characteristics were obtained by increasing the amount of gamma-prime phase that contributes to precipitation-hardening and the amounts of molybdenum and tungsten that contributes to solid-solution within the range that hot formability is not impaired in order to recover strength by reducing nickel.

1. Introduction

In general, high-manganese heat-resistant steel 21-4N (SUH35) has been widely used for the exhaust valves of 4-wheel vehicles. However, this material does not have adequate strength and hardness at high temperatures, so in high performance engines, hard-facing is used on the valve seat face as necessary. Since 1979, all of the exhaust valves of Honda's 4-wheel vehicles have been made of nickel-based heat- resistant alloy without hard-facing, from the viewpoints of cost reduction and process simplification.

The reasons for using nickel-based heat-resistant alloy for the exhaust valves of 4-wheel vehicles are as follows.

(1) It eliminates the necessity of hard-facing the valve seat face.
(2) It has reliable high-temperature strength, and enables the valve stem to be made thinner.
(3) It has reliable oxidation resistance.

In particular, because of the demand to reduce the cost of the valves, NCF3015 (30Ni-15Cr) has been used in mass-produced vehicles, and high-nickel heat-resistant alloy NCF440 (70Ni-19Cr) has been used in high performance engines. In recent years, lean burning is being adopted to meet the increasingly severe exhaust gas regulations and realize enhanced fuel economy, resulting in increasingly high exhaust temperatures. Thus, in mass-produced vehicles as well, the needs for exhaust valves that have high-temperature strength are increasing. On the other hand, the requirement for cost reduction remains large. Consequently, a new nickel-based heat-resistant alloy NCF5015 was developed. This new alloy, based on current high-nickel heat-resistant alloy NCF440, contains less nickel in order to reduce cost, and also has the same high- temperature strength and abrasion resistance characteristics.

2. Development Goals

In the development of a high-strength, low-nickel valve, each characteristic was made the same as that of the high-nickel heat-resistant alloy. Also, regarding the following six development goals, the material was set identical to the current material.

(1) Hardness at normal temperatures
(2) High-temperature hardness at 800°C
(3) High-temperature fatigue strength at 800°C
(4) Value of impact energy after heating to 800°C for 400 hours
(5) Oxidation resistance
(6) Forgeability

* Automobile R&D Center
** Daido Steel Co., Ltd.
*** Hitachi Metals, Ltd.

3. Alloy Design

The main feature of the newly developed NCF5015 is the attainment of high heat resistance due to the optimization of the gamma-prime phase and the amount of nickel, the amount of molybdenum and tungsten, and the amount of chrome, while maintaining long term microstructural stability of the material. In order to obtain high fatigue strength while reducing the amount of nickel, it is necessary to increase the gamma-prime phase (the total of the intermetallic compounds of aluminum, titanium, niobium, and nickel). However, when the amounts of aluminum, titanium, and niobium are increased, high-temperature strength is increased, but on the other hand the hot forming ability is reduced.

With the current mass production line, the hot forming ability decreases markedly when the gamma-prime amount exceeds 30 at%. For this reason, the gamma-prime amount for the newly developed NCF5015 was set to 27 at% in order to maintain the hot forming ability. Chromium is added in order to enhance the oxidation resistance, and molybdenum and tungsten are added for increased strength through strengthening of solid solution. If a large amount of any of these elements is added, s embrittlement in the form of a sigma phase or a Laves phase will appear, reducing strength and toughness as well as hot forming ability[1]. From Fig. 1, the amounts of molybdenum and tungsten added to NCF5015-D were made 1.0% and 1.5%, respectively, from the viewpoint of preventing the formation of a Laves phase. Figure 2 suggests that if the amount of nickel is 50%, and the amount of chromium is 19%, which is the same level as that of the 70Ni-19Cr alloy, a sigma phase will occur at 800°C. For this reason, chromium was added to 15%.

In NCF5015-H, the use of molybdenum, which has the effect of strengthening the solid solution of the austenite and of increasing the high-temperature fatigue strength, was studied. When setting the amount of molybdenum, first the amount of chromium added was set to 16% in consideration of the oxidation resistance and current material market achievements. From the 800°C molybdenum and chromium phase diagrams shown in Fig. 3, the maximum amount of molybdenum added was set to 3.7%, at which level a harmful sigma phase is not formed when the amount of chromium added is 16%.

From the above alloy design, development of an exhaust valve nickel-based heat-resistant alloy, which has

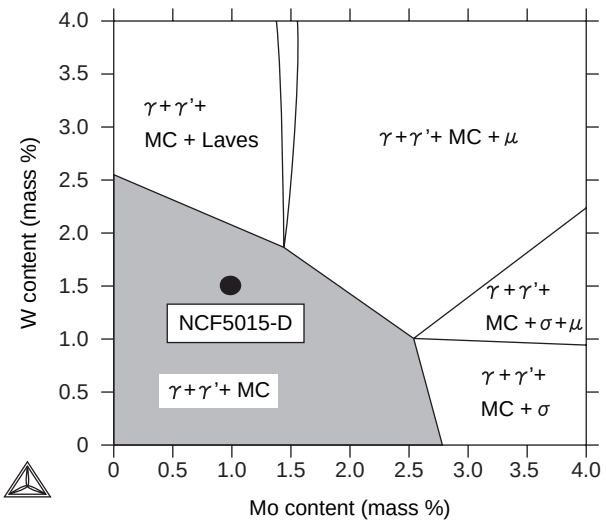


Fig. 1 Phase diagrams of Ni-15Cr-Mo-W after heat treatment at 800 °C

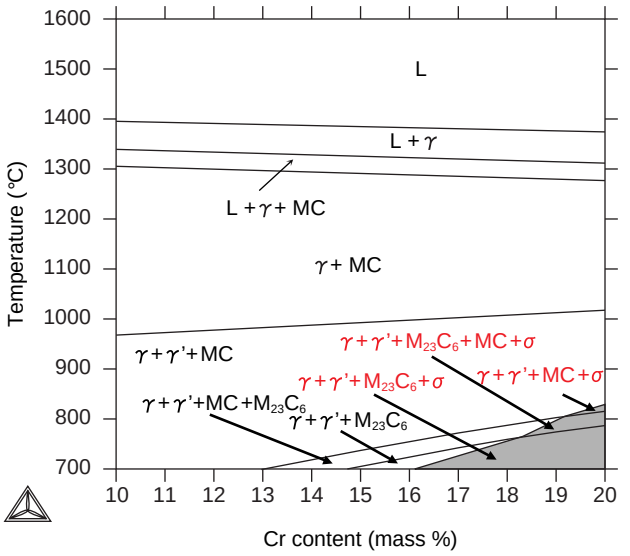


Fig. 2 Phase diagrams of 50Ni-Cr-Mo-W alloy

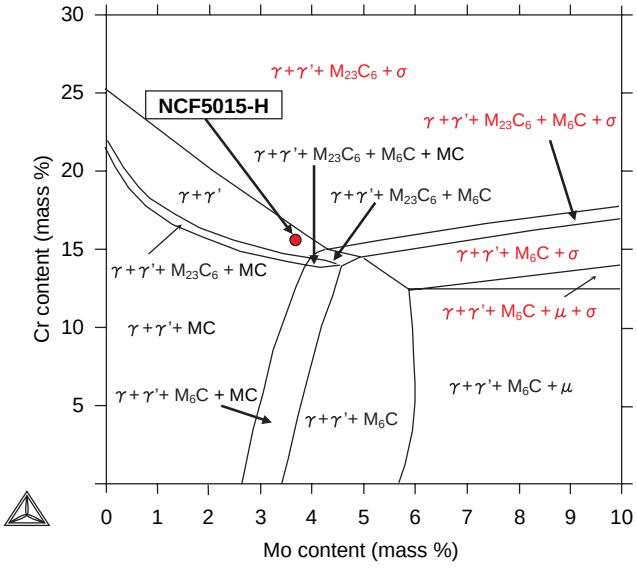


Fig. 3 Phase diagrams of 0.03C-Cr-1.8Al-2.1Ti-1.2Nb-55Ni-Mo-Fe after heat treatment at 800 °C

Table 1 Nominal chemical composition

Material	Composition (mass %)												Theoretical amount (atomic %)
	C	Si	Mn	Ni	Cr	Fe	Mo	W	Ti	Al	Nb	Others	γ' Ni_3 (Al, Ti, Nb)
NCF5015-D	0.05	0.1	0.1	50	15	26	1.0	1.5	2.5	1.4	1.3	0.004 B 0.003 Mg	26.7
NCF5015-H	0.03	0.1	0.1	55	16	20	3.7	–	2.1	1.8	1.2	0.004 B 0.004 Mg	27
NCF440	0.05	0.1	0.1	70	19	3	1.0	1.5	2.5	1.4	1.3	0.004 B 0.003 Mg	26.9
Inconel751	0.05	0.1	0.1	72	16	7	–	–	2.3	1.2	1.0		23.4
NCF3015	0.03	0.1	0.1	32	16	47	–	–	2.7	1.2	0.8	0.004 B	23.6

NCF5015-D (Developed material with Daido Steel Co., Ltd.)
NCF5015-H (Developed material with Hitachi Metal, Ltd.)

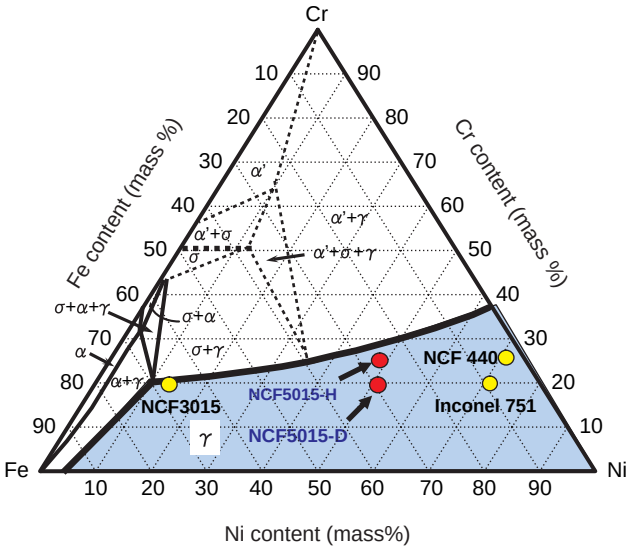


Fig. 4 Phase diagrams of matrix after heat treatment at 800 °C

reliable high-temperature strength and oxidation resistance and can also maintain high strength when used over a long period, was carried out. Table 1 shows the component set values of the developed materials containing reduced nickel. From Fig. 4, it can be seen that both developed materials belong to the structurally stable austenite zone.

4. Phase Stability

4.1. Impact Value

The impact value is a characteristic value that indicates the toughness of the valve stem. When structure is unstable, impact characteristics may fall after prolonged use at high temperatures, leading to valve breakage. Figure 5 shows the impact value after the valve was heated to 800°C for 400 hours. The impact values obtained for the developed materials were superior to the impact values of the target high-nickel heat-resistant alloy NCF440 and Inconel751.

4.2. Structure

Figure 6 shows photograph of the structure after solution heat treatment, aging treatment, and over-aging of the developed material at 800°C for 400 hrs. From this structure photograph, it was found that after over-aging at 800°C for 400 hrs there was no trace of the harmful

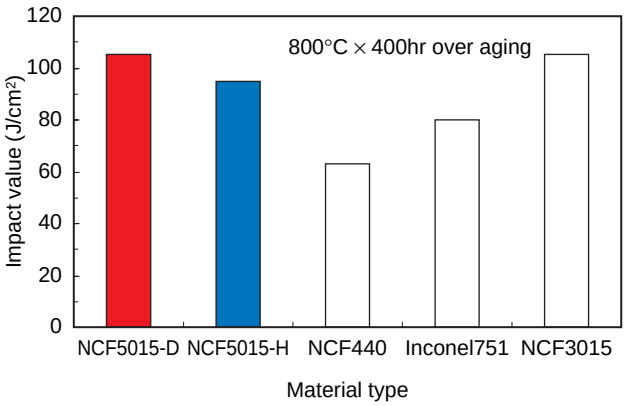
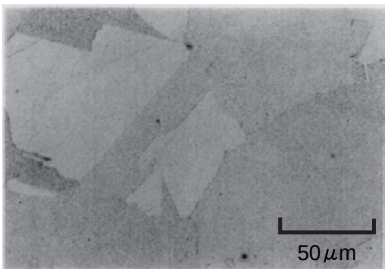
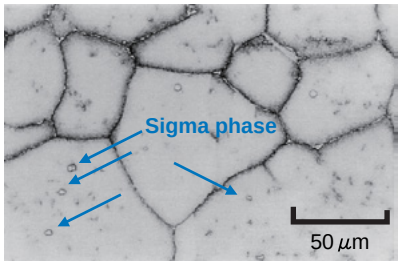


Fig. 5 Impact value of each material type



NCF5015-H after solution heat treatment, aging treatment, and over-aging at 800 °C × 400 hr

Fig. 6 Microstructure of developed materials



Trial material after solution heat treatment, aging treatment, and over-aging at 800 °C × 400 hr

Fig. 7 Microstructure of sigma phase

sigma phase sludge, shown in the example of Fig. 7, which reduces strength.

5. Material Characteristics

5.1. High-temperature Hardness

The high-temperature hardness is an important characteristic value that indicates the abrasion resistance of the valve seat face. Figure 8 shows the hardness of NCF5015 at room temperature and at high temperature. At a high temperature of 800°C, the developed materials had the same degree of hardness as the hardness of the target high-nickel heat-resistance alloy NCF440. In particular, the high-temperature hardness at 600°C or higher, which is the temperature zone of the valve face, was of the same level as that of NCF440 (70Ni-19Cr), and was higher than that of Inconel751 (72Ni-16Cr). Consequently, it can be said that the developed materials have the same order of abrasion resistance as that of high-nickel heat-resistant alloy.

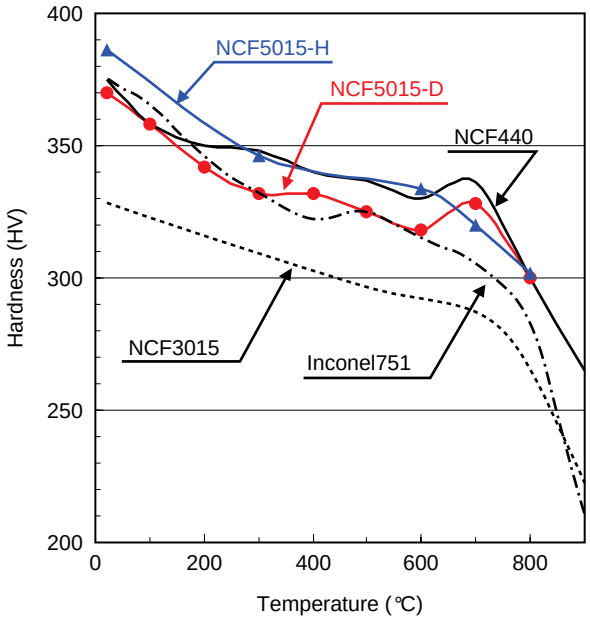


Fig. 8 Hardness at elevated temperature

5.2. Tensile Strength

The tensile strength is a characteristic value that determines the strength of the valve stem. The valve stem temperature reaches a temperature of at least 800°C, and when the valve is seating, a tensile stress is generated together with a bending stress. In the case of a high output high-speed engine, an excessively large stress is generated during over-revving[2]. Figure 9 shows the tensile characteristics of the developed materials at room temperature and at high temperature. The tensile strength of the developed materials is the same level as that of the high-nickel heat-resistance alloy NCF440 (70Ni-19Cr), and is higher than that of Inconel751 (72Ni-16Cr) at temperatures of 500°C and higher.

5.3. Fatigue Strength

The high-temperature fatigue strength is an important characteristic value that indicates the fatigue strength of

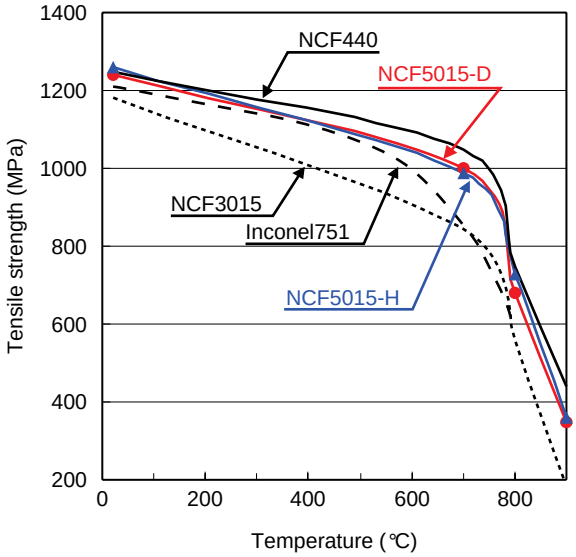


Fig. 9 Tensile properties at elevated temperature

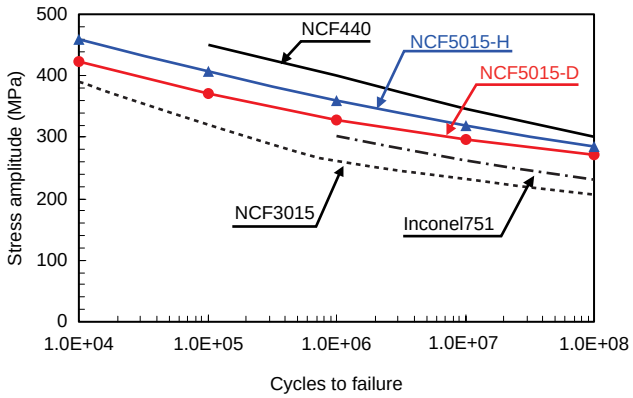


Fig. 10 Fatigue strength at 800 °C

the valve stem. Figure 10 shows the results of the rotary bending fatigue test at 800°C. The developed materials had a fatigue strength of roughly the same as that of the target high-nickel heat-resistant alloy NCF440 at 800°C.

5.4. Oxidation Resistance

The exhaust valves are used under the valve seat contact conditions, and are used under a thermo cycle accompanying a high-temperature oxidation environment and engine acceleration and deceleration load change. Oxidation of the valve generates abrasive scale, which increases abrasion and sometimes causes leakage from the valve face. Figure 11 shows the increase by oxidation after the valve is heated at 850°C for 400 hrs. The developed materials have the same oxidation resistance as that of high-nickel heat-resistant alloy NCF440 (70Ni-19Cr), and have reliable oxidation resistance to Incone1751 (72Ni-16Cr). It is thought that the addition of aluminum caused the Al_2O_3 oxide film to function even more efficiently with respect to Inconel751.

5.5. Physical Characteristics

Among the various physical characteristics, the coefficient of thermal expansion affects the elongation, that is, the tappet clearance, the thermal conductivity affects the heat reducing ability of the valve, and the specific gravity affects the weight of the valve. In general, the coefficient of thermal expansion should be small, to reduce thermal stress and minimize the effect on the tappet clearance; the thermal conductivity should be large, to enhance the heat reducing ability; and the specific gravity should be small from the viewpoint of lightness[3]. Figure 12 shows the coefficient of thermal expansion, Fig. 13 the thermal conductivity, and Table 2 the specific gravity. The coefficient of thermal expansion and the thermal conductivity of the developed materials exhibit the same characteristics as those of high-nickel heat-resistant alloy, and the specific gravity has become smaller due to the reduction of the amount of nickel.

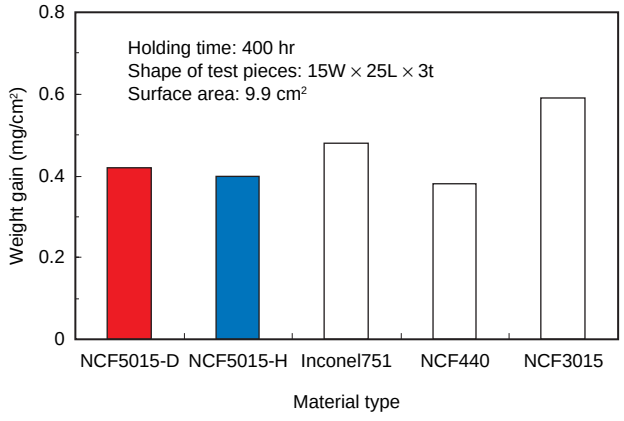


Fig. 11 Oxidation resistance at 850 °C

Table 2 Specific gravity

g/cm³

NCF5015-D	NCF5015-H	NCF440	Inconel751	NCF3015
8.09	8.17	8.24	8.25	7.90

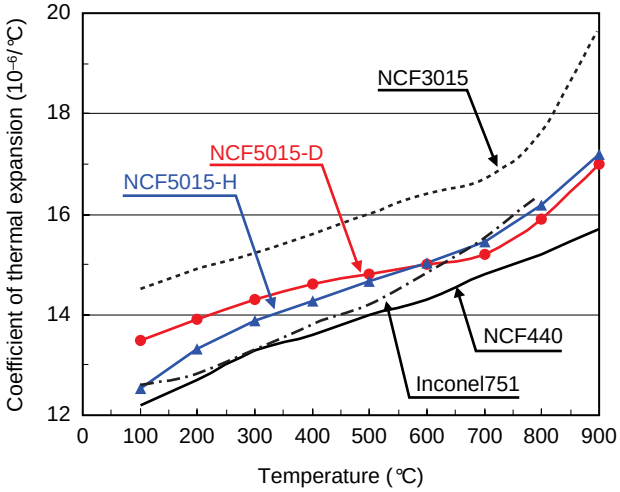


Fig. 12 Coefficient of thermal expansion

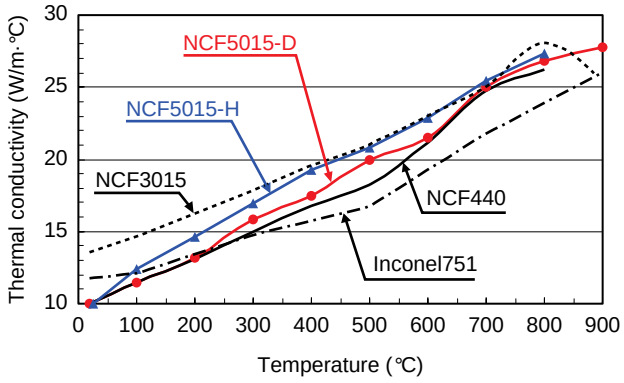


Fig. 13 Thermal conductivity

6. Part Unit Characteristics

6.1. Hot Formability

Hot formability is used to evaluate the forming ability of the valve. Figure 14 shows the results of performing a hot high-speed tension test using a Grebl examination machine. In general, the temperature region in which a contraction of area of at least 50% can be obtained in the Grebl test is the formable range. The temperature range over which the contraction of area of the developed materials is at least 50% has a temperature of at least 250°C, and has the hot formability of the current material.

6.2. Part Unit Characteristics

Figure 15 shows the results of the valve sliding examination. The developed materials have the same

frictional resistance as that of the high-nickel heat-resistant alloy NCF440. The abrasion is no more than one half that of the current mass production material NCF3015.

6.3. Durability in an Actual Vehicle

Figure 16 shows the amount of valve face abrasion after 100 hrs of operation at 7100 rpm in a 2.4-liter engine that runs on unleaded gasoline. The developed material has the same abrasion resistance in an actual vehicle as that of the high-nickel heat-resistant alloy NCF440.

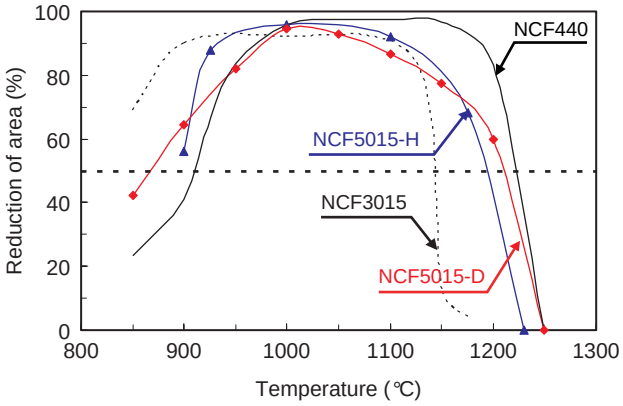


Fig. 14 Hot forgeability

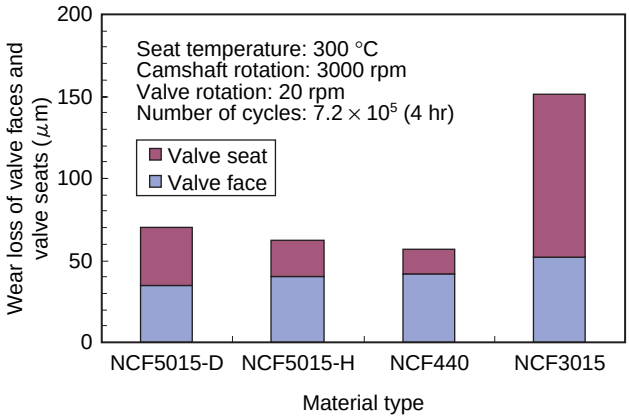


Fig. 15 Valve sliding examination

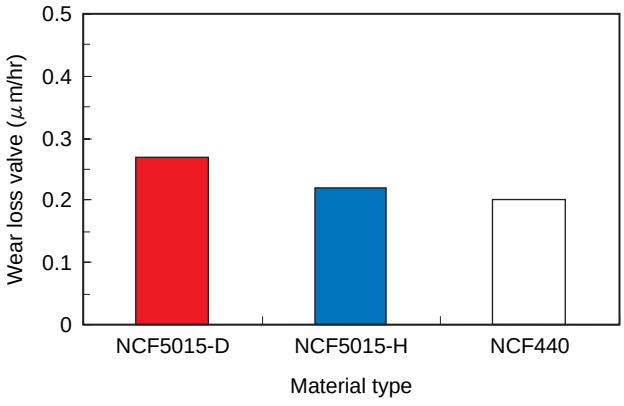


Fig. 16 Wear loss of exhaust valve faces

7. Conclusion

The characteristics called for exhaust valve materials in recent years were reexamined, and a resource-saving low-cost NCF5015 material was developed. A summary of the characteristics of the developed material is set out below.

(1) The material is a nickel-based high heat-resistant alloy that does not require hard-facing and has phase stability, even after it is heated for a long period.

(2) The abrasion resistance and fatigue resistance at high temperatures are the same as those of the high-nickel heat-resistant alloy.

(3) The features of the material are that the amount of gamma-prime phase generated in the range where the hot formability is not allowed to fall is increased, while low-nickel is realized, as well as molybdenum and tungsten, which are elements for strengthening of solid solution, are optimally added.

(4) As a result of the application of this alloy, a cost reduction of approximately 16% was realized compared to the use of the conventional high-nickel heat-resistant alloy. Mass production of the newly developed material started from the 2008 model year ACCORD.

References

(1) Morinaga, M., Yukawa, N., Adachi, H.: Theory of the d Electrons Alloy Design, Iron and Steel, Vol.11, p.159(1985)

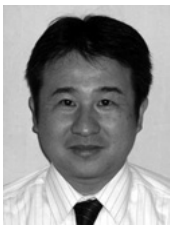
(2) Sato, K., Saka, T., Ohno, T., Noda, T.: Development of Low-Nickel Heat-Resistance Alloy for Exhaust Valves, HONDA R&D Technical Review, Vol.9, p.185-190

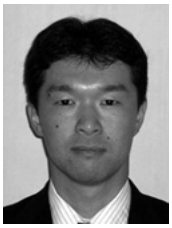
(3) Hagiwara, Y., Ishida, M., Oka, T.: Development of Nickel- base Superalloy for Exhaust Valves, HONDA R&D Technical Review, Vol.4, p.63-72

Author


Katsuhiko TOMINAGA


Tetsuya SHIMIZU


Shigeki UETA


Seiji KURATA


Akihiro TOJI

Development of Low Volatile Organic Compound Dust Sealing Material

Naoki TSURUTA*

ABSTRACT

A dust sealing material displaying low levels of volatilization of acetaldehyde and toluene has been developed in order to enhance the air quality of automobile cabins. Volatilization of acetaldehyde has been reduced by more than 90% and that of toluene by more than 45% in the developed dust sealing material, as compared to the former sealing material.

As component materials, an acrylic resin and a urethane resin have been used for the base resin of the sealing material, and a toluene-free diluent has been employed. From the perspective of the production method, the use of toluene has been discontinued in the production processes of all materials to help eliminate any residual toluene content. In addition, the use of solvents containing toluene has been discontinued in the factories where the dust sealing material is produced, and the level of toluene in the air in the factories has been controlled to a specified level or below.

1. Introduction

In order to enhance air quality by reducing volatile organic compounds (VOC) such as formaldehyde, acetaldehyde, and toluene from automobile cabins, in February 2005 a voluntary approach to vehicle cabin VOC reduction was announced by the Japan Automobile Manufacturers Association(JAMA)[1]. Under this voluntary approach, Japanese auto manufacturers will attempt to satisfy guideline figures for the 13 substances shown in Table 1 stipulated by the Ministry of Health, Labour and Welfare in new vehicle models marketed from 2007, and will attempt to achieve further reductions in later models.

Reducing VOC emissions from cabin components is one method of reducing the VOC level of automotive cabins. Therefore, an effective method of reducing VOC levels is to focus on materials that display a high level of VOC emissions and are extensively used, and on components that are commonly used. An example is a sealant for door hole seals displaying reduced xylene and ethyl benzene volatilization[2] which has been developed and has gone into use.

Approximately 80 components used in automotive cabins were studied with regard to VOC emissions and multiple uses. As shown in Table 2, the results of this study indicated that volatilization of acetaldehyde and toluene from dust sealing materials displayed a high rate of contribution to cabin VOC levels, regardless of vehicle type.

Dust sealing materials are applied in the coating

Table 1 Materials selected for indoor density level reductions to comply with Ministry of Health, Labor and Welfare guidelines

No	Materials
1	Formaldehyde
2	Acetaldehyde
3	Toluene
4	Xylene
5	Ethylbenzene
6	Styrene
7	Tetradecane
8	Di-n-butyl phthalate
9	Di-2-ethylhexyl phthalate
10	Paradichlorobenzene
11	Chlorpyrifos
12	Diazinon
13	Fenobucarb

Table 2 Contribution rate of dust sealer to indoor VOC

Vehicle type	Acetaldehyde (%)	Toluene (%)
Sedan A	15	13
Sedan B	13	6
SUV A	23	6
SUV B	15	9

* Automobile R&D Center

Table 3 Acetaldehyde volatilization and contribution rate of raw materials

Basic raw material	Concentration of acetaldehyde volatilization		Contribution rate of acetaldehyde volatilization %
	μg/ 1 g raw material	μg/ 1 g dust sealer	
PVC homopolymer	1	0.10	8.6
PVC/PVAc copolymer	10	1.00	85.9
Plasticizer	0.05	0.02	1.3
Filler	0.05	0.02	1.9
Diluent	1	0.02	1.7
Adhesive agent	0.3	0.01	0.5
Moisture absorption prevention agent	0.01	0.00	0.0
	Total	1.16	100

Table 4 Alternative resin from PVC/PVAc copolymer

Resin		PVC homopolymer	Acrylic resin	Urethane resin	Epoxy resin
Material properties	Tensile strength	Good	Poor	Good	Excellent
	Elongation	Good	Good	Excellent	Fail
Workability	Applicability	Good	Good	Fail *2	Fail
	Storage stability	Good	Good *3	Good	Poor
Environment		Fail *1	Good	Good	Good
Cost		Low	Middle	High	High

*1 Increased chlorine density in automobile shredder residue.
*2 Difficult to lower viscosity due to plasticizer mixing.
*3 Use of acrylic resin core shell structure.

process of automobile manufacture to prevent water infiltrating the vehicle cabin from the joints between the steel sheets. The same dust sealing material is normally used in all the vehicles produced on a single assembly line. The development of a dust sealing material displaying low volatilization of acetaldehyde and toluene would therefore be an effective means of reducing cabin VOC levels.

This paper reports on the development of a dust sealing material that displays lower levels of acetaldehyde and toluene volatilization than that of the conventional sealing material.

2. Reduction of Acetaldehyde

As shown in Table 3, the concentration of volatilized acetaldehyde in 1 g of each of the constituents of the conventional dust sealing material were measured in order to specify the cause of volatilization of this substance from the material. The rate of contribution of each constituent of the dust sealing material to the concentration of volatilized acetaldehyde was calculated based on the results of these measurements and the composition of each constituent. The results of this study indicated that a copolymer of vinyl chloride and vinyl acetate (PVC/PVAc copolymer) displayed the highest rate of contribution, and this copolymer was therefore specified as the main cause of acetaldehyde volatilization.

A vinyl acetate monomer is used as a raw material in the production of the PVC/PVAc copolymer, and it is conjectured that some of this monomer is hydrolyzed in the reaction shown in Eq. (1) and taken up in the copolymer as an impurity.

$$CH_2=CH–OCOCH_3 + H_2O \rightarrow CH_3COOH + CH3CHO \quad (1)$$
(Vinyl acetate monomer) (Water) (Acetic acid) (Acetaldehyde)

Following this, methods of substituting another resin for the PVC/PVAc copolymer were studied to reduce the acetaldehyde content of the dust sealing material. The dust sealing material is applied following e-coating of the white body, and is cured in two ovens, for the primer surfacer and top coat, and the substitute resin was therefore required to be a resin that is cured by heating.

Table 4 shows the characteristics of standard resins of this type. The substitution of a vinyl chloride homopolymer for the PVC/PVAc copolymer would represent a low-cost solution, and material properties and workability would also match requirements. However, the Law for the Recycling of End-of-Life Vehicles, which took effect in January 2005, stipulates that the recycling rate of shredder dust must be increased to 70% or higher by 2015[3]. It is therefore not desirable from the viewpoint

Table 5 Toluene volatilization and contribution rate of raw materials

Basic raw material	Concentration of toluene volatilization		Contribution rate of toluene volatilization %
	μg/ 1 g raw material	μg/ 1 g dust sealer	
PVC homopolymer	0.5	0.05	0.1
PVC/PVAc copolymer	1.5	0.15	0.4
Plasticizer	0.5	0.15	0.4
Filler	0.0	0.00	0.0
Diluent	2000	40.00	98.6
Adhesive agent	10	0.20	0.5
Moisture absorption prevention agent	0.0	0.00	0.0
	Total	40.55	100

of recycling to increase the amount of the vinyl chloride homopolymer to a level higher than that of the conventional dust sealing material.

The possibility of substituting urethane resins or epoxy resins was also low from considerations of workability and cost.

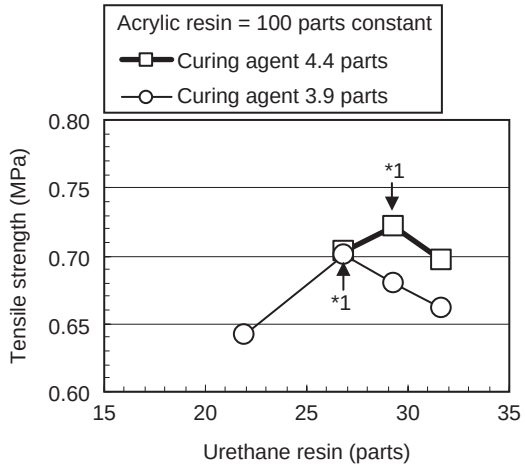
Acrylic resins possess slightly less tensile strength than vinyl chloride homopolymers, but would be candidates as substitute materials if their tensile strength could be increased. Urethane resin, which possesses excellent tensile strength and elongation, and a curing agent were therefore added to acrylic resin, and the effect on the tensile strength of the dust sealing material was studied. The results are shown in Fig. 1. As Fig. 1 shows, the use of a higher ratio of urethane resin to acrylic resin, in addition to the addition of urethane resin and a curing agent that equalized their reaction ratios, has resulted in an increase in the tensile strength of the dust sealing material.

In addition to replacing the PVC/PVAc copolymer with an acrylic resin and a urethane resin, this development project also eliminated the vinyl chloride homopolymer employed in the conventional dust sealing material in order to enable simpler recycling of the shredder dust.

3. Reduction of Toluene

As in the case of analysis of acetaldehyde volatilization, the concentration of volatilized toluene in 1 g of each of the constituents of the dust sealing material was measured, and the rate of contribution of each constituent of the dust sealing material to the concentration of volatilized toluene was calculated from the measurement results and the composition of each constituent. The results are shown in Table 5. The diluent displayed the highest rate of contribution, and this constituent was therefore specified as the main cause of toluene volatilization. A number of organic solvents are mixed in the diluent, one of which is toluene. This project therefore used a diluent that did not contain toluene.

The effect of the adhesion promoter, which displayed



*1 Equivalent reaction ratio of urethane and curing agent

Fig. 1 Compound ratio and tensile strength of acrylic resin, urethane, and curing agent

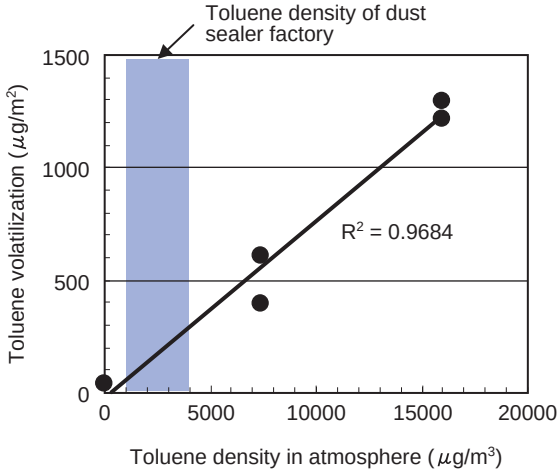


Fig. 2 Influence of toluene density in atmosphere on toluene volatilization

Table 6 Acetaldehyde and toluene volatilization of raw materials

Basic raw material	Concentration of acetaldehyde volatilization		Concentration of toluene volatilization	
	μg/ 1g raw material	μg/1g dust sealer	μg/ 1g raw material	μg/1g dust sealer
Acrylic resin	0.1	0.02	2.5	0.38
Urethane resin and curing agent	0.1	0.01	3.5	0.21
Plasticizer	0.2	0.07	1.5	0.45
Filler	0.0	0.00	0.0	0.01
Diluent	0.0	0.00	0.1	0.00
Moisture absorption prevention agent	0.0	0.00	0.0	0.00
Total		0.10	Total	1.05

a low rate of contribution to the concentration of volatilized toluene but contained a large amount of toluene, was next examined. Toluene is used as a solvent in the production of the adhesion promoter, it was therefore assumed that toluene was incorporated in the substance as impurities. Toluene was therefore also eliminated from the production process of the various constituents used in the developed material.

However, in many cases, solvents containing toluene are used to clean production equipment, pipes, etc. in the factories where dust sealing materials are produced. The toluene concentration in the air in the factories is 1000-4000 μg/m^3. The possibility of the toluene present in the air being incorporated in the dust sealing material during the production process was therefore investigated. As Fig. 2 shows, a correlation was determined between the concentration of toluene in the air and toluene volatilization from the dust sealing material. In parallel with this development project, solvents containing toluene were therefore eliminated from the factories where dust sealing materials are produced, and the concentrations of toluene in the factories have been controlled to a specified level or below.

4. Performance of Developed Material

Table 6 shows the results of measurements of the acetaldehyde and toluene volatilization concentrations in 1 g of each of the constituents of the newly developed dust sealing material. Based on these results and the composition of each constituent, 1 g of the dust sealing material was calculated to contain 0.10 μg of acetaldehyde. Using the same method, 1 g of the material was calculated to contain 1.05 μg of toluene.

Test pieces were formed using the newly developed and conventional dust sealing materials as shown in Fig. 3, and the volatilization concentrations of acetaldehyde and toluene were measured. The results are shown in Fig. 4. In comparison to the conventional dust sealing material, acetaldehyde volatilization has been reduced by more than 90% and toluene volatilization by more than 45% in the newly developed material.

The performance of the material as a dust sealing material was next examined. The material properties of the conventional and newly developed dust sealing materials were compared using the automotive sealant test method specified by JASO M323-86. The results are shown in Table 7. The newly developed sealing material displayed identical material properties to the conventional sealing material, indicating its potential for use as an automotive dust sealing material.

The use of the developed low-VOC dust sealing material enabled vehicle cabin VOC levels to satisfy the voluntary standards adopted by JAMA[(1)], and the

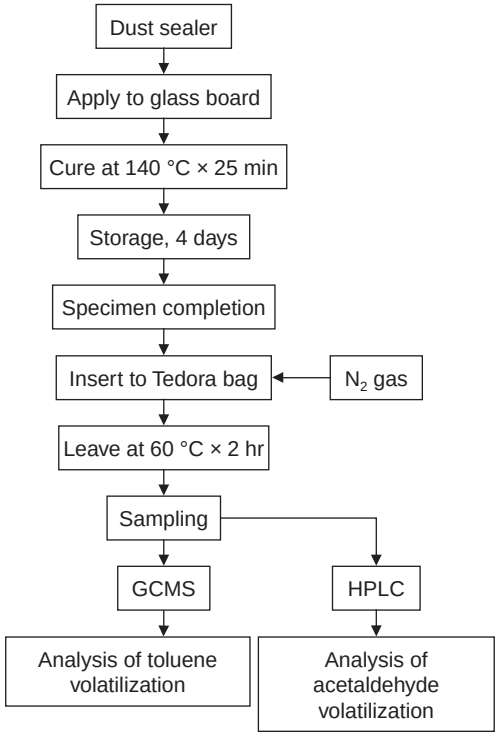


Fig. 3 Measurement method of volatilization

Table 7 Material performance

No	Confirmation item	Developed material	Conventional material
1	Tensile strength	1.3 MPa	1.3 MPa
2	Elongation	290%	150%
3	Shearing adhesion strength	1.4 MPa	1.3 MPa
4	Hardness	74	82
5	Water resistance	1.2 MPa	1.2 MPa
6	Low temperature resistance	Acceptable	Acceptable
7	High temperature adhesion strength	0.60 MPa	0.40 MPa
8	Vibration resistance	Acceptable	Acceptable
9	Watertightness	No water leakage	No water leakage
10	Viscosity	100 Pa·s	90 Pa·s
11	Storage stability	107 Pa·s	97 Pa·s
12	Fluidity	0 mm	0 mm
13	Self-leveling characteristics	No color transparency	No color transparency
14	Coating pollution	Acceptable	Acceptable

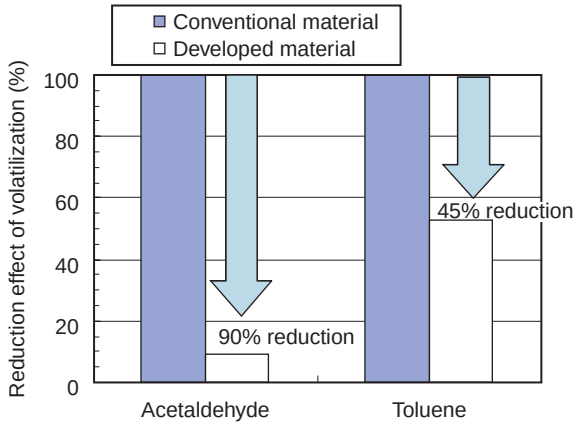


Fig. 4 Reduction effect of acetaldehyde and toluene

developed sealing material has been confirmed as having contributed to a reduction in VOC emissions in automobile cabins.

5. Conclusion

The following are the salient points in the development of a low-VOC dust sealing material that displays low concentrations of volatilized acetaldehyde and toluene.

(1) In order to control production of acetaldehyde and to increase the ease of recycling of shredder dust, vinyl chloride was eliminated by changing the base resin to an acrylic resin from PVC/PVAc copolymer and a vinyl chloride homopolymer. In addition, urethane resin was also employed to increase tensile strength to a level matching that of the conventional sealing material.

(2) A toluene-free diluent was used.

(3) The use of toluene in the production process of the constituents of the dust sealing material was shown to result in the incorporation of toluene into the constituents as impurities, and toluene was therefore eliminated from the production process.

(4) Toluene is present in the air of factories where dust sealing materials are produced and is incorporated in sealing materials. Therefore, the use of solvents containing toluene has been discontinued, and the level of toluene in the air in the factories has been controlled to a specified level or below.

References

(1) Voluntary Approach to Vehicle Cabin VOC Reduction, JAMA Report, No. 98 (2005)

(2) Hasegawa, K., Yaguchi, M.: Development of Low VOC Sealant for Door Hole Seal, Honda R&D Technical Review, Vol. 18, No. 1, p. 172-176

(3) Vehicle Recycling and Waste Reduction, The Motor Industry of Japan 2006, Japan Automobile Manufactures Association, Inc., p. 34-35 (2006)

■ Author ■



Naoki TSURUTA

Interior Sound Enhancement of Vehicle Acceleration for New Model ACCORD

- Transfer Path Analysis Using Principal Component Regression Method -

Atsushi SAKAMOTO* Mutsuru OZAKI*

ABSTRACT

The development of the new model ACCORD set targets for interior sound during acceleration based on target user characteristics, and analyzed sound transfer paths using the principal component regression method to enable these targets to be achieved. This method of analysis enabled the degree of contribution of structure-borne paths and airborne paths to interior sound to be clarified. Synthesized sound, produced on the basis of the results of the analysis, was incorporated in a sound quality evaluation system. This enabled identification of the areas in which measures should be applied, and the extent to which they should be applied, to satisfy interior sound targets. As a result, targets for interior sound in the new model ACCORD were achieved.

1. Introduction

Today, there is an increasing tendency to desire the interior sound of a vehicle during acceleration to match the vehicle concept. For example, while the vehicles may fall into the same category, the difference in the concepts of a sedan and a sports coupe results in different interior sound requirements on the part of users. This has led to the proposal of setting vehicle interior sound with consideration of differences in markets, user preferences, etc.[1]

Transfer path analysis using principal component regression (PCR-TPA)[2] has also been proposed as an effective method of realizing target interior sound. The major characteristics of this method as compared to conventional transfer path analysis are as follows:

(1) The method can simultaneously analyze structure-borne and airborne paths, enabling evaluation of their contribution to overall interior sound.
(2) Following separation of the contributions of the transfer paths, numerical processing can be employed to accurately reproduce the sound via sound synthesis, enabling a sound quality evaluation to be conducted.
(3) Using the results of transfer path analyses and a sound quality evaluation system, the specific areas in which measures should be applied and the extent to which measures should be applied to achieve the target sound can be determined.

These characteristics enable a transition from conventional transfer path analysis, in which the focus has been centered on the reduction of sound pressure and analysis of the target areas mainly limited to analysis of structure-borne paths, to a transfer path analysis that focuses on the enhancement of sound quality and takes the overall interior sound as its object of analysis.

The new model ACCORD sedan and ACCORD coupe share a basic platform, and targets were set for the interior sound in each vehicle during acceleration, based on the vehicle concept. This paper reports on the results of using PCR-TPA in order to realize these interior sound targets.

2. Interior Sound Matching Vehicle Concept

2.1. Target Vehicles

Different body, engine, and transmission combinations are employed in a number of new ACCORD models, but this paper focuses on a model featuring a V6 gasoline engine and 5-speed automatic transmission in a 4-door sedan body (“sedan” below), and one featuring a V6 gasoline engine and 6-speed manual transmission in a 2-door coupe body (“coupe” below).

* Automobile R&D Center

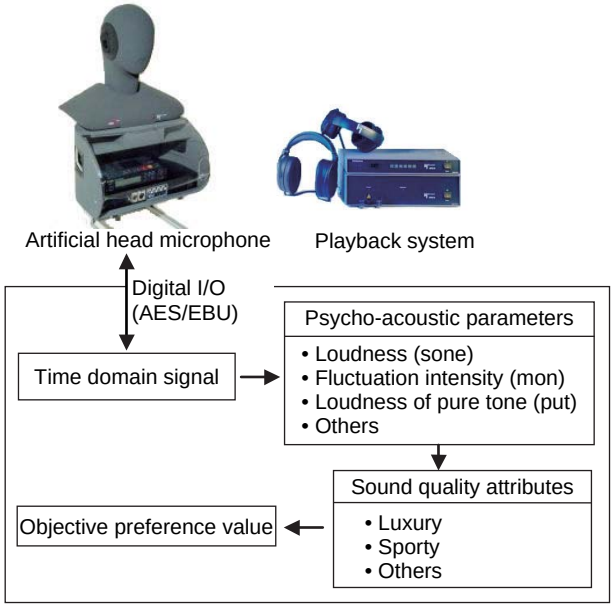
2.2. Setting Target Sound

The objective preference evaluation system[3] shown in Fig. 1 was employed in setting interior sound targets. In this system, sounds are classified in advance into different categories ("quiet and smooth," "quiet and alive," "powerful," etc.), and the level of user preference is expressed as an objective numerical value.

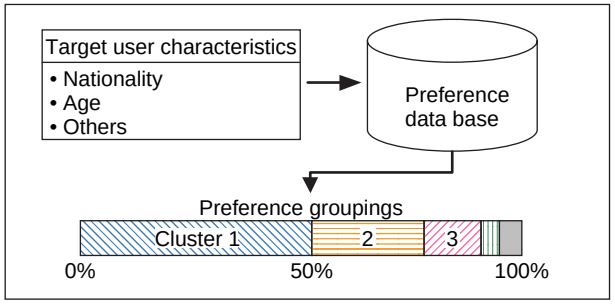
Figure 1(a) shows the results of calculation of objective preferences for the previous ACCORD model using metrics for the level of auditory stimulus ("magnitude," "fluctuation intensity," etc.), and complex sound quality evaluation metrics ("alive," "smooth," etc.). Interior sound was measured using an artificial head microphone, and preference values calculated by applying numerical processing to the objective preference evaluation system.

Figure 1(b) shows the results of setting objective sound preference values based on the development concept for the new model ACCORD sedan and coupe, using a preference database as a reference and taking into consideration the age, nationality, and other characteristics of target users. The clusters in the figure represent "quiet, smooth sound," etc.

A variety of interior sound targets were established to enable the interior sound of the previous model to be modified to match the preferences established for the new model ACCORD sedan and coupe. Figure 2(a) shows a color map of the interior sound of the previous model, which served as the benchmark; Fig. 2(b) shows a color map of the target interior sound for the new sedan; and Fig. 2(c) shows the 3rd order component of the target interior sound of the new coupe, as well as the interior sound of the previous (benchmark) model against engine speed.

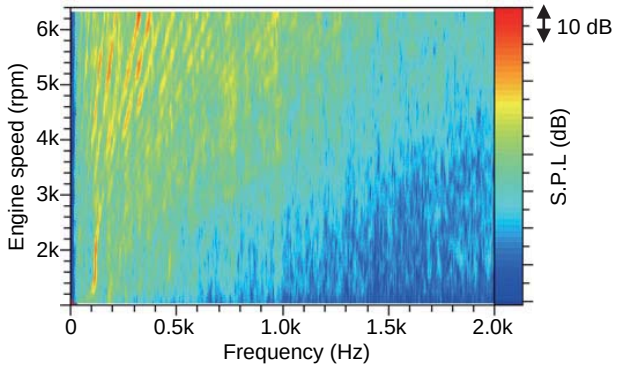


(a) Calculation of preference value

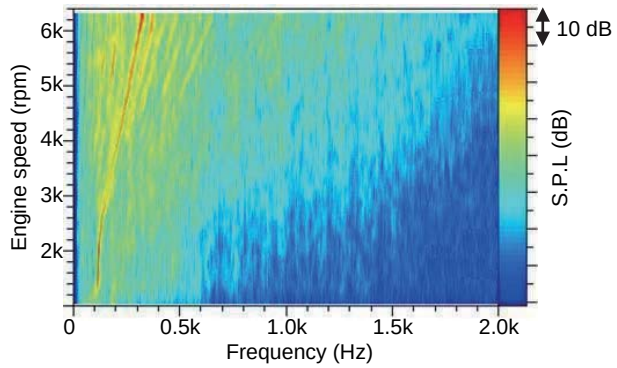


(b) Calculation of preference rate

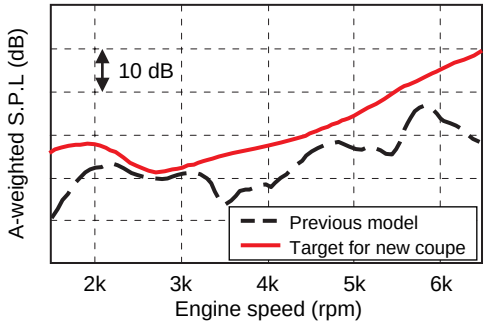
Fig. 1 Preference evaluation system



(a) Previous model



(b) Target for new sedan



(c) Target for new coupe (3rd order)

Fig. 2 Interior sound

The focus in the case of the target interior sound of the sedan was to achieve a sound that was suitable for a wide range of users by reducing the conspicuous high-frequency components against those of the previous model, and the sound pressure increase characteristic was set linear and appropriate for the main order components in relation to engine speed during acceleration.

In the case of the coupe, the focus was on users with a higher level of interest in cars than in the case of the sedan. During cruising and slow acceleration, the sound targets for the coupe were identical to those for the sedan, but during acceleration at WOT, the target was to highlight the sound pressure of the 3rd order component against engine speed.

3. Enhancing Interior Sound

The employment of PCR-TPA to analyze the interior sound of the benchmark model and the application of sound quality evaluation enabled the areas in which measures should be employed, and the degree of measures to be employed, to be specified to achieve the targets established for the interior sound of the sedan and coupe during acceleration.

3.1. Test Method

The previous ACCORD model, which featured a V6 gasoline engine and 5-speed automatic transmission in a 4-door sedan body, was used in the tests.

Measurement points for structure-borne and airborne transfer paths were set as shown in Fig. 3. Two response

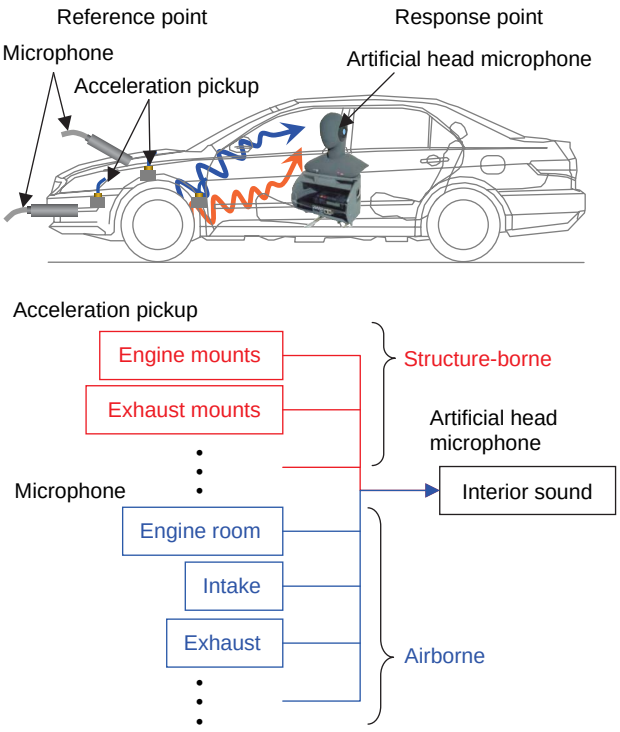


Fig. 3 Measurement setup

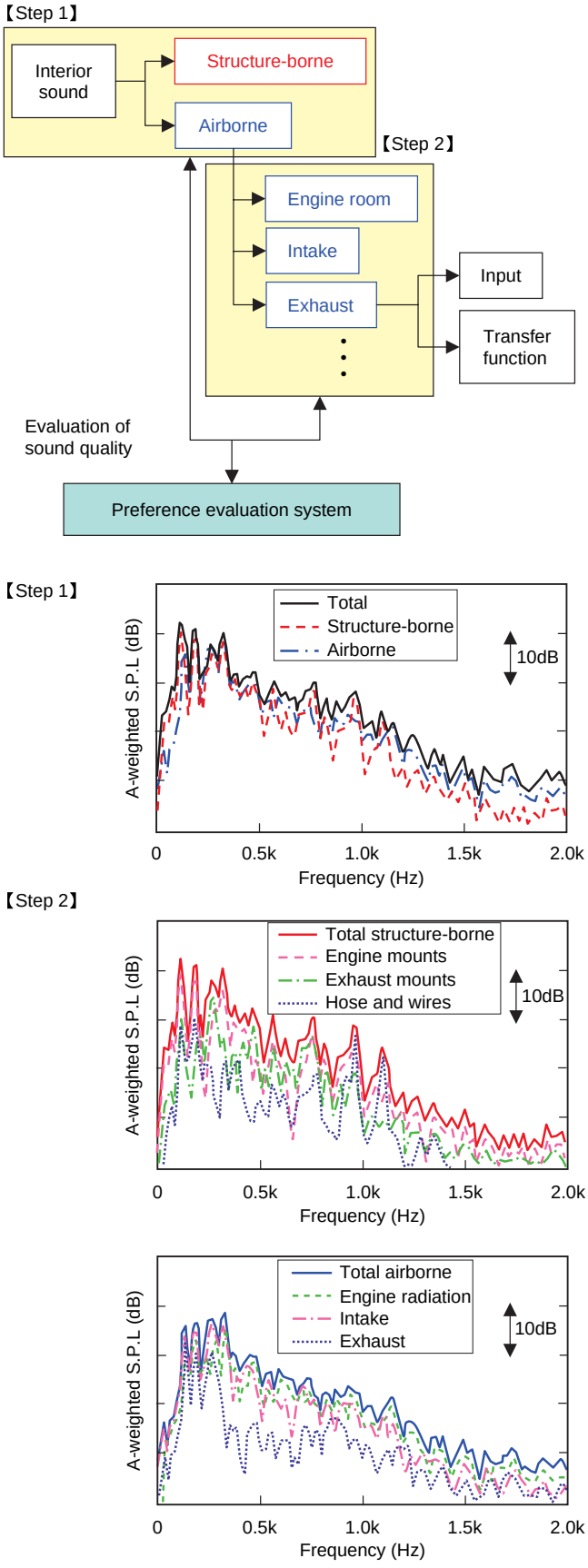


Fig. 4 Analysis result of PCR-TPA

points were employed, at the level of the left and right ears of an artificial head microphone in the passenger seat. The vehicle was placed in a chassis dynamometer that absorbed the torque of the drive wheels, and measurements were conducted under varying load conditions.

3.2. Study for Sedan

The results of an analysis of high-frequency components, conducted in order to increase quietness, are shown in Fig. 4 as a representative example of the results of PCR-TPA conducted to enable achievement of the interior sound targets for the sedan.

In Step 1, the structure-borne and airborne transfer paths were separated. The results showed that while the airborne transfer path made the greatest contribution to interior sound at 1.2 kHz and above, the contribution of the structure-borne transfer path was higher at around 750 Hz, 1 kHz, and 1.1 kHz. In Step 2, the structure-borne and airborne transfer paths were divided into engine mounts, exhaust mounts, engine radiation noise, intake noise, exhaust noise, etc., to determine the transfer paths for which measures should be applied, as well as the extent of the measures to be applied. The results of this analysis showed that the engine mount and exhaust mount paths were main factors in the sound at 750 Hz and overlap of these paths encourages sound of this frequency, while the paths for the hoses and wires that connect the engine and body of the vehicle were the main factor in the sound at 1 kHz and 1.1 kHz. In relation to airborne transfer paths, the engine housing and intake noise paths were selected for examination. On the basis of the results of these analyses, the transfer paths where measures should be applied were resolved into inputs and transfer functions, and measures were applied in the main areas.

This resulted in the achievement of the interior sound shown in Fig. 5.

3.3. Study for Coupe

Figure 6 shows the results of PCR-TPA of the 3rd order component of interior sound during acceleration at WOT, conducted in order to achieve the target sound for the coupe. These results show that at engine speeds less than 3000 rpm, the contribution of the exhaust noise transfer path was highest, while at engine speeds of above 3000 rpm, the contribution of the intake noise transfer path was highest. Considering that the target in this case was to maintain an identical interior sound to that of the sedan when the vehicle was cruising or accelerating slowly, it was more appropriate to apply measures to the intake and exhaust noise transfer paths than the structure-borne transfer paths. These two transfer paths were resolved into inputs and transfer function, and measures were applied to the main areas.

The interior sound that was achieved is shown in Fig. 7.

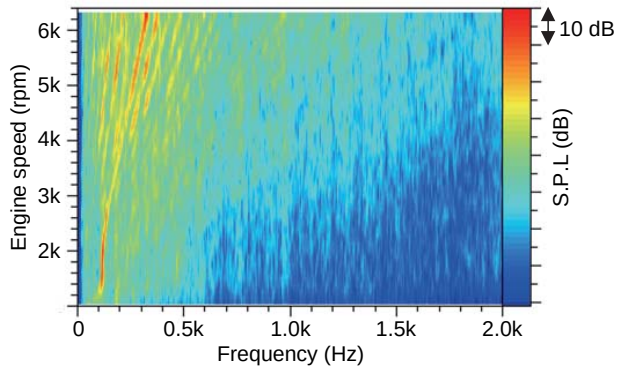


Fig. 5 Interior sound of new sedan

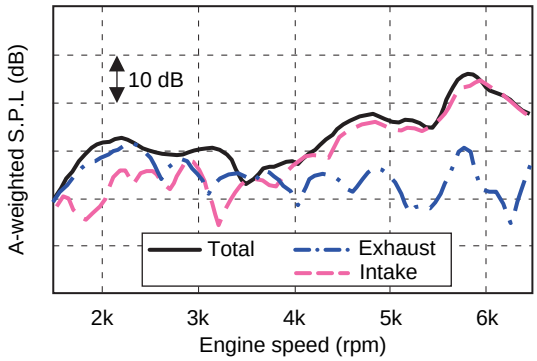


Fig. 6 Analysis result of PCR-TPA (3rd order)

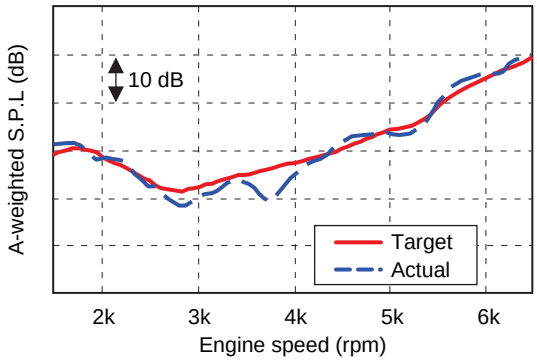


Fig. 7 Interior sound of new coupe (3rd order)

4. Conclusion

The project discussed in this paper used PCR-TPA to enhance the interior sound of the new ACCORD models during acceleration. The salient points of the project are as follows:

(1) A system enabling evaluation of objective preferences with regard to sound quality was employed to establish targets for the interior sound of the sedan and coupe for target users.

(2) The application of PCR-TPA to the benchmark vehicle and the analysis of the synthesized sound as a result using the sound quality evaluation system enabled the specification of the areas in which measures should be applied in order to achieve the interior sound targets for the sedan and coupe. The application of measures in these areas resulted in the achievement of the interior sound targets.
(3) PCR-TPA was demonstrated to be an effective method of achieving interior sound targets, enabling the areas of highest contribution in structure-borne and airborne transfer paths to be determined, and targets for measures to be set.

References

(1) Noumura, K., Yoshida, J.: Quantification of Luxury and Sporty Car Interior Sounds Perceived by the General Public in Different Markets, Honda R&D Technical Review, Vol. 14, No. 1, p. 237-246
(2) Noumura, K., Yoshida, J.: Method of Transfer Path Analysis for Interior Vehicle Sound Using Principal Component Regression Method, Honda R&D Technical Review, Vol. 18, No. 1, p. 136-141
(3) Noumura, K., Yoshida, J.: Study of Interior Sound Preferences at Acceleration, Honda R&D Technical Review, Vol. 18, No. 1, p. 142-148

■ Author ■


Atsushi SAKAMOTO


Mutsuru OZAKI

Development of High Performance Floor Insulation Structure of 2008 Model Year ACCORD

Yoshihiro NOGUCHI* Kenji TANAKA* Hiroko TADA*
Fumihiko IDE* Kazuhito MISAJI*

ABSTRACT

The development of the new model ACCORD set out to produce a sound proof package that would result in competitive NV performance, while at the same time demonstrate good weight performance. The study of the sound proof package employed a variety of methods that have demonstrated effectiveness in other development projects, as follows: A hybrid statistical energy analysis (hybrid SEA) modeling method, a technique enabling prediction of the acoustic characteristics of multilayered materials, and FEM analysis. The results of these analyses showed that the floor, including the tunnel, displayed a high rate of contribution to road noise in the vehicle cabin. This enabled the development of a sound insulating floor structure that balanced reduced weight with enhanced sound insulating performance, which has contributed to the achievement of increased quietness in the new model ACCORD.

1. Introduction

The quietness of automobile cabins is an important element in increasing commercial appeal. The achievement of weight savings is also important from the perspective of fuel efficiency. However, in many cases, the achievement of increased quietness (enhanced sound insulation performance) and the achievement of weight savings are mutually contradictory objectives. The specifications of sound proof packages should be studied from the early stage of vehicle development in order to achieve a superior balance between these two aspects of performance[1]. Hybrid statistical energy analysis (SEA) modeling methods[2, 3], a technique enabling estimation of the acoustic characteristics of multilayered materials[4, 5], and FEM analysis are available as proven and effective methods of studying the specifications of sound proof packages.

These techniques were used in the development of the new model ACCORD, which employs a V6 gasoline engine, in an attempt to realize a sound proof package that displayed good weight performance but also enabled the achievement of competitive NV performance. The project resulted in the development of a floor insulation structure that balanced weight savings with increased sound insulation performance. This paper will provide details of the project.

2. Method of Development of Floor Insulation Structure

The project studied sound insulation specifications for the floor carpet and the structure of the floor panels as floor insulation structures. The floor carpet acoustic specifications were established on the basis of the following set of procedures from the initial stages of the development process:

(1) Establishment of targets for interior cavity sound pressure level
(2) Analysis of rate of contribution using a hybrid SEA modeling method
(3) Based on the result of the contribution analysis, the establishment of targets for acoustic performance (sound absorption performance and sound insulation performance) for areas displaying the higher contribution to interior cavity sound pressure level enabling achievement of the targets established for interior cavity noise
(4) Establishment of targets for acoustic characteristics of sound insulating materials (absorption coefficient, transmission loss) to enable achievement of the above targets
(5) Use of technique for prediction of acoustic characteristics of multilayered materials to study specifications for sound insulating materials (material, thickness, area) to

* Automobile R&D Center

enable achievement of targets for acoustic characteristics of materials

(6) Verification of effectiveness in actual vehicle

In the development of the floor panel structure, a genetic algorithm was employed to enable simultaneous optimization of the shape of the panels and the shape and positioning of the damping materials, to assist in the determination of specifications that would minimize sound radiation from the panels at the minimum weight[6].

3. Study of Floor Specifications

3.1. Results of Analysis of Contribution to Noise

During the study of the sound insulating specifications, hybrid SEA modeling method was used to analyze contributions to interior cavity sound pressure level in the previous mass production model. The results of these analyses are shown in Fig. 1. The contribution of sound radiation and transmission by the floor, including the tunnel, is higher at medium frequencies, in particular at around 250 Hz, the frequency of sympathetic resonance of the air column. In addition, the contribution of sound transmission from the floor is higher in high frequency range. Based on these results, it was judged that countermeasures for sound radiation and sound transmission of medium frequency range and transmission of high frequency range would be necessary in the floor. As shown in Table 1, the concept with regard to the specifications of the floor sound proof package was to develop a floor carpet that would enhance sound insulation performance, acting as a countermeasure to the sound radiation and transmission from the floor in the previous mass production model, and that would also enhance sound absorption performance in the interior cavity. In addition, it was judged necessary to study the shape of the floor panels in order to enable reduction of the vibration of the panels, an important element of countermeasures against sound radiation from the panels, with the minimum amount of asphalt sheet.

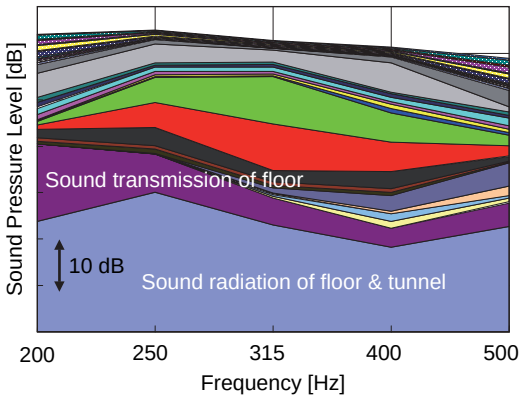


Fig. 1 Power contribution to interior cavity sound pressure level

Table 1 Countermeasure method of sound radiation and sound transmission

	Sound radiation	Sound transmission
Floor carpet	Enhancement of sound insulation performance	Enhancement of insulation performance and absorption performance
Floor panel	Reduction of panel vibration	–

3.2. Floor Carpet Specifications

The floor carpet configuration shown in Fig. 2, which displays both sound insulation and sound absorption performance, was proposed in order to reduce sound radiation and transmission and enhance the sound absorption performance in the interior cavity. The carpet has a porous layer as a sound absorbing structure on the interior cavity side and a heavy layer with porous layer as a sound insulating structure on the panel side. As Fig. 3 shows, for ensuring the aerodynamic performance of the under floor, the layout of the floor frame for the new model ACCORD has been modified to inside the cabin from outside the cabin. As a result of a contour map of the thickness of the sound insulating materials at the back of the carpet as shown in Fig. 4 and the thickness distribution of the floor carpet as shown in Fig. 5, an adequate level of thickness was able to be employed compared to the previous mass production model. The average thickness of the carpet is increased by approximately 30%.

The possibility that user treadling comfort would be affected by the use of increased thickness was a concern in the study of floor carpet specifications (selection of

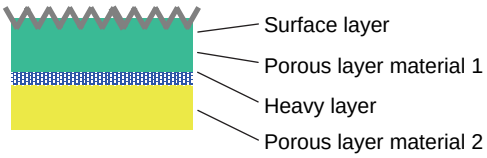


Fig. 2 Multi-layer sound-proof package

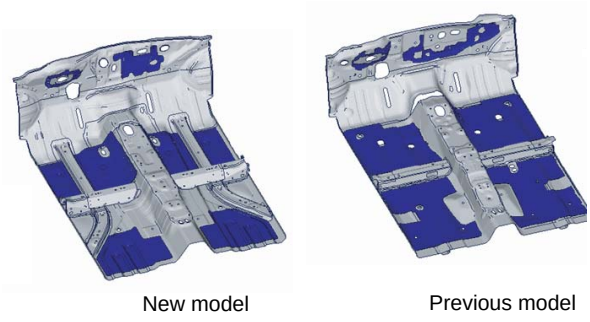


Fig. 3 Comparison of floor structure between previous and new model

material characteristics, thickness, area, etc.), and it was necessary to select materials considering this aspect of performance. Therefore, with considering the user treadling comfort, the specifications were studied using the method of predicting the acoustic characteristics of multilayered materials. The use of high-rigidity expanded polypropylene beads underneath the porous material covering the panels has enabled the achievement of a balance between sound insulation performance and user treadling comfort (Fig. 6).

3.3. Floor Panel Specifications

In the development of the floor panel structure, an FEM model of the vehicle was constructed and used to study sound radiation power with an excitation on the suspension mounting points. In addition, a genetic algorithm was employed simultaneously to optimize the shape of the panels and the shape and positioning of the asphalt sheet. As shown in Fig. 7, the flat panels were optimized with dimple shape and bead shape. As a result, the reduction in the sound radiation power from the panel surfaces was achieved as compared to that of the previous model (Fig. 8). The thickness of the asphalt sheet was also reduced as compared to the previous model, which contributes to the achievement of weight savings.

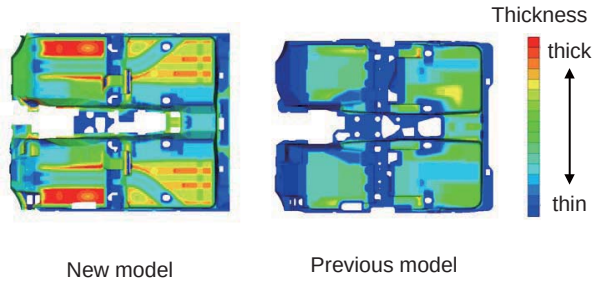


Fig. 4 Comparison of floor carpet thickness distribution between previous and new model

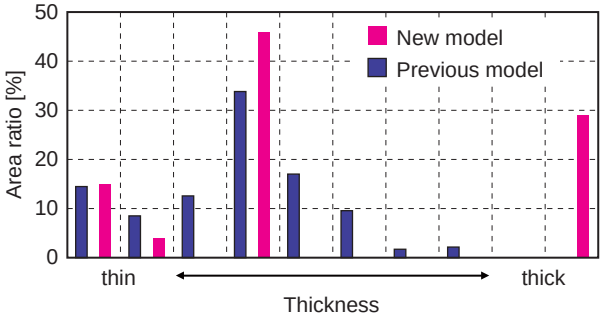


Fig. 5 Floor carpet thickness distribution of previous and new model

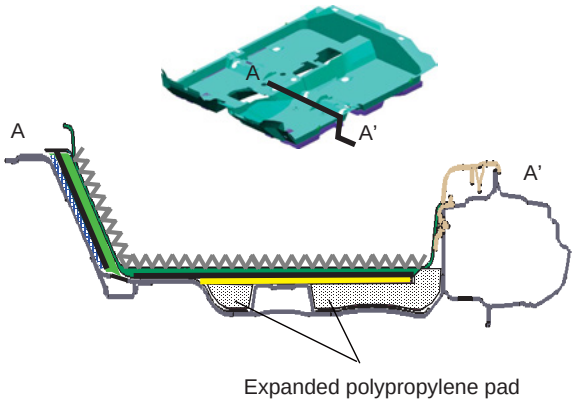


Fig. 6 Cross section of floor carpet

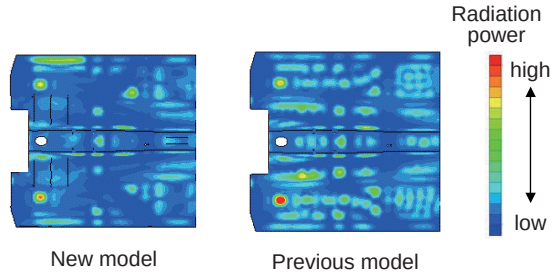


Fig. 7 Comparison of radiation power from panel

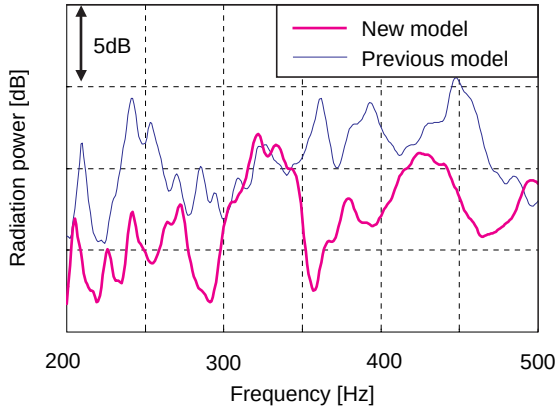


Fig. 8 Radiation power from floor panel

4. Performance of Completed Vehicle

The use of the sound-absorbing and sound-insulating floor carpet and the low-vibration floor panel structure described above has reduced the level of both radiated and transmitted sound in the new model ACCORD, in addition to increasing the sound absorption performance of the interior cavity. These countermeasures have reduced the level of road noise in mid and high-frequency range as compared to that of the previous mass production model.

5. Conclusion

The development of the new model ACCORD set out to produce a sound proof package that would result in

competitive NV performance, while at the same time demonstrate good weight performance. The project employed hybrid SEA modeling method, a technique for predicting the acoustic characteristics of multilayered materials, and FEM analysis to study the specifications of the sound proof package, with the following results:

(1) The floor of the vehicle, including the tunnel, was demonstrated to display a high contribution to interior cavity under road noise test condition.
(2) A sound-absorbing and sound-insulating floor carpet that achieved a superior balance between sound absorption and sound insulation characteristics was proposed as a countermeasure against sound radiation and sound transmission from the floor, which demonstrated a high rate of contribution to interior cavity sound pressure level, and to enhance the sound absorption performance of the cabin.
(3) Dimple and bead shapes were employed on the floor panel as a countermeasure to reduce sound radiation and to enable the achievement of weight savings by using the minimum amount of asphalt sheet.

The project resulted in the development of a sound insulating floor structure that both contributes to weight reduce and acoustic performance enhancement. The use of this floor structure has contributed to increased quietness in the new model ACCORD.

References

(1) Noguchi, Y., Doi, T., Tada, H., Misaji, K.: Selection Technique of Sound Absorption Type Acoustic Insulation Material by Applying SEA Modeling Method, Honda R&D Technical Review, Vol. 18, No. 1, p. 149-153
(2) Misaji, K., Tada, H., Yamashita, T., Nakamura, M., Tanaka, H., Kokabu, S., Morie, D.: Testing Uniqueness of Hybrid SEA Modeling Solution for a Passenger Car, SAE Paper, 2003-01-1408 (2003)
(3) Misaji, K., Tada, H., Yamashita, T., Kokabu, S., Tanaka, H., Koshigoe, S.: Hybrid SEA Modeling Scheme for Analysis of High-frequency Noise in Passenger Car, Review of Automotive Engineering JSAE, Vol. 26, No. 1, p. 3-8 (2005)
(4) Misaji, K., Tada, H., Yamashita, T., Mantovani, M., Gaudino, C., Falk, T.: Prediction of the SEA Input Parameters for the Sound Package, SAE Paper, 2003-01-1022 (2003)
(5) Misaji, K., Tada, H., Noguchi, Y., Kuruhara, Y., Yamashita, T.: Prediction of Vehicle SEA Model Input Parameters a Sound Package, Honda R&D Technical Review, Vol. 15, No. 1, p. 181-186
(6) Caprioli, D., Bertolini, C., Gaudino, C.: Improved NVH Performance Via Genetic Optimization of Damping and Shape of Vehicle Panels, SAE Paper, 2005-01-2329 (2005)

Author


Yoshihiro NOGUCHI


Kenji TANAKA


Hiroko TADA


Fumihiko IDE


Kazuhito MISAJI

Development of Aluminum Liner in Die-cast Cylinder Block for High-power and High-displacement V6 Engine

Takashi KOMATSUDA* Masayuki TAKAHASHI* Katsuhisa YASUKAWA*
Junichi OHMURA* Noriyuki NAMBA**

ABSTRACT

A 3.7 L V6 engine has been developed for the 2007 model year MDX. The new engine was developed based on the framework of the 3.5 L V6 engine employed in the previous MDX, but the engine's displacement and power have been increased.

The use of an aluminum alloy cylinder liner is an effective method of simultaneously increasing engine displacement and power. In employing an aluminum alloy cylinder liner in the new engine, the development focused on the sliding characteristic between the liner and piston rings. The reliability of the sliding characteristic has been ensured by the application of two main new technologies to the sliding surface of the bore: Detailed specification of the exposure of the particles on the liner, and the achievement of increased adhesion between the liner and cylinder block to increase the resistance of the bore to thermal distortion. This paper discusses the development of the aluminum liner for use in a cast iron cylinder block in the new high-power, high-displacement V6 engine, and provides an overview of the main technologies employed.

1. Introduction

Today, there is a growing requirement to increase the power and displacement of automotive engines while also achieving compactness. As a major engine component, these requirements have an effect on the cylinder block in particular. Effectively cooling the combustion chambers and pistons to reduce temperatures and prevent abnormal combustion is an important factor in the achievement of increased engine power. To balance increased displacement with compactness, it is important to increase the diameter of the cylinder bores without increasing the dimensions of the engine. However, reducing the dimensions of the bore bridges by increasing the diameters of the bores increases the likelihood that higher temperatures will be generated in the block. Reducing the temperature of the cylinder bores to make certain that it does not exceed limits for strength is an important point to be considered in achieving increased displacement.

Making the transition from a die-cast cylinder block using cast iron liners, as currently employed in the majority of automobiles, to an all-aluminum cylinder block with a high heat transfer coefficient would represent an effective means of enhancing the cooling performance of the engine[(1)-(4)].

A variety of aluminum alloy cylinder blocks have been developed to this end. An all-aluminum cylinder block using a hypereutectic Al-Si alloy ("A390 alloy" below) has been put into practical use. To ensure quality in the inner surfaces of the bores, low-pressure die casting or low-speed medium-pressure die casting are employed when manufacturing a cylinder block using A390 alloy. Compared to high-pressure die casting methods ("HPDC" below) in which injection is conducted at high speeds and under high pressure, these techniques result in a higher average wall thickness, making it a challenge to achieve weight savings in the cylinder block as a whole, and they also result in a longer production cycle.

In order to continue to benefit from the cooling performance of all-aluminum cylinder blocks, while achieving higher quality and increased productivity by sharing production facilities and processes with die cast

* Automobile R&D Center

** Honda Engineering Co., Ltd.

cylinder blocks using cast-iron liners, it was necessary to develop a technology enabling the use of die casting to manufacture a die cast cylinder block with aluminum liners[2), 4)].

2. Establishment of Targets for Development of Cylinder Block with Aluminum Liners

Honda's V6 engines for both the domestic and overseas markets have increased in power (over 220 kW) and displacement, as can be observed in the LEGEND models. As a major engine component, the cylinder block should respond to these demands, but it is also necessary to ensure quality and productivity. To satisfy these requirements, the following targets were set for the development of aluminum liners for a high-power, high-displacement 3.7 L V6 engine.

(1) To achieve high power and high displacement by increasing the diameter of the bores, without increasing the external dimensions of the cylinder block against the previous 3.5 L V6 engine.
(2) To ensure quality and productivity by sharing production facilities and processes with the die cast cylinder block with cast iron liners used in the previous 3.5 L V6 engine.

The material for aluminum liners is produced by adding high concentrations of silicon, alumina, or other hard substances to the aluminum base material. The composition of the material therefore differs fundamentally from that of the material used for cast-iron liners.

The hard materials help make certain that no abnormal wear, seizure, or scoring of the inner surfaces of the bores occur due to the pressure of the sliding surfaces of the piston rings and pistons. It is important to use hard materials with appropriate properties and to specify an appropriate degree of exposure of particles in order to achieve functional surface properties on the inner surface of the bores, or it would be unlikely to ensure the sliding characteristic of the piston rings, pistons, and aluminum liners.

With regard to the cylindrical stiffness of the liners, bore stiffness may decline due to the fact that aluminum, the base material, has a lower Young's modulus than cast iron. The issues discussed above can be summarized as follows:

(1) Ensuring the sliding characteristics between the aluminum liners and the piston rings and pistons, to increase reliability with respect to seizure and scoring.
(2) Ensuring the stiffness of the area around the cylinder block bores in which the aluminum liners are fitted, to help prevent heat distortion and reduce oil consumption and degradation.

These two issues are related to the characteristics of the materials used in the aluminum liners and structure of the cylinder block employing the aluminum liners. Issue (1) necessitates a new way of thinking and new criteria of evaluation with regard to the conventional die cast cylinder block with cast-iron liners, and issue (2) necessitates the same with regard to the A390 alloy cylinder block.

The following techniques were employed to respond to these issues:

(1) Optimal materials were selected for the hard materials used for the aluminum liners and the materials used for the piston rings. In addition, hard particles were exposed on the inner surfaces of the bores of the aluminum liners to enhance the sliding characteristic.
(2) Minute projections were employed on the outer surfaces of the cylinder liners to enhance adhesion, and stiffness has been increased by the integration of the liners and the bores. A method of evaluating liner adhesion was also developed.

3. Development of Cylinder Block with Aluminum Liners

A width of 3 mm was set for the die cast aluminum between the liners, the part in which the main change was made. In order to achieve increased displacement, the bore diameter was increased to ϕ 90 mm from ϕ 89, used in the previous 3.5L V6 engine, without changing the 98 mm bore pitch.

The aluminum liner materials provided the advantage

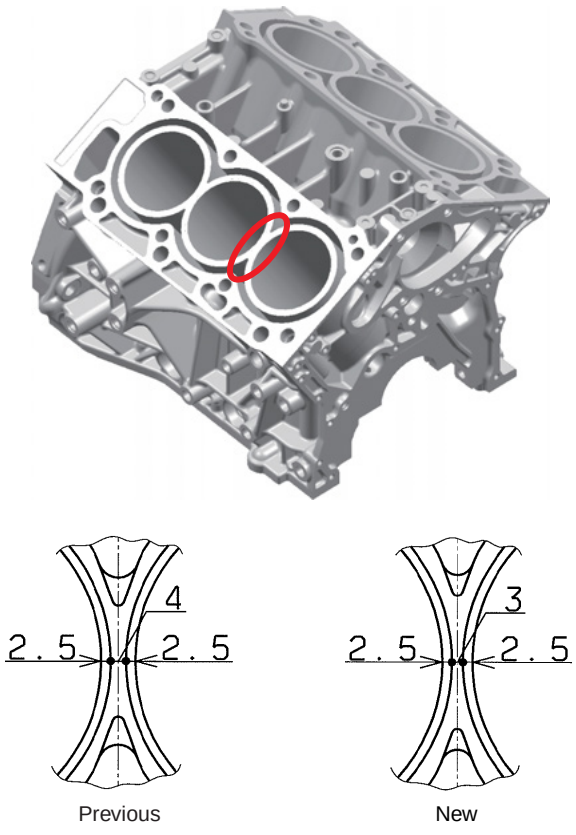


Fig. 1 Cylinder block and bore bridge section

Table 1 Specifications of cylinder blocks

	Previous	Developed
Total displacement (cm^3)	3471	3664
Bore (mm)	89	90
Stroke (mm)	93	96
Bore pitch (mm)	98	98
Block height (mm)	235	235
Block material	Aluminum alloy	Aluminum alloy
Liner material	Cast iron	AL (Spray compacted) High-Si aluminum alloy
Liner thickness (mm)	2.5	2.5
Weight (kg)	27.4	25.3

of increased castability, enabling the dimensions of the die cast aluminum between the liners to be reduced. The materials used in the aluminum liner and die cast aluminum have similar linear coefficients of expansion, thereby reducing the residual stress in the bore bridges caused by contraction as the material solidifies. This reduces the tendency for cracks to appear in the die cast aluminum used in the bore bridges, enabling the dimensions of the aluminum between the liners to be reduced from 4 to 3 mm.

Figure 1 shows an exterior view of the cylinder block and liners, and a magnified diagram of the bore bridge section.

By means of changing only the liners from cast iron to aluminum in a die cast cylinder block, the bore diameter was able to be expanded while maintaining compactness, with the external height and width of the cylinder block identical to those of the cylinder block employed in the previous model. In addition, the use of a shared exterior form for the block and shared die cast aluminum materials has enabled the existing HPDC facilities and exterior surface machining facilities to be shared. The use of the aluminum liners also enables the achievement of weight savings, reducing the weight of the cylinder block by approximately 2 kg against that of a die cast cylinder block using a cast-iron liner.

Table 1 shows the specifications of the cylinder blocks.

3.1. Selection of Aluminum Liner Material

The sliding surfaces of the liners are constantly exposed to high pressures from the pistons and piston rings. In addition, if impurities are present, scoring can occur. The base material for the aluminum liners has a low level of hardness, and hard materials are therefore added to ensure the hardness of the sliding surfaces. Alumina and silicon are currently the major hardening materials used in aluminum liners.

Table 2 shows the materials used in comparative tests.

As has already been indicated in a variety of reports, the amount of hardening material used, and the diameter and form of the particles in the materials, are important factors in ensuring the sliding characteristic[(1), (2), (4)].

However, the decision on whether to use alumina or silicon was a higher priority than the amount of hardening material to be used or the diameter and form of the particles, and it was therefore necessary to determine the areas in which these materials differed.

Table 2 Liner samples for engine tests

	Sample A	Sample B	Sample C
Particulate material	Al_2O_3	Al_2O_3	Si
Particle diameter (μm)	3	30	5
Liner manufacturing method	Powder metal	Melt-in	Spray forming

Table 3 Material property of aluminum liner

	Item	Unit	Sample A	Sample B	Sample C
Particle	Material	—	Al_2O_3	Al_2O_3	Si
	Hardness	Hv	2600	2600	1000
Liner	Tensile strength	(MPa)	250	240	250
	Young's modulus	(GPa)	100	95	90
	Thermal conductivity	(W/m·K)	120	115	120
	Thermal expansion coefficient	($\times 10^{-6}$/K)	16	19	16

Table 4 Comparison of hardness

	Piston ring		
	Top	2nd	Oil
Average hardness (Hv)	1150	900	1050

Table 3 shows a comparison of hardening material and aluminum liner properties.

Table 4 shows the hardness of the piston ring material that the liner material would be sliding against.

Alumina is harder than the nitrided stainless steel that is generally employed in the piston rings used in hypereutectic A390 alloy cylinder blocks, while the hardness of silicon is basically identical. Silicon is therefore the preferred hardening material.

Because these liner materials are compound materials of aluminum and hardening materials, the important factor is the retention capacity of both materials.

A microscope was used to study the dropping out of particles from the inner surface of the bores due to machining as a means of evaluating the retention capacity of the hardening material with respect to the aluminum base material.

Figures 2 and 3 show microscope photographs of the inner surface of a liner following machining.

Resistance during honing made particles drop out of the surface of Sample A, using a material to which alumina particles had been added. Machining conditions were optimized and the sample was checked again, but the status of particle dropouts did not improve. This confirms the generally held belief that

ensuring retention between alumina and aluminum is challenging. Silicon particle dropouts were not observed in the case of Sample C.

Tests of seizure and scoring resistance were conducted in an actual engine to assure accurate reproduction of factors affecting lubrication and surface pressure.

The results of the durability tests are shown in Fig. 4.

Piston seizure occurred when Sample A was used, and the material did not satisfy the target durability time requirement. Given that aluminum particles dropped out at the machining stage, it is likely that additional dropouts occurred due to the sliding of the piston rings during actual operation, resulting in seizure of the pistons. Sample B was a material formed from chemical bonding between alumina and an aluminum base material, and no particle dropouts and consequent piston seizure was observed in this case.

When adding alumina to aluminum, it is necessary to modify the form of the alumina, for example by producing fibrous shapes, in order to ensure retention by the aluminum[1]. In the case of Sample C, no abnormal dropouts of silicon particles were observed following the durability tests, highlighting the basic retention between aluminum and silicon.

Figure 5 shows a comparison of piston ring wear and blow-by gas deterioration rate between Samples B and C after the target durability time had elapsed.

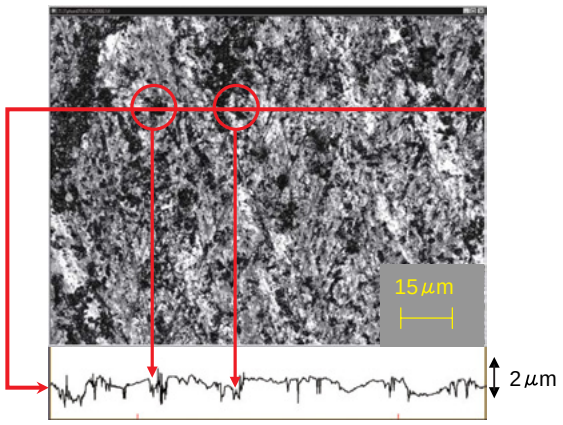
Abnormal wear occurred in the case of Sample B, and blow-by gas increased during the durability tests. The high degree of hardness of alumina makes it important to select the amount to be added and the diameter of the particles to be employed. Sample B could not be modified due to the manufacturing method employed for the liners.

Based on these results, Sample C, in which silicon had been used as the hardening material, was selected as the material for the aluminum liners.

3.2. Form of Inner Surfaces of Bores

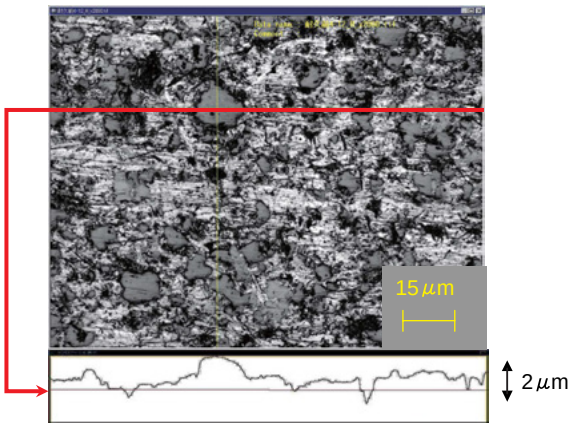
The initial form of the inner surfaces of the bores produced by machining, prior to break-in, is an important factor in ensuring the sliding characteristic of the aluminum liner. The achievement of an appropriate degree of exposure of the silicon particles on the bore surface is a key factor in preventing piston seizure and scoring during the initial operation of the cylinders. Figure 6 shows a diagram of the sliding of the piston rings and pistons over the inner surface of a bore. The exposed silicon particles form a sliding surface that prevents seizure and scoring by the piston rings[4].

A three-stage honing process was developed as a new



Pitting caused by particles dropping

Fig. 2 Sample A



Particles do not drop out

Fig. 3 Sample C

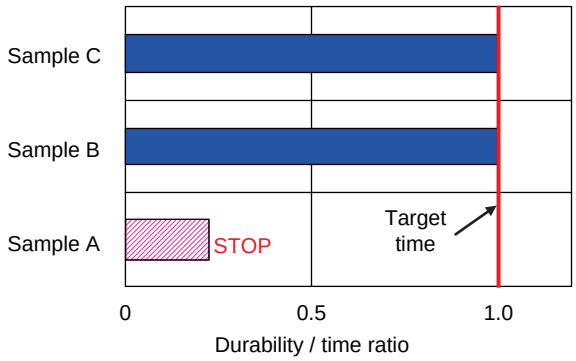


Fig. 4 Durability test results

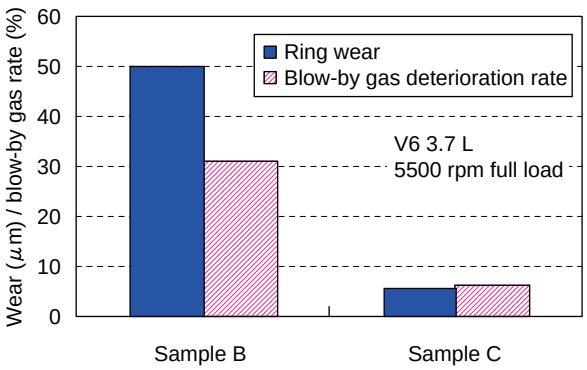


Fig. 5 Wear result

machining method for exposure of the silicon particles. A diagram of this process is shown in Fig. 7.

In the first stage of the process, the inner surface and inner diameter are machined. In the second stage, a smooth surface with a roughness of 0.9-1.8 μm is achieved. The third stage of the process, the finishing stage, removes the small amount of remaining aluminum from around the silicon.

Figure 8 shows the results of laser micrography of the surface of the bore following the second and third stages of the process.

These images show that from the second through the third stages, the aluminum covering the silicon particles is removed, and the surface made smoother.

Figure 9 shows the results of scoring tests in an actual engine, conducted prior to break-in under dry lubrication conditions with different heights of exposure of the silicon particles.

The results indicate that while there is no impairment to function (engine shutdown, abnormal noise, etc.) even at a particle height of below around 0.1 μm, some scoring of the inner surface of the bore did occur. No scoring occurred at particle heights of 0.15 μm or higher, and a figure of at least 0.15 μm was therefore selected as appropriate for the initial height of the particles from considerations of function[3].

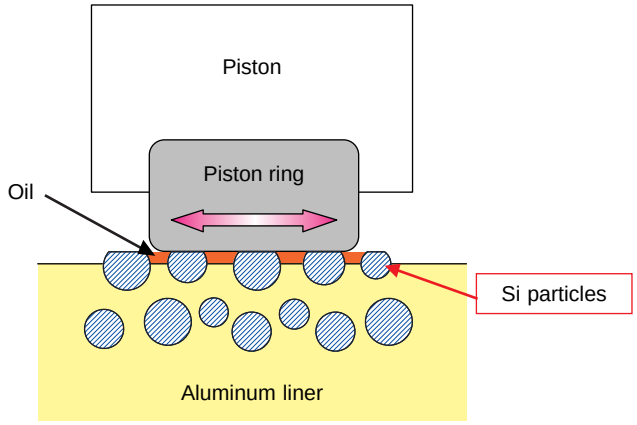


Fig. 6 Function of bore surface

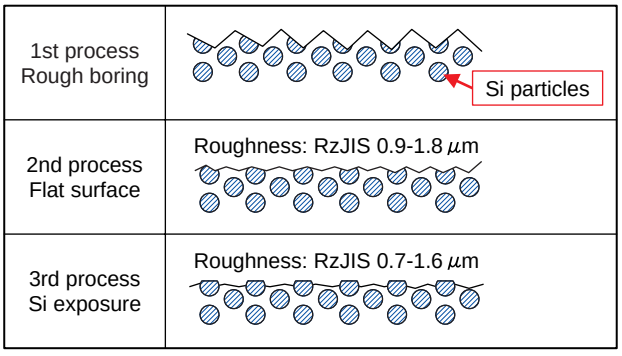


Fig. 7 Bore honing process

Figure 10 shows changes in the roughness of the bore surface, from the initial state to completion, of a 1 800-hour bench durability test (simulation of 240 000 km of high-speed driving for EU standards). There is virtually no change in the figures, from initial figures of 0.9-1.4 μm after machining, to 0.9-1.15 μm following the completion of the durability tests.

The wear characteristic in an actual engine resembles the grinding characteristic of the third stage of the honing process. Honing proceeds by wearing away a greater amount of the soft aluminum than the hard silicon. At the same time, microscopic silicon particles drop out, and the

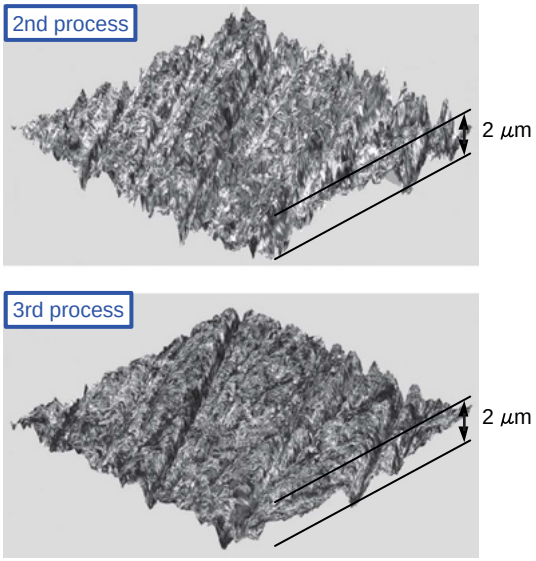


Fig. 8 Bore honing process surface measurement result

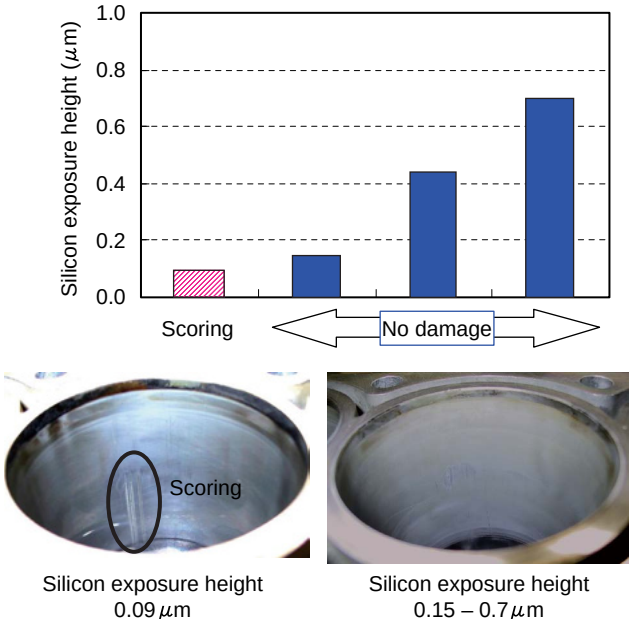


Fig. 9 Engine scoring test result

Table 5 Comparison of piston ring materials

Base metal	17Cr 0.8C	13Cr 0.6C	10Cr 0.5C
Cr nitride/carbonization particle size (μm)	5 – 8 μm	Under 2 μm	Under 2 μm
Average hardness of nitrided case (Hmv)	1150	1050	1050

repetition of this produces a uniform surface, ensuring that a particle exposure height of 0.15 μm or more is maintained until the liner reaches the end of its durable life. This three-stage honing process enabled an equivalent sliding surface to that produced following initial break-in in an actual engine by means of machining to be achieved.

3.3. Selection of Piston Ring Material for Use with Aluminum Liners

The nitrided stainless steel generally used in hypereutectic A390 alloy cylinder blocks was used as a base material, and the optimum amount of Cr for addition was determined.

Table 5 shows the piston ring materials examined in this process.

It is not necessarily the case that the harder material is an appropriate choice. The degree of wear of the piston rings and the liners when the piston rings are used in combination with aluminum liners containing silicon should also be considered.

The wear resistance of the ring material and the liner material was tested for each amount of Cr added. The change in the amount of Cr added had virtually no effect on surface hardness, but the diameter of the Cr carbonitride particles varied from 5-8 μm at 17Cr to 2 μm or less at 13Cr. Figure 11 shows the microstructure of the piston ring.

The degree of wear of the aluminum liner material was measured in component sliding tests. Figure 12 shows the results of these tests. The low-Cr material in which the diameter of the nitrocarbide particles was lower displayed reliable results, leading to the conclusion that Cr nitrocarbide particles of lower diameter caused less impact with the aluminum liner.

Durability tests were conducted for 100 hours in an actual engine to determine the level of wear of the piston rings themselves and of the cylinder liner. Figure 13 shows the results of these tests.

Lower wear was displayed by the piston rings using the 13Cr material, while wear in the aluminum liner was identical, and sufficiently low, for both the 10Cr and the 13Cr materials. The 13Cr material was selected as the piston ring material based on these results.

3.4. Bore Stiffness of Cylinder Block with Aluminum Liners

Table 6 shows a comparison of the material properties of the materials making up the cylinder block.

The linear coefficient of expansion of the aluminum liner material is similar to that of the aluminum material

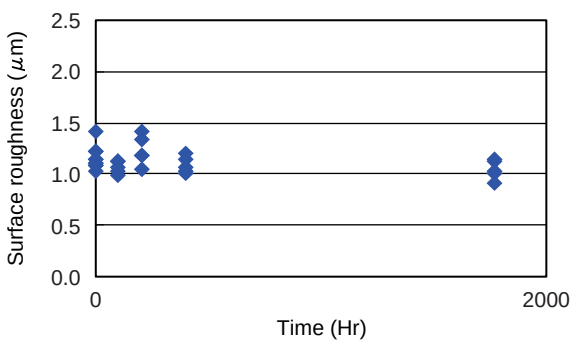


Fig. 10 Variations in bore surface roughness

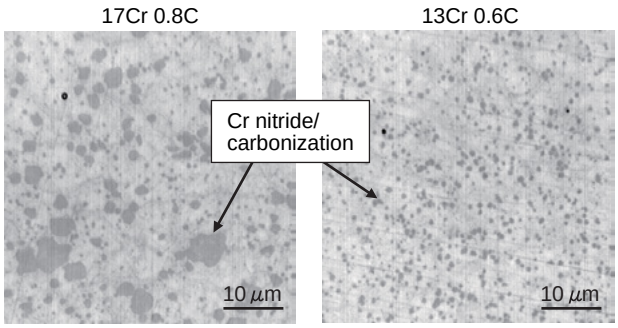


Fig. 11 Piston ring microstructure

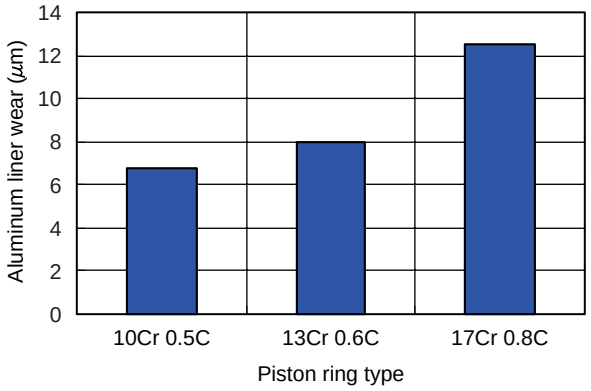


Fig. 12 Aluminum liner wear in Component jig test

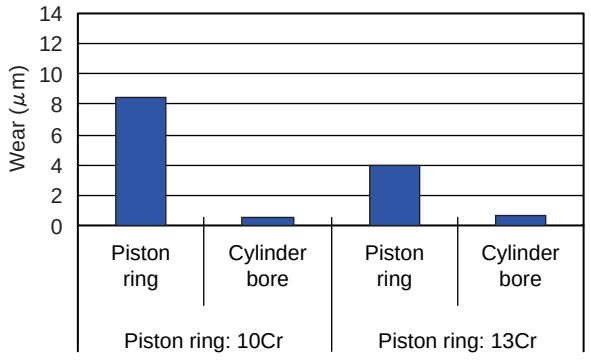


Fig. 13 Aluminum liner wear in actual engine

Table 6 Comparison of material properties

Item	Unit	Cylinder block ADC12	Cast iron liner	Aluminum liner
Young's modulus	(GPa)	72	110	90
Thermal expansion coefficient	($\times 10^{-6}$/K)	23	11.5	16

used in the cylinder block. The change in the dimensions of the materials under heating therefore matches well, enabling the cylindrical shape of the bore to be maintained. Because of this, the aluminum liners display greater resistance than the cast-iron liners to bore distortion caused by combustion temperature.

The level of bore stiffness is also lower in the aluminum liners because the Young's modulus of these liners is lower than that of the cast-iron liners.

Figure 14 shows a cross-section of the cylinder block with aluminum liners.

In order to prevent distortion of the bore from being exacerbated by the tightening of the cylinder head, the total bore thickness (a basic dimension of the aluminum liner) is increased by 1 mm in the 3.7 L V6 engine against that in the 3.5 L V6 engine.

3.5. Adhesion of Aluminum Liner

Another key factor in ensuring bore stiffness is the integration of the liners and the bores, achieved by increasing the adhesion between the two. Because the linear coefficient of expansion of the liner material is similar to that of the aluminum material used in the cylinder block, less residual tension is generated by contraction as the material cools following casting, and ensuring sufficient retaining force for the liner therefore represents a challenge.

The roughness of the outer surface of the liner, prior to casting, is an important factor in the achievement of increased adhesion.

Figure 15 shows an external view of the aluminum liner and the roughness of the outer surface of the liner.

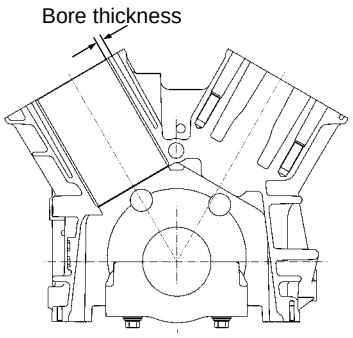


Fig. 14 Cylinder block section view

The minute projections on the surfaces of the liners are designed to increase the area of concavities and convexities on the surface, thus increasing the mechanical retaining force and the adhesion of the liners.

In the initial stage of development, the roughness of the liner surfaces was approximately 30 μm. However, following the casting of the cylinder block, it was determined that good adhesion was not achieved at this level of roughness.

Balancing the maintenance of equivalent productivity (mainly in terms of the casting tact time) in the HPDC process to that achieved when manufacturing cast iron liners with increased liner adhesion represented a challenging issue. The optimization of the roughness of the outer surface of the liners enabled an equivalent level of productivity to be maintained while increasing the adhesion of the liners.

3.6. Evaluation Method for Adhesion of Aluminum Liners

In the die cast cylinder blocks with cast iron liners that are in general production today, the stiffness of the liners themselves is the basis of the stiffness of the area around the bores. In the case of the aluminum liners, as it was necessary to integrate the liners and the bores to ensure stiffness, non-destructive ultrasonic measurement[4] was employed as a new method of evaluating gaps in the outer surfaces of the liners.

Eliminating gaps at the boundary between the outer surface of the liner and the bore aluminum is a key element in the achievement of adhesion. Microscopic observation of the boundary between the liner and the bore aluminum following casting showed complete adhesion, other than localized gaps of 5 μm or less.

Figure 16 shows an enlarged photograph of the boundary between the liner and the bore.

If the area of the outer surface of the liner in which there are no gap increases, the retaining force of the liner then also increases. An ultrasonic tester was employed for



Aluminum liner | Surface roughness processing at shotblast processing.

Fig. 15 Exterior view of liner / liner outer surface

measurements. The dimensions of the gaps in the liner boundary surface (as determined by the rate of reflection of the ultrasonic waves) were color-coded, with acceptable gaps of 5 μm or less shown as yellow, and gaps of more than 5 μm shown as red. The rate of adhesion was defined as the specific area ratio of the acceptable areas shown as yellow, where there were no gaps, to the area of the outer surface of the liner.

Figure 17 shows measurement data.

3.7. Method of Increasing Adhesion of Aluminum Liners

As discussed in Section 3.6., the roughness of the surfaces of the liners was varied, liners were cast in cylinder blocks, and their adhesion was evaluated. Differences in the level of adhesion of the liners affect the distortion of the bore caused by exposure to combustion heat. It is therefore necessary to ensure stiffness by taking into consideration both heat distortion and the distortion caused by the initial tightening of the cylinder heads.

The relationship between the roughness of the outer surfaces of the cylinder liners and adhesion is shown in Fig. 18.

Figure 19 shows the relationship between liner adhesion and bore distortion following a durability test in an actual engine. The degree of bore distortion following the durability test is reduced as the adhesion rate of the liner increases.

Having measured the rate of adhesion of liners that satisfied the target for bore distortion following durability tests, a standard was set for the roughness of the outer surfaces of the liners. Figure 20 shows a comparison of the bore distortion, with the cylinder head tightened, of an aluminum liner and a cast iron liner in cylinder blocks that satisfied this standard for liner adhesion.

The increased thickness of the bores and enhanced adhesion of the liners have ensured the achievement of a level of bore distortion equivalent to that of a cast iron liner.

Figure 21 shows the bore distortion at a high temperature (150 °C). Because the linear coefficient of expansion of the aluminum liner material is similar to that of the aluminum material used in the cylinder block, the change in their dimensions matches well, even at high

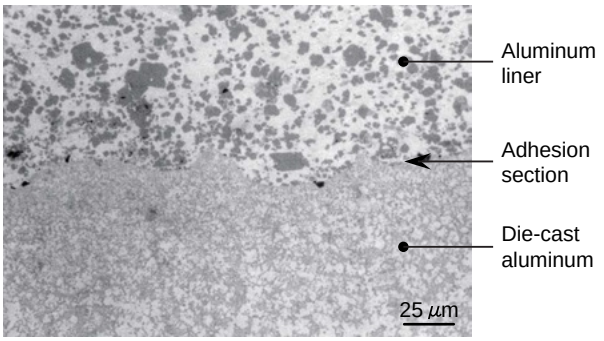


Fig. 16 Cross-section of adhesion section

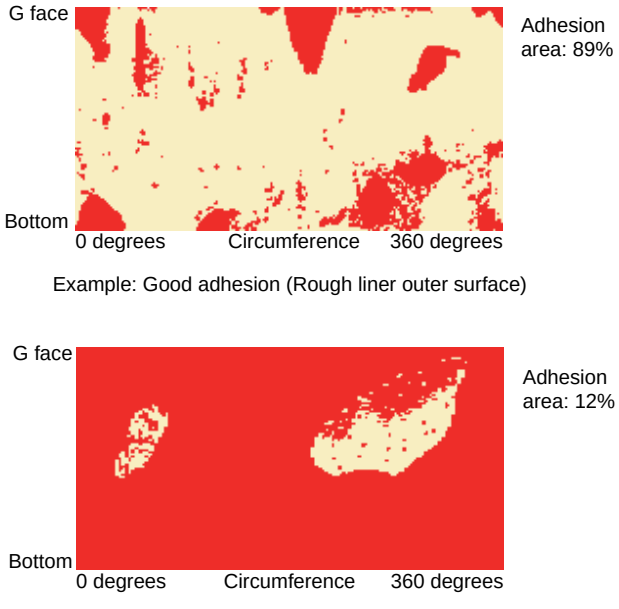


Fig. 17 Ultrasonic test results (C scope image)

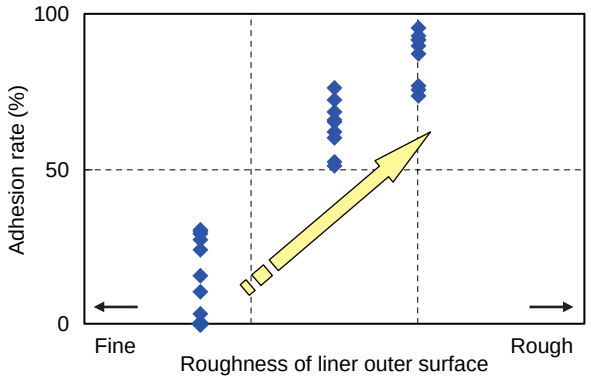


Fig. 18 Correlation between roughness of liner outer surface and adhesion

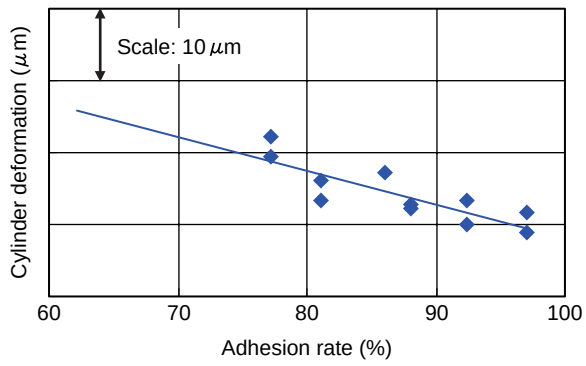


Fig. 19 Correlation between roughness of liner outer surface and bore distortion after durability test

temperatures, and the shape of the bore remains acceptable, even at the bottom of the water jacket, where the level of change is greatest.

3.8. Performance Enhancements due to Use of Cylinder Block with Aluminum Liners

The heat transfer characteristic of the aluminum liner material helps make certain that the temperature of the hottest area of the cylinder block remains cooler than in a cast iron liner cylinder block at the same water temperature.

Figure 22 shows the effect of the aluminum liners in reducing the temperature of the bore bridges, the areas of the cylinder block in which the temperature is highest.

From 190 °C, the strength of aluminum begins to decline, and this therefore represents the durability limit for the bore bridge temperature[1]. However, increased engine power may lead to increased temperatures due to heat production. The use of the aluminum liners reduces the temperature of the bore bridges by 12 °C against that of the cast iron liners. Compared to the cast iron liners, engine output can be increased by approximately 51 kW before the aluminum liner temperature reaches 190 °C, indicating that the use of the aluminum liners is compatible with the achievement of increased power.

The enhanced cooling of the cylinder block has also increased the cooling of the combustion chamber, resulting in an enhanced compression ratio and enhanced performance.

Figure 23 shows the effect of the aluminum liners on reducing the temperature of the pistons.

The temperature of the piston ceilings has been reduced by approximately 20 °C. This cooling effect increases the knocking limit, making it possible to advance ignition timing by 2 to 5 degrees.

Figure 24 shows spark advance data.

The cooling effect of the aluminum liners has resulted in a 1.5 kW increase in power and 9.8 Nm increase in torque.

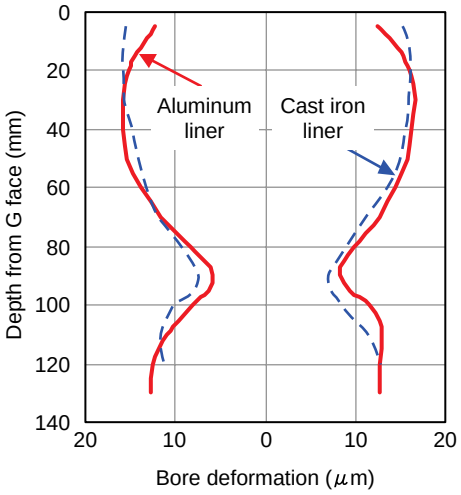


Fig. 20 Bore distortion with cylinder head tightening

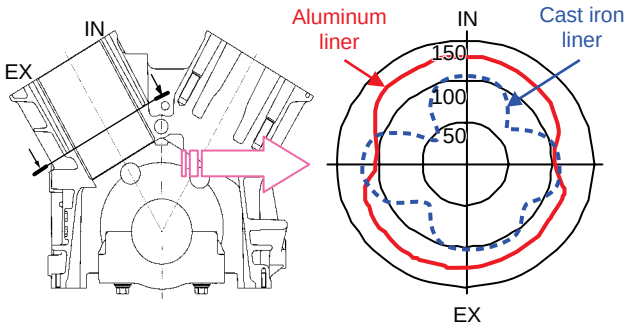


Fig. 21 Bore distortion at high temperature

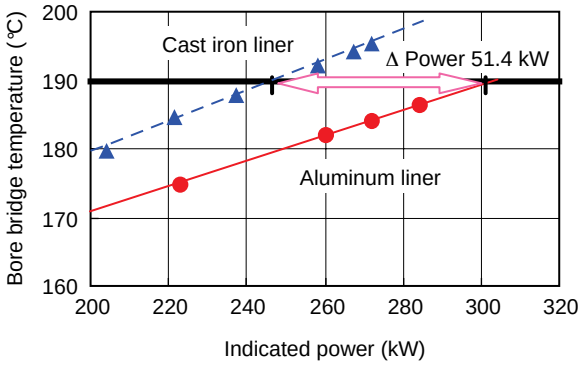


Fig. 22 Cooling effect for bore bridge

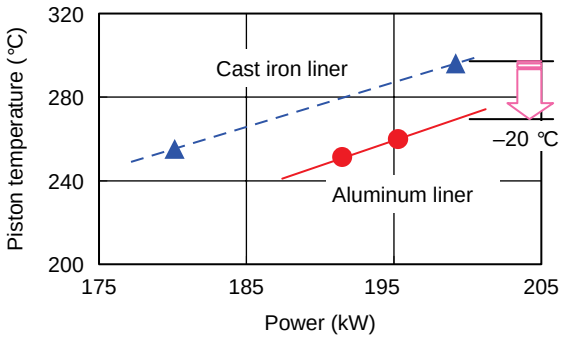


Fig. 23 Piston temperature reduction effect

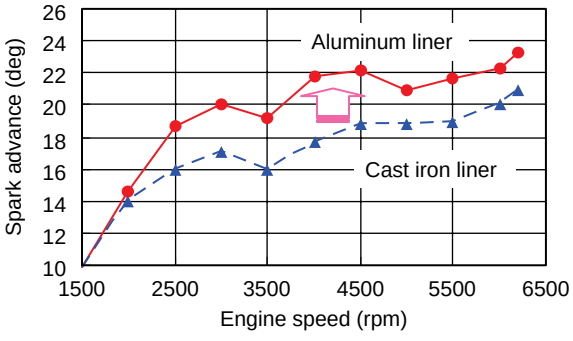


Fig. 24 Cooling effect for bore bridge

3.9. Durability and Reliability

Durability tests were conducted in an actual vehicle.

Figure 25 shows liner wear, wear of the outer surface of the piston rings, and bore distortion at the completion of the durability tests.

Figures are low for all three parameters, and satisfy engine function requirements.

Figure 26 shows oil consumption in the durability tests.

This is also a reliable result, with no significant change in oil consumption from initial figures. This demonstrates the reliability of the engine employing the die cast cylinder block with aluminum liners.

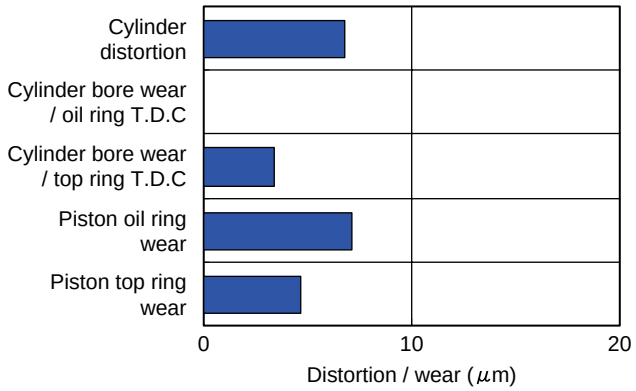


Fig. 25 Wear and distortion in durability test

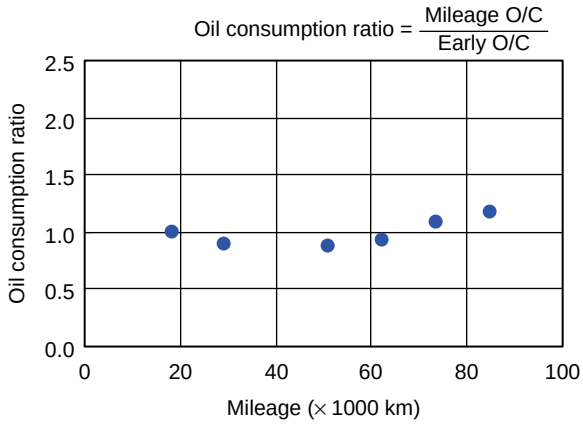


Fig. 26 Oil consumption in vehicle durability test

4. Conclusion

As demonstrated by points (1) to (3) below, the development of a die cast cylinder block with aluminum liners for a high-power, high-displacement V6 engine has enabled the achievement of increased power and displacement.

(1) A high-Si content material was selected for the aluminum liners, and 13Cr stainless steel was selected as the material for the piston rings. The combination of the two materials has ensured the achievement of higher wear and seizure resistance.

(2) The exposure of hard silicon particles on the sliding surface of the aluminum liners prevents scoring.

(3) The employment of minute projections on the outer surface of the liners has increased adhesion, ensuring adequate bore stiffness.

The use of these technologies has enabled a 3.5 L, 193 kW V6 base engine to be increased in power and displacement to produce a 3.7 L, 224 kW V6 engine. The technologies have been applied in the 3.7 L engine employed in the 2007 year model MDX.

References

(1) Hayashi, T., Ushio, H., Fujisawa, Y., Hata, T., Shibata, K., Ebisawa, M.: Properties of Hybrid Fiber Reinforced Metal and Application for Engine Block, HONDA R&D Technical Review, Vol. 1, p. 55-66

(2) Koya, E., Hagiwara, Y., Suzuki, T., Miura, S., Sanada, M., Tsuno, H., Yanagida, K.: Development of Aluminum Powder Metalluegy Composite for Cylinder Liners, HONDA R&D Technical Review, Vol. 6, p. 126-136

(3) Kurita, H., Ymagata, H.: Development of All Aluminum Cylinder Using a Hypereutectic Al-Si Alloy, YAMAHA MOTOR TECHNICAL REVIEW, No. 38, p. 124-131 (2004)

(4) Stocker,P., Ruckert, F., Hummert, K.: The New Aluminum Silicon Cylinder Liner Technology for Die-Cast Aluminum Crankcases, MTZ Motortechnische Zeitschrift, Vol. 58, p. 2-7 (1997)

■ Author ■


Takashi KOMATSUDA


Masayuki TAKAHASHI


Katsuhisa YASUKAWA


Junichi OHMURA


Noriyuki NAMBA

Study on Estimation Method of Anti-oxidation Performance for Engine Oil Deterioration Monitoring System

Yosuke OKUYAMA* Koichiro AIKAWA*
Wataru HOSHIKAWA* Masashi MARUYAMA*

ABSTRACT

The research discussed in this paper demonstrated the existence of a strong correlation between the anti-oxidation performance of engine oil and the production of sludge. Analysis of the deterioration mode of anti-oxidation performance in component tests and engine bench tests of engine oil indicated that the reaction mechanisms causing engine oil deterioration could be approximated by the superpositioning of zero- and first-order reactions. The results of these tests also demonstrated that heat, air, NOx and unburnt fuel are major factors in the deterioration of anti-oxidation performance. Detailed analysis resulted in the proposal of a general equation for the deterioration of oil anti-oxidation performance, which enabled the degree of deterioration to be estimated.

Actual vehicle tests showed that the use of the equation enabled accurate estimation of the deterioration rate of anti-oxidation performance, indicating that the method has potential for onboard use.

1. Introduction

Increasing efforts are today being made to protect the environment, spurred by issues such as global warming. This trend has extended to the area of automotive lubricating oils, generating demands for reductions in the volume of waste oil[1]. In the case of engine oil, in particular, the high volume of waste oil, high frequency of oil changes, and high degree of public awareness of the product make the extension of the period between engine oil changes an important factor to consider for automotive manufacturers[2), (3)].

However, engine oil quality issues have emerged in Europe and the U.S., including the production of black sludge. Because of this, simply extending the period between engine oil changes might result in damage to the engine[4].

An engine oil deterioration monitoring system would represent an effective method of protecting the engine while extending the period between engine oil changes. If such a system could indicate the appropriate time to change the oil to the user, engine protection could be balanced with environmental protection.

The key to judging when engine oil needs to be changed is determining whether the oil is continuing to fulfill its functions of lubrication, cleaning, rust protection, corrosion protection, and sealing. In addition to additives that enable these functions to be fulfilled, engine oil contains additives to help prevent oxidation and control the progress of deterioration. It is known that as the depletion of anti-oxidant additives progresses, oxide polymerization reactions occur, and there is a rapid decline in the performance of the oil. There are indications that this may cause major engine issues, such as low lubrication performance and clogging of the oil channels due to the production of varnish and sludge.

The anti-oxidation performance of the oil therefore has an important effect on the degree of oil deterioration, and the remaining usable life of the oil can be judged from the remaining anti-oxidation amount[5)-(7)]. An engine oil deterioration monitoring system that judges the remaining usable life of the oil on the basis of cleaning performance has been developed[8]. The combination of two indicators, anti-oxidation performance and cleaning performance, could be expected to provide a more accurate means of judging the remaining usable life of the oil. However,

* Automobile R&D Center

analysis of both these indicators calls for the use of special equipment, and vehicle users could not be expected to independently employ them to judge the usable life of their engine oil.

The research discussed in this paper developed a technology of estimating the remaining anti-oxidation performance of engine oil, based on data from engine sensors, without the necessity of actually measuring remaining performance indicators. The project also verified the fact that the new technology could be employed in an on-board anti-oxidation performance monitoring system.

2. Analysis of Depletion of Anti-oxidant Additives

2.1. Mechanism of Prevention of Oxidation Deterioration of Engine Oil

As Fig. 1 shows, when RO· radicals and ROO· radicals are produced in the base oil of an engine oil, a chain oxidation reaction begins to proceed. Anti-oxidants and extreme pressure agents are additives that are known to help prevent this oxidation reaction[9), (10)]. Anti-oxidants function by means of a mechanism called chain termination, which renders RO· and ROO· radicals inactive. The mechanism of functioning of extreme pressure agents is called peroxide decomposition. These additives function to help prevent the inactive substance ROOH from being reconverted into RO· and ROO·.

2.2. Experimental Oil Compositions and Engine Bench Tests

An engine oil was formulated using a phenol-based anti-oxidant (selected as a representative type) and secondary zinc dialkyl dithiophosphate (sec-ZnDTP) as an extreme pressure agent, and subjected to engine bench tests (Table 1). The oil was removed at fixed intervals and analyzed to determine the mode of depletion of each of the additives. The anti-oxidant was analyzed using gas chromatography, and the sec-ZnDTP was analyzed using phosphorous-31 nuclear magnetic resonance (^{31}P-NMR).

Table 1 Engine specification and test conditions

Engine specification	Water-cooled 4-cylinder 2.4L gasoline	
Mode	Medium speed mode	
Engine oil formulation	Antioxidants	0.2 wt%
	Sec-ZnDTP	0.5 wt%
	Detergents	3 wt%
	Succinic imide	5 wt%
	Base oil	PAO

The results of this analysis of the mode of depletion of the anti-oxidant additive and the sec-ZnDTP are shown in Fig. 2. Differential calculus was used to determine the reaction rates of the additives. The anti-oxidant additive demonstrated linear depletion, which can be approximated by the zero-order reaction shown in Eq. (1). The sec-ZnDTP, by contrast, demonstrated exponential depletion, which can be approximated by the first-order reaction shown in Eq. (2).

$$[AH] = -k_{AH}t + [AH]_0 \quad (1)$$

$$[Zn] = [Zn]_0 e^{-k_{Zn}t} \quad (2)$$

$[AH]$: Concentration of chain terminator
$[Zn]$: Concentration of peroxide decomposer
k_{AH}: Reaction rate constant of chain termination mechanism
k_{Zn}: Reaction rate constant of peroxide decomposition mechanism
t: Time
$[AH]_0$: Initial concentration of chain terminator
$[Zn]_0$: Initial concentration of peroxide decomposer

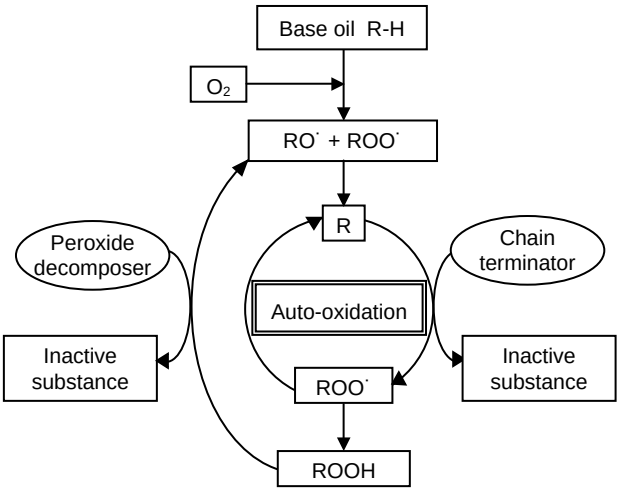


Fig. 1 Mechanism of engine oil auto-oxidation and terminal reaction

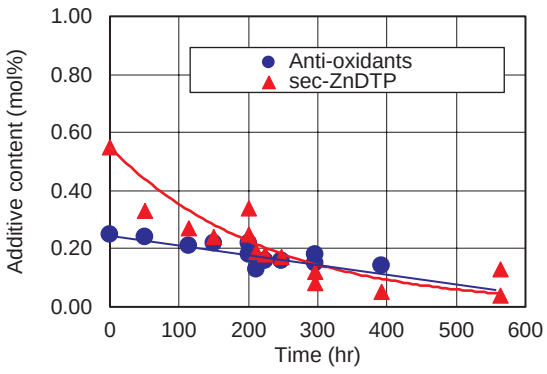


Fig. 2 Deterioration mode of anti-oxidants and sec-ZnDTP in engine bench tests

3. Analysis of Relationship between Remaining Anti-oxidation Performance and Production of Sludge

3.1. Estimation Method of Remaining Anti-oxidation Performance

A number of indicators of the anti-oxidation performance of engine oils have been proposed to date. Pressure differential scanning calorimetric (PDSC) was employed in the research discussed here, from considerations of the correlation between anti-oxidation performance and the production of sludge, and the convenience of the method in enabling analysis of infinitesimal quantities of test oil[11]. In this method, test oil and a reference substance are subjected to high temperatures and high pressures, and the difference in heat balance between the oil and the reference substance is measured. As Fig. 3 shows, PDSC measurements enable determination of oxidation induction time (OIT), a parameter that provides an index of anti-oxidation performance.

3.2. Relationship between Sludge, OIT and Insolubles

Insolubles are known to normally be produced in engine oil before sludge is produced. Figure 4 shows the

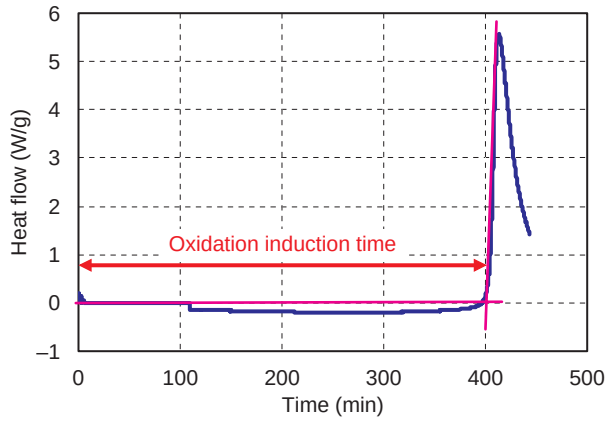


Fig. 3 PDSC analysis chart for fresh API SG grade oil

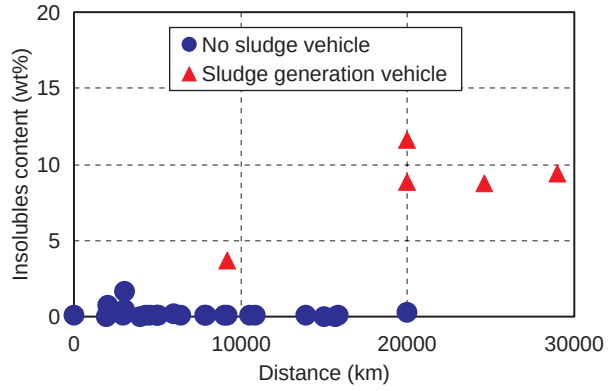


Fig. 4 Market data for recovered oil (nPB method)

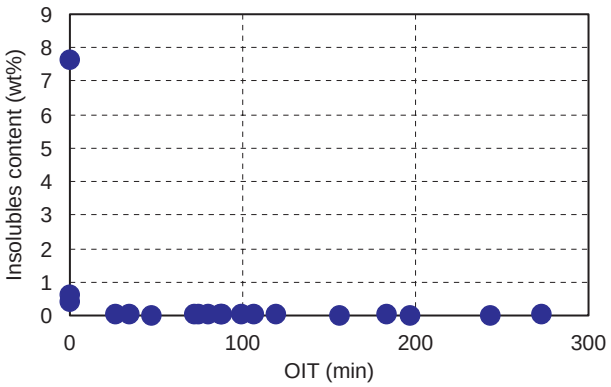


Fig. 5 Relationship between OIT and nPB insolubles

relationship between the production of sludge, insolubles content (determined using the nPB method: JPI-15S-18-80), and driving distance. The production of insolubles preceded the production of sludge in all the engine oils tested. Given that this was the case, even in an oil to which deliberately low amounts of dispersants had been added to promote the production of sludge, it can be predicted that this tendency will hold true for almost all engine oils.

The relationship between insolubles content (nPB method) and remaining OIT is shown in Fig. 5. Insolubles were not produced in any of the engine oils tested if there was remaining OIT. This indicates that OIT would provide a valid criterion for judging deterioration in engine oils.

4. Test Determination of Equation for Rate of OIT Deterioration

4.1. Causes of OIT Deterioration

Oxygen in the air is the first factor that can be indicated as a cause of OIT deterioration. Engine oil is constantly exposed to oxygen, and the base oil and additives react directly with oxygen, causing a deterioration of OIT. NOx is a second factor in deterioration. NOx is highly reactive, and may rapidly cause an oxidation reaction when it comes into contact with engine oil, resulting in the deterioration of OIT. Unburnt fuel can be indicated as a third factor. Unburnt fuel, present for example in blow-by gases, is reactive, and may cause an instantaneous reaction when it comes into contact with oil, again causing a deterioration of OIT. In addition, because it has lower oxidation stability than the base oil, the presence of unburnt fuel in the engine oil may cause OIT deterioration even if an instantaneous reaction does not occur. The effect of water can be indicated as a fourth factor. The conversion of water molecules into highly reactive hydroxyl radicals can result in the deterioration of OIT. However, market surveys indicated that the level of water content of engine oils would have almost no effect on OIT, and the effect of water was therefore not considered in the present study.

The effect of the catalyst can be indicated as a fifth factor in causing OIT deterioration. Metals functioning as catalysts also form part of the metallic component of engine oils caused by metal wear. A market survey found no vehicles in which the metallic component of the oil (oils with OIT remaining) was high enough to cause deterioration of the OIT, and the effect of the metallic catalyst was therefore not considered in this study.

Numerous research reports mention the deterioration of engine oil around the pistons and cylinders[2), 6)]. However, this research project assumed that the deterioration of the oil in the oil pan was the dominant factor in the deterioration of the engine oil as a whole. The basis for this conjecture is the fact that the volume of oil in the oil pan is far greater than the volume of oil around the pistons and cylinders. For this reason, this research focused exclusively on the deterioration of oil in the oil pan.

4.2. Reaction Mechanisms Causing Deterioration of OIT

As indicated above, the representative reaction mechanisms causing OIT deterioration are the chain termination mechanism and the peroxide decomposition mechanism. Analyzing multiple reaction mechanisms as a single unit and determining a reaction rate would be complex, and would thus represent a challenge. However, if the depletion of additives caused by the chain termination and peroxide decomposition mechanisms could be independently analyzed, the process would be comparatively simple and more accurate. Engine bench tests were therefore conducted, and numerical analysis employed to separate the reaction mechanisms. Because the depletion of the chain terminator is a zero-order reaction and the depletion of the peroxide decomposer is a first-order reaction, the research attempted to determine whether the line of superposition between the reactions corresponded to the actual mode of OIT deterioration. Figure 6 shows the results of superposition, using fitting to determine appropriate constants for Eqs. (1) and (2). The results show a reliable correspondence between the superposition line and the mode of OIT deterioration. This indicates that despite the existence in engine bench tests of a variety of factors causing a deterioration of OIT, the dominant reaction mechanisms in OIT deterioration are zero-order and first-order reactions. Given this, Eqs. (3)-(5) can be proposed as differential equations enabling estimation of the deterioration of OIT.

$$-\frac{d[OIT]}{dt} = \frac{d[OIT_{AH}]}{dt} - \frac{d[OIT_{Zn}]}{dt} \tag{3}$$

$$\frac{d[OIT_{AH}]}{dt} = [OIT_{AH}]^0 \times \alpha \tag{4}$$

$$\frac{d[OIT_{Zn}]}{dt} = [OIT_{Zn}]^1 \times \beta \tag{5}$$

$[OIT]$: Total OIT concentration
$[OIT_{AH}]$: OIT concentration due to chain terminator
$[OIT_{Zn}]$: OIT concentration due to peroxide decomposer
α: Deterioration caused by chain termination mechanism
β: Deterioration caused by peroxide decomposition mechanism

4.3. Deterioration of OIT due to Air and Heat

Air and heat cannot be eliminated from the environment in which engine oils are used. Air and heat were therefore taken up as factors causing deterioration, and their effect on the depletion of OIT was analyzed. Figure 7 shows Arrhenius plots of the reaction rate constants determined by numerical analysis of the results of an air bubbling test.

As Fig. 7 shows, the results for both the zero-order and first-order reactions display reliable linearity. This indicates that both reaction mechanisms can be expressed as Arrhenius-type reaction rate equations. Expression of the effect of the deterioration due to air and heat in each reaction mechanism as reaction rate equations gives Eqs. (6) and (7).

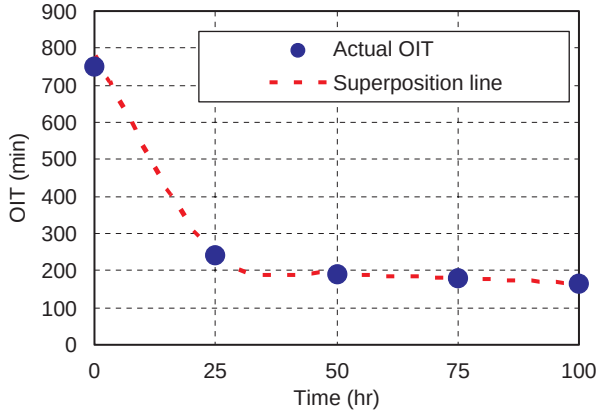


Fig. 6 Comparison of actual OIT with superposition line

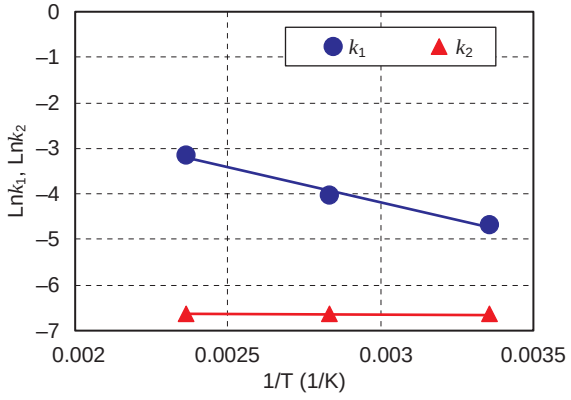


Fig. 7 Influence of air and heat on reaction rate constants k_1 and k_2

$$\frac{d[OIT_{AH}]_{Air,\,Heat}}{dt} = [OIT_{AH}]^0 \times (k_1) \quad (6)$$

$$\frac{d[OIT_{Zn}]_{Air,\,Heat}}{dt} = [OIT_{Zn}]^1 \times (k_2) \quad (7)$$

k_1-k_6: Reaction rate constants

4.4. Deterioration of OIT due to NOx

The effect of air, heat, and NOx on the mode of OIT deterioration was studied using a NOx bubbling device. Because deterioration occurs even when no NOx is present, it was conjectured that deterioration due to NOx is independent of deterioration due to air and heat. Denominating the term representing the rate of deterioration due to NOx A_{NOx} in the zero-order equation and B_{NOx} in the first-order equation gives Eqs. (8) and (9). The second term in Eqs. (8) and (9) can be obtained in tests by determining the difference in the rate of deterioration when NOx is present and when NOx is not present. Figure 8 shows the results of employing differential calculus to analyze the relationship between NOx concentration and A_{NOx} and B_{NOx}. Figure 8 can be used to determine the reaction order of NOx deterioration for each reaction mechanism. Expressing these as reaction rate equations gives Eqs. (10) and (11). Figure 9 shows Arrhenius plots of the reaction rate constants k_3 and k_4. The plots for both reaction mechanisms display reliable linearity.

$$\frac{d[OIT_{AH}]_{Air,\,Heat,\,Nox}}{dt} = [OIT_{AH}]^0 \times (k_1 + A_{NOx}) \quad (8)$$

$$\frac{d[OIT_{Zn}]_{Air,\,Heat,\,Nox}}{dt} = [OIT_{Zn}]^1 \times (k_2 + B_{NOx}) \quad (9)$$

$$\frac{d[OIT_{AH}]_{Air,\,Heat,\,Nox}}{dt} = [OIT_{AH}]^0 \times (k_1 + k_3[NOx]^2) \quad (10)$$

$$\frac{d[OIT_{Zn}]_{Air,\,Heat,\,Nox}}{dt} = [OIT_{Zn}]^1 \times (k_2 + k_4[NOx]^2) \quad (11)$$

As in the case of the analysis of the mode of the deterioration of OIT due to NOx, OIT deterioration due to unburnt fuel was considered as an independent term. Denominating OIT deterioration due to unburnt fuel as C_{Fuel} in the zero-order equation and D_{Fuel} in the first-order equation gives Eqs. (12) and (13).

Studying the effect of unburnt fuel using a NOx bubbling device would represent a challenge, and this study therefore employed engine bench tests to analyze the mode of OIT deterioration due to unburnt fuel. In bench tests, the ratio of unburnt fuel that can be present in the oil is largely determined by the temperature of the oil. It is therefore challenging to create conditions in which the concentration of unburnt fuel is varied, while maintaining a constant oil temperature, and to maintain those conditions for an extended period. This makes it challenging to conduct an analysis using differential calculus in which the reaction order is analyzed by plotting the logarithm of OIT on the vertical axis and the logarithm of the concentration of unburnt fuel on the

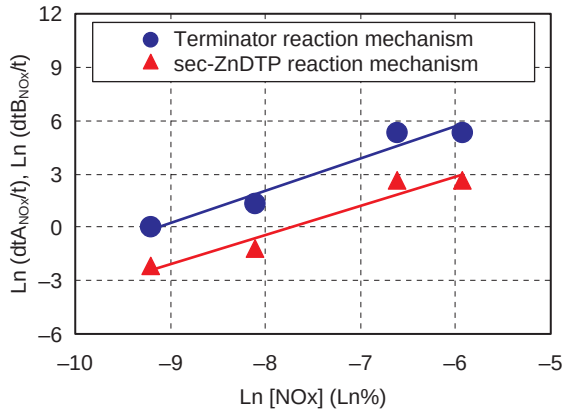


Fig. 8 NOx-dependence of OIT deterioration speed

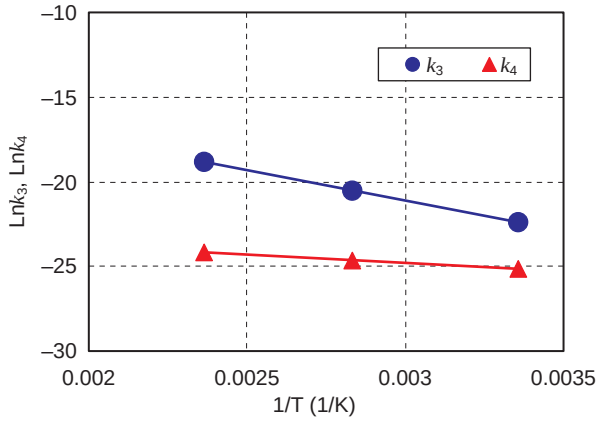


Fig. 9 Influence of NOx on reaction rate constants k_3 and k_4

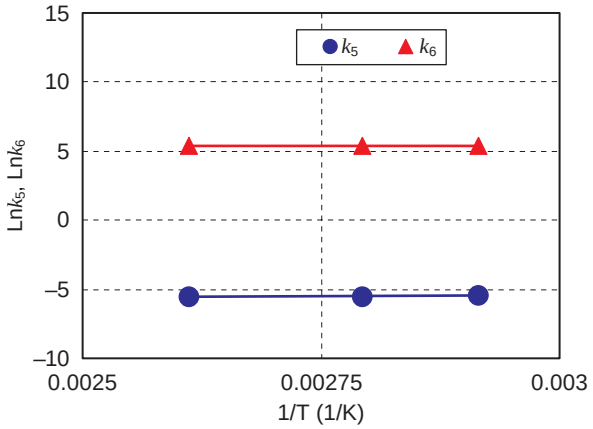


Fig. 10 Influence on dilution reaction rate constants k_5 and k_6

horizontal axis. The present project therefore assumed that the reaction order for unburnt fuel could be approximated using simple integral multiplication. When fitted, both reaction mechanisms could be approximated by 2. Equations (3), (14), and (15) are obtained by reflecting these reaction orders in reaction rate equations.

Figure 10 shows Arrhenius plots of the reaction rate constants for both reaction mechanisms when the reaction order is approximated by 2. As Figure 10 shows, reliable linearity is obtained for both reaction mechanisms.

$$\frac{d[OIT_{AH}]_{Air,\ Heat,\ Nox}}{dt} = [OIT_{AH}]^0 \times (k_1 + k_3[NOx]^2 + C_{Fuel}) \quad (12)$$

$$\frac{d[OIT_{Zn}]_{Air,\ Heat,\ Nox}}{dt} = [OIT_{Zn}]^1 \times (k_2 + k_4[NOx]^2 + D_{Fuel}) \quad (13)$$

$$\frac{d[OIT_{AH}]_{Air,\ Heat,\ Nox}}{dt} = [OIT_{AH}]^0 \times (k_1 + k_3[NOx]^2 + k_5[Fuel]^2) \quad (14)$$

$$\frac{d[OIT_{Zn}]_{Air,\ Heat,\ Nox}}{dt} = [OIT_{Zn}]^1 \times (k_2 + k_4[NOx]^2 + k_6[Fuel]^2) \quad (15)$$

5. Verification of OIT Deterioration in Vehicle Tests

5.1. Deterioration Rate Equation for Vehicle Tests

Equations (3), (14), and (15) provide numerical expressions of different causes of OIT deterioration. However, other than the term for unburnt fuel, all the terms in these equations were obtained from tests using a NOx bubbling device. In order to enable these numerical models to be used in verifications in actual vehicle tests, the contact efficiency between the engine oil and each of the factors causing deterioration of OIT inside an engine was denominated η and employed in the air, heat, and NOx terms. The necessary data for vehicle verification was measured or estimated using the following methods:

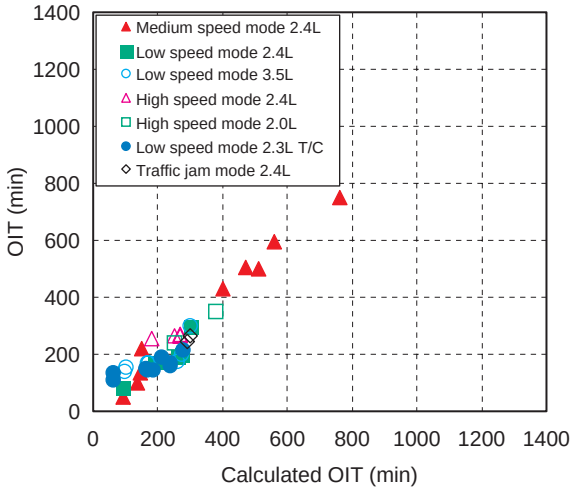


Fig. 11 Correlation between calculation results and OIT measurement values

(1) Oil temperature
The oil temperature at the oil drain bolt was measured using a thermocouple.

(2) NOx
The level of NOx in the crankcase was employed as the benchmark figure, and NOx levels were estimated on the basis of driving conditions.

(3) The level of unburnt fuel in the crankcase was employed as the benchmark figure, and unburnt fuel levels were estimated on the basis of driving conditions[12].

5.2. Results of Vehicle Verification and Estimation Accuracy

A Honda vehicle and Honda genuine engine oils were employed in vehicle tests. OIT was predicted using Eqs. (3), (16), and (17). Figure 11 shows the correspondence between OIT measurements and calculations in different test modes. There is a reliable correspondence between measured values and simulation results, indicating that the estimation method is sufficiently accurate for practical use.

$$\frac{d[OIT_{AH}]_{Air,\ Heat,\ Nox}}{dt} = [OIT_{AH}]^0 \times \{\eta \times (k_1 + k_3[NOx]^2) + k_5[Fuel]^2\} \quad (16)$$

$$\frac{d[OIT_{Zn}]_{Air,\ Heat,\ Nox}}{dt} = [OIT_{Zn}]^1 \times \{\eta \times (k_2 + k_4[NOx]^2) + k_6[Fuel]^2\} \quad (17)$$

6. Discussion

The accuracy of the OIT estimation method developed in this research was verified using a number of different types of engine oil. The method was employed for all the oils used in tests, indicating that it possesses an acceptable level of general applicability. This is considered to be because the basic phenomena of causation and mode of OIT deterioration remain unchanged, even when different oils are used. This can be explained in particular by the fact that despite the use of different additives, the mode of OIT deterioration can still be approximated by the superposition of zero- and first-order reactions.

For onboard estimation of the deterioration of OIT, it will be necessary to use sensors or estimation equations to provide accurate data on the temperature of the engine oil, the concentration of NOx, and the concentration of unburnt fuel, which represent the main factors causing deterioration of OIT. In addition, the ability to discriminate between different types of oils employed would be desirable in terms of enabling accurate estimation of OIT. Substitution of the initial OIT level, the threshold value, the deterioration factor, and other parameters for different engine oils would enable more accurate estimation of OIT.

The combination of these techniques and methods of application would enable more accurate estimation of OIT, thus increasing the feasibility of balancing environmental protection with protection of the engine.

7. Conclusion

The research discussed in this paper demonstrated the existence of a strong correlation between OIT, an indicator of engine oil deterioration, and the production of sludge. General equations for OIT deterioration were proposed on the basis of unit tests and engine bench tests of engine oil. The equations enabled accurate estimation of OIT deterioration in an actual vehicle. This demonstrates the viability of constructing an onboard system for the estimation of OIT deterioration using these equations.

Acknowledgments

The authors wish to express their gratitude to all the staff members of Showa Shell Sekiyu, K. K. and Shell Global Solutions who generously assisted in the development and application of methods of analysis of engine oil in the course of this research.

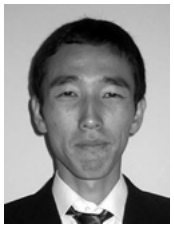
References

(1) Suzuki, K.: Trends in Used Lubricating Oil Recycling, Triborogists, Vol. 51, No. 4, p. 282-287 (2006)
(2) Igarashi, J.: Enjinyuno chyoujyumyouka nitaisururirontekitorikumi, Nisseki Mitsubishi Review, Vol. 41, No. 2, p. 20-30 (1999) (in Japanese)
(3) Tanaka, M.: Jidousyayou enjinyunorekkato oirukoukanjiki, PETEROTECH, Vol. 12, No. 12, p. 992-997 (1989) (in Japanese)
(4) Moritani, K., Kawamura, M.: Development and Application of Simulator for Engine Oil Sludge Formation, R&D Review of Toyota CRDL, Vol. 28, No. 1, p. 35-41 (1993)
(5) Schwartz, S. E., Smolenski, D. J.: Development of an Automatic Engine Oil-Change Indicator System, SAE Paper, 870403 (1987)
(6) Mahoney, L. R., Korcek, S.: The Effect of Fuel Combustion Products on Antioxidant Consumption in a Synthetic Engine Oil, Ind. Eng. Chem. Prod. Res. Vol. 19, p. 11 (1980)
(7) Korcek, S., Mahoney, L. R.: Mechanism of Anti oxidant Decay in Gasoline Engines: Investigation of Zinc Dialkyldithiophosphate Additives, SAE Paper, 810014 (1981)
(8) Aikawa, K., Maruyama, M.: Development of an Oil Deterioration Monitoring System by Estimating Base Number, Honda R&D Technical Review, Vol. 18, No. 2, p. 176-181
(9) Sakurai, T.: Sekiyuseihintenkazai, Saiwai Shobo, p. 509 (1973) (in Japanese)
(10) Okabe, H., Okatsu, Y.: Sekiyuseihintenkazainokaihatsu, CMC Syuppan, p. 174 (1998) (in Japanese)
(11) Method to evaluate oxidation life of used engine oils, Research Disclosure Journal, Research Disclosure Database Number 510074
(12) Sagawa, T., Nakamura, K.: Study of Fuel Dilution Direct-Injection and Multipoint Injection Gasoline Engines, SAE Paper, 2002-01-1647 (2002)

■ Author ■


Yosuke OKUYAMA


Koichiro AIKAWA


Wataru HOSHIKAWA


Masashi MARUYAMA

Development of Cylinder Pressure Measurement System Using Adaptive Calculation

Yuji YAMAMOTO* Shusuke AKAZAKI*
Masanori OHARA* Takahide MIZUNO*

ABSTRACT

This paper discusses the development of a system enabling real-time measurements of combustion pressure in an internal combustion engine, using a comparatively low-cost polycrystalline piezoelectric element. Tests conducted using a mass production vehicle showed that by using the measured cylinder pressure, the status of combustion could be measured across the entire range of driving conditions, enabling misfires to be precisely detected. To date, despite their comparatively low cost, the use of piezoelectric elements in mass production vehicles has represented a challenge, because the temperature characteristics of the elements in the use environment, age degradation, and other factors may cause variations in output. This research therefore studied the variation in sensor output in terms of each causal factor. In addition, adaptive calculations were performed to enable the identification of corrective parameters to be used, to match the measured cylinder pressure to estimated reference pressures for vehicle operation, thus enabling stable cylinder pressures to be measured, even if temperature characteristics change or the output deteriorates.

1. Introduction

Today's increasing focus on environmental issues is generating demands for enhanced exhaust gas cleaning performance and increased combustion efficiency in automotive gasoline engines. In general, the air-fuel ratio of conventional gasoline engines is precisely controlled to maximize the performance of the catalytic converter. Additional enhancement of combustion efficiency and the ability to maintain an optimum state of combustion are now necessary to enable controllability to be increased. This would necessitate the use of a cylinder pressure sensor that measures the state of combustion in each cylinder in real time. However, reaching the stage of mass production of such a sensor represents a considerable technological challenge. Years of research have been expended on development, but few sensors have reached the stage of mass production[(1)-(4)]. Research has been conducted on the application of a simple using a piezoelectric element in a diesel engine[(5), (6)] in recent years.

Piezoelectric elements can be divided into single crystal and polycrystalline types. Single crystal piezoelectric elements possess a reliable temperature characteristic, ensuring stable output across the range of engine operating temperatures, from low to high. However, they are comparatively expensive, and are therefore not suitable for use as sensors in mass production engines. By contrast, polycrystalline piezoelectric elements are comparatively inexpensive, but display major changes in sensitivity in response to changes in temperature. For this reason, it would be challenging to achieve a stable output using these elements as cylinder pressure sensors in automotive engines, a use environment in which the temperature range exceeds 210 °C (-40 to 170 °C).

The research discussed in this paper therefore developed a system enabling real time monitoring of the status of combustion, based on a correction method using adaptive calculation in which software is employed to correct changes in the sensitivity of a polycrystalline piezoelectric element. This research has enabled stable measurement of the cylinder pressure of a mass production engine using a polycrystalline piezoelectric element.

* Automobile R&D Center

Table 1 Engine specifications

Engine type	V6
Displacement (cm^3)	2997
Bore × stroke (mm)	86 × 86
Compression ratio	10.0
Valve train	24-valve SOHC VTEC
Fuel	Regular unleaded

2. System Configuration

2.1. Test Engine

The US ACCORD 3.0 L V6 engine was used in the development of the system. Table 1 shows the specifications of the engine.

2.2. Cylinder Pressure Sensors

As shown in Fig. 1, the cylinder pressure sensors are fixed in place between the cylinder heads and the plugs. The use of this layout means that no major modification of the valve layout of mass production engines is required, giving the sensors a higher degree of general applicability.

Figure 2 shows the sensor structure. The sensor is basically a piezoelectric element contained in a cylindrical housing, forming a simple washer structure that senses strain between the heads and the plugs. An electrode at one end of the element is connected to the exterior by means of a terminal that sits alongside the sensor housing. This layout enables the sensor on the engine assembly line to fit without affecting the ability to mount the plugs.

Figure 3 shows the principle of detection of cylinder pressure. When combustion pressure is generated, the pressure generates strain in the direction the plugs are pushed. This strain is transmitted by the plugs and reaches the sensors. This strain changes the pressure on the piezoelectric element in the sensor, producing a minute ΔL deformation of the element. This deformation produces drift in the electrical charge at each end of the element. When a change in the electrical charge is detected, it is converted into a voltage using a charge amplifier, enabling detection of the cylinder pressure (Fig. 4).

2.3. System Configuration

In order to realize high-speed calculation processing of the signal from the cylinder pressure sensor in real time, a cylinder pressure unit was newly developed to enable data transfer to the Engine Control Unit (ECU) by means of a Controller Area Network (CAN). The system

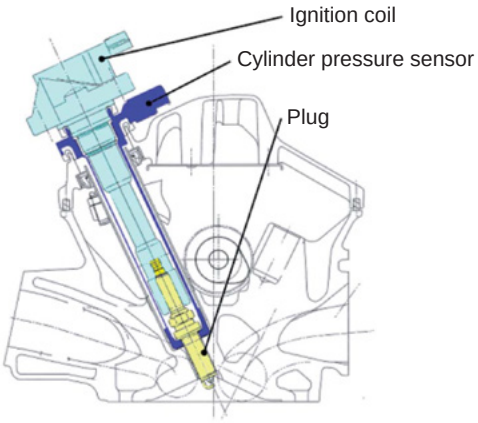


Fig. 1 Installation of cylinder pressure sensor

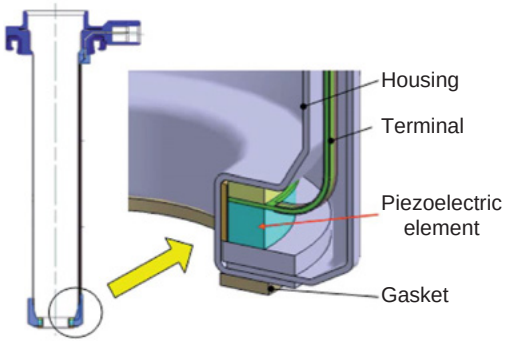


Fig. 2 Cylinder pressure sensor structure

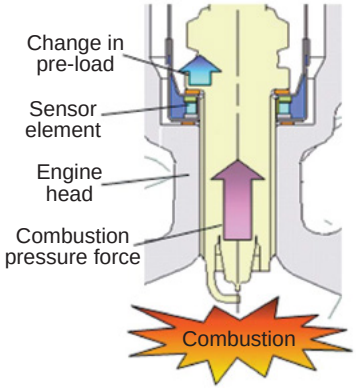


Fig. 3 Pressure sensing mechanism

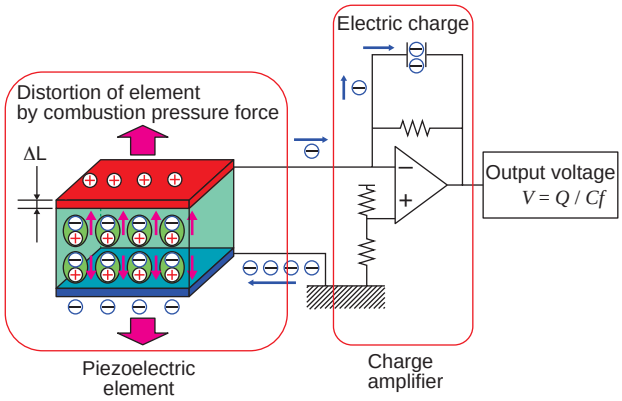


Fig. 4 Function of charge amplifier

configuration is shown in Fig. 5.

Within the cylinder pressure unit, the change in the electrical charge of the sensor element is converted to a voltage by a charge amplifier. An AD converter is then used to convert this voltage into a digital signal, after which it is input to a Central Processing Unit (CPU). The CPU calculates the crank angle based on the crank pulse and the cylinder pulse, and calculates the cylinder pressure for each crank angle. A 100 MHz CPU was used in the prototype unit, and the AD converter employed a 50 kHz sampling rate. This enables cylinder pressure for every 1 deg. of crank angle to be measured up to the red zone of 6800 rpm and above.

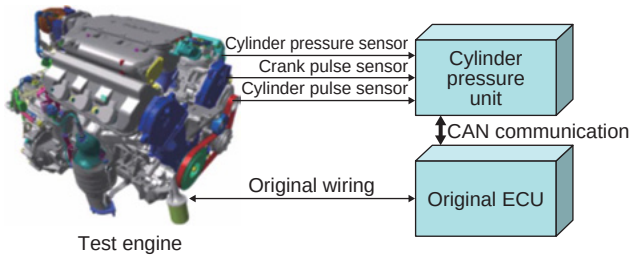


Fig. 5 System configuration for cylinder pressure sensing

3. Correction of Sensor Output using Adaptive Calculation

3.1. Variation in Sensor Sensitivity

The basic properties of lead titanate ($PbTiO_3$) are that it possesses a perovskite-type crystal structure, like standard polycrystalline piezoelectric materials, and produces piezoelectricity (ferroelectricity) by means of asymmetrical displacement of crystals. In addition, the piezoelectric constant and relative dielectric constant of the material display a comparatively high rate of increase with increases in temperature, and a noticeable increase at around the Curie temperature. In other words, it displays a high rate of change in sensitivity and a high level of pyroelectricity in relation to changes in temperature. To enable this material to be used as a cylinder pressure sensor in an automotive engine, it was necessary to study other factors causing variation in sensitivity and degradation of characteristics, in addition to the range of variation and degradation. The various factors were therefore isolated, and the variation in the sensitivity of the sensor in an actual use environment was studied, including consideration of durability.

(1) Initial variations
Variations that occur after production caused by variations in the solid parts of the element, the shape of the case, and the load applied during assembling.

Table 2 Sensor variation

Initial variation	2500 pC/MPa	±27% *
Axial tension characteristics	Maximum axial tension	+2% *
	Minimum axial tension	–25% *
Temperature characteristics	170 °C	+160% *
	–40 °C	–35% *
Engine revolution characteristics	3000 rpm or more	–44% *
Durability degradation	550000 mile	–30% *

* 3σ variation

(2) Axial tension characteristics
Changes due to variations in torque when the plugs are mounted and the settling of the screws.

(3) Temperature characteristics
The piezoelectric constant changes with changes in temperature. This temperature-dependence of polycrystalline piezoelectric elements represents an impediment to their use as mass produced sensors.

(4) Engine speed characteristic of screws
Combustion pressure that enters through gaps in the screws in the plugs and heads differs at low and high engine speeds, resulting in changes in the sensitivity characteristic. This characteristic should be considered due to the adoption of a configuration in which the sensor is fixed in place between the plugs and the heads.

(5) Decline in durability
Degradation of piezoelectric elements can be divided into electrical degradation (decline in piezoelectricity) and mechanical degradation (damage to the element). With regard to mechanical degradation, this project used the guaranteed pressure resistance; it determined electrical degradation from use conditions and usable life.

Table 2 shows the range of each of these variations in a 3.0 L V6 engine. The respective variations were calculated using 3σ.

Multiplying the variables in the case of an increase in sensor output

$$\begin{aligned} Vout &= a \times b \times c \times d \\ &= 2500 \times 1.27 \times 1.02 \times 2.6 \\ &= 8420 \end{aligned} \quad (1)$$

a: Initial median value
b: Initial maximum coefficient
c: Maximum axial tension coefficient
d: Upper limit of temperature sensitivity coefficient

Multiplying the variables in the case of a decrease in sensor output

$$\begin{aligned} Vout &= a \times e \times f \times g \times h \times i \\ &= 2500 \times 0.73 \times 0.75 \times 0.65 \times 0.56 \times 0.7 \\ &= 368 \end{aligned} \quad (2)$$

a: Initial median value
e: Initial minimum coefficient
f: Minimum axial tension coefficient
g: Lower limit of temperature sensitivity coefficient
h: Engine speed characteristic coefficient
i: Decline in durability coefficient

As the results of Eqs. (1) and (2) above show, the sensitivity of the sensor varied from 368 pC/MPa to 8420 pC/MPa, necessitating correction of a more than 20-fold variation.

In addition to the piezoelectric constant (sensitivity), the relative dielectric constant of the sensor also varies with changes in the temperature of the sensor. This means that a pyroelectric effect producing variance in the output voltage of the charge amplifier according to temperature changes.

As Fig. 6 shows, in order to correct this characteristic, the sensor output is reset at top dead center before intake, and the voltage before and after the reset is monitored and its gradient is corrected.

3.2. Correction of Sensor Output Using Adaptive Calculation

Having elucidated the variation in sensitivity characteristics of a polycrystalline piezoelectric element above, this section discusses a real-time measurement method in which adaptive calculation is employed to correct sensitivity.

A single crystal piezoelectric element of the type generally employed as cylinder pressure sensors, manufactured by Kissler (Type 6052B) was employed as the benchmark sensor, and the new method was developed to achieve an output equivalent to that of this benchmark sensor.

Figure 7 shows an outline of the sensor output correction method.

(1) Calculations are conducted to determine the cylinder pressure from engine operating conditions (*Pmodel*).

(2) The cylinder pressure when the engine is motoring is measured using the benchmark sensor, and the calculated cylinder pressure is corrected using a correction coefficient in order to match the measurement from the benchmark sensor, producing a benchmark estimated cylinder pressure during motoring (*Pmodelk*).

(3) Because the cylinder pressure during the compression stroke does not vary, even if there is a change in the status of combustion, the estimated motoring cylinder pressure determined in (2) can be used to enable real-time correction of the sensor signal via adaptive calculation, thus enabling the determination of cylinder pressure for each crank angle.

These points are explained in detail below.

(1) An engine model is calculated from the engine operating state. From the configuration of the engine, the crank angle and piston position can be expressed by Eq. (3) as Fig. 8 shows.

$$x = r\left\{(1-\cos\theta)+\lambda-\sqrt{\lambda^2-\sin^2\theta}\right\} \qquad \because\lambda = l/r \quad (3)$$

The cylinder volume, *V*, can therefore be expressed by Eq. (4).

$$V = Vdead + Apstn \cdot r\left\{(1-\cos\theta)+\lambda-\sqrt{\lambda^2-\sin^2\theta}\right\} \quad (4)$$

Vdead: Dead volume
Apstn: Piston TOP area

From the gas equation of state, the cylinder pressure, *P*, can be expressed by Eq. (5).

$$P = GRT/V \quad (5)$$

G: Intake air amount
T: Intake air temperature
R: Gas constant

Because compression is adiabatic, the gas temperature varies with the volume *V*, and can be expressed by Eq. (6).

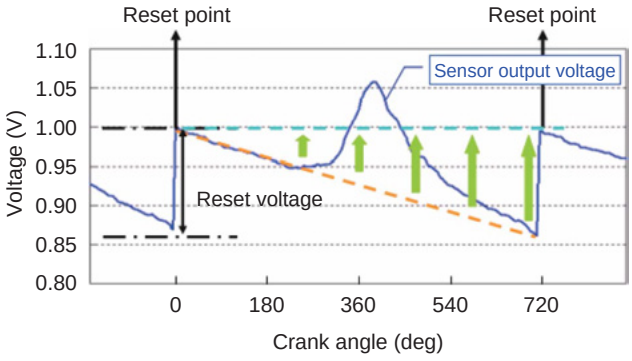


Fig. 6 Reset timing of sensor signal and signal correction

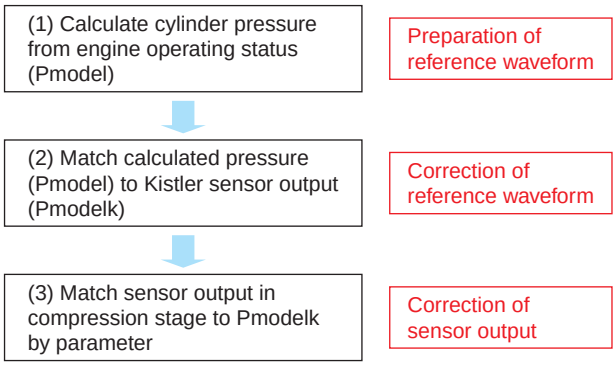


Fig. 7 Method of sensor signal correction

$$Pmodel = GR\frac{T_1}{(V_2/V_1)^{k-1}} / V \qquad (6)$$

(2) Because of inter-molecular force in the gas, the cylinder pressures in the physical model and the measured cylinder pressures do not match. The correction factors K_0 and C_0 are employed to make the cylinder pressure previously measured using the benchmark sensor and the model equation discussed above match. Following correction, the model equation becomes Eq. (7), and *Pmodelk* matches the output of the benchmark sensor. A figure of 1.330 was used for the ratio of specific heat, *k*.

$$Pmodelk = GR\frac{T_1}{(V_2/V_1)^{k-1}} / V \times K_0 + C_0 \qquad (7)$$

As Fig. 9 shows, the correction coefficients K_0 and C_0 are set as a map of engine speed and amount of intake air.

(3) In this section, the method of identifying the actually measured sensor output in the engine model equation will be explained. Exploiting the fact that the cylinder pressure during the compression stroke matches that of the engine model regardless of the state of combustion, a waveform during the compression stroke that corresponds with the waveform in the model is identified. Here, the least squares method is employed, with Eq. (8) being used to minimize error in terms of the difference between the designated pressure during the compression stroke, *Pmodelk*, and the actually measured cylinder pressure, *P'*. Partial differentiation of the error functions *a* and *b* to make *Pmodelk* – *P'* = 0 gives $a = K_1$ and $b = C_1$.

$$\begin{pmatrix} \sum Y(i) \times X(i) \\ \sum Y(i) \end{pmatrix} = \begin{pmatrix} \sum X\wedge 2(i) & \sum X(i) \\ \sum x(i) & n \end{pmatrix} \begin{pmatrix} a \\ b \end{pmatrix} \qquad (8)$$

$$a = K_1 = \left\{n \times \sum Y(i) \times X(i) - \sum X(i) \times Y(i)\right\} / DET \qquad (9)$$

$$b = C_1 = \left\{-\sum X(i) \times \sum Y(i) \times X(i) + \sum X^{\wedge 2(i)} \times \sum Y(i)\right\} / DET \qquad (10)$$

Cylinder pressure, *P*, following correction can therefore be expressed as Eq. (11).

$$P = P' \times K_1 + C_1 \qquad (11)$$

4. Results of Vehicle Tests

Figures 10 and 11 show the 100 cycle combustion waveform at a vehicle speed of 50 mph. The engine speed was 1500 rpm, and the pressure in the intake cylinders was 43 kPa. Figure 10 shows results for a sensor with a sensitivity of 2000 pC/MPa, and Fig. 11 shows results for a sensor with a sensitivity of 380 pC/MPa. The calculated *Pmodelk* displays the same values as the measured pressure, but because the sensitivity of the 380 pC/MPa sensor is low, the obtained cylinder pressure is low.

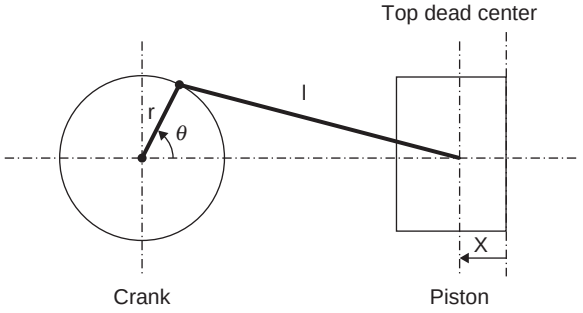


Fig. 8 Crank angle and piston geometry

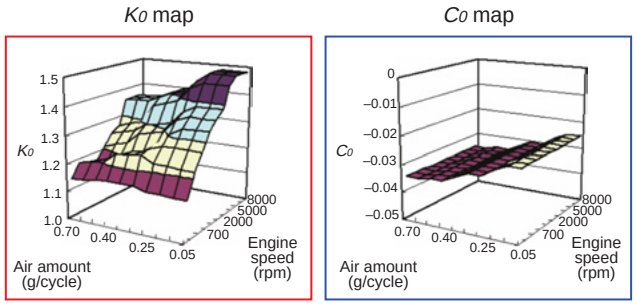


Fig. 9 K_0, C_0 mapping result

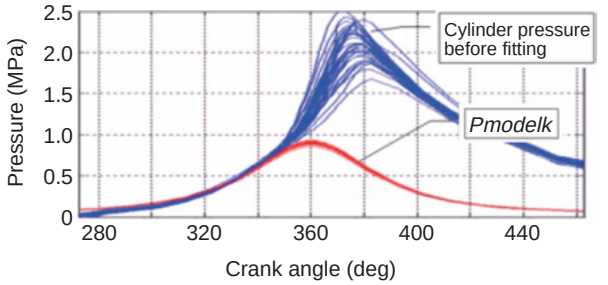


Fig. 10 Cylinder pressure before fitting (Sensor sensitivity: 2000 pC/MPa)

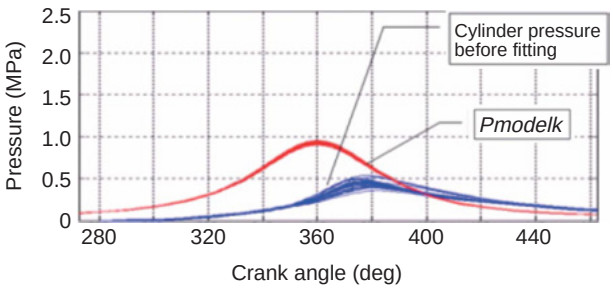


Fig. 11 Cylinder pressure before fitting (Sensor sensitivity: 380 pC/MPa)

Figures 12 and 13 show results following correction, when the waveform during the compression stroke is identified with the model motoring cylinder pressure. Before identification, there are variations between the pressure measured by the sensor during the compression stroke and the model pressure, but following identification, the waveform during the compression stroke matches the model waveform. In addition, the output of the 380 pC/MPa sensor was increased using the correction coefficient K_1 to match the output of the 2000 pC/MPa sensor. The range for identification was set at between 284 and 340 deg after intake top dead center.

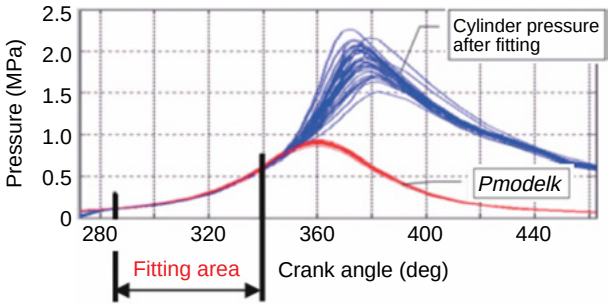


Fig. 12 Cylinder pressure after fitting (Sensor sensitivity: 2000 pC/MPa)

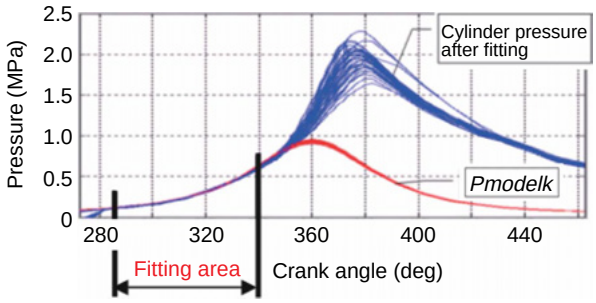


Fig. 13 Cylinder pressure after fitting (Sensor sensitivity: 380 pC/MPa)

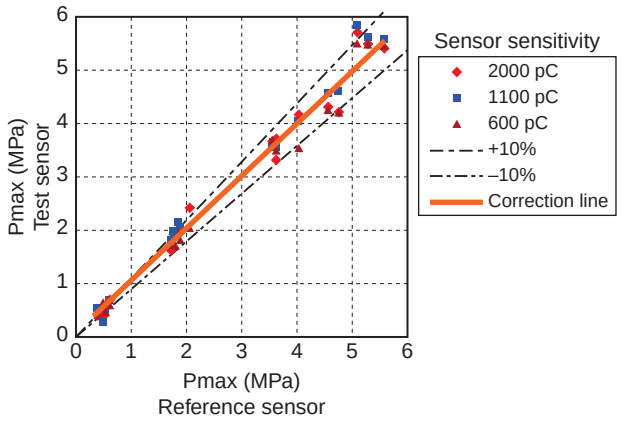


Fig. 14 Pmax comparison between test sensor and reference sensor

Real time correction was able to be performed despite differences in vehicle operating conditions and the sensitivity of sensors. Figure 14 shows a comparison of Pmax (maximum cylinder pressure) obtained using the benchmark sensor and the system discussed here, using sensors with sensitivities of 600, 1100, and 2000 pC/MPa at engine speeds between 500 and 4000 rpm and engine loads varying between an intake cylinder pressure of 20 kPa and WOT. The new system produced figures with only a 10% degree of error against the benchmark sensor.

5. Example of Application to Misfire Detection

In conventional mass production vehicles, misfires are detected on the basis of changes in the angular velocity of the crank. However, in engines with a large number of cylinders and engines with compression strokes that are unequally spaced in time, in which the combustion period of any cylinder overlaps with the combustion period of other cylinders, setting misfire detection criteria for this method is challenging, and requires considerable man hours. Because the developed system enables measurement of pressure for combustion in each cylinder, no error is produced by external disturbances, thus enabling stable detection of misfires. As Fig. 15 shows, cylinder pressure increases as combustion proceeds during normal combustion, but matches the model motoring cylinder pressure when misfires occur.

This characteristic can be exploited to enable the state of combustion to be monitored. Misfires can be judged by integrating the ratio between the integrals of the cylinder pressure waveform during combustion and the model motoring cylinder pressure waveform [Eq. (12)]. During combustion, the ratio is higher than 1. If a misfire occurs, the cylinder pressure matches the model motoring cylinder pressure, and the ratio becomes 1.

$$\text{Integral ratio in combustion} = \int \frac{P(\textit{Cylinder pressure})}{P(\textit{Pmodelk})} \quad (12)$$

This enables complete misfire detection at low and high temperatures and at high altitudes. These results have

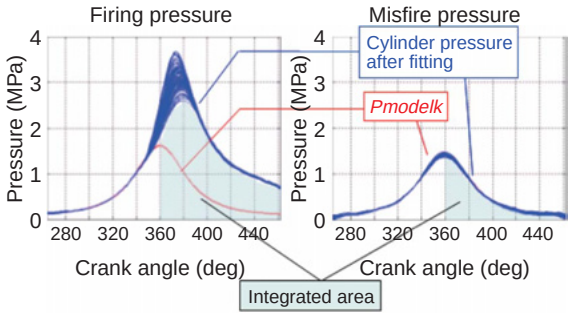


Fig. 15 Difference between firing pressure and misfire pressure

demonstrated the viability of this low-cost sensor for misfire detection in an actual vehicle.

6. Conclusion

A system enabling real time measurement of cylinder pressure has been developed using a polycrystalline piezoelectric element that is able to be mass produced. The system displays good prospects as a technology enabling mass production of cylinder pressure sensors.

The following are the salient points of this research project.

(1) The variation in the sensitivity of the sensor was elucidated, and a method of automatic correction of changes in sensitivity using adaptive calculation was developed.

(2) Operating tests using a mass production vehicle indicated that the cylinder pressure measured in real time could be used as a simple and accurate method of detecting misfires.

It will be necessary to increase the accuracy of the sensor in order to expand its range of application to other control systems, and thus also to perform additional research.

References

(1) Kondo, K., Niimi, A., Nakamura, T.: Indiscope-A New Combustion Pressure Indicator with Washer Transducers, SAE Paper, 750883 (1975)

(2) Sawamoto, K., Kawamura, Y., Kita, T.: Individual Cylinder Knock Control by Detecting Cylinder Pressure, SAE Paper, 871911 (1987)

(3) Kusakabe, H., Okauchi, T., Takirawa, M.: A Cylinder Pressure Sensor for Internal Combustion Engine, SAE Paper, 920701 (1992)

(4) Wlodrczyk, M. T.: High Accuracy Glow Plug-integrated Cylinder Pressure Sensor for Closed Loop Engine Control, SAE Paper, 2006-01-0184 (2006)

(5) Hasegawa, M., Shimasaki, Y., Yamaguchi, S., Kobayashi, M., Sakamoto, H., Kitayama, N., Kanda, T.: Study on Ignition Timing Control for Diesel Engines Using In-cylinder Pressure Sensor, SAE Paper, 2006-01-0180 (2006)

(6) Shimasaki, Y., Kobayashi, M., Sakamoto, H., Ueno, M., Hasegawa, M., Yamaguchi, S., Suzuki, T.: Study on Engine Management System Using In-cylinder Pressure Sensor Integrated with Spark Plug, SAE Paper, 2004-01-0519 (2004)

■ Author ■



Yuji YAMAMOTO



Shusuke AKAZAKI



Masanori OHARA



Takahide MIZUNO

Dynamic Simulation of Oil Pump Chain Using Link-by-link Method

Hiroshi TAKAGISHI* Atsushi NAGAKUBO**
Kazuto MUGURUMA* Nobuharu TAKAHASHI*

ABSTRACT

Simulation technology for predicting load on the oil pump chain of engines with high accuracy was established. In the development of this technology, attention was focused on the ability to take into consideration the centrifugal and inertial forces that occur in the chain, and the ability to predict the chain load from the blade tensioner, which undergoes large transversal vibration, to the system, which uses a hydraulic tensioner. To this end, a link-by-link model in which one link is replaced by one mass and adjacent masses are joined to each other by a spring was developed. As a result of this research, the features of the oil pump chain system were clarified, and the behavior of the oil pump chain, as well as the load on it, were able to be predicted with a high degree of accuracy.

1. Introduction

In recent years, there have been an increasing number of cases in which chain systems have been used as a means of linking the rotating shafts in the engine, in order to meet the needs of durability and compactness. One of these systems is an oil pump chain, which links the oil pump to the balancer and the crankshaft. When the vehicle is running, large load fluctuations occur in this chain. This is considered to be due to the combustion force resulting from the combustion of gasoline, and to the fluctuation of angular velocity of the crankshaft, generated by the inertia force that is due to the reciprocating motion of the pistons. These fluctuations interfere with the transmission of stable rotational speed, and cause wear of the chain and noise. In order to overcome such problems, tension is applied to the chain with tensioners, and the running path of the chain is restricted by guides. These tensioners are divided into types that use hydraulic pressure and types that use a spring.

Figure 1 shows an oil pump chain system that uses a hydraulic tensioner. The hydraulic method used is a system in which the end of the arm, which rotates about a pivot, is retained by a hydraulic tensioner. This method positively prevents transversal vibration of the chain, but it requires a path for supplying working oil, has a complicated structure, and is expensive.

In contrast, the spring method applies a pre-tension force using only a spring, has a simple structure, and is inexpensive. Particularly, a blade tensioner is a spring-type

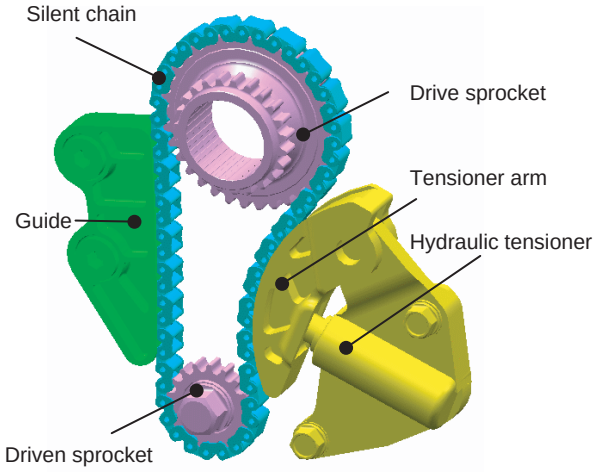


Fig. 1 Chain system with hydraulic tensioner

* Automobile R&D Center
** PSG CO., LTD.

tensioner, which functions as both a guide and a tensioner. Figure 2 shows the oil pump chain system, which uses a blade tensioner. A blade tensioner consists of a number of metal leaf springs that are fitted into a plastic guide and preloaded. As shown in Fig. 3, the leaf springs, which are fixed to a pivot, bend while rotating, thus reducing transversal vibration of the chain. The number of cases in which blade tensioners are being used is increasing from an economic viewpoint. However, due to increased combustion pressures and lightening of piston to enhance fuel economy in recent years, fluctuations in the angular velocity of the crankshaft have increased in the low speed region. As a result, the fluctuations in chain tension have increased, and there are cases in which the blade tensioner is unable to retain the oil pump chain. Accordingly, it is necessary to perform simulations that enable the applicable limit of the blade tensioner to be predicted.

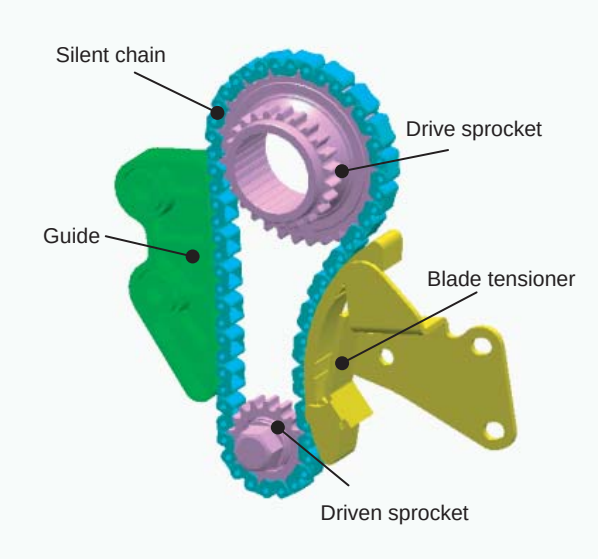


Fig. 2 Chain system with blade tensioner

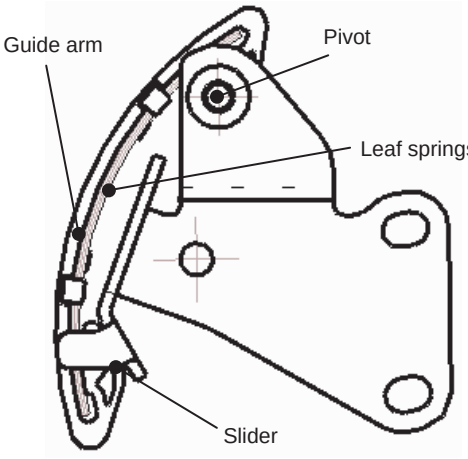


Fig. 3 Blade tensioner

Table 1 General specifications of verified engine

Engine type	Liquid-cooled 4-cylinder turbocharged engine
Displacement	2300 cm^3
Camshaft number	2
Number of valves	Intake: 2 Exhaust: 2
Valve system	VTEC
Maximum torque	353 Nm / 4500 rpm
Maximum power	179 kW / 6000 rpm
Balancer drive system	6.35-mm pitch silent chain with blade tensioner

2. Issues and Action Concerning Conventional Simulation

Until now, simulations of the behavioral load on a timing belt or a chain have generally employed a method using a longitudinal vibration model[(1)-(3)]. However, in the conventional method, the following issues have existed in the prediction of the oil pump chain load.

(1) It is not possible to reproduce the transversal vibration of the chain, which is generated in the case where a blade tensioner is used.
(2) In the case of an oil pump chain that has a high speed, centrifugal force is added to the chain load, but a longitudinal vibration model cannot reproduce it.
(3) The blade tensioner is greatly deformed by the chain load, but the longitudinal vibration model cannot reproduce this behavior.

Accordingly, in this research, a link-by-link chain model, a blade tensioner model consisting of a number of beam elements, and a hydraulic tensioner model, which can solve these issues, were constructed. As a result, a simulation method that cannot only reproduce the transversal vibration of the chain, but also take into account the effect of centrifugal force and inertia force, and the engagement with the sprocket was established. By using this method, the behavior and load of the chain were predicted with high accuracy, and the features of the oil pump chain system were clarified.

3. Making a Model of the Chain System

3.1. Chain

In order to validate the simulation, an inline 4-cylinder turbo supercharged gasoline engine having 2300 cm^3 of displacement was used. An outline of the engine is shown in Table 1. A silent chain having 6.35 mm of pitch was used. The link-by-link method[(4), (5)] was constructed using a 2-dimensional model in order to obtain the transversal vibration of the chain. In the modeling process, one link of the chain was substituted for by one mass point. These mass points have a degree of freedom that permits

horizontal and vertical displacement and rotation, and there are two connecting points at each pin position. In order to join adjacent links to each other, a rotatable spring and a damping element are defined at each connecting point. Also, a rear face and tooth profile are defined at each link, enabling the chain to touch the guide and mesh with the sprocket. This chain model is shown in Fig. 4.

3.2. Blade Tensioner

Figure 5 shows the blade tensioner model. The blade tensioner was modeled using a number of divided mass points and beam elements joining them to each other. These mass points have three degrees of freedom, as in the case of the chain. Each mass point was divided into five parts. This was decided upon taking into consideration the smoothness of the contact with the chain, the number of resonance modes that can be reproduced, the installation of the pivot and the slide part, and so on. Adjacent mass points were connected to each other by beam-type leaf springs, which can take account of bending deformation, and damping elements.

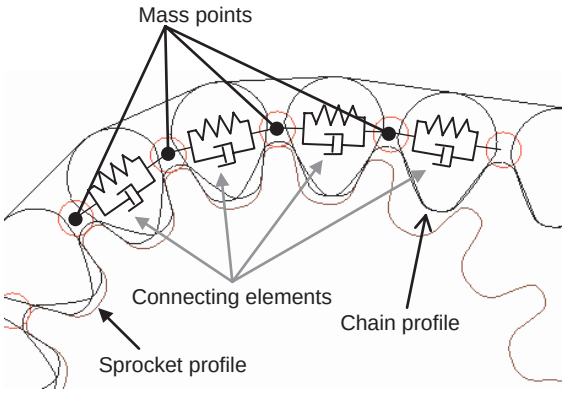


Fig. 4 Ling-by-link model

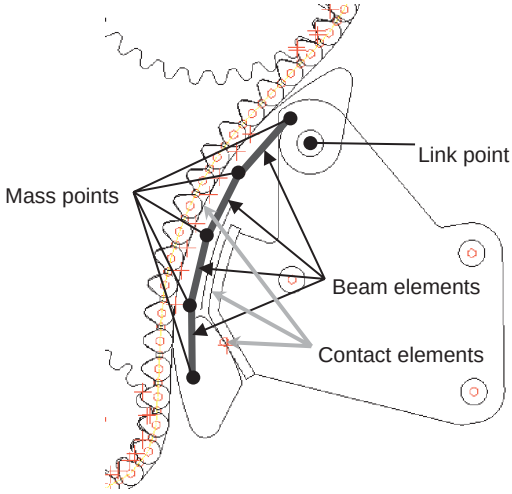


Fig. 5 Blade tensioner model

Connecting points were provided at the top ends of the connected mass points, and were retained in such a way that they could rotate. At the bottom ends, the contact elements where the blade tensioner slides along the holder were defined. As a result, the simulation enables the deformation of the blade tensioner to be reproduced in the same way as that of an actual blade tensioner. In addition, at each mass point, a profile that guides the chain was defined, and could apply tension to the chain. Also, preload was set by changing the curvature when a bending load is not applied to the beam. To increase the preload as in the case of an actual blade tensioner, the curvature is reduced. Conversely, to reduce the preload, the curvature is increased. The stiffness of the blade tensioner set in this way, as well as the appropriateness of the preload, were validated by comparing the results of the simulation with the quasi-static load test results. Figure 6 shows an outline of the test method. The center part of the tensioner constrained by the jig was pushed by the plunger, and the load and displacement at this time were measured. Also, the simulation model was calculated under similar conditions. Figure 7 shows a comparison between the measured and simulated results. As indicated by these results, it can be seen that the blade tensioner has high hysteresis characteristics. These characteristics were reproduced by adding a friction element to each sliding part. It can be seen that the hysteresis and load characteristics exhibited by the blade tensioner, which

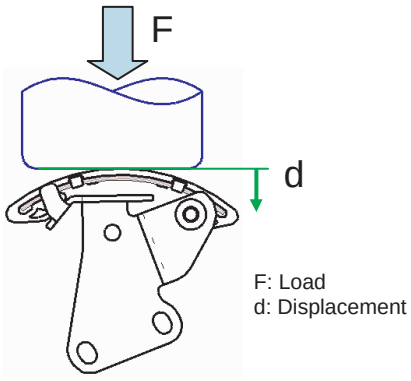


Fig. 6 Static load test of blade tensioner

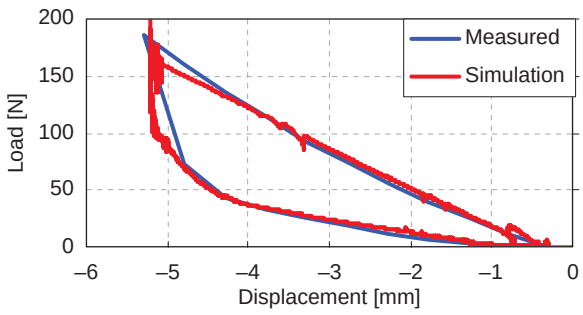


Fig. 7 Static stiffness of blade tensioner

bends when rotated about the pivot, are reproduced with adequate accuracy.

3.3. Hydraulic Tensioner

Figure 8 shows the hydraulic tensioner. The hydraulic tensioner is installed on the end of the movable arm and regulates the motion of the chain. This tensioner is substituted by a coupled vibration model of the plunger, spring, high pressure chamber oil, and tensioner body. The main spring and the high pressure chamber model are installed between the plunger and the tensioner body, and the nonlinear bulk modulus of the oil that is due to the inclusion of air is also taken into account. Also, the oil suction check valve is incorporated in the high pressure chamber model. The discharge of oil is added to the amount that leaked from the clearance between the piston and the housing, and the discharge from the relief valve is also modeled. The relief valve is contained in the plunger. The plunger operates according to the load balance indicated in Eq. (1), and the relief valve according to the load balance indicated in Eq. (2).

$$F_p = M\ddot{X} + C\dot{X} + KX + PS + F_{pr} + c\dot{x} + kx + f_{pr} \quad (1)$$

$$Ps = m\ddot{x} + c\dot{x} + kx \quad (2)$$

Where,

F_p: Plunger load
X: Plunger displacement
M: Plunger weight
C: Viscous damping between the plunger and the body
K: Main spring stiffness
P: High pressure chamber pressure
S: Plunger pressure receiving area
F_{pr}: Main spring preload
x: Relief valve displacement
c: Viscous damping between the relief valve and the plunger
k: Relief valve spring stiffness
f_{pr}: Relief valve spring preload
s: Relief valve pressure receiving area
m: Relief valve weight

The pressure loss when the relief valve is operating can be approximated using Eq. (3).

$$\Delta p = \frac{\zeta\rho}{2}\left(\frac{Q}{\pi dl}\right)^2 \quad (3)$$

Where,

Δp: Pressure loss
ξ: Loss coefficient
ρ: Density
Q: Flow rate
d: Valve seat diameter
l: Valve lift

The model created in the above way was subjected to a unit excitation test using a hydraulic exciter, and the accuracy was validated[1].

4. Chain System Resonance Frequency Characteristics

In the accuracy validation of the simulation model, the resonance frequency of the chain system that governs the dynamic characteristics of the chain was confirmed. The resonance frequency was identified by performing frequency analysis of the fluctuation of angular velocity when a step torque is applied to the oil pump sprocket. Figure 9 shows the results of identification.

The resonance frequency of the hydraulic tensioner system is 186 Hz. The value[6] calculated from the chain stiffness and the inertia of the balancer and the pump agrees with this resonance value, and it can be seen that the link-by-link method reproduces the resonance frequency characteristics of the chain system. In contrast to this, the resonance frequency of the blade tensioner system is only 133 Hz. One possible reason for this is that the stiffness of the blade tensioner is lower than that of

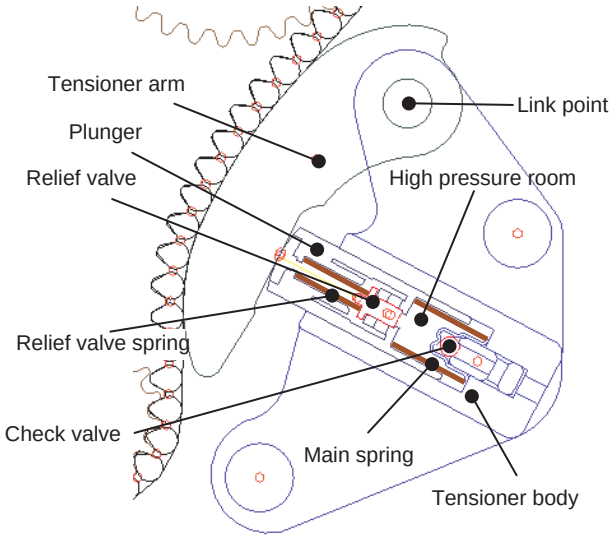


Fig. 8 Hydraulic tensioner model

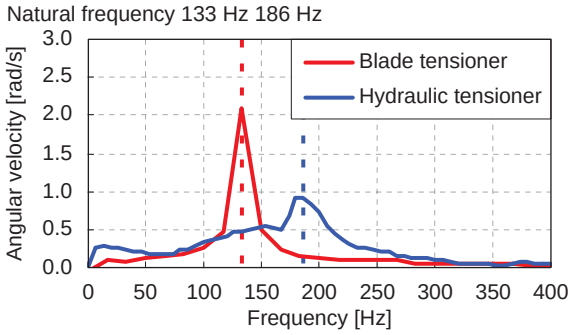


Fig. 9 Step response of chain system

the hydraulic tensioner. In the case of the hydraulic tensioner, the tensioner stiffness is higher than the chain stiffness. Consequently, the slack side chain stiffens, and together with the tension side chain, it governs the eigenfrequency. In the case of the blade tensioner, on the other hand, the tensioner stiffness is lower than the chain stiffness. For this reason, regarding the slack side chain, the chain load is lower and the chain cannot stiffen, and the eigenfrequency, which is determined by the chain stiffness on the tension side, and the inertia of the balancer, as well as the oil pump, govern the behavior of the chain system[6].

In this way, if the blade tensioner is used, the apparent chain stiffness becomes 1/2, and the resonance frequency becomes $\sqrt{1/2}$ = 0.7 times that of the hydraulic tensioner.

5. Validation of Dynamic Characteristics due to the Chain Load

5.1. Centrifugal Force

In order to reproduce the chain load under operating conditions, a model in which the crankshaft, chain, and balancer shaft were linked was constructed. Figure 10 shows the lump mass simulation model. The chain is wound between the crankshaft and the balancer shaft to transmit motive power. The two balancer shafts are coupled by a gear element that takes into account the gear reaction and backlash. The piston connecting rod is coupled to the crankshaft model, and is driven by cylinder pressure in the same way as in an actual chain. Also, the crankshaft model was that of a torsional model, which took into account rotation alone. Because the fluctuation of angular velocity of the crankshaft governs the chain load fluctuation, it was judged that there was no issue with accuracy, and hence the bending deformation was omitted for the purpose of simplification.

Compared to the timing chain, the sprocket pitch circuit radius of the oil pump chain on the crankshaft is large, and the peripheral velocity is high. The fluctuation of angular velocity of the oil pump chain is small at the high rotation side. In contrast, the centrifugal force of the chain is large, and it is necessary to check the effect of centrifugal force when predicting the load. Accordingly, a validation was performed concerning whether or not a link-by-link model could reproduce the effect of centrifugal force. Figure 11 shows the results of a simulation of the chain load when only the rotational speed was raised, without applying fluctuation of angular velocity. The chain load increases parabolically according to the increase of the rotational speed. The chain load at 7000 rpm increased by 200 N compared to the chain load at 1000 rpm. This was compared with the results obtained using the theoretical equation. The increase in the chain load due to centrifugal force is indicated according to the following Eq. (4)[7]-[9].

$$F_f = mv^2 \quad (4)$$

Where,

F_f: Chain load due to centrifugal force

m: Chain weight per unit length

v: Chain speed

According to this theoretical equation, the chain load at 1000 rpm is 4 N, and at 7000 rpm is 210 N. In the simulation model, preload and oil pump torque are applied to the blade tensioner. Consequently, the static chain load is 300 N on the tension side. As a result, the tension side chain load is 304 N at 1000 rpm, and 510 N at 7000 rpm, which agree with the results of simulation. It thus became clear that the chain load, which takes into account the centrifugal force in the high speed region by using the link-by-link model, could accurately be reproduced.

5.2. Chain Load when a Blade Tensioner is Used

In addition, the prediction accuracy of the chain load generated in the oil pump chain was validated.

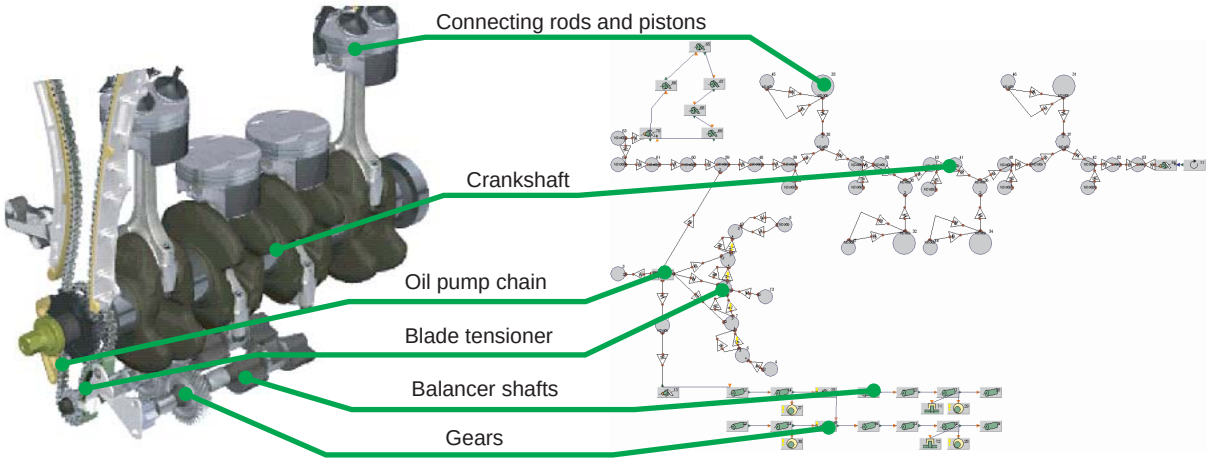


Fig. 10 Whole simulation model

Measurement of the chain load was performed by forming a thin part on the crankshaft sprocket and installing a strain gauge on that section. The torque measured here was multiplied by the effective radius of the sprocket and converted into a chain load.

Figure 12 shows a comparison of the chain load obtained by simulation and by measurement. Measurement was performed using a new chain. The chain load increased in the vicinity of 2000 rpm and then fell again at higher speeds. When the engine speed rose past 4000 rpm, the chain load increased again. The simulation also showed the same tendency.

Next, validation was performed with the blade tensioner exceeding the load retaining limit. If the blade tensioner has exceeded the load retaining limit and is unable to reduce the transversal vibration of the chain, a high chain load that exceeds the allowable range may occur. Conceivable causes of this include the increase in the fluctuation of angular velocity of the crankshaft, insufficient preload of the tensioner, and the like. The prediction of the limit of occurrence of a high chain load due to transversal vibration is important from the viewpoint of the development of an engine.

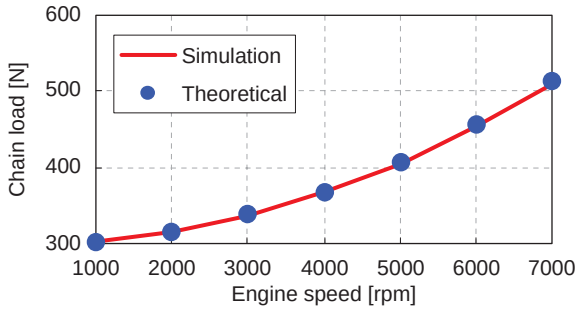


Fig. 11 Influence of rotational speed for chain load

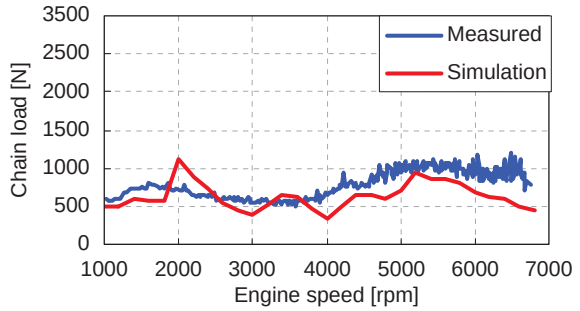


Fig. 12 Maximum chain load of normal chain with blade tensioner

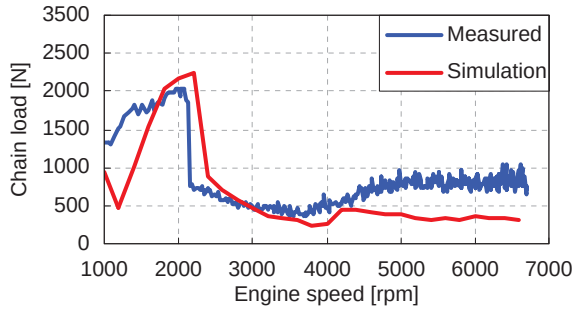


Fig. 13 Maximum chain load of elongated chain with blade tensioner

A high chain load is likely to occur when the chain becomes worn. When the chain becomes worn and stretches, the geometry of the blade tensioner changes, thus reducing the preload applied to the chain. Reduction of preload causes the transversal vibration of the chain to increase. Accordingly, a chain stretched by 0.7% was used, and a comparative validation using specifications such that a high chain load is generated was carried out. Figure 13 shows the chain load when a 0.7% elongated chain was used.

With a new chain, the chain load was reduced in the vicinity of 1000 N. In the case of a 0.7% elongated chain, a peak chain load in the vicinity of 2000 N was generated at 2000 rpm. In this way, the simulation was able to reproduce the high chain load generated due to the elongation of the chain. Also, the engine speed at which the limit is exceeded and the chain load abruptly increases, the load generated, and the phenomenon whereby the chain load abruptly falls in the vicinity of 2200 rpm were also accurately predicted with this simulation.

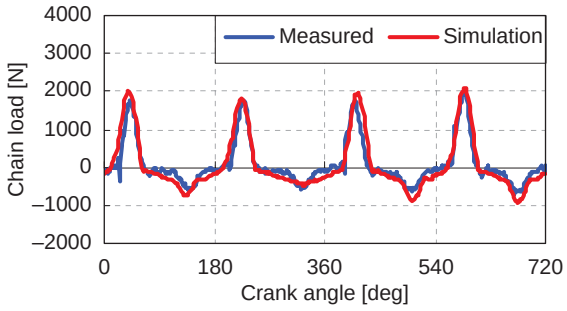
Next, a measurement comparison of the chain load generated in a 0.7% elongated chain and the time series waveform of the simulation was performed. This comparison was performed at 2000 rpm, at which a high chain load occurred, and at 2600 rpm, at which the chain load fell. The results are shown in Fig. 14. A negative chain load occurs at 2000 rpm. A negative value expresses the chain load on the slack side. It is believed that on the slack side, the blade tensioner has not absorbed and buffered the chain load.

In addition, the detailed mechanism pertaining to why such a chain load occurs is estimated from the simulation. Figure 15 shows the chain load on the tension side and on the slack side. At 2600 rpm, the chain load on the tension side fluctuates, causing the load to become zero. On the tension side, the condition in which the chain is subjected to a load, and in which it is not subjected to a load, appear alternatively. In contrast, on the slack side, a soft blade tensioner receives the displacement of the chain, and compared to the tension side, the load is low and load fluctuation is constant. The absorption of chain load fluctuations using a soft spring is a feature of the blade tensioner. The fact that the blade tensioner can keep the chain load lower than the hydraulic tensioner can is considered to be an advantage of the blade tensioner. However, if the fluctuation of angular velocity of the crankshaft is large, causing the blade tensioner to strike the stopper, a large chain load will occur. By focusing

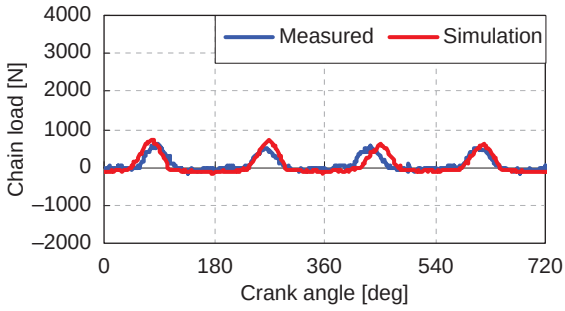
attention on the chain load at 2000 rpm, it can be seen that the slack side chain load rises abruptly. As a result of the reaction to this high slack side chain load, a large chain load occurs on the tension side as well. This chain load is generated by an impact between the chain and the guide, or between the chain, tensioner, and stopper.

Once an impact occurs, it occurs repeatedly and continuously using only a small amount of energy, resulting in a high chain load. This is shown in Fig. 16.

In addition, regarding the apparent chain stiffness, when the chain strikes the stopper, a symmetrical increasing stiffness of the spring abruptly occurs. This results in a jumping phenomenon of the resonance point at the high frequency side. The jumping phenomenon actually occurs on a stretched chain in the vicinity of 2200 rpm. As shown in Fig. 13, the simulation also accurately reproduces this jumping phenomenon.

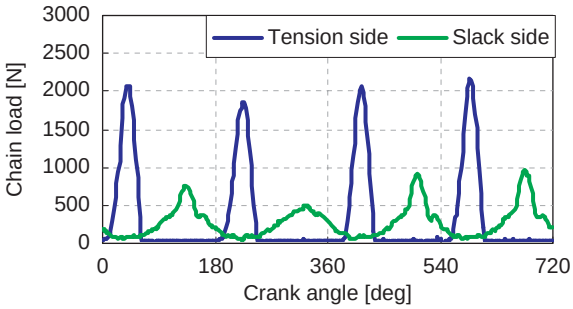


(a) Engine speed 2000 rpm

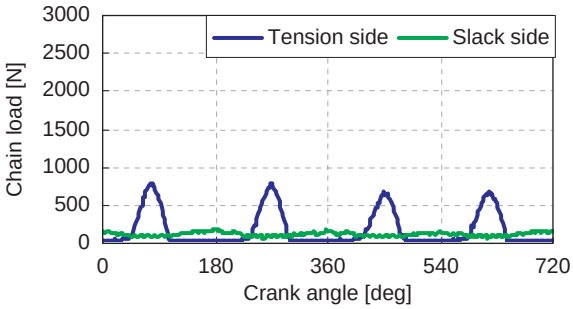


(b) Engine speed 2600 rpm

Fig. 14 Chain load of elongated chain with blade tensioner

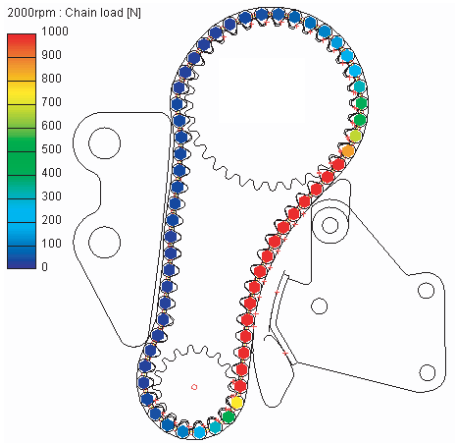


(a) Engine speed 2000 rpm

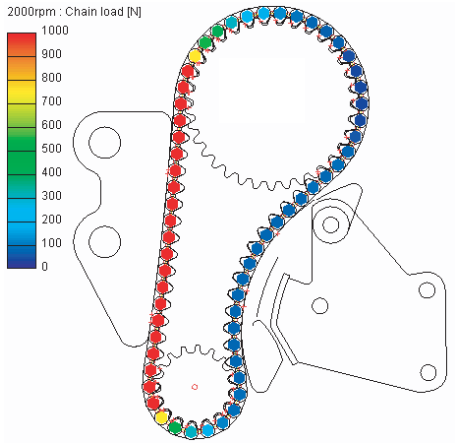


(b) Engine speed 2600 rpm

Fig. 15 Simulated chain tension with elongated chain and blade tensioner



(a) Loaded slack side



(b) Loaded tension side

Fig. 16 Simulated chain behavior at 2000 rpm with elongated chain and blade tensioner

5.3. Chain Load when a Hydraulic Tensioner is Used

Conceivable methods of reducing the occurrence of a high chain load include increasing the spring load of the blade tensioner, reducing the fluctuation of angular velocity, and changing over from a blade tensioner to a hydraulic tensioner. Of these countermeasures, it is easiest to increase the spring load. However, there are space limitations, and the friction loss of the chain and guide shoe increases, so it is not always possible to increase the spring load as desired. The fluctuation in angular velocity can be reduced by a method in which vibration is isolated by a long torsion spring damper. It can also be canceled by using an elliptical sprocket. Also, changing over to a hydraulic tensioner with a strong damping force is an effective method of reducing transversal vibration.

Accordingly, Fig. 17 shows the maximum chain load for the case where a blade tensioner is replaced by a hydraulic tensioner. A hydraulic tensioner has greater stiffness than a blade tensioner. It can regulate the lateral vibration of the chain, and reduce the excessive chain load at 2000 rpm. It was confirmed by simulation as well that the chain load could be kept low. At the same time, the maximum chain load at 5000 rpm could also be reproduced accurately, and the maximum chain load as well as the rotational speed at which it occurred could be predicted accurately. From the time series waveform comparison at 2000 rpm of Fig. 18 as well, it can be seen that the simulation can accurately reproduce the chain load.

Figure 19 shows the results of predicting the chain behavior. It can be confirmed that the chain slackness that had been seen in the blade tensioner has disappeared, and that the hydraulic tensioner keeps the chain load low.

In the above way, a simulation method that enabled the behavior of the chain and the load to be reproduced, even when using different tensioners, was established, and it became clear that this simulation method could be developed as a prediction tool at the layout stage.

6. Conclusion

Simulation technology for an oil pump chain was established using a link-by-link model, and the following information was acquired.

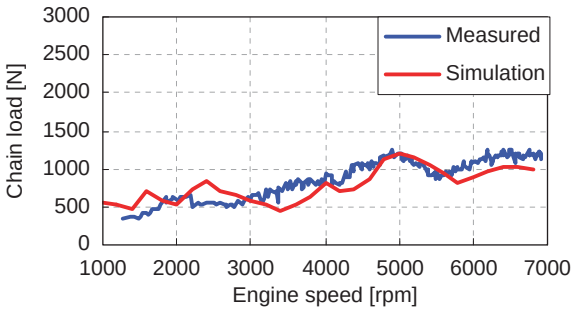


Fig. 17 Maximum chain load of elongated chain with hydraulic tensioner

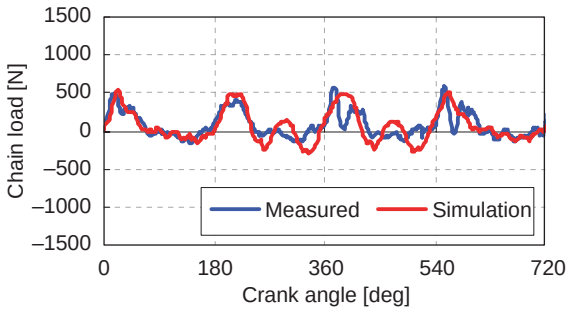
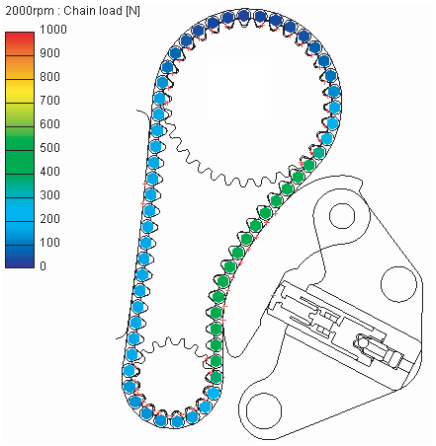
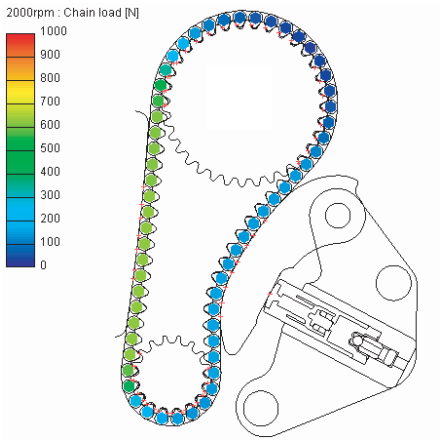


Fig. 18 Chain load of elongated chain with hydraulic tensioner at 2000 rpm



(a) Loaded slack side



(b) Loaded tension side

Fig. 19 Simulated chain behavior at 2000 rpm with elongated chain and hydraulic tensioner

(1) By using the link-by-link chain model, the chain engagement, seating behavior, centrifugal force, and inertia force could all be reproduced, and the transversal vibration predicted.
(2) The resonance frequency of the blade tensioner system is lower than that of the hydraulic tensioner. Also, the chain load sometimes increases abruptly, along with the increase of the fluctuation of angular velocity of the crankshaft. This indicates that the tension-retaining performance of the blade tensioner has reached its limit. Prediction of this limit is an important design guideline.
(3) If the blade tensioner exceeds its tension-retaining limit, it is necessary to replace the tensioner with a hydraulic tensioner. By doing this, the transversal vibration of the chain will be limited, and the chain load could also be kept low.

A blade tensioner model consisting of a number of beam elements and a hydraulic tensioner model were constructed as described above, and technology for predicting the maximum chain load at the layout stage, and the rotational speed at which it occurs, was established.

References

(1) Takagishi, H., Sugawara, H.: Prediction of Chain Load in Timing Chain System, Honda R&D Technical Review, Vol. 14, No. 1, p. 223-230
(2) Hellinger, W., Priebsch, H. H., Rainer, G. Ph.: Auslegung von Ventiltrieben fuer Hochleistungsmotoren - Rechnerische und Experimentelle Verfahren, 16. Internationales Wiener Motorensymposium (1995)
(3) Takagishi, H., Shimoyama, K., Asari, M.: Prediction of Camshaft Torque and Timing Chain Load for Turbo Direct Injection Diesel Engine, SAE Paper, 2004-01-0611 (2004)
(4) Sopouch, M., Hellinger, W., Priebsch, H. H.: Simulation of Engines Structure Borne Noise Excitation due to the Timing Chain Drive, SAE Paper, 2002-01-0451 (2002)
(5) AVL: Tycon User's guide H (2005)
(6) Takagishi, H., Katsuki, M., Kawamura,Y., Nagakubo, A.: Prediction of Transmitted Load for Turbo Direct Injection Diesel Engine, FISITA Paper, F2004-F387 (2004)
(7) Niemann, G., Winter, H.: Maschinenelemente Band 3, Springer-Verlag, p. 117-118 (1986)
(8) Ohgoshi, J.: Roller chain, Corona publishing Co., LTD, p. 28-29 (1976)
(9) Funk, W.: Zugmittelgetriebe, Springer-Verlag, p. 81 (1995)

Author


Hiroshi TAKAGISHI


Atsushi NAGAKUBO


Kazuto MUGURUMA


Nobuharu TAKAHASHI

Prediction of Mesh Misalignment of External Gear for Transmission

Yoshikazu TATENO* Yoshiomi FURUI* Kazuhiro NORITA*

ABSTRACT

To increase the accuracy of meshing analysis of the external gear of the transmission, attention was focused on mesh misalignment of the gear. A gear in an actual vehicle is supported by a number of parts. An appropriate fitting stiffness was assigned to the point of contact between the gear and each support part, and a misalignment theoretical prediction technology having feasible accuracy and calculation times was constructed using linear analysis. By applying misalignment created using the method described in this paper to gear mesh analysis, it was confirmed that there was good correlation with the actual status of gear tooth flank contact and damage prediction. Also, analysis on the misalignment effect factors and their role in misalignment was possible as well, which made efficient reduction of misalignment possible.

1. Introduction

In recent years, reduced-weight automobile transmissions are being demanded in order to reduce CO_2 emissions and increase fuel economy. On the other hand, due to there being increases in engine torque and the increasing need for development of high-weight automobiles represented by SUV (sports utility vehicles), the load on the power transmission parts, such as the gears, is increasing.

For this reason, the shaft, bearings, housing, and other parts that support the gears undergo elastic deformation[1] due to load. In addition, because there are clearances between the parts that support the gears, the gear pairs are operated in a condition different from that of normal meshing conditions. It is necessary that the gears have adequate strength under such a condition. Consequently, in designing gear strength, it is necessary to take into account the meshing conditions. Methods of designing gear strength that take into account the meshing condition have already been proposed[2].

However, in the calculation of shaft stiffness alone, which had been performed during the conventional design stage, other factors were not taken into consideration, and calculation accuracy that matched an actual vehicle could not be obtained about the meshing condition of a gear pair. Also, although there is a method of observing the contact condition of the tooth flank when the vehicle is actually being driven, this method cannot confirm it before the vehicle is completed, and it is challenging from which to make a quantitative judgment. Accordingly, in this paper, factors other than the shaft (the bearings, housing, and clearance between the gear support parts) were also considered at the design stage, and the meshing condition of a gear pair could be predicted in a more practical calculation time and to a more practical degree of accuracy. A report is set out below.

2. Conventional Prediction Technology and Related Issues

While a gear pair is meshing, the relative displacement of the shaft that occur in the direction of line of action at the effective face width ends are defined as Al_1 and Al_2. The difference between them is called the misalignment and is defined as AL (Fig. 1).

$$AL = Al_1 - Al_2 \quad (1)$$

Previously, prediction of the misalignment at the design stage was done using a shaft deflection analysis program, which only took into account shaft stiffness. However, the gears are supported by multiple parts, and there are clearances between the respective parts (Fig. 2). Consequently, accurately predicting the misalignment from

* Automobile R&D Center

only the shaft stiffness is challenging[3], and the influence of other factors could not be determined, so issue was that much testing was necessary to analyze the root cause of misalignment and to perform enhancements.

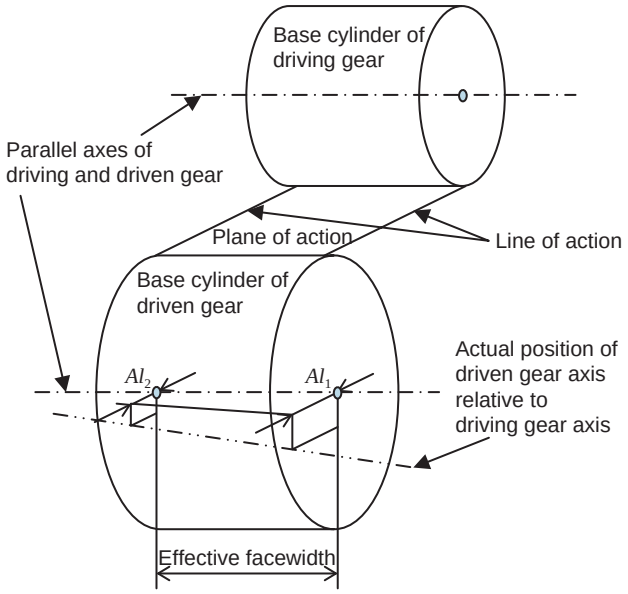
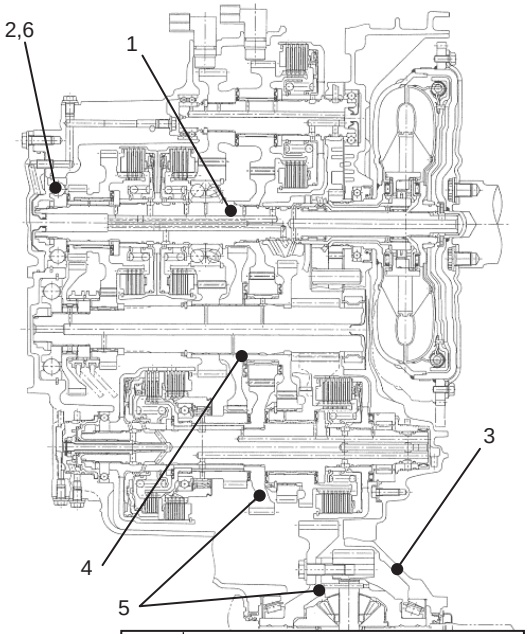


Fig. 1 Definition of mesh misalignment



1	Stiffness of shaft
2	Stiffness of bearing
3	Stiffness of housing
4	Clearance for assembly
5	Stiffness of construction part (e.g, Differential case etc.)
6	Internal clearance of bearing

Fig. 2 Factor of mesh misalignment

3. Establishing Misalignment Prediction Technology

In the establishment of misalignment prediction technology, the displacement of the gears, shaft, and bearings in an actual vehicle were measured, and the correlation of the analysis results with an actual vehicle was validated.

3.1. Measurement of Each Displacement in an Actual Vehicle

The displacement of the gears, shaft, and bearings was measured using a torsion tester on a transmission bench. In order to reduce the influence of sticking, the absorption side was not fixed and measurement was performed at extremely low rotational speed by means of a powder brake. Figure 3 shows the configuration of the measuring equipment. In order to measure the displacement of the object parts, a laser displacement sensor, a linear gauge, and an eddy current gap sensor were used. Also, regarding the housing, shape optimization technology[4] was used to fabricate and use a housing that has the stiffness of an actual vehicle, from which parts that interfered with measurement had been excluded, and which did not affect the support stiffness of the gear [Fig. 4(a)]. An example of the displacement measurement position of a gear is shown in Fig. 4(b).

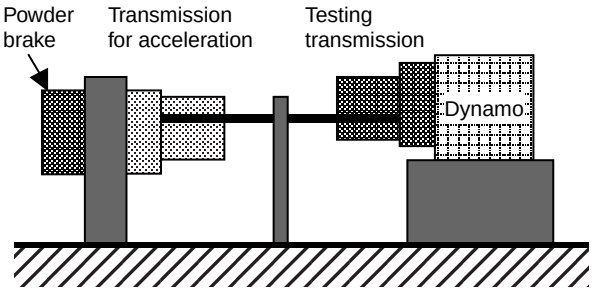


Fig. 3 Structure of testing equipment

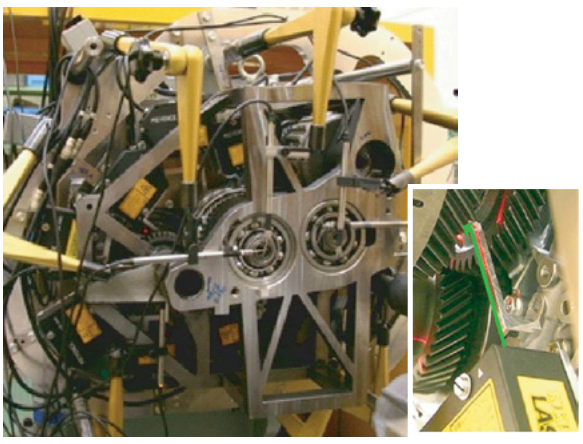


Fig. 4(a) Appearance of testing equipment

3.2. Outline of Misalignment Analysis Model

Figure 5 shows an outline of the misalignment analysis model. The shape and material characteristics (Young's modulus and Poisson's ratio) of each part are defined. The fitting stiffness between parts is defined for each pair of parts. A model for one transmission is made, the stiffness of each part and defined fitting stiffness between parts are coupled by linear analysis and the misalignment is calculated.

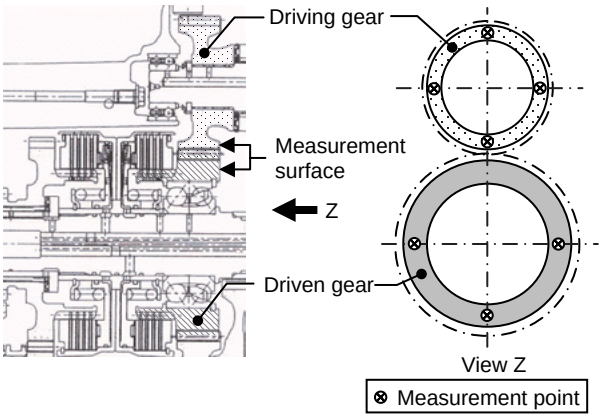


Fig. 4(b) Measurement point of gear displacement

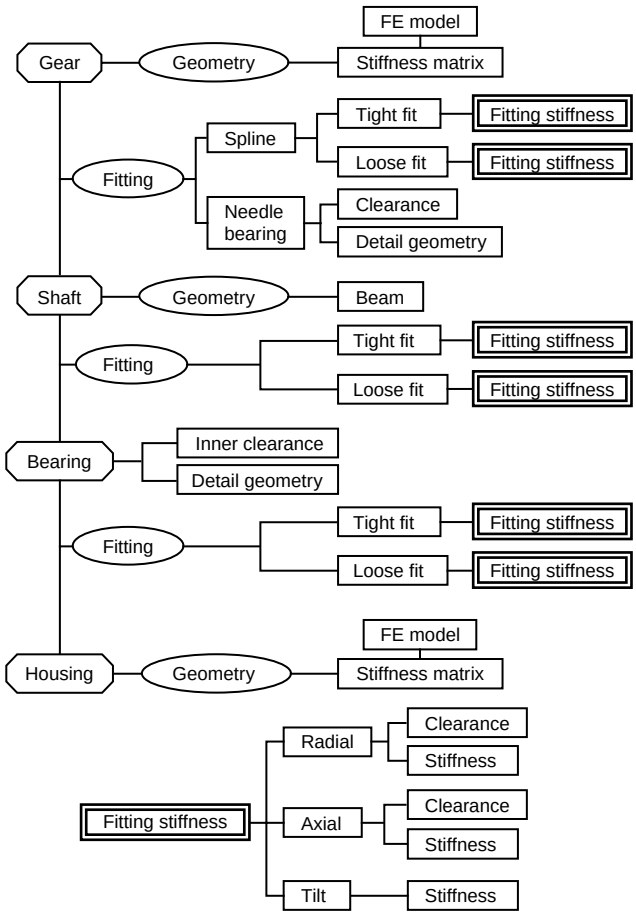


Fig. 5 Outline of mesh misalignment analysis model

3.3. Fitting Stiffness Definition

In the misalignment analysis model, the fitting stiffness that is defined between parts should be defined for each pair of parts in the radial direction, axial direction, and tilt (Fig. 5). Regarding this fitting stiffness, if a uniform value is used irrespective of the location, correlation between the measured and calculated results could not be

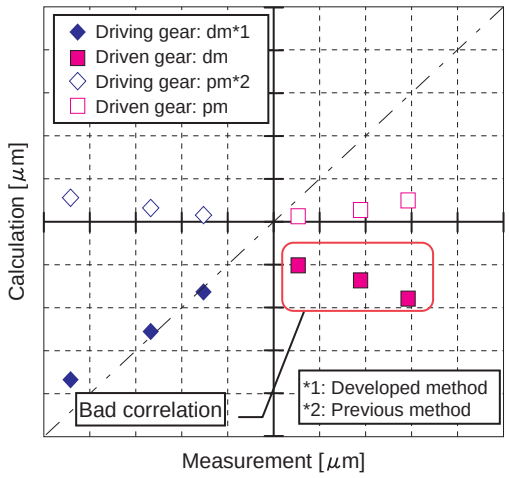
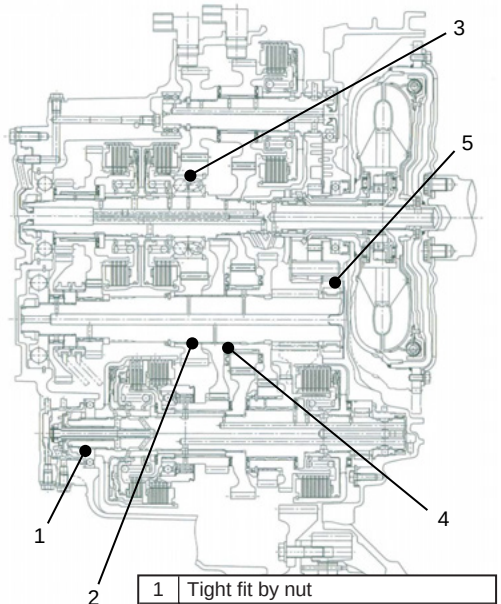


Fig. 6 Correlation of mesh misalignment



1	Tight fit by nut
2	Spline fit
3	Radial stiffness between parts
4	Axial stiffness between parts
5	Between bearing and housing

Fig. 7 Stiffness item definition

acquired, like the case of the conventional prediction method (Fig. 6). Accordingly, the measured results and the contact analysis were compared concerning the displacement of gears and gear support parts, using multiple transmission structures, and in order to acquire correlation with an actual vehicle, an appropriate fitting stiffness was defined for each component element shown in Fig. 7.

3.3.1. Radial direction fitting stiffness definition

As an example of fitting stiffness in the radial direction, the process concerning the definition of the fitting stiffness between the bearing and the housing is shown below. In linear analysis, the bearing load is added to the center node of the bearing hole in the housing. The center node and the bearing hole are connected to each other by a rigid bar. Consequently, the bearing hole in the housing is subjected to compression in the bearing load direction, and a tension force in the opposite direction. In contact analysis, the bearing load is applied to the rigid body, hence a compression force in the load direction acts in the bearing hole in the housing, but no tension occurs in the opposite direction (Fig. 8). Regarding the fitting stiffness in the radial direction between the bearing and the housing, the bearing load F_{brg} divided by the difference in the shift of the bearing center node ($L_n - L_l$) is defined as the fitting stiffness K. Also, the ratio between F_{brg} and the housing hole contact area A of the bearing O.D. (bearing O.D. x π x bearing contact width) is defined as P.

$$K = \frac{F_{brg}}{L_n - L_l} \tag{2}$$

$$P = \frac{F_{brg}}{A} \tag{3}$$

The correlation between K and P was obtained by using multiple transmission structures (Fig. 9). Because a roughly linear relationship is obtained, the fitting stiffness between the bearing and the housing was defined by a linear equation (4) obtained from the above relationship.

$$K = aP + b \tag{4}$$

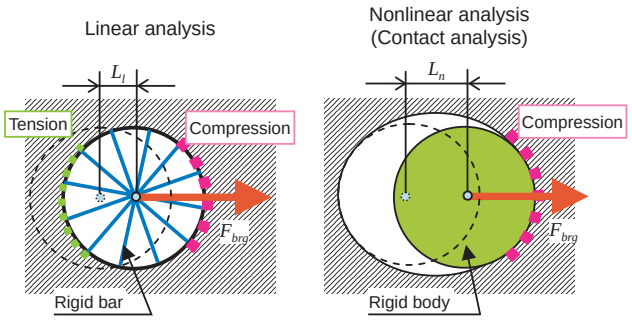


Fig. 8 Comparison of linear analysis and nonlinear analysis

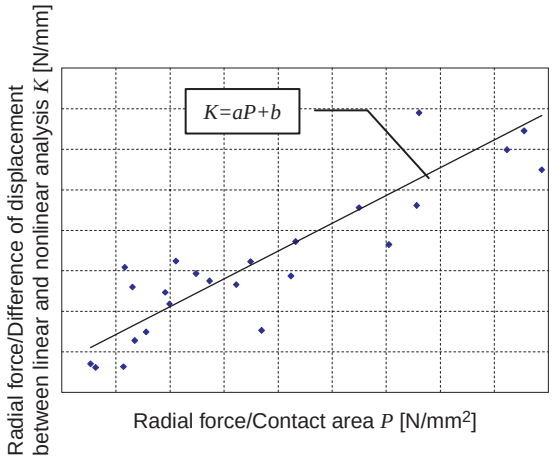


Fig. 9 Definition of stiffness between bearing and housing

3.4. Gear Cross-sectional Shape

Regarding the cross-sectional shape of the gear, in the software used, there is a method of creating a gear as a shaft model, and a method of taking in the stiffness matrix as an FEM model. Regarding the end face displacement of the gear, the analysis results were compared with the actual results for both methods, and a method that takes in an FEM model that has higher correlation with an actual vehicle was employed (Fig. 10).

3.5. Misalignment Analysis Prediction Accuracy

A correlative comparison with measurement was performed regarding the conventional misalignment prediction technology (shaft deflection analysis) and the misalignment prediction technology established by taking into account the above-mentioned boundary condition definition. In contrast to the conventional prediction

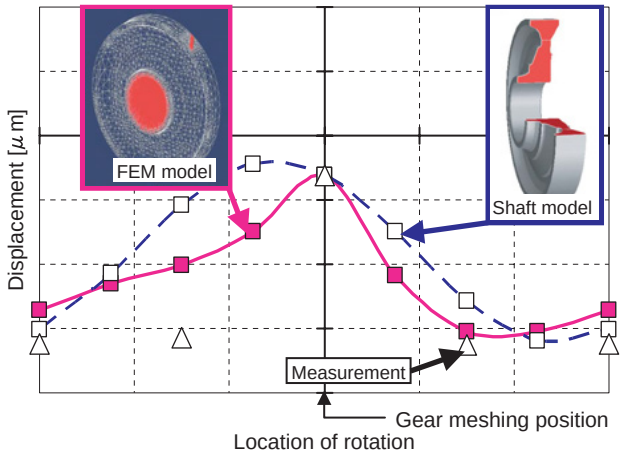


Fig. 10 Displacement of gear rim

technology, which only took into account the stiffness of the shaft, the new technology, established by taking into account the stiffness of the gear itself and the stiffness of the support parts, has enhanced correlation with measurement, and enables the design study accuracy of misalignment to be enhanced (Fig. 11).

3.6. Misalignment Analysis Time

As a method of calculating misalignment, non-linear analysis is also conceivable, but it involves the use of a large scale model, and issues concerning operability and calculation time (convergence) arise, so it can be impractical to use as an everyday design and development tool[5]. Figure 12 shows a comparison of the man-hours that is necessary for modeling and calculating the misalignment for one transmission. A comparison between linear analysis and non-linear analysis (estimated values) was performed based on the modeling and calculation times of the conventional method. In this research, misalignment prediction technology was established using linear analysis.

In contrast to the conventional method, the newly developed method employs assembly analysis, so the modeling and calculation times increase. However, analysis in the assembly condition can be performed in several tens of minutes, and it was confirmed that the new method was a sufficiently practical method, even for everyday design and development, which necessitates calculations of a variety of conditions.

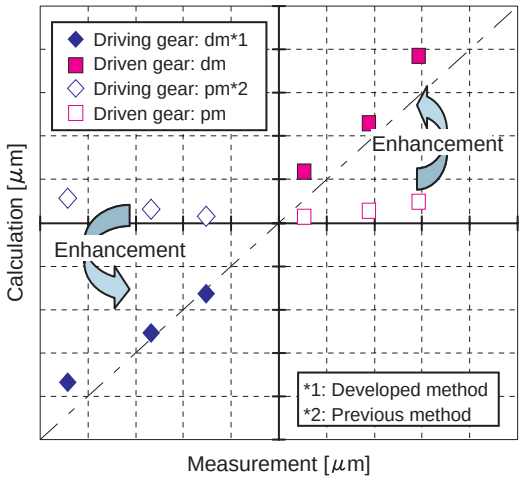


Fig. 11 Comparison of correlation for mesh misalignment

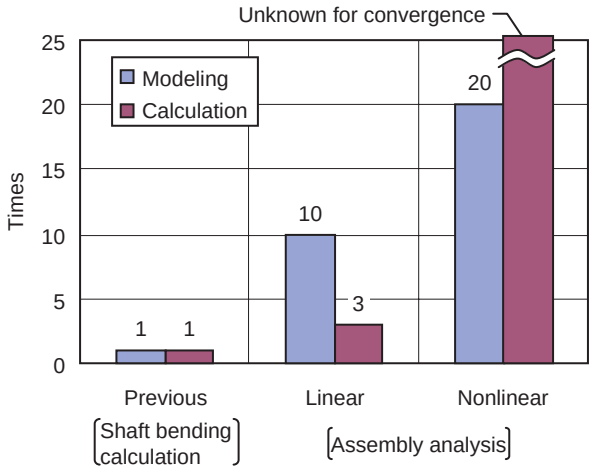


Fig. 12 Required time comparison for prediction of mesh misalignment

4. Actual Vehicle Test Conformity Validation

A gear analyzing program "GRANPLI"[2], which permits the load distribution on the tooth flank when the gears are meshed to be calculated, was used taking into account misalignment and tooth profile, the gear meshing condition was analyzed, and the conformity of the newly developed technology to an actual vehicle test was validated.

4.1. Strength Test Conformity

In the development of transmission Type-A, pitting occurred on the tooth flank of the shift gears. Looking at the tooth flank, it can be seen that there is deviation of contact pattern in the tooth flank.

Regarding the driving gear and the driven gear, the contribution of the driving gear to misalignment is large (Fig. 13). An analysis of the factors responsible for misalignment was performed, and as a result, it was found that clearances and stiffness of the gear (cross-sectional shape) were the important factors (Fig. 14). Changing the clearances due to machining and assembly considerations poses a challenge, so the misalignment was reduced by

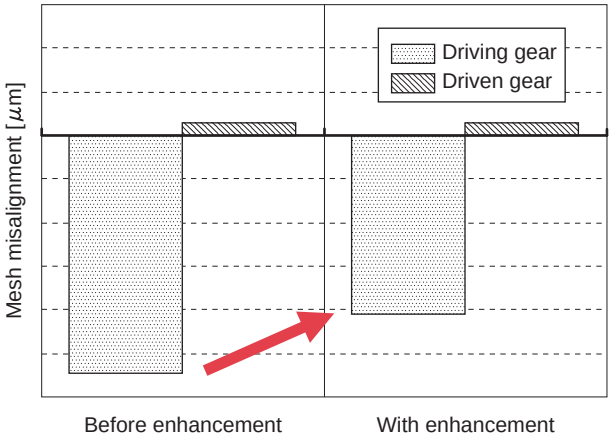


Fig. 13 Contribution rate of mesh misalignment (Driving gear and driven gear)

changing the stiffness of the gear (Fig. 15), and as a result, the tooth flank damage was reduced (Fig. 16).

4.2. Tooth Contact Test Conformity

The function of the transmission gears is to transmit the output force from the engine to the drive wheels. From the viewpoint of marketability, noise vibration during meshing should be kept as low as possible. To this end, meshing should take place smoothly. The test used to check tooth flank meshing is a tooth contact test. The misalignment obtained using the conventional prediction technology (shaft deflection analysis), and the newly established prediction technology, were applied to "GRANPLI," and the calculated tooth flank meshing condition was compared with the actual vehicle tooth contact test results. By applying the misalignment obtained using the newly established technology to "GRANPLI," higher conformity with an actual vehicle was obtained compared to the use of conventional technology (Fig. 17).

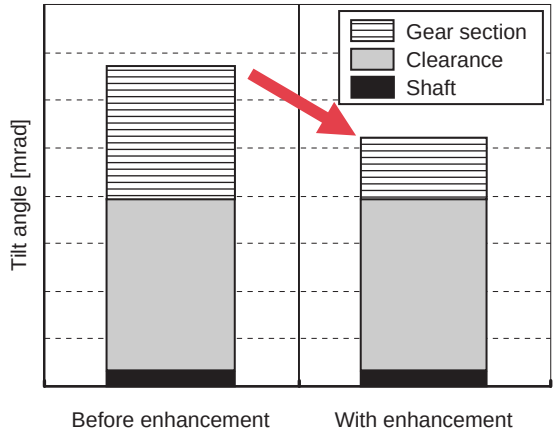


Fig. 14 Contribution rate of driving gear tilt

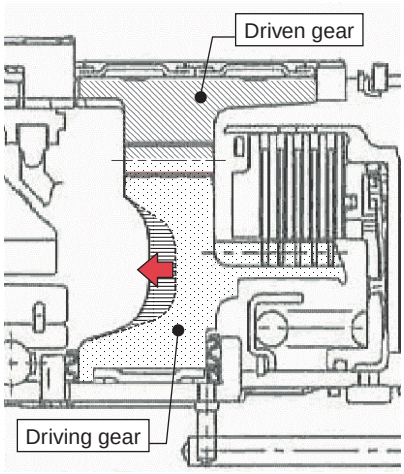


Fig. 15 Enhanced driving gear

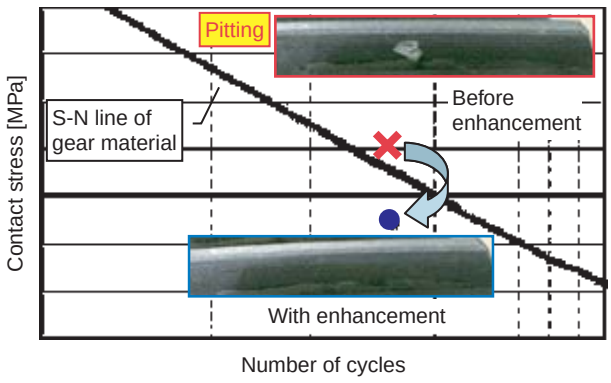


Fig. 16 Enhancement of gear flank damage

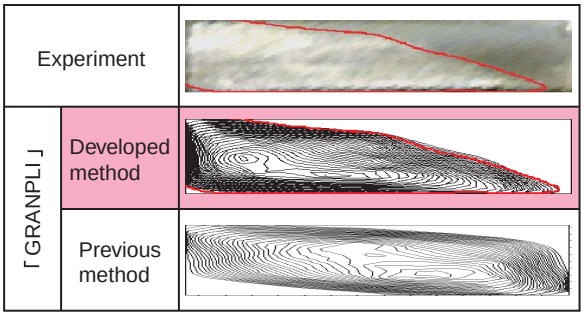


Fig. 17 Comparison of tooth contact patterns

5. Conclusion

Concerning the technology for predicting misalignment that affects gear meshing:

(1) A method that provides results that have a higher degree of correlation with an actual vehicle, as compared to results obtained with the conventional prediction method, was established.

(2) By using linear analysis, results were obtained in a practical calculation time.

Also, the following aspects were confirmed by means of an actual vehicle conformity validation.

(3) By applying misalignment created by the newly established technology to the meshing analysis program "GRANPLI," the design prediction accuracy of the gear strength and tooth contact study was enhanced.

(4) By performing contribution analysis, it was found that the prediction accuracy was adequate for studying effective countermeasures against misalignment.

References

(1) Komori, M., Kubo, A.: Total Optimum Design Method of Involute Helical Gears and Its Support Stiffness, Transactions of The Japan Society of Mechanical Engeneers, Vol. 69, No. 685, p. 265-272 (2003)

(2) Uzuki, C., Hiraoka, M., Nakada, M., Tateno, Y., Mizuno, K.: Application of Helical Gear Tooth-Root Bending Stress Simulation for Automotive Transmission, Honda R&D Technical Review, Vol. 13, No. 1, p. 81-90
(3) Pears, J., Curtis, S., Roberts, S.: Investigation of Methods to Predict Parallel and Epicyclic Gear Transmission Error, SAE Technical Papers, 2005-01-1818 (2005)
(4) Ogata, Y., Suzuki, S., Iijima, Y.: Optimization Method for Reduction of Transmission Housing Weight, Honda R&D Technical Review, Vol. 16, No. 2, p. 103-108
(5) Natsumeda, S.: Computer Simulation Technique for Predicting Performance of Rolling Bearings, NSK Technical Journal, No. 673, p. 31-35 (2002)

Author


Yoshikazu TATENO


Yoshiomi FURUI


Kazuhiro NORITA

Simulation of Stress on Elements of Metal Pushing V-belt for CVT under Transient Operating Conditions

Toshihiro SAITO*

ABSTRACT

The metal pushing V-belt of a torque converter-equipped CVT receives a sudden thrust load from the pulleys when the CVT starts operation, and is required to begin transmitting torque from a stationary state in a very short time span. In the research discussed in this paper, the stress history of the area around the element neck under the transient conditions of CVT start-up was studied using a technology enabling simultaneous simulation of the dynamic behavior of the metal pushing V-belt and stresses on the elements. The results of this study indicated that the load on the V surface of the element is the dominant factor in the generation of stress on the element necks, and that bending stress generated by the pushing force between the elements also acts on the element necks. To confirm the accuracy of the simulation, results were compared with the results of tests conducted to determine the load distribution on the element. The two sets of results demonstrated a good qualitative correlation. This paper also discusses the method employed to evaluate transient stress.

1. Introduction

Against the backdrop of today's intensifying demands for enhanced automotive environmental performance, the CVT is attracting attention from automakers as a transmission type that balances driving performance with high fuel efficiency. In terms of driving performance, CVTs offer quietness and smooth acceleration without shift shock. From the perspective of fuel efficiency, cooperative control between an engine and CVT, to maintain engine speed in the range of higher combustion efficiency, enables the achievement of a level of fuel efficiency surpassing that of an AT. Given this, there will be a requirement to increase the capacity of CVTs in the future[1), 2)]. Figure 1 shows a CVT equipped with a torque converter. When a CVT of this type starts operation, a powerful takeoff characteristic generated by a torque amplification effect is balanced with the smooth and open-ended acceleration characteristic that is particularly associated with CVTs.

Vehicle takeoff represents the most severe condition for a CVT in terms of the maximum input torque transmitted to the drive train. The pulleys and the metal pushing V-belt of a CVT equipped with a torque converter are subjected to a sudden increase in pulley thrust load from a stationary state, and are required to transmit maximum input torque in a minimal amount of time. The most important consideration under these conditions is ensuring the dynamic strength of the metal pushing V-belt. The dynamic strength of the belt is not only determined by the maximum input torque. Consideration must also be given to the ratio and to transient phenomena, such as changes over time in pulley side pressure and pulley speed.



Fig. 1 CVT with torque converter

* Automobile R&D Center

However, while there has been a considerable amount of research on transmission capacity focusing on the sliding characteristic of the metal pushing V-belt and the pulleys when the CVT starts up[3), (4)], almost no studies have considered the dynamic strength of the belt itself[(5)]. This is because it is generally too challenging to measure the dynamic behavior of V-belt and the stress on the elements, parameters that are necessary to judging the strength of the metal pushing V-belt when the CVT is operating[(6)].

A previous research project focused on the dynamic stress generated in the rings when the belt is in operation, and developed a technology to simulate dynamic behavior of V-belt[(3)]. The effect of the stiffness of the pulleys on ring stress has also been studied[(7)]. In addition, a method of calculating the detailed stress on the individual elements using the element contact pressure obtained from simulations of the dynamic behavior of the belt has been developed, and the distribution of element stress across the belt as a whole has been elucidated[(8)]. This paper reports on research that used simulations to elucidate for the first time the stress history on the necks of the belt elements under transient conditions at CVT start-up.

2. Development Goals

Figure 2 shows a cutaway of the main section of a CVT. Drive torque is shifted and transmitted from the drive pulley to the driven pulley by the friction force generated between the belt elements and pulleys. This friction force is generated by the constriction of the belt by the side pressure on the pulleys. The level of stress

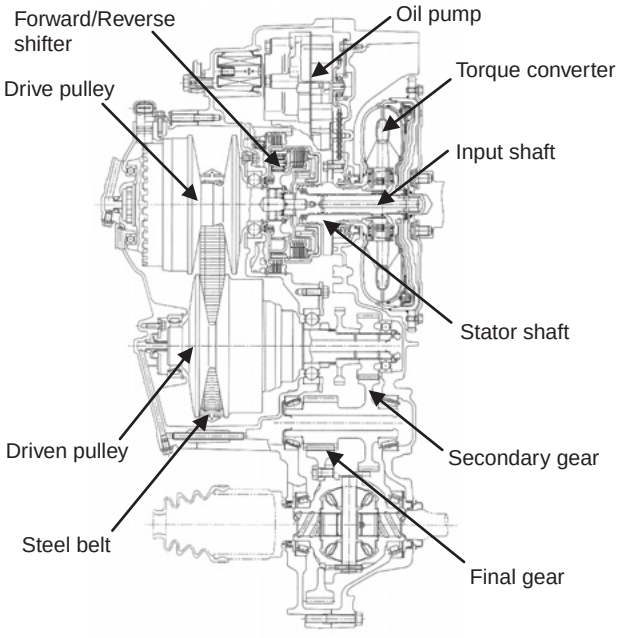


Fig. 2 CVT main section

generated in the rings and elements of the belt when the CVT is in operation is determined by the shift ratio, the side pressure on the pulleys, the belt speed, and the level of transmitted torque[(9)]. The number of repeated loads against fatigue life is known to be lower for the pulleys and elements than that for the rings[(10)]. For this reason, the reduction of impurities in the materials employed in the manufacture of the rings has been adopted as a method of increasing the fatigue strength of metal pushing V-belts[(11)].

However, the increasing requirement to expand the ratio range of CVTs and to employ them in combination with high-displacement engines makes it important to also study the fatigue strength of elements under torque amplification at CVT start-up. The strength of the rings has been increased by the enhancement of materials and application of heat treatments[(12)], and because of this the elements, rather than the rings, have become the source of fractures in durability tests under high load conditions[(13)]. To enable a response to this situation, it is necessary to study the dynamic behavior of the metal pushing V-belt at CVT start-up and the stresses this generates on the elements.

The research discussed in this paper therefore set out to use simulations to quantify the stress history of the elements under transient operating conditions representative of CVT start-up, in order to clarify the level of strength of the metal pushing V-belt.

3. Element Stress Prediction Technology

A simulation technology that enables simultaneous simulation of the dynamic behavior of the belt and stress on the elements, which formed the subject of the previous report, was employed in this project to predict element stress at CVT start-up. This is the standard method of determining element stress, but when studying the dynamic strength of the rings in steady state operation, a considerable amount of calculation time is required in order to gradually increase the rotation of the pulleys from a stationary state to the speed employed in steady state operation. However, this project succeeded in reducing the calculation time to less than half that previously required, by dividing the analytical model of the belt into multiple computational domains to increase computational efficiency, and by focusing on the short period during which the CVT starts up from a state in which the pulleys are stationary.

3.1. FEM Model of Metal Pushing V-belt

The FEM model of the metal pushing V-belt employed in this research is shown in Fig. 3. Two deformable solid elements were used in the direction of thickness of each of the belt elements to enable bending deformation to be reproduced. In addition, the R section of the element neck, where stress is thought to concentrate, was divided into

three deformable solid elements.

However, the nose and hole sections were modeled using rigid elements, because the reproduction of detailed form was the priority in this case. By contrast, each ring layer was modeled using four deformable shell elements in the direction of width, in order to reproduce the crownings. In addition, contact surfaces were defined between the rings and the elements, between each element, between each ring, and between the elements and the pulleys, and appropriate friction characteristics were assigned to each.

3.2. Load Conditions at CVT Start-up

The torque input to the drive train can be divided into torque from the engine and torque from the wheels. Engine torque is considered to be the main torque input to the drive train, but the wheels have also been indicated as contributing a relatively high torque[14]. Care must be exercised in the case of CVTs equipped with torque converters, because the lack of a clutch mechanism on the driven pulley side prevents isolation from wheel torque. Figure 4 shows an example of measurements of changes over time in the load conditions on a metal pushing V-belt at CVT start-up. There is an immediate increase in pulley pressure when the throttle is completely opened, and the torque input to the metal pushing V-belt begins to increase as the pulleys begin to rotate. During this period, the ratio remains LOW. The shorter the response time of the drive train to throttle operation, the more powerful the takeoff of the vehicle will be. Note that in this example it is engine torque that is input to the metal pushing V-belt.

3.3. Stress History of Elements at CVT Start-up

In an actual vehicle, the target ratio is maintained by feedback control of the side pressure on the pulley in which axial thrust is higher. In the simulation method used in this project, the side pressure on the drive and driven pulleys, the speed of the drive pulley, and the torque transmitted to the driven pulley are input as waveforms that change over time. A time history waveform of element stress obtained using this method is shown in Fig. 6. The dotted line shows the forward stress on the rear of the right side of the element neck, and the solid line shows the stress on the same position of the left side of the element neck (Fig. 5). Both waveforms show that maximum stress is generated immediately before the elements reach the exit of the drive pulley.

There is almost no difference in results for right and left, indicating that a symmetrical load acts on the right and left sides of the element neck. Figure 7 shows a comparison of the stress on the front and rear of an element in the direction of forward motion. Until the belt is approximately two-thirds of the distance around the

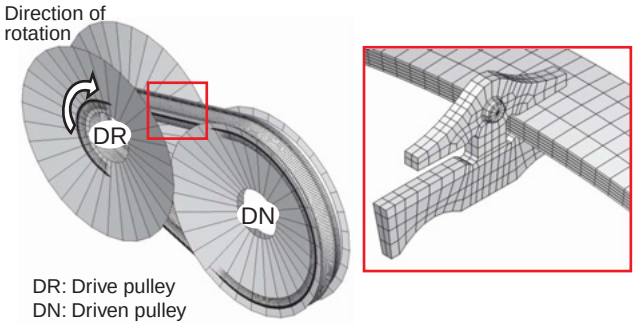


Fig. 3 Belt model defined as flexible bodies

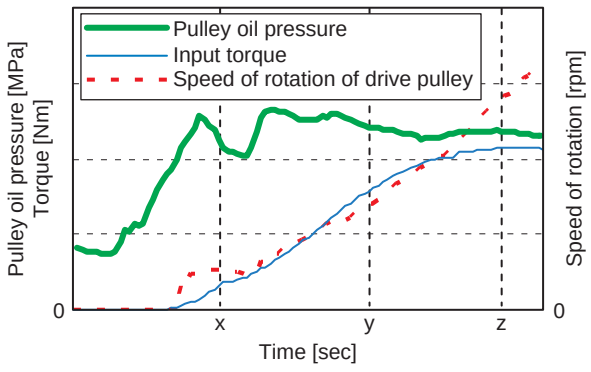


Fig. 4 Load conditions on CVT at start-up

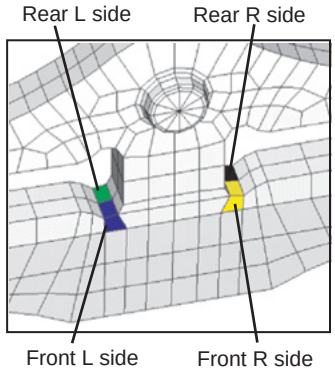


Fig. 5 Evaluation points for element stress

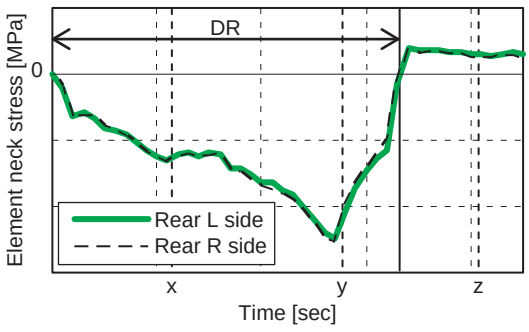


Fig. 6 Time history of element stress

drive pulley, both sides of the element neck are subjected to compression stress, and the absolute value of this stress is identical on both sides. After this, however, differences in the values begin to appear, and there is a change to the tensile stress present on the rear of the elements, immediately after the belt exits the drive pulley. This is considered to be because a pushing force between the elements, which is responsible for transmitting torque, begins to be generated when the elements are one-third of the distance from the pulley exit. The pushing force acts on the front and rear of the elements, but when the belt is wrapped around the drive pulley, it is higher on the front of the elements in the direction of forward motion (Fig. 8). Because of this, the elements display concave bending deformation in the direction of forward motion, and retain this deformation even after exiting the drive pulley (Fig. 9).

3.4. Distribution of Element Stress across the Entire Circumference of the Belt

The previous section focused on a single element, and determined a time history waveform of the stress on the element neck at CVT start-up. A time history waveform of element stress across the entire circumference of the belt can be obtained under steady-state operating conditions, but under the transient conditions of start-up, the elements have only moved a very small distance in relation to the entire belt. Because of this, obtaining the stress distribution of the elements across the entire belt represents a challenge. Figure 10 shows a contour diagram of the stress across the entire circumference of the belt at a specific time. Figure 11 shows the results of extracting the stress on the necks of all the elements. The times used here are x, y, and z in Fig. 4. The results shown in Fig. 11 indicate that the amplitude of stress on the necks is highest before and after the elements exit the drive pulley, and the figures demonstrate a good match with figures for the amplitude of stress in Fig. 7.

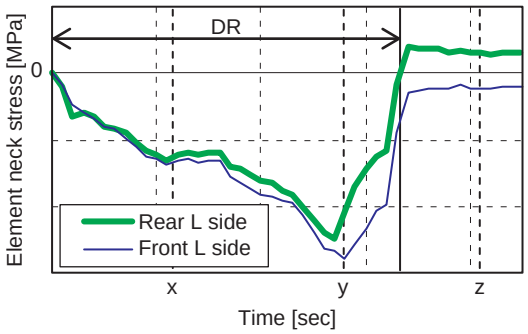


Fig. 7 Comparison of stress on front and rear of element

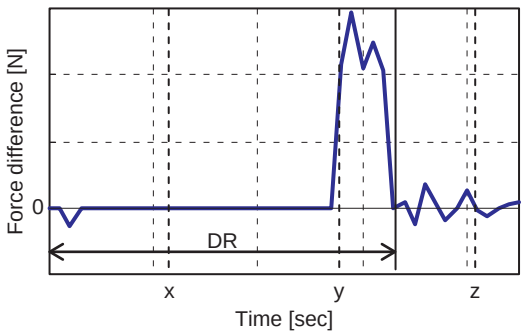
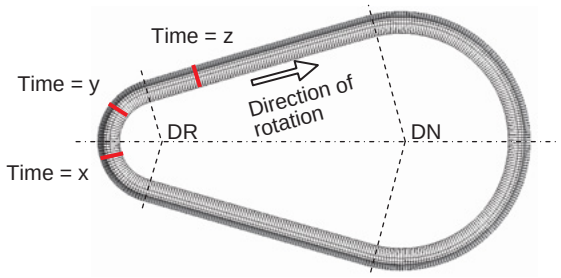


Fig. 8 Force difference between front and rear of element



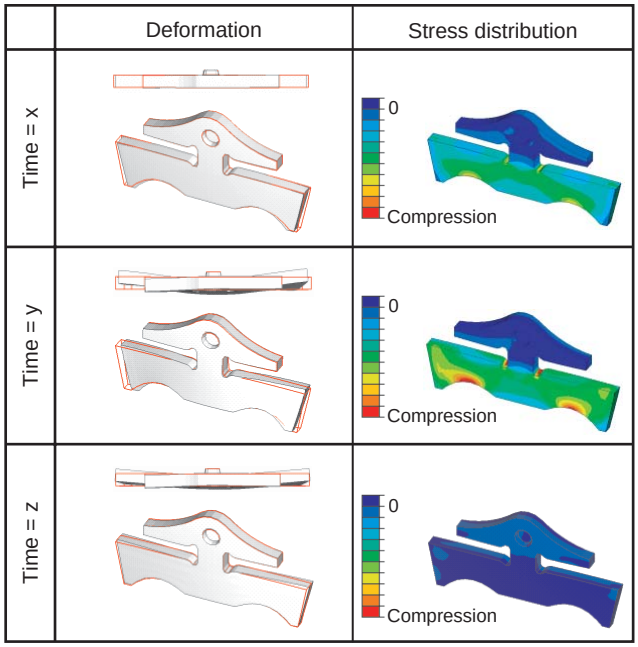


Fig. 9 Deformation of element at start-up

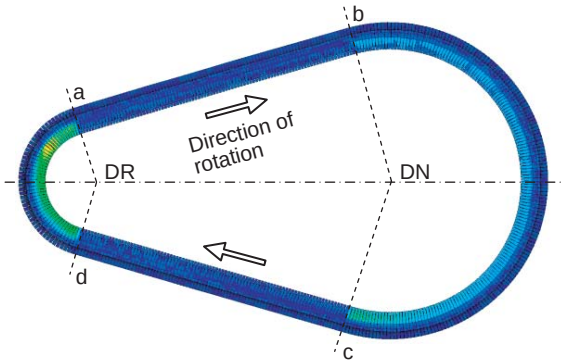


Fig. 10 Element stress distribution

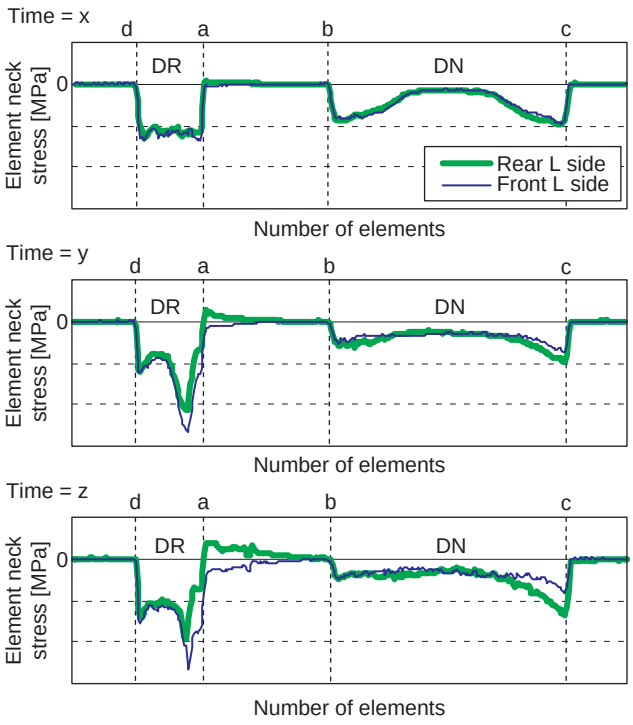


Fig. 11 Instantaneous stress distribution on element neck

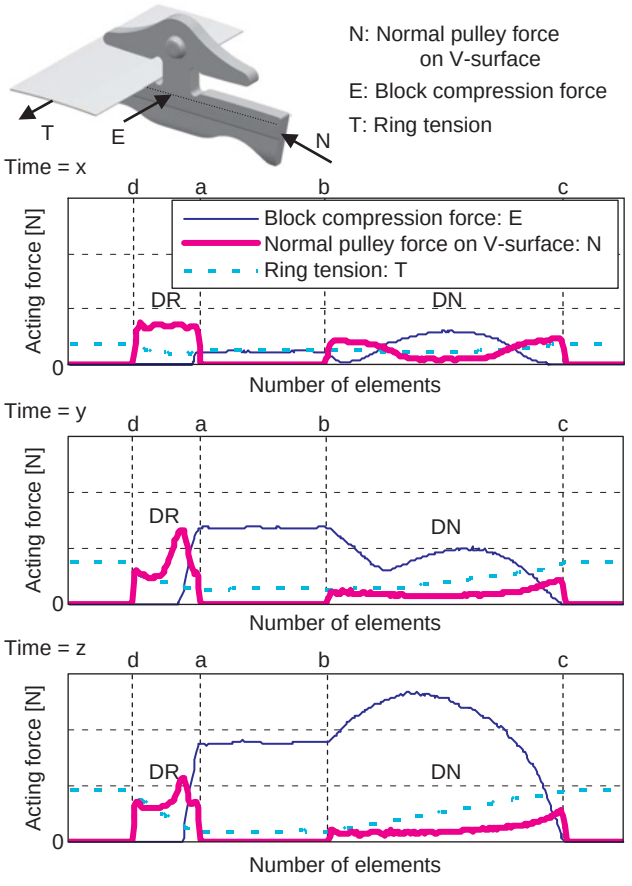


Fig. 12 Instantaneous acting forces across belt

3.5. Mechanism of Generation of Element Stress under Transient Operating Conditions

The torque transmission mechanism was next studied in order to clarify the dominant factors generating element stress. It is known that the torque transmitted by a metal pushing V-belt consists of a component transmitted by the pushing force between the belt elements, and a component transmitted by the difference in tensile force between the rings. Figure 12 shows the pushing force between the elements, the tensile force in the rings, and the distribution of load on the element V-surface under transient operating conditions at start-up. The block pushing force increases with time in section ab. The difference in tension between the rings also increases with time in sections cd and ab, and this contributes to torque transmission.

An examination of the distribution of load on the element V-surface reveals that it is similar to the distribution of element stress shown in Fig. 11. The results also show that element stress changes before and after the point at which the change in the pushing force between the elements is greatest. Given this, it is conjectured that the dominant factor in stress on the element necks is the load on the element V-surface, to which the bending caused by the pushing force between the elements is added.

4. Element Strength under Transient Operating Conditions

Using a vehicle to test the durability of the elements under transient operating conditions would be impractical due to the enormous amount of test time required to repeat the starting and stopping of the CVT. The present project therefore employed durability tests under steady-state operating conditions, with throttle opening as a parameter.

4.1. Element Stress under Steady-state Operating Conditions

Figure 13 shows the stress waveform for the element necks under specific steady-state operating conditions obtained from a simulation.

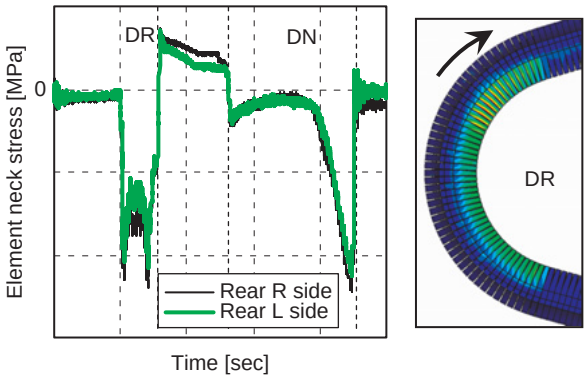


Fig. 13 Element stress in steady-state

4.2. Validation of Element Stress Results

In order to confirm the validity of the figures for element stress obtained from the simulation, they were compared with figures for loads acting on the elements during one revolution of the belt obtained from tests. The elements were additionally machined to increase the sensitivity of test results for loads in specific directions[15]. This made it unable to verify the figures quantitatively, but there was a reliable qualitative correlation between the load distribution in the simulation results and the test results (Fig. 14).

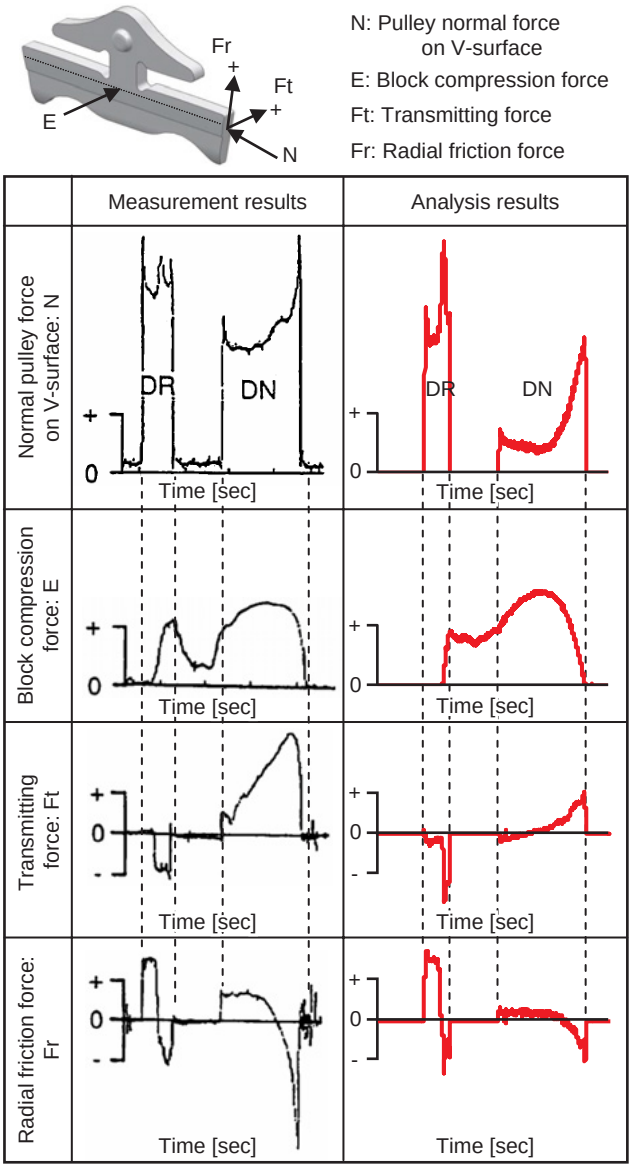


Fig. 14 Comparison of acting forces on element

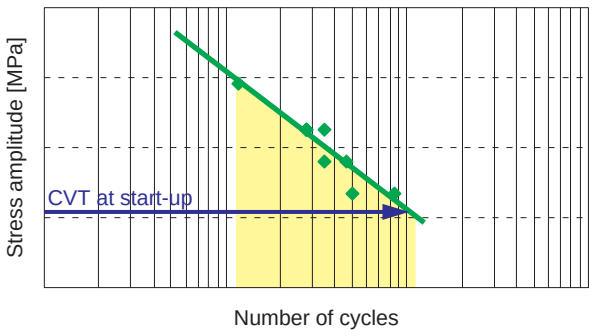


Fig. 15 Stress number diagram

4.3. Level of Belt Strength under Transient Operating Conditions

Figure 15 shows an S-N diagram for the belt, obtained from the results of steady-state durability tests conducted using a LOW ratio under four different load conditions. The vertical axis shows the amplitude of stress on the element necks obtained from the simulation under steady-state operating conditions. The results indicate that there is a correlation between element strength and the amplitude of stress on the necks of the elements. The stress amplitudes from Fig. 11 were superimposed on the S-N diagram as a horizontal line to enable the positioning of the strength of the elements under transient operating conditions to be determined. The point at which the S-N diagram and the horizontal line intersect indicates that the conditions of the present durability test include transient conditions of the type occurring at CVT start-up, and confirm that the metal pushing V-belt possesses sufficient dynamic strength under these conditions.

5. Conclusion

The following results were obtained by applying a technology enabling prediction of element stress in a metal pushing V-belt to transient operating conditions:

(1) At CVT start-up, the maximum stress amplitude on the element necks is generated before and after the drive pulley exit.

(2) The load on the element V-surfaces is considered to be the dominant factor in stress on the element necks, to which bending deformation caused by the pushing force between the elements is added.

(3) An S-N diagram for the neck section of the elements was formulated from the results of simulations and durability tests conducted under steady-state conditions, and the level of strength of the metal pushing V-belt under transient conditions was clarified. This indicates that the method used in this project can also be successfully employed to study the dynamic strength of metal pushing V-belts under transient operating conditions.

6. Afterword

The requirement to increase the transmission capacity of the metal pushing V-belts employed in CVT is today increasing rapidly. The research discussed in this paper has indicated that a simulation can be used to shed light on the stress history of a belt element under transient

operating conditions. It is expected that the accuracy of this method will be increased in the future, and that it will be used to assist in the development of highly responsive high-capacity CVTs.

References

(1) Sato, Y., Urano, J., Ohashi, A., Sakuma, S., Yamaguchi, M.: Development of CVT for 2004 Model Odyssey, Honda R&D Technical Review, Vol.16, No.2, p.87-94

(2) Katoh, Y., Yamashita, H., Kawano, Y.: A Study on the Torque Capacity of Belt CVTs for 2.0-liter and 3.5-liter Front-Drive Cars, JSAE Autumn Convention, No.65-03, p.1-4(2003)

(3) Kobayashi, D., Mabuchi, Y., Katoh, Y.: A Study on the Torque Capacity of a Metal Pushing V-Belt for CVTs, SAE Paper, 980822(1998)

(4) Pennings, B., Drogen, V. M., Hepp, M., Ginkel, V. E., Brandsma, A.: Van Doorne VDT Fluid Test: A Test Method on Belt-Pulley Level to Select Fluids for Push Belt CVT Applications, SAE Paper, 2003-01-3253(2003)

(5) Okada, T., Nozawa, H., Hattori, Y., Tani, H.: Stress Analysis of Metal V-belt Considering Pulley Rigidity, Proceedings of JSAE, No.47-06, p.15-18(2006)

(6) Shimizu, H., Kobayashi, D., Kawashima, J., Katoh, Y.: Development of 3-D Simulation for Analyzing the Dynamic Behavior of a Metal Pushing V-Belt for CVTs, JSAE Spring Convention, No.8-99, p.9-12(1999)

(7) Saito, T., Okano, T.: Application of Metal Pushing V-Belt Stress Simulation with CVT pulley stiffness, Honda R&D Technical Review, Vol.14, No.1, p.191-196

(8) Saito, T., Miyamoto, K.: Application of Technique for Prediction of Stress in Elements of Metal Pushing V-belt by Simulation of Dynamic Behavior, SAE Paper, 2006-01-1307(2006)

(9) Kanehara, S., Fujii, T.: A Study on Power Transmitting Mechanism of Metal Pushing V-Belt, HONDA R&D Technical Review, Vol.7, p.49–67

(10) Pennings, B., et al.: New Push-Belt Design to Increase Power Density of CVTs Featuring a New Maraging Steel, San Francisco, VDI-Verlag(2004)

(11) Yagasaki, T., Aoyama, H., Saito, T., Ishii, K., Okada, Y., Arikawa, M.: Development of Metal Pushing V-Belt for Continuously Variable Transmission, Honda R&D Technical Review, Vol.14, No.1, p.181-190

(12) Sluis, V. D., et al.: Stress reduction in push belt rings using residual stresses, Proceedings of CVT2002 Congress, VDI-Berichte 1709, Munich, p.383-402(2002)

(13) Yagasaki, T., Aoyama, H., Ohnuki, M., Okada, Y., Kataoka, R.: Development of Metal Pushing V-Belt for Continuously Variable Transmission for 2L Class Vehicle, Honda R&D Technical Review, Vol.16, No.2, p.95-102

(14) Yamashita, K., Naruse, T.: Technique for Prediction of Main Input Torque to Drive Train, MAE Technical Report, No.13(2004)

(15) Kanehara, S., Fujii, T., Kitagawa, T.: A Study of a Metal Pushing V-Belt Type CVT - Part 3: What Forces Act on Metal Blocks?-, SAE Paper, 940735(1994)

Author



Toshihiro SAITO

Establishment of Evaluation Method for Riding Comfort of Motorcycle Seats

Mitsue KOYANO* Tsutomu TAKEUCHI*
Takeshi OHARA* Motoharu YOKOI*

ABSTRACT

To enhance the riding comfort of a motorcycle seat, a riding comfort evaluation tester that can reproduce the road vibration felt when the motorcycle is running was designed and fabricated. The riding sensation felt by the rider and the necessary seat vibration characteristics for a motorcycle were determined, and methods were established to enable evaluation of riding discomfort and the dynamic stroke feeling (the motion of the seat cushion, in response to impact from the road). In addition, a 3D mesh cushion made of thermoplastic elastomer, which has the reliable low-frequency vibration characteristics necessary for a motorcycle, was fabricated, and its riding comfort was compared to that of a conventional urethane foam cushion. As a result, it was clearly established that the 3D mesh cushion provides superior dynamic stroke feeling and riding comfort.

1. Introduction

In recent motorcycle development, enhancing the rider's ability to reach the ground and an increase in the number of parts located below the seat has limited the seat cushion thickness, creating concerns over a drop in riding comfort. On the other hand, enhanced riding comfort has a strong appeal for users, and demands are growing for improved performance in this area. New cushion materials that can provide the necessary motion for motorcycles must be developed in order to enhance riding comfort within the limits of seat cushion thickness. Therefore, a dynamic evaluation method that can clearly show the difference in riding comfort performance of the developed cushion materials is also necessary.

Previously, the conventional dynamic evaluation of seats has consisted of dropping dummy buttocks onto seats, or placing the dummy buttocks on seats and applying dynamic input from below to obtain the necessary parameters. In addition, seat dynamic states were measured during actual running, and the obtained parameters were analyzed together with sensory evaluation by rider during actual runs. However, each of these methods presented challenges that needed to be overcome when establishing a correlation with the sensory evaluation. The use of the dummy buttocks allowed repeated measurement under the same conditions, so the parametric accuracy was high, but the evaluation conditions differed from those during actual running. Measuring dynamic seat states under the evaluation conditions allowed parameters to be obtained and sensory evaluation to be performed at the same time, but repeated measurement under precisely the same conditions also presented challenges, so accurate measurement values could not be obtained.

Making the measurement conditions as close as possible to those that exist during actual running was considered an effective means of overcoming these issues. Therefore, an attempt was made to establish a dynamic evaluation method by fabricating a motorcycle riding comfort evaluation tester that can both reproduce the input conditions during running and accurately measure data.

This paper describes the results of comparing a newly developed 3D mesh cushion made of thermoplastic elastomer (hereinafter referred to as "3D mesh cushion") with a conventional urethane foam cushion (hereinafter referred to as "foam cushion"), evaluating riding comfort according to frequency and establishing methods for evaluating the dynamic stroke feeling (the motion of the seat cushion in response to impact from the road) and riding discomfort.

* Motorcycle R&D Center

2. Vibration Characteristics During Actual Running of Motorcycle and Perception by Human Body

2.1. Vibration Characteristics when Riding a Motorcycle

In order to fabricate a riding comfort evaluation tester, longitudinal and vertical acceleration was measured at three locations on the motorcycle during runs at a specified speed on an evaluation road that simulated a public road (Road I). Acceleration was measured on the head pipe, the point at which the rider is seated, and the seat rail behind the passenger. The longitudinal and vertical acceleration was measured at each location. Figure 1 shows the measurement results for vertical acceleration during runs on the evaluation road by various vehicles. The results show that a large input is applied to motorcycles in the low frequency range of 1 to 3 Hz, at which motion of the seat cushion is easily felt. A riding comfort evaluation tester that was able to reproduce this characteristic acceleration was fabricated to dynamically measure and accurately evaluate motorcycle seats.

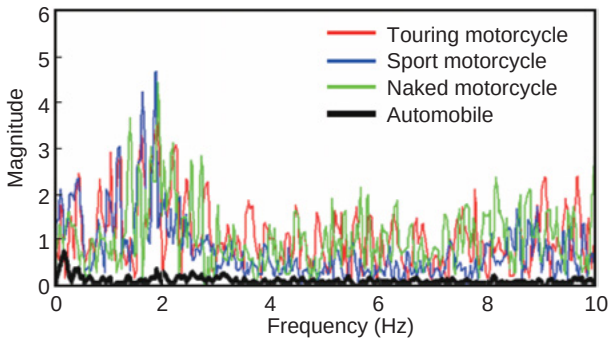


Fig. 1 Fourier spectra of acceleration in road I

2.2. Riding Comfort Evaluation Tester

The riding comfort evaluation tester is a three axis exciter[1] that can reproduce the vertical motions of the front and rear of the seat, and the longitudinal motion of the vehicle body, using acceleration data measured at three locations. Reproducing the motion at these three locations added a pitching motion and longitudinal motion to the vertical striking motion from below the seat. This enabled the buttocks of test subjects to reproduce complex pressing motions on the seat. An actual motorcycle seat, handlebars, foot rests, and a fuel tank were installed on the exciter table, and the seat was measured and evaluated with the test subjects sitting on the seat. Figure 2 shows the test equipment.

2.3. Perception of Motion of Seat Cushion and Sensitivity when Riding Motorcycle

The manner in which the rider experiences seat cushion motion when riding a motorcycle was investigated

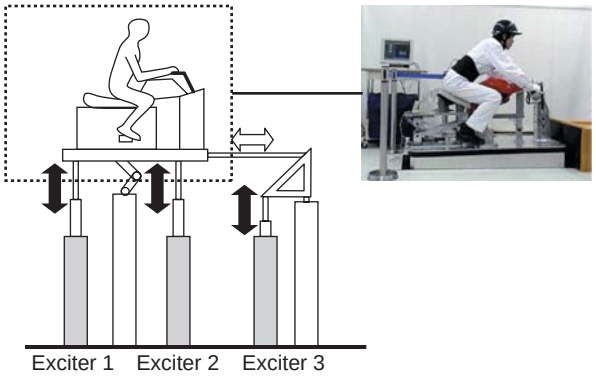


Fig. 2 Dynamic evaluation testing machine for motorcycles

Table 1 Vibration perception level on motorcycle

A: Insensitive to seat vibration
B: Sensitive to seat vibration
C: Indistinct seat vibration at resonating

1: Internal organ resonated
2: Upper body resonated
3: Head resonated

Frequency Hz \ Displacement mm	±5	±10	±20	±30	±40	±50
0.5	A	A	A	A	A	A
1	A	A	B	B	B	B
2	B	B	B	B1	C	C
3	B	B	B	C		
4	B1	B1	B1	C		
5	B1	B2	C	C		
6	B1	C2	C			
7	C2	C2	C			
8	C2	C2				
9	C3					
10	C3					

by having three test subjects with differing body weights ride the riding comfort tester and evaluate the feeling. Seat cushion motion is challenging to interpret in terms of riding comfort at frequencies of 20 Hz or more, so the evaluation range was set as 20 Hz or less. Table 1 shows the sensory evaluation results for the 0.5 to 10 Hz range, which exhibited a particularly large change in how riding comfort was perceived. These results show that riders are sensitive to motion of the motorcycle seat cushion over the range from 1 to 3 Hz, and that large motion of seat cushion in this range was felt to provide excellent riding comfort with a good dynamic stroke feeling. In the 4 to 8 Hz range the seat stroke was not able to be felt as strongly, and the motion of the seat cushion became a source of discomfort to the rider. The large motion of the seat cushion in this range resonated throughout the riders' internal organs and upper body, and was felt as an unpleasant rough vibration. Therefore, it was felt that minimizing the motion of the seat cushion in this range was better for riding comfort. These results indicated that providing appropriate motion in the low frequency range of 1 to 3 Hz and suppressing motion of the seat cushion in the 4 to 20 Hz range are important for enhancing motorcycle riding comfort.

3. Dynamic Performance Evaluation Method

3.1. Evaluation of Dynamic Stroke Feeling

The method investigated as a way to dynamically evaluate seat cushion characteristics consisted of fixing a seat on a jig, dropping dummy buttocks, and measuring the seat cushion displacement when the dummy buttocks struck the seat (Fig. 3). The total of a, b, and c in Fig.3 was obtained as the displacement that expresses the dynamic stroke feeling, or the amount of motion of the seat cushion in response to shocks from road. Sensory evaluation of the dynamic stroke feeling was performed by locating a suitable road surface allowing low frequency from 1 to 3 Hz (Road II), and performing an evaluation according to the scale given in Table 2. Figure 4 shows the correlation between the total of displacements a, b, and c and the sensory evaluation. A somewhat weak correlation was confirmed, but it is not sufficient for practical use.

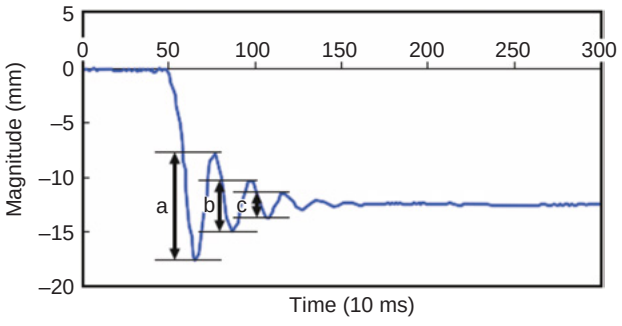


Fig. 3 Displacement data in dummy hip drop test

Table 2 Evaluation scale for dynamic stroke feeling

Score	Definitions
5	Extreme feeling
4	Fair feeling
3	Moderate feeling
2	Somewhat felt
1	Slight feeling

The displacements that represent the dynamic stroke feeling on the newly developed riding comfort evaluation tester were investigated as follows. A motorcycle was run over the Road II to evaluate dynamic stroke feeling, and the data from accelerometers attached to the chassis in three locations was measured. The acceleration at these three locations was reproduced on the riding comfort evaluation tester, and vertical acceleration of the seat was measured with test subjects weighing 70 kg riding the tester, and the displacement of the seat cushion was calculated (Fig. 5). Sensory evaluation was performed at

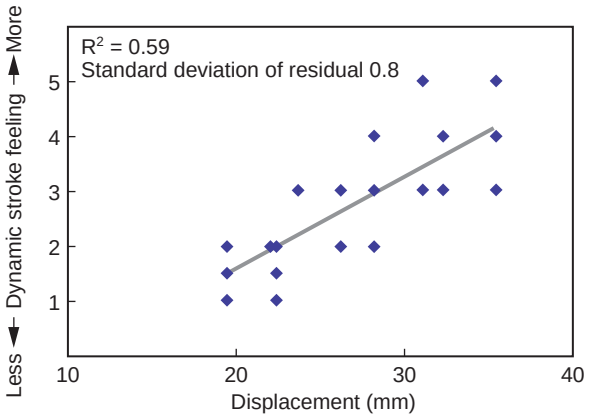


Fig. 4 Relationship between total displacement of dummy hip drop test and dynamic stroke feeling

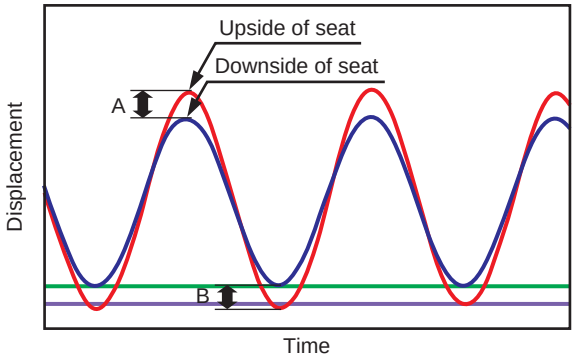


Fig. 5 Displacement data in road II

the same time, and three test subjects each weighing 70 kg evaluated the dynamic stroke feeling according to the scale given in Table 2. The parametric analysis was limited to the low frequency range of 1 to 3 Hz, data sections suitable for analysis were extracted, and parameters such as the total displacement and phase difference were obtained. The correlation between these parameters and the sensory evaluation results was highest for the total of displacements A and B, shown in Fig. 5. Figure 6 shows the relationship between the total of displacements A and B and the dynamic stroke feeling. The total of displacements A and B and the dynamic stroke feeling exhibit a high correlation, and it can be inferred that the test subjects are evaluating the difference in seat cushion motion relative to the input under these conditions.

3.2. Riding Discomfort Evaluation Method

The parameters that represent riding discomfort on the riding comfort evaluation tester were investigated as follows. A motorcycle was run over a road that easily produces unpleasant vibrations (Road III), and the data from accelerometers attached to the chassis in three locations was measured to evaluate the range of riding discomfort. The acceleration at these three locations was reproduced on the riding comfort evaluation tester, and vertical accelerations of the upside and downside of the seat were measured with test subjects weighing 70 kg riding the tester. Sensory evaluation was performed at the same time, and three test subjects, each weighing 70 kg, evaluated the dynamic stroke feeling according to the scale given in Table 3. Degree of riding discomfort is determined by evaluating a wide of range of frequencies felt by the human body, so the magnification factor for the 5 to 20 Hz range was obtained, and the magnification factor tendencies were compared for various seat cushion materials (Fig. 7). The magnification factors differ somewhat, but they exhibit similar tendencies at each frequency. Therefore, area S, the integration value of the magnification factor for the 5 to 20 Hz range, was used as the parameter expressing the riding discomfort evaluation. This parameter is expressed as an area, raising the issue that magnitude of the magnification factor becomes an average. However, the results shown in Fig. 8 confirm that there is sufficient correlation between sensory evaluation and magnification factor area S, so it was judged that this parameter can accurately express riding discomfort.

Table 3 Evaluation scale for dynamic comfort quality

Score	Definitions
5	Very comfortable
4	Slightly comfortable
3	Acceptable
2	Slightly uncomfortable
1	Very uncomfortable

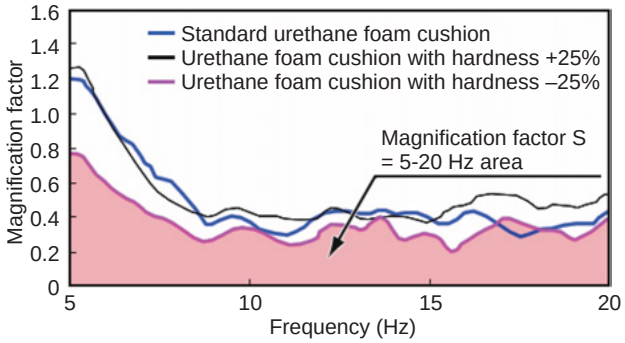


Fig. 7 Magnification factor in road III

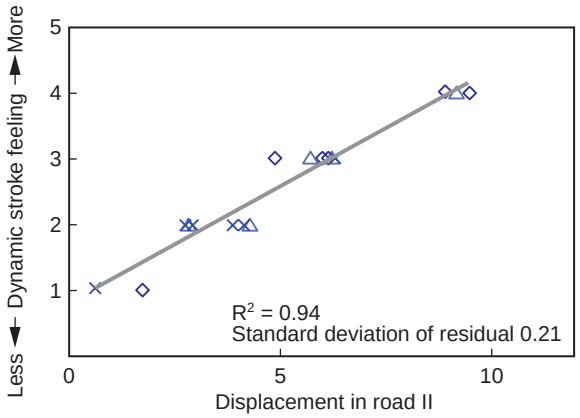


Fig. 6 Relationship between displacement and dynamic stroke feeling in road II

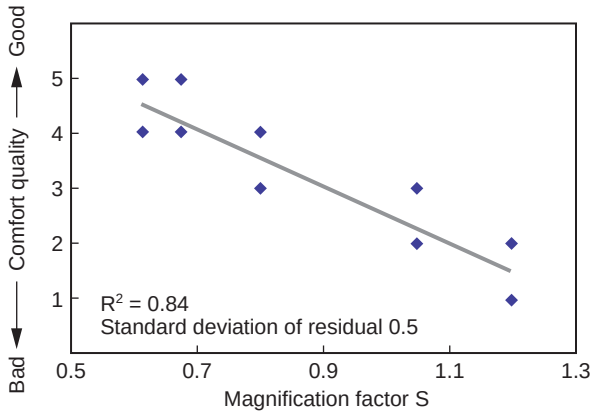


Fig. 8 Relationship between magnification factor S and comfort quality in road III

4. Comparison of 3D Mesh Cushion and Foam Cushion Performance

4.1. 3D Mesh Cushion Characteristics

The cushioning characteristics of cushion materials change according to the combination of materials and their density, so it is important to determine the proper cushion characteristics in accordance with the concept of a motorcycle. Decreasing the hardness of conventional foam cushions can produce low frequency motion, but these characteristics are not maintained over long-term use. The foam cushion loses its resiliency, which has significant adverse effects, such as an unchanging body pressure distribution. This makes it necessary to make the cushion so hard that it provides insufficient motion at low frequencies. The low rebound materials used in recent years provide superior shock absorption and body pressure dispersion, but when subjected to a load, these materials lose resiliency and are unable to produce the seat cushion motion necessary for motorcycles. The 3D mesh cushion that was the focus of this study uses thermoplastic elastomer materials, and diverse cushion characteristics can be set by changing the material, density, wire diameter, intermingling point density, and other factors. The residual strain in compression under high temperatures and repeated hardness changes, which have been weak points for thermoplastic elastomers, were modified for this newly developed 3D mesh cushion, and the material specifications were set to realize the required characteristics. Test pieces of the same size and hardness, without the seat fabric, were fabricated from conventional foam cushion and the newly developed 3D mesh cushion, to investigate the ability of the 3D mesh cushion to enhance the dynamic stroke feeling. The vibration characteristics of these test pieces were measured in conformity with JAS0 B 407-87; the test results are shown in Table 4. The 3D mesh cushion has a lower resonance frequency and a higher magnification factor, and exhibits similar effects to decreasing the hardness of the conventional foam cushion. Therefore, it was assumed that the 3D mesh cushion can provide a superior dynamic stroke feeling while maintaining the same hardness as the foam cushion.

4.2. Evaluation Results of Dynamic Stroke Feeling

In the following experiment, a 3D mesh cushion with a foam cushion upper layer was compared with a conventional foam cushion having the same upper surface shape. Figure 9 shows the structural diagram.

The riding comfort evaluation tester was used to quantitatively evaluate the dynamic stroke feeling enhancement effects of the 3D mesh cushion by reproducing the accelerations measured in test runs on Road I (see Section 3.1) and measuring the total of displacements A and B. Figure 10 shows the results of comparing the total of displacements A and B for the 3D

Table 4 Characteristics of vibration by test piece

	Foam cushion	3D mesh cushion
Resonance frequency (Hz)	6.10	5.41
Magnification factor of resonance	3.82	4.62

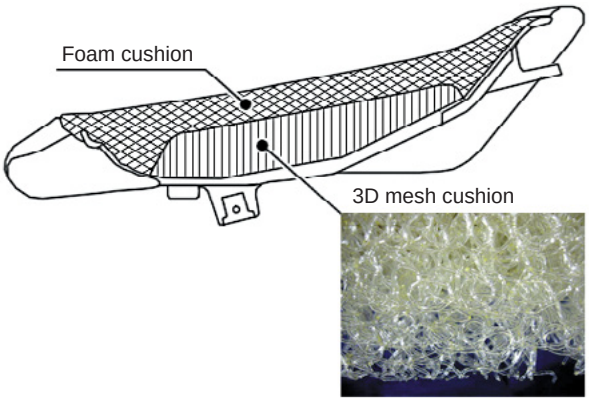


Fig. 9 Structure of new seat with 3D mesh cushion

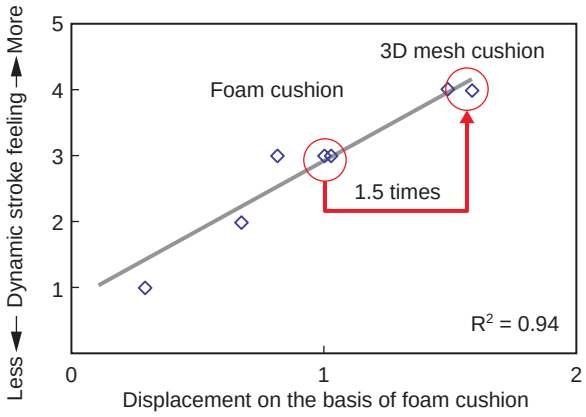


Fig. 10 Relationship between displacement and dynamic stroke feeling

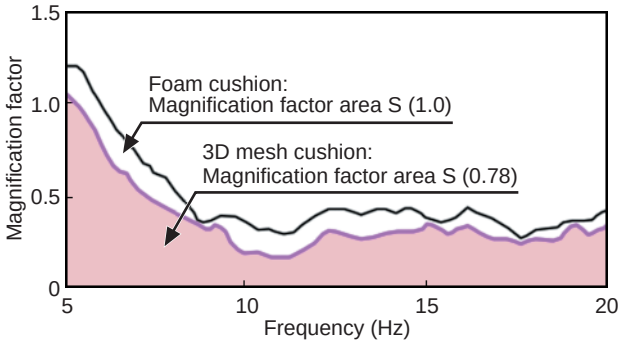


Fig. 11 Magnification factor of 3D mesh cushion and foam cushion in road III

Table 5 Verification results of dynamic stroke feeling and discomfort evaluations in actual driving

Dynamic stroke feeling evaluation

	Expectancy	Actual measurement	Residual
3D mesh cushion	4.2	4.0	0.2
Foam cushion	3.5	3.7	– 0.2

Discomfort evaluation

	Expectancy	Actual measurement	Residual
3D mesh cushion	3.9	4.2	– 0.3
Foam cushion	2.9	3.3	– 0.4

* Displacement: bench mark is foam cushion
* Magnification factor S: bench mark is foam cushion

mesh and foam cushions. Here, the displacement for the 3D mesh cushion was confirmed to be 1.5 times that of the foam cushion. This indicates that the 3D mesh cushion provides a noticeable enhancement in the dynamic stroke feeling, and that the material specifications are appropriate.

4.3. Evaluation Results of Riding Discomfort

The riding comfort enhancement effects of the 3D mesh cushion were quantitatively evaluated by using the riding comfort evaluation tester to reproduce an uncomfortable road vibration as described in Section 3.2, measuring the seat vertical acceleration, and obtaining magnification factor area S. Figure 11 shows that the magnification factor area S of the 3D mesh cushion is 22% less than that of the foam cushion, which clearly establishes that the 3D mesh cushion effectively reduces riding discomfort.

5. Verification Results by Actual Running

The dynamic stroke feeling and riding discomfort evaluation results obtained using the riding comfort evaluation tester were verified by having three test subjects ride motorcycles on Road III to evaluate the dynamic stroke feeling and riding discomfort experienced with the two types of cushions. Past experimental results[(2)] showed that the variance in sensory evaluation was approximately 0.3 to 0.7 points, so the expected value target was set within ±0.5 points or less; Table 5 shows the expected values and measured values (test subject average values) for the 3D mesh cushion and foam cushion. The residual was within ±0.5 points, which confirmed that this is a valid method of evaluating dynamic stroke feeling and riding discomfort.

6. Conclusion

A dynamic seat evaluation method using a motorcycle riding comfort evaluation tester was established, and the difference in performance between a 3D mesh cushion and foam cushion was clarified quantitatively.

(1) A riding comfort evaluation tester was used to establish a riding comfort evaluation method that divides the evaluation into the dynamic stroke feeling domain and riding discomfort domain.
(2) A motorcycle riding comfort evaluation tester was used to find the low frequency motion of seat cushion necessary when riding a motorcycle. This enabled the development of a 3D mesh cushion of thermoplastic elastomer that provides a superior dynamic stroke feeling.
(3) It was clearly established that the newly developed 3D mesh cushion increases displacement, which represents the dynamic stroke feeling, by 1.5 times and reduces the magnification factor area, which represents riding discomfort, by 22%, compared to the foam cushion.

Acknowledgements

The authors wish to express their deep thanks to everyone at NHK Spring Co., Ltd. for their immense cooperation with this development project.

References

(1) Harashima, S., Shinomiya, K., Takahashi, H., Kadota, M., Yasuda, K.: Development of Multi-Use Road Simulator, HONDA R&D Technical Review, Vol. 3, p. 153-162
(2) Koyano, M., Kimishima, T., Nakayama, K.: Quantification of Fitness Feeling of Motorcycle Seats, HONDA R&D Technical Review, Vol. 12, No. 2, p. 113-118

Author


Mitsue KOYANO


Tsutomu TAKEUCHI


Takeshi OHARA


Motoharu YOKOI

Image Fusion for Night-time Pedestrian Recognition Assistance

Junji EGUCHI* Izumi KONDO* Hiroyuki KOIKE*

ABSTRACT

Fusion images have been generated by combining near infrared images of road areas and far infrared images in order to reduce vehicle-pedestrian accidents at night. In past studies, fusion images were generated by combining the entire area of near infrared images and far infrared images, which resulted in image information unnecessary for pedestrian recognition being fused, such as street illumination and the headlights of oncoming vehicles. It might be achievable to enhance efficiency in providing visual driving assistance by reducing these influences. The current research applied gradation processing to combine only the road area of near infrared images and far infrared images, and generate partial fusion images that primarily provide pedestrian and road area information. The effectiveness of this type of fusion image in providing visual assistance was compared to that of other image types in a volunteer test. Increased accuracy in identifying the location of pedestrians was shown when the new images were employed.

1. Introduction

Road accident statistics indicate that night-time accidents account for approximately 70% of all pedestrian fatalities every year in Japan, and that the leading cause of these accidents is delay in recognition of pedestrians by vehicle drivers[1]. The development of a visual driving assistance system that would help assist drivers to recognize pedestrians at night has been suggested as a means of reducing the incidence of these accidents. Up to the present, research has focused on visual driving assistance systems that detect pedestrians at night and make the driver aware of their presence[2, 3]. The effect of visual driving assistance could be further increased by adding to these functions the presentation of images to make the driver visually aware of the presence of the pedestrian prior to the operation of the detection function.

When a visual driving assistance system displays images to a driver, a process commences in which the driver becomes aware of the presence of a pedestrian and its position by comparing the image with the actual road environment. The road area information such as the shape of the road and the position of the white lines is considered important in assisting drivers to detect the presence of pedestrians and to identify their position at night from the image. It is therefore helpful to present image information on pedestrians and the road simultaneously. The use of far infrared camera images that map the temperature distribution of the human body is useful in making drivers aware of pedestrians at night[2]. However, it is challenging to obtain information on the environment including the road surface using a far infrared camera.

In this case, it is necessary to use near infrared cameras suited to imaging of the environment at night[4]. The combination of these two types of images to generate fusion images would enable two types of image information to be presented in the form of one single image. Herrington et al. have proposed a method of image fusion in the frequency domain for the entire road area to create these fusion images[5].

In order to enhance the effectiveness of visual driving assistance systems in assisting driver's recognition of the presence of pedestrians at night, the current research studied a partial image fusion method that uses only limited information required for recognition of the presence and position of a pedestrian, relative to the conventional method that formed fusion images using information from the entire road environment. The method proposed by Herrington et al. uses the Discrete Haar

* Automobile R&D Center

Wavelet Transform to generate a fusion image that shows the entire road environment at night as comparatively bright. However, because the area around the pedestrian is also made brighter, the pedestrian may become correspondingly harder to identify, thereby reducing the accuracy of pedestrian recognition. For this reason, pedestrian recognition at night requires image information to possess contradictory characteristics: The area around the pedestrian should be comparatively dark, while the entire road area should be displayed brightly. Similarly, it is also necessary to reduce light noise such as the headlights of oncoming vehicles that may cause halation in images and consequently make it harder to identify pedestrians. This paper therefore proposes a method of formulating partial fusion images that combine only the road area by applying gradation processing to near infrared images that contain the road area information required for the recognition of pedestrians at night. The results of verification of the effectiveness of this method in providing visual driving assistance will also be discussed.

2. Formulation of Fusion Images using Gradation Processing

2.1. Issues in Conventional Method

Figure 1 shows an example of the generation of a fusion image using the method employed by Herrington et al. This fusion image is generated using the entire road environment (termed an "all area fusion image" below), and in some cases, these images may not provide sufficient visual assistance for pedestrian recognition due to the saturation of the brightness of the image caused by environmental light and light noise. The following two examples can be indicated:

(1) Environmental light: Areas close to city streetlights [Fig. 2(a)]
(2) Light noise: The headlights of oncoming vehicles [Fig. 2(b)]

As shown in Fig. 2(a), pedestrian recognition could be challenging when the light from streetlights is combined with the pedestrian image. As can be seen in Fig. 2(b), when the light from the headlights of oncoming vehicles directly enters a near infrared camera, it may be shown in the fusion image as close to the upper limit for image brightness and cause halation.

With regard to the illumination from streetlights, a method may be considered in which only the road area of the near infrared image is isolated and combined with a far infrared image. However, this would have a minimal effect in reducing halation, because the headlights of oncoming vehicles would also be shown brightly in the image due to reflection from the surface of the road and other factors. In addition, there would be a significant variation in brightness between the areas near the boundary of the road area, which would produce a sense of visual incongruity. For these reasons, this research applied gradation processing to near infrared images in

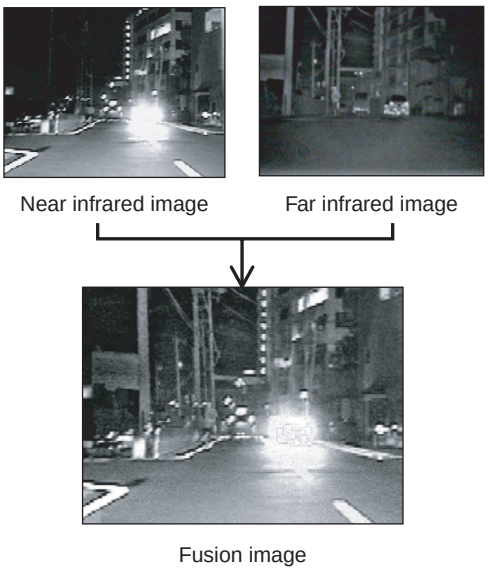


Fig. 1 Fusion image



(a) Surrounding illumination (b) Headlights of oncoming vehicle

Fig. 2 Examples of halation in all area fusion image

order to create fusion images with reduced halation that combined only the road area.

2.2. Gradation Processing

A gradation processing was established in which the brightness of the areas of a near infrared image other than the area to be fused (the "fusion area") was attenuated to 0. Figure 3 shows an image of the process. The boundary value y_b is used to determine the fusion area. The brightness value $I(x, y)$ is multiplied by the gradation coefficient $G(y)$ to determine a new brightness value, $I_g(x, y)$ [Eq. (1)]. The gradation coefficient $G(y)$ attenuates brightness in such way that the brightness value of a pixel is closer to 0 for the pixel closer to the boundary of the fusion area, $y = y_b$ and all the pixels beyond the boundary are given the brightness value of 0 [Eq. (2)]. The process of attenuation is more gradual for higher gradation gain. When a fusion image is generated, the use of high gradation gain reduces discrepancies in brightness that occur near the boundary of the fusion area, $y = y_b$. However, the near infrared image becomes darker overall, and the amount of information from the near infrared image incorporated in the fusion image declines. This makes it important to select the level of gradation gain appropriate to the environment. Below, fusion images generated using gradation processing will be termed "gradational fusion images."

$$I_g(x, y) = I(x, y) \cdot G(y) \qquad (1)$$

$I(x, y)$: Brightness value of near infrared image at coordinates (x, y)
$I_g(x, y)$: Brightness value of near infrared image at coordinates (x, y) following gradation processing
$G(y)$: Gradation coefficient

$$G(y) = 1 - 1/\exp(A \cdot (y - y_b)) \quad (y \le y_b)$$
$$G(y) = 0 \quad (y > y_b) \qquad (2)$$

y_b : Boundary value of fusion area in y-axis
A : Gradation gain, $(A \ge 0)$

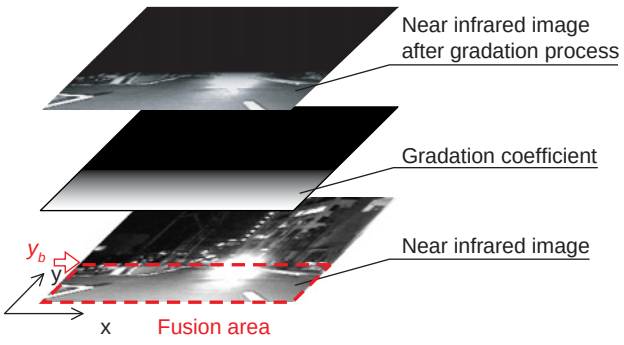


Fig. 3 Gradation process

3. Verification Test for Effectiveness of Gradational Fusion Image

Gradational fusion images were generated using a far infrared camera and a near infrared camera mounted on a real vehicle to verify the effectiveness of the images in visual assistance. Figure 4 shows the system layout used in the test. A far infrared camera was set up at the front of the test vehicle, with a near infrared camera also positioned on the vehicle. An image processing unit generated fusion images from the images obtained by these cameras, which were then presented to the driver on a head-up display (HUD). The size of the images from both the far infrared and near infrared cameras was 640 x 480 pixels. The procedure employed to generate the gradational fusion image is shown in Fig. 5. Following application of gradation processing to the near infrared images, the images were fused in the frequency domain using the Discrete Haar Wavelet Transform.

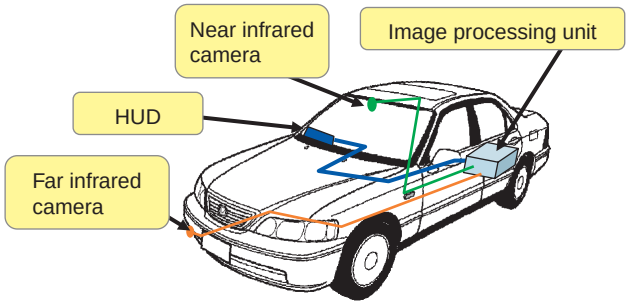


Fig. 4 System layout

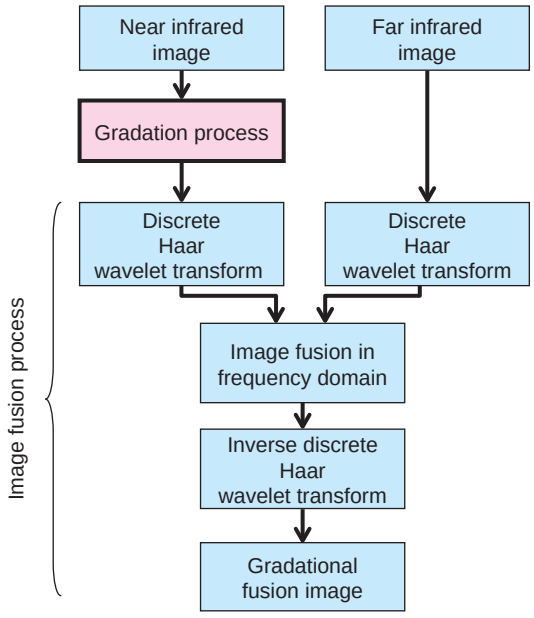


Fig. 5 Flow of construction of gradational fusion image

3.1. Effectiveness of Gradational Fusion Image

Figures 6(a) and 6(b) show a comparison of fusion images with and without gradation processing. In Fig. 6(a), gradation gain was set at 0, resulting in the generation of a partial fusion image using only the road area, without gradation processing. By contrast, Fig. 6(b) shows a gradational fusion image generated using a gradation gain of 0.05. In both cases, the boundary value of the fusion area (y_b) was set at 180. As the graph in Fig. 7 indicates, in the gradational fusion image shown in Fig. 6(b), the gradation coefficient becomes progressively smaller as the y-coordinate of the pixel approaches y_b(80 < y < 180), and reaches 0 when it becomes greater than y_b. By contrast, in the partial fusion image shown in Fig. 6(a), the gradation coefficient does not change progressively, simply changing from 1 to 0 when the fusion image boundary, y_b, is crossed.

As discussed above, the verification of the effectiveness of the images in assisting the driver to recognize the position of the pedestrian focused on the road information and brightness around the pedestrian. In both the partial fusion image with only the road area combined [Fig. 6(a)] and the gradational fusion image [Fig. 6(b)], road information, such as the white lines, is shown together with the image of the pedestrian. In addition, the area around the pedestrian is shown as comparatively dark in both images. This indicates that the effectiveness of the two images is identical in terms of assisting pedestrian position identification, whether or not gradation is employed.

With regard to the headlights of oncoming vehicles, in the partial fusion image (Fig. 6(a)), the lights in the road area are shown as bright, without reduction of halation. In the gradational fusion image (Fig. 6(b)), however, the brightness of the lights in the road area has been attenuated, and halation has therefore been reduced. This indicates that gradation processing is effective in reducing halation.

3.2. Comparison with Images Generated Using Conventional Methods

Figure 9 compares a far infrared image, a near infrared image, an all area fusion image, and a gradational fusion image. All images were created for the road scene described in Fig. 8. The far infrared image [Fig. 9(a)] allows recognition of the presence of the pedestrian, while the position of the pedestrian is challenging to identify due to the lack of road information such as the white lines. Although the near infrared image [Fig. 9(b)] contains relatively plenty of road information, the headlights of the oncoming vehicle and the surrounding illumination such as streetlights could cause halation, making it challenging to identify the presence of the pedestrian. The all area fusion image [Fig. 9(c)] that fused the entire area of these images allows recognition of the presence and position of the pedestrian. However, the effect of the environmental



Fig. 6 Comparison of partial fusion image and gradational fusion image

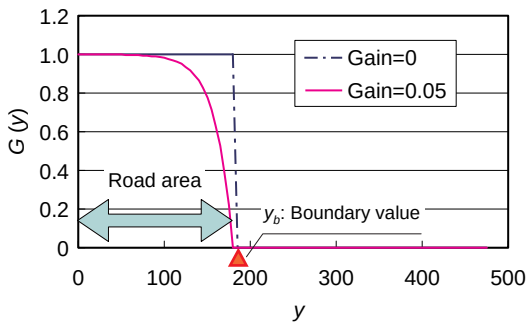


Fig. 7 Gradation coefficient G (y)

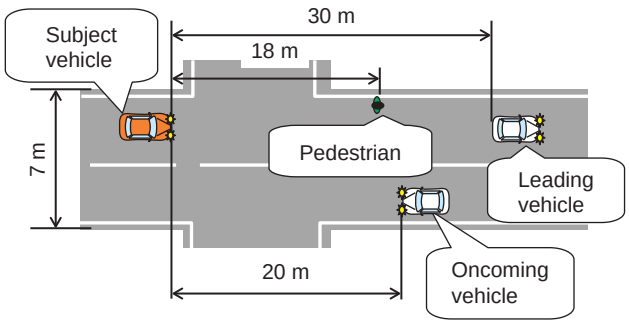
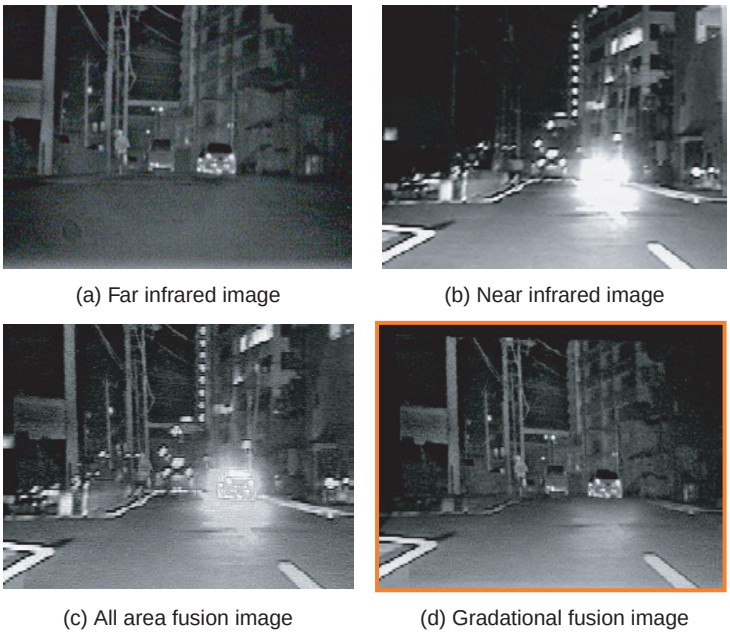


Fig. 8 Road scene



(a) Far infrared image (b) Near infrared image

(c) All area fusion image (d) Gradational fusion image

Fig. 9 Comparison of images

light and light noise is still an issue with this image. Compared to these three images, the gradational fusion image [Fig. 9(d)] is with reduced halation due to the surrounding illumination and the headlights of the oncoming vehicle. Given these results, it is anticipated that the gradational fusion images are more effective in providing visual assistance for the recognition of pedestrians than the other image types.

4. Verification Tests for Effectiveness of Visual Assistance with Test Subjects

Tests were conducted with test subjects in order to verify the effectiveness of the gradational fusion images in providing visual assistance for accurately identifying the position of pedestrians.

4.1. Test Method

4.1.1. Test device

It was desirable to verify the effectiveness of the gradational fusion images in providing visual assistance under conditions close to those encountered in actual driving environment. The simulator shown in Fig. 10, a mock-up of the driver's seat of a real vehicle, was constructed based on this requirement. A HUD positioned above the instrument panel in front of the driver was used to display images for visual driving assistance. A screen was set up in front of the driver's seat, and the images of driving environments shot using an ordinary video camera were displayed in order to simulate actual driving conditions.

4.1.2. Test procedure

The effectiveness in providing visual driving assistance was compared by showing either of the far infrared images or gradational fusion images on the HUD shown in Fig. 10 (a), and measuring the time to detect the pedestrian position. Ten different images covering different scenes were prepared. From among these images, the simulator randomly selected the one to be displayed. Alarms were used to notify the test subjects that images would be displayed. The amount of time spent looking at an HUD changes with the actual driving load, becoming shorter as the driving load increases. The following image

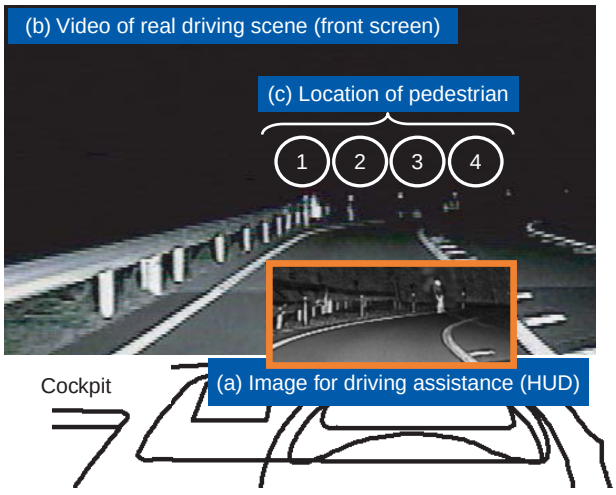


Fig. 10 Outline of experimental set-up

display times were employed in order to reproduce this situation:

High driving load: 0.3 sec

Medium driving load: 0.5 sec

Low driving load: 1.0 sec

To quantify the effectiveness of the two types of images in providing visual driving assistance, the road scene displayed on the screen shown in Fig. 10 (b) were divided into four areas [Fig. 10 (c)]. Each test subject was asked to identify the area in which the pedestrian was located for each image display time, and the percentage of correct answers was calculated.

4.2. Test Results

Test subjects consisted of six men and one woman ranging in age from their 20s to 40s. Figure 11 shows the percentage of correct answers for each test subject and image display time. All test subjects, with the exception of one (subject e at a display time of 1.0 sec), produced a higher percentage of correct answers for gradational fusion images than for far infrared images. Figure 12 shows a comparison of the percentage of correct answers for gradational fusion images and far infrared images for each display time. The percentage is approximately 1.4 times higher for gradational fusion images for all display times. This indicates that gradational fusion images are more effective than far infrared images in assisting recognition of pedestrian position, regardless of the driving load.

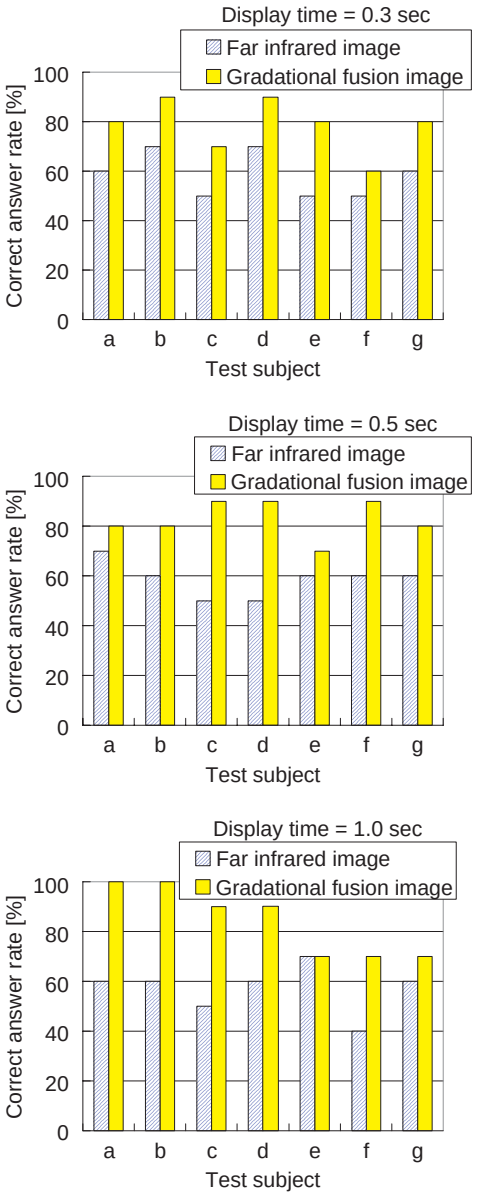


Fig. 11 Location recognition rate of pedestrian

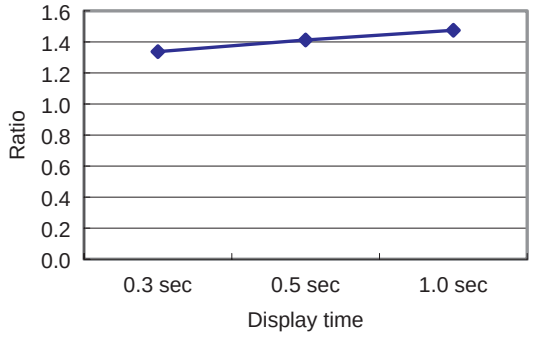


Fig. 12 Correct answer rate for gradational fusion images normalized by that for far infrared images

5. Conclusion

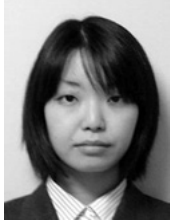
A method of generating fusion images limited to the road area through the application of gradation processing to near infrared images containing road area information has been developed in order to help provide visual assistance to drivers in recognizing pedestrians at night. The halation in images caused by the surrounding illumination and the headlights of oncoming vehicle was a factor in determining that the conventional image fusion method was less adequate in helping provide visual driving assistance. Gradational fusion images were generated using the road area from near infrared images in order to respond to this factor, and were shown to be more effective in assisting recognition of pedestrians. In addition, the halation caused by the headlights of oncoming vehicles was reduced. Simulator tests with test subjects of the effectiveness of the gradational fusion images in helping provide visual assistance to drivers for the recognition of pedestrians showed that the images increased the accuracy with which the location of pedestrians was identified. These results indicate that the use of this method in a visual driving assistance system can potentially reduce the incidence of pedestrian accidents at night.

References

(1) Traffic accident statistics annual report 2003, Institute for Traffic Accident Research and Data Analysis,(2004)
(2) Tsuji, T., Hattori, H., Watanabe, M., Nagaoka, N.: Development of Night Vision System, IEEE TRANSACTIONS ON INTELLIGENT TRANSPORTATION SYSTEMS, Vol. 3, No. 3, p. 203-209(2002)
(3) Suard, F., Rakotomamonjy, A., Bensrhair, A., Broggi, A.: Pedestrian Detection using Infrared images and Histograms of Oriented Gradients, IEEE IV2006, p. 206-212(2006)
(4) Toyofuku, K., Iwata, Y., Hagisato, Y., Kumasaka, T.: The “Night View System” Using Near-Infrared Light, SAE Paper, 2003-01-0018(2003)
(5) Herrington, W. F., Horn, B. K. P., Masaki, I.: Application of the Discrete Haar Wavelet Transform to Image Fusion for Nighttime driving, IEEE IV2005, p. 273-277(2005)

■ Author ■


Junji EGUCHI


Izumi KONDO


Hiroyuki KOIKE

Research of High Fatigue Strength for Powder-forged Connecting Rods

Kentaro TAKADA* Ryosuke KOGURE* Teruo KOBAYASHI*

ABSTRACT

This paper reports the results of research on increasing the fatigue strength of powder-forged connecting rod materials.

The fatigue strength of powder-forged materials was increased without adding special alloy elements or lowering workability by adjusting the ratios of the conventional main mixed powders (iron, carbon, copper) and by controlling the sintering temperature conditions. In addition to solid solution strengthening of the ferrite using copper, reducing porosity, which is a material internal defect, is also an effective method of increasing fatigue strength. Reducing carbon content greatly reduced the occurrence of defects in the forging stage.

The results of this research showed that the fatigue strength of high strength powder-forged materials can be increased by 30% or more over that of conventional materials, resulting in powder-forged connecting rods to be applied to even higher output and higher load engines than before.

1. Introduction

Weight reduction is an important means of increasing automobile fuel economy and output, and this applies to engine components as well. In particular, reducing the weight of the main moving components, such as the pistons, crankshaft, and connecting rod, has a large effect on enhancing engine performance. In addition to steel materials, titanium alloys and other materials are sometimes applied to reduce the weight of connecting rods[(1)]. However, the cost is high. So for passenger car engines, the connecting rod weight is reduced by increasing the steel material strength to enable a reduction in size[(2)].

In Europe and Japan, hot forging technology has advanced, and is often used to increase the steel material strength. In contrast, powder forging is the main method used in North America, and has had the advantage of being able to make use of the brittleness of the materials to fracture-split the large end of the connecting rod to streamline the shape and reduce weight. However, progress in weight reduction has been made in the hot forging method, with the development of steel materials that not only have high strength, but also result in fracture splitting in the same manner as that of powder-forged materials[(3)-(5)]. The strength of powder-forged materials can be enhanced by increasing the amounts of additive alloy elements[(6)] or adding new components. However, as the hardness increases, the machinability decreases, and the resulting drop in efficiency makes it impractical for mass production.

For this reason, the strength of connecting rods manufactured by hot forging is 30% or more than that of powder-forged connecting rods. This means that the two types cannot be designed with the same weight, which has hindered a flexible production response according to the production base.

Therefore, powder-forged materials that have the same strength and productivity as hot-forged materials were necessary to provide interchangeability in engines with the same specifications.

2. Research Goals

The material strength should be increased to reduce the connecting rod weight. This increase in strength is primarily responsible for an increase of the fatigue strength.

In addition, assuming a high-volume mass production line flow like that for conventional powder-forged connecting rods, lower machinability means increased replacement frequencies for cutters and other tools. This may cause costs to rise, and gives rise to concerns about drops in productivity. Therefore, the goals were to provide

* Automobile R&D Center

the same machinability as the conventional method, and to utilize the existing mass production lines without modifications. It was assumed that the fracture splitting method, which has become the main machining method for connecting rods in recent years, would be used.

3. Material Component Design

3.1. Approach towards Material Component Design

The main components of conventional powder-forged connecting rods are Fe-0.5%C-2.0%Cu, and MnS as the free-cutting component.

Possible methods for increasing the strength of this type of connecting rod are as follows.

(1) Increasing the base material strength by increasing the C and Cu contents
(2) Increasing the hardenability by adding Cr, Si, and Mn
(3) Strengthening the base by adding V, Ti, and Nb to precipitate carbides

However, the base material strengthening method (1) causes the machinability to drop as the hardness rises. For this reason, there are reports of adding special powders that effectively increase machinability[7], but this increases the cost relative to the conventional powder mix. Elements (Cr, Si, Mn) that are effective at increasing hardenability (2) oxidize easily during the sintering process, and these oxides form defects that lower the connecting rod strength, so this method is not appropriate. In addition, elements (V, Ti, Nb) that strengthen the base through carbide precipitation (3) also oxidize easily when mixed simultaneously in powder form, so reduction is necessary. However, reduction of carbides is challenging when mixing the powders, so these elements should be alloyed and mixed as pre-alloy powders. In this case, work should start from development of the pre-alloy powders, so costs are expected to rise. Therefore, optimization of the powder ratios and sintering conditions, without changing the main components, was investigated with the target of increasing strength without lowering machinability.

3.2. Adjusting the Ratios of the Main Material Components

First, the relationship between hardness and fatigue strength was investigated with respect to the ratios of C and Cu, which are main components in conventional powder-forged connecting rods. Figure 1 shows the relationship between the material hardness and rotary bending fatigue strength with respect to the C and Cu contents. Both the fatigue strength and the hardness increase with the C or Cu content, but the C content has a greater effect on the increase in hardness than the Cu content. Thus, reducing the C content and increasing the Cu content is an effective means of increasing the fatigue strength, while at the same time minimizing the increase in hardness which influences the machinability. Figure 2 shows the structure of these materials. This figure shows that reducing the C content reduces the hard pearlite, which is a cause of increased hardness, and increases the soft ferrite. However, this also lowers the strength, so the ferrite is strengthened using the solid solution

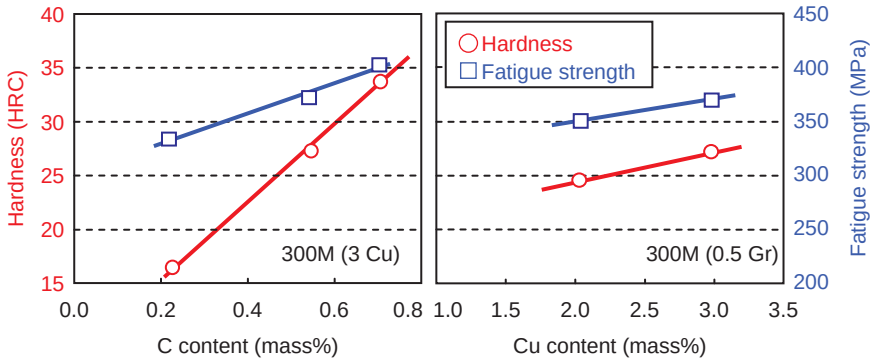


Fig. 1 Relationship between C, Cu content and hardness, fatigue strength

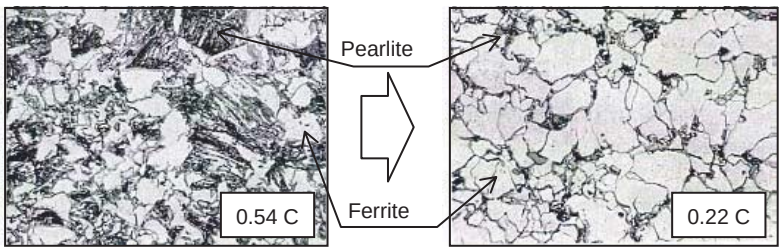


Fig. 2 Change in microstructure due to decreased C% of powder metal-forged test pieces (originally at 400X)

strengthening element Cu. Increasing the ratio of ferrite, which easily forms a solid solution with Cu, also increases the Cu saturation limit, resulting in larger amounts of Cu to enter the solid solution. This effectively reduces the hard pearlite that is a cause of increased hardness, and strengthens the soft ferrite, achieving to increase the fatigue strength without raising the hardness.

Next, the effects of C and Cu on machinability were investigated. The machined test material consisted of powder-forged materials manufactured under approximately the same conditions as those of an actual connecting rod, and the cutter was a carbide drill used to machine connecting rod joint holes. Figure 3 shows the drilling test conditions and results. When the C content is kept constant and the Cu content is increased, the hardness rises, causing the cutter wear to increase. However, when the C content is reduced to reduce the hard pearlite and the Cu content is increased, the hardness increases slightly, but the cutter wear can be decreased. This indicates that reducing the C content and increasing the Cu content is an effective method.

In addition, the sintering density is generally an important factor affecting the fatigue strength of sintered materials, and when powder forging is performed, the sintering density rises to near the true density throughout the entire part. However, a large number of microscopic pores are present near the surface layers. In the outermost surface layers, this porosity can be crushed by shot peening or other methods, but it remains in the inner layers and becomes a starting point for fatigue fractures, which lowers the fatigue strength. Figure 4 shows the porosity in the pole portion of a conventional powder-forged connecting rod. This type of porosity is generally said to be generated when the material is cooled by contact with the die during hot forging. In other words, when a powder compact formed by pressurizing and hardening powder is sintered, the mixed powder Cu (melting point 1083°C) melts and disperses in a solid solution into the ferrite. At this time, if the gaps produced from the melting copper, are completely crushed during hot forging, then there would be no porosity. The center portion of the materials and portions with large degrees of deformation are almost completely filled. However, the surface layers contact the forging die, causing the temperature to drop and increasing the deformation resistance, so the gaps in these portions are resisting crush and could easily remain as porosity. Therefore, it is expected that surface layer porosity can be reduced by lowering the deformation resistance at low temperatures. In addition, the material temperature during hot forging is around 1000°C, so the generation of surface layer

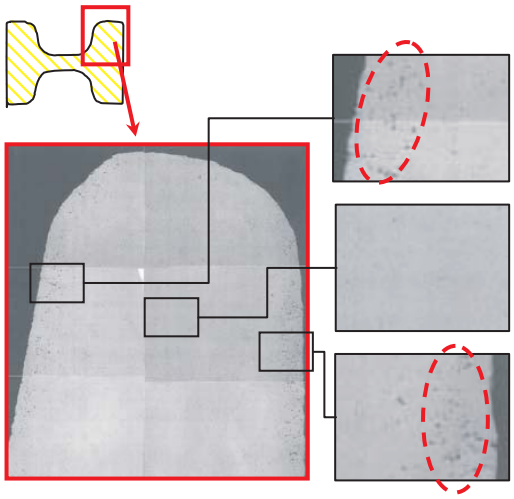


Fig. 4 Porosity of “I-Beam” for connecting rod (after shot-peening)

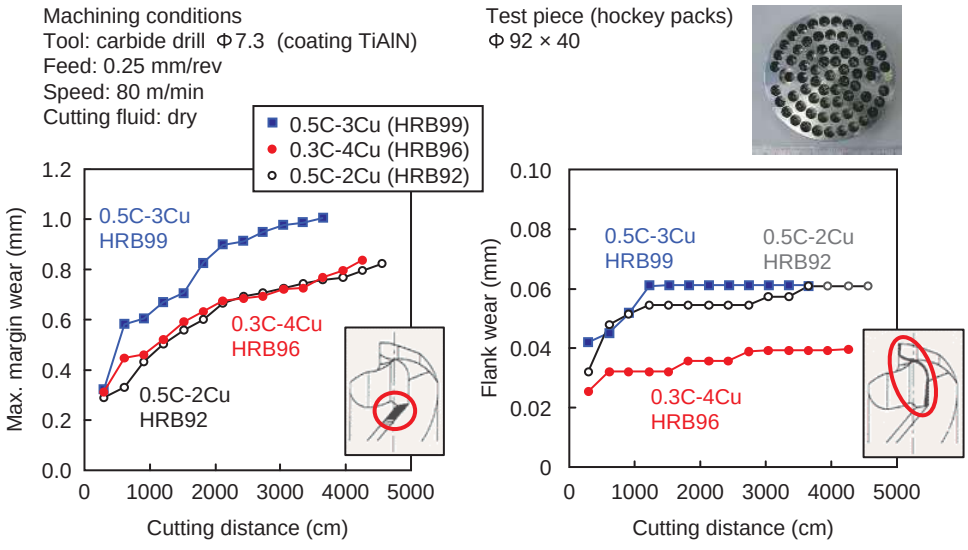


Fig. 3 Margin and flank wear in function of drilling length

porosity should be suppressed in the temperature range somewhat lower than this temperature. Figure 5 shows that reducing the C content lowers the deformation resistance within the temperature range of 850 to 900°C[8], so porosity existing in the surface layers is considered to be less than that of the conventional materials.

The above results indicate that reducing the main component C and increasing the main component Cu is an effective method of increasing the connecting rod strength without lowering the machinability.

3.3. Material Component Design of the Developed Connecting Rod

As part of the material component investigations, prototype connecting rods were manufactured and verified to take into account the fracture splitting performance and effects of surface porosity on fatigue strength. The powder mixture consisted of atomized pure iron powder (300 ME), graphite, 2.0% Cu powder by weight, and 0.32% MnS alloy powder. The mixture was adjusted so that the component ratios, after forging, varied between 0.13 to 0.57% C and 1.6 to 4.6% Cu. Figure 6 shows the test connecting rod prototype manufacturing process.

First, optimization of the C content was investigated. Figure 7 shows the relationship between the C content and the results of image analysis of the number, size and shape of the pores over a section 0.5 mm wide and 0.5 mm deep from the surface of the I-Beam of the test connecting rods. Reducing the C content, which was approximately 0.5% with the conventional method, reduced both the size and number of pores. In addition, the pore shapes were confirmed to be spherical when the

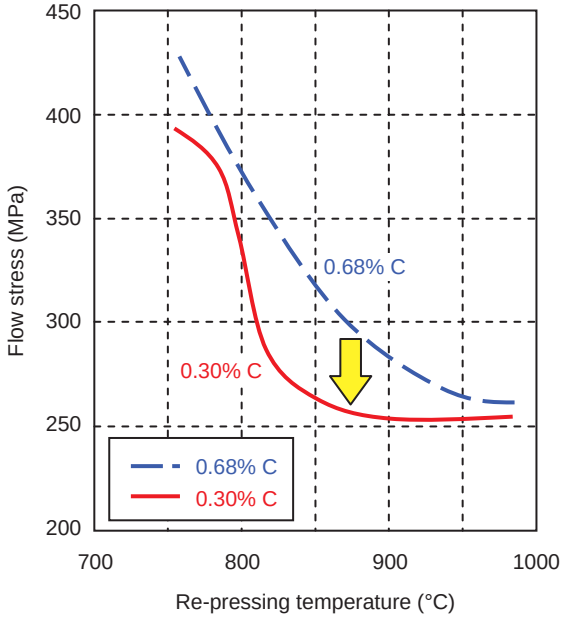


Fig. 5 Relation between flow stress and pressing temperature

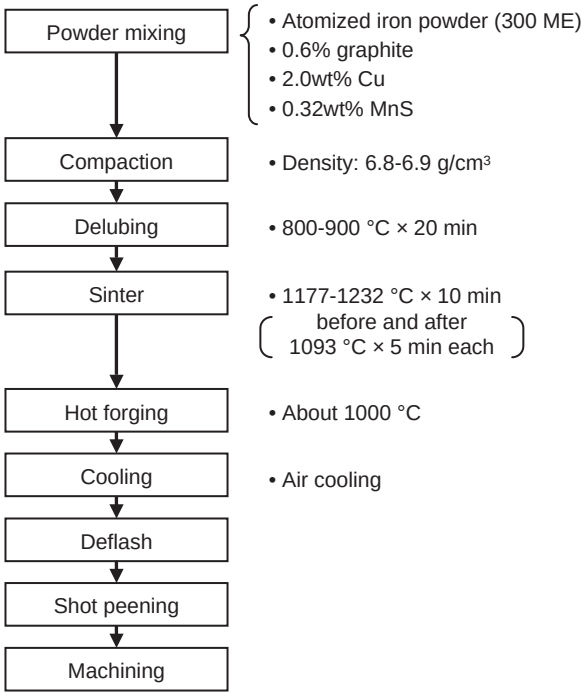


Fig. 6 Production process and condition of connecting rod

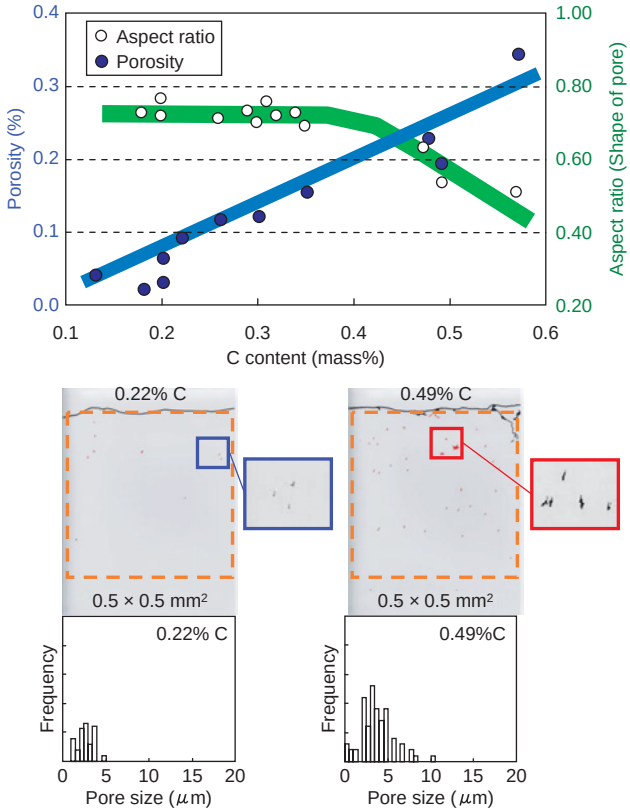


Fig. 7 Relation between C% and porosity, shape of pore (Photo: result of pore image analysis for C content)

C content was reduced to 0.35% or less.

Reducing the amount of porosity, pore size, and making the pores spherical can be presumed to reduce the concentration of stress on the pores. This reduces the potential for porosity near the surface of connecting rods to become a starting point for fatigue fractures, so it is necessary to aim for C content of 0.35% or less.

Figure 8 shows the relationship between the C content and the impact characteristics. Here, the tests were conducted at normal temperatures using a V-notched impact test piece as prescribed by JIS Z 2202. The impact value rises at a C content of 0.25% or less. Unlike a Charpy impact test piece, connecting rods have bolt holes for coupling with the crankshaft in the fracture split

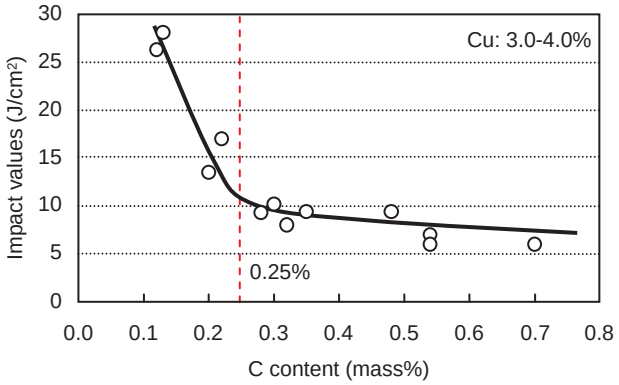


Fig. 8 Relation between impact value and C content

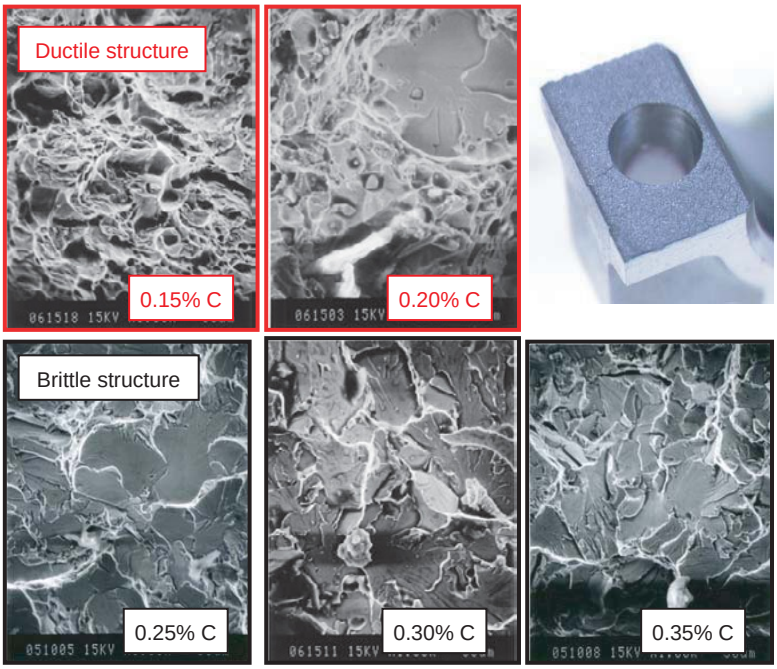


Fig. 9 SEM micrographs of fracture surface

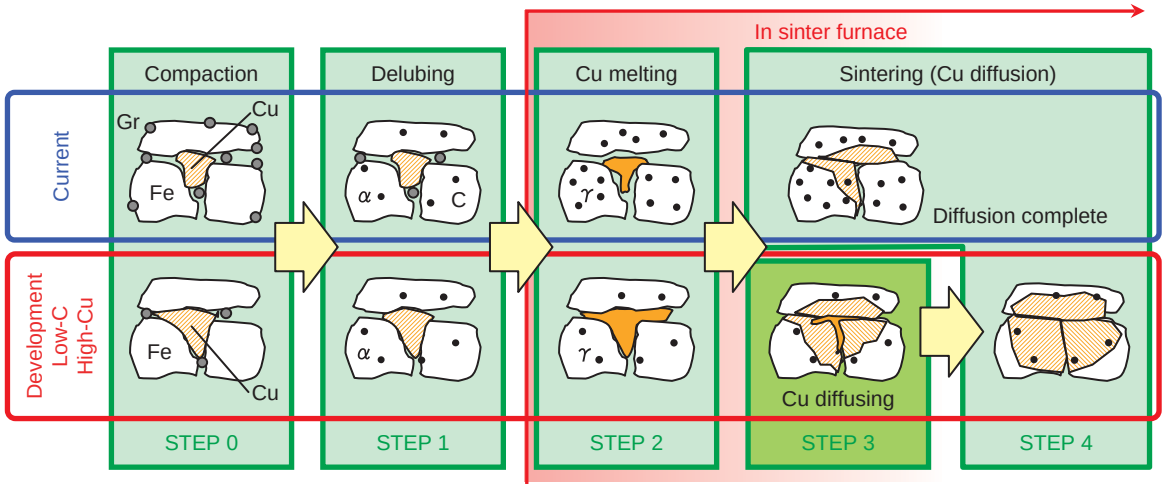


Fig. 10 Image of Cu melting and diffusion for high Cu rods in heat treatment process

portion, so an actual connecting rod was fracture-split and the surface properties were confirmed. Figure 9 shows an electron microscope image of the fractured surface of an actual connecting rod. Here, a V-notch approximately 1.0 mm deep was machined into the large end, which was the fracture starting point. The fracture-split portion exhibited the same surface properties over almost the entire surface. The fracture-split surface of connecting rods with a C content of 0.25% or more exhibited cleavage fracture surfaces, but dimples indicating ductile fracture surfaces appeared on the split surface at a C content of 0.2% or less. These dimples impede proper fit of the split surfaces when the connecting rod is reassembled after fracture splitting. These results indicate that reducing the C content by too much has an adverse effect on fracture splitting, so it is necessary to aim for C content of 0.25% or more in cases where fracture splitting is necessary.

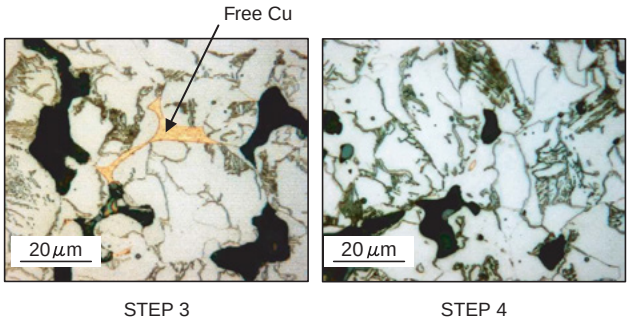


Fig. 11 Microstructure for high Cu rods in heat treatment process

Next, optimization of the Cu content was investigated. Figure 10 shows a concept drawing of Cu melting and diffusing. When the Cu content is increased the Cu melts inside the sintering oven (STEP 2) and then starts to diffuse in the same manner as the conventional materials, but the Cu diffusion is incomplete (STEP 3) even under conditions where diffusion was completed in the conventional materials. In this case, not only is it unable to obtain the full strengthening effects, but free Cu detracts from the strength. Therefore, it is necessary to completely diffuse the increased Cu (STEP 4). Figure 11 shows the actual structures with unmelted Cu remaining due to insufficient diffusion inside the sintering oven (STEP 3), and with the Cu completely diffused (STEP 4). The remaining unmelted Cu is confirmed to enter the gaps between the iron powder particles and interfere with adhesion between the iron powder particles. Therefore, a method was investigated of promoting diffusion to shift from STEP 3 to STEP 4 when increasing the Cu content.

When Cu diffusion is considered in terms of the one-dimensional diffusion distance, the diffusion distance is proportional to the diffusion coefficient and the time. In addition, the temperature dependence of the diffusion coefficient conforms to an Arrhenius equation as shown below, so the diffusion is proportional to temperature and time.

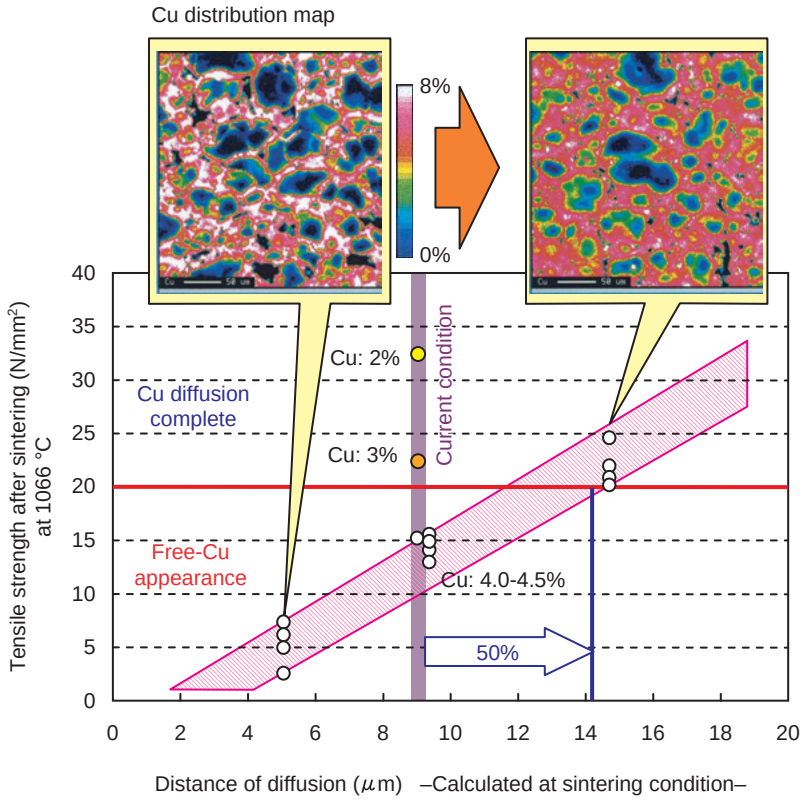


Fig. 12 Relation between high temperature strength and Cu diffusion

Diffusion distance: $d \propto \sqrt{Dt}$

Diffusion coefficient: $D = D_0 exp(-\frac{Q}{RT})$

Q: activation energy
R: gas constant
T: temperature
t: time

High temperature tensile strength tests were conducted using test pieces manufactured with different sintering temperature and time conditions in order to investigate the Cu diffusion conditions. These tests were performed at 1066°C, which is the connecting rod temperature immediately after removal from the sintering oven. Figure 12 arranges the first-order diffusion distances, calculated from the above diffusion equation according to the respective sintering conditions. In addition, the Cu density distribution within the test piece is also mapped to show the Cu solid solution diffusion status. These results show that in areas with low strength after sintering, the Cu is distributed in high density in the surface layers of the original powder particles. In contrast, in areas where sufficient strength is provided, the diffusion is uniform. Strength at high temperatures cannot be provided unless the Cu is sufficiently dispersed, so when increasing the Cu content it is necessary to set sintering conditions that diffuse the Cu uniformly throughout the particles.

In a pure Fe-Cu system, the Cu content in solid solution inside the austenite is said to be approximately 7.5 to 9% at a temperature of 1094°C[9], and in a Fe-C-Cu system, the theoretical solid solution limit to the inside of the austenite is reported as approximately 6%[9]. In addition, even in a powder-forged connecting rod with a dual-layer ferrite-pearlite structure, when the C content is reduced it is considered that the Cu solid solution limit tends to increase together with the ferrite ratio. Under the conventional conditions shown in Fig. 12, the Cu can be diffused evenly to the inside of the particles up to approximately 3%. However, when the Cu content is increased by 1.5 times to 4.5% under these conditions, Cu diffusion should also be promoted by approximately 1.5 times the conventional amount. Therefore, Fig. 13 shows the relationship between this sintering temperature and time and the calculated Cu diffusion distance. In the initial stages, there is much diffusion per unit time, and increasing the temperature further increases the diffusion

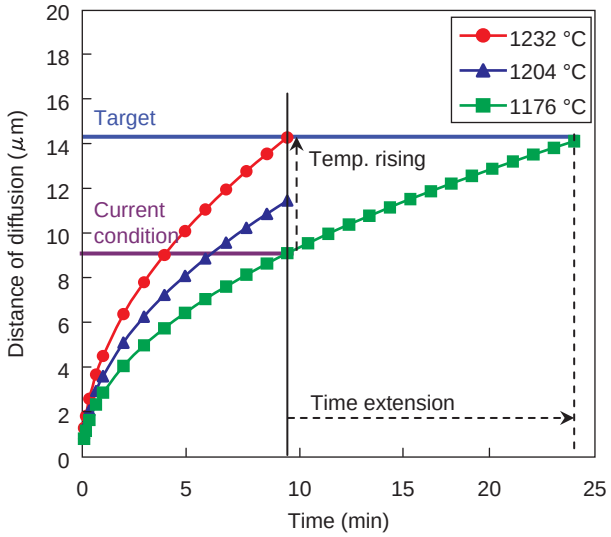


Fig. 13 Calculated results for Cu diffusion distance

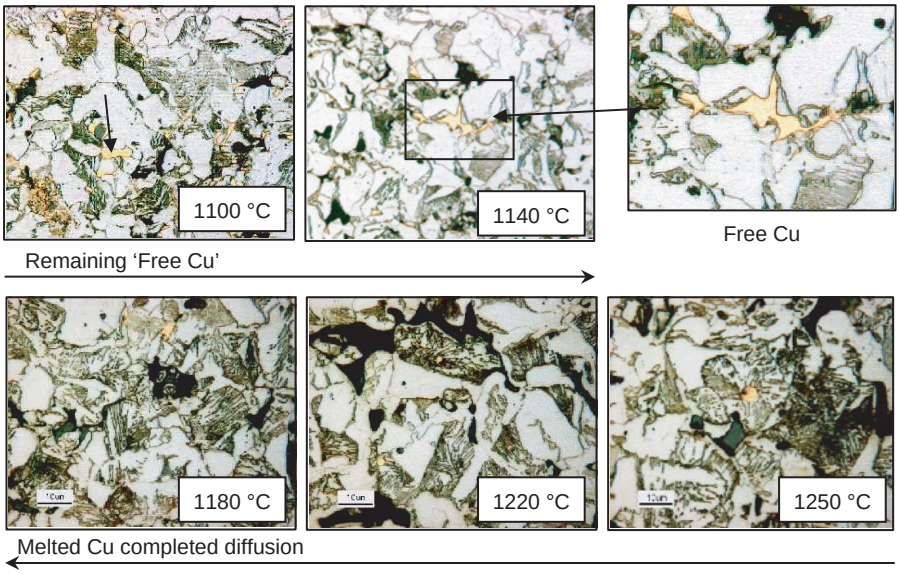


Fig. 14 Microstructure of test piece (0.35% C - 4.5% Cu) for sintering temperature (originally at 400X)

Table 1 Chemical composition for fatigue strength of connecting rod

(mass%)

	C	Cu	MnS
Development PF	0.26	3.59	0.32
	0.30	3.87	0.32
	0.35	4.27	0.32
	0.20	3.00	0.32
	0.13	3.42	0.46
	0.13	4.52	0.46
Current PF	0.39	1.64	0.30
	0.49	1.98	0.32
	0.54	2.14	0.30
High C/Cu	0.46	3.04	0.34
	0.51	2.93	0.33
	0.57	3.26	0.30

PF: Powder – forged rods

effects. After a certain amount of time has passed, the diffusion potential is reduced and the rate of diffusion also decreases. These calculated results indicate that increasing the sintering temperature and lengthening the sintering time can be considered as methods of promoting diffusion. However, the results also show that raising the temperature by 50 to 60°C and approximately doubling the time both provide roughly the same diffusion promoting effects. If the mass production conditions have room for raising the sintering temperature, this is considered to be a more effective method of promoting Cu diffusion than lengthening the sintering time. Therefore, in consideration of mass production performance, this study kept the sintering time constant and increased the Cu content by raising the sintering temperature. Taking into account the sintering oven performance and capability, the upper limit for the sintering temperature was set at approximately 1260°C.

The Cu content can be increased up to the solid solution limit within the target C content range of 0.25 to 0.35%, but it is considered that in this case, a long time will be needed for complete diffusion unless the sintering temperature is increased even further. Therefore, in consideration of mass production performance, the Cu content upper limit was set at 4.5%. Figure 14 shows the results of confirming the effects of the sintering temperature when using materials with a C content of 0.3% and Cu content of 4.5%. It was confirmed that there is no remaining unmelted free Cu at temperatures of 1180°C or higher, indicating that the Cu is completely in solid solution. These results confirmed that increasing the sintering temperature to 1180°C or more results in complete solid solution of approximately 4.5% Cu in a connecting rod with a C content of 0.3%.

From the above, the approach toward the component ratios of C and Cu, which are main connecting rod components, and the sintering conditions is as follows.

The C content should be reduced to 0.35% or less to minimize porosity and make the pores spherical, but it should also be 0.25% or more to obtain cleavage fracture surfaces during fracture splitting. Cu can be added up to the solid solution limit, but should be 4.5% in consideration of mass production performance. When using the same sintering time as the conventional method, the sintering temperature should be approximately 1180°C or more to completely diffuse the Cu. However, the upper limit is approximately 1260°C, in consideration of the mass production oven capability.

The relationship between hardness and fatigue strength was verified using actual connecting rods based on the above component ranges.

4. Connecting Rod Fatigue Strength

Fatigue tests were performed using actual connecting rods to evaluate the strength of the I-Beam of connecting rods with different main material component ratios. Table 1 shows the ratios of the main components C and Cu of the connecting rods used in the fatigue tests. In addition, fatigue tests were also performed on powder-forged connecting rods with a C content of 0.25% or less, which is unsuitable for fracture splitting. The C and Cu component ratios of these unsuitable connecting rods, a conventional ordinary powder-forged connecting rod, and a high hardness powder-forged connecting rod with both the C and Cu content increased are also shown in the table for comparison.

Figure 15 shows the fatigue test results for the connecting rods with various component ratios. The fatigue tests were performed in tension-compression mode (R=-1), and the fatigue limit of each connecting rod was obtained from the hardness around the fracture location and the S-N curve. These results show that when the C

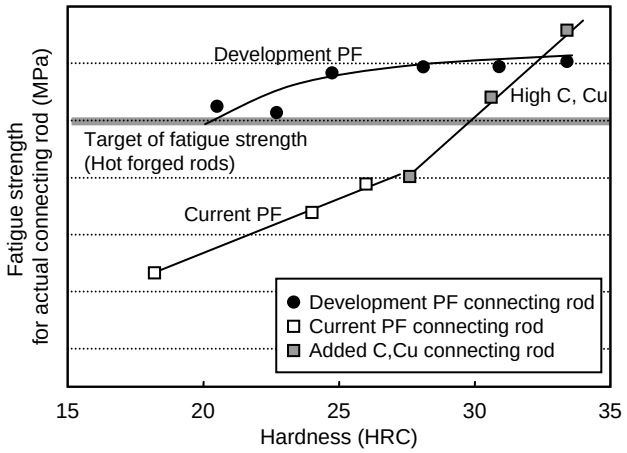


Fig. 15 Comparison of fatigue strength (tension and compression / R = -1) between developed connecting rods and current PF connecting rods

and Cu contents are simply increased in the conventional powder, the fatigue strength increases but at the same time the hardness also increases. To provide the target strength equal to that of a hot-forged connecting rod, the hardness rises to HRC30 or more, which impairs machinability. However, the newly developed powder-forged material with reduced C content and increased Cu content was confirmed to provide the target fatigue strength without corresponding hardening.

5. Effects of Increasing the Fatigue Strength

The powder-forged connecting rod material obtained by changing the material powder ratios and optimizing the manufacturing conditions achieved a fatigue strength guarantee value 30% or more than that of the conventional material while maintaining the same machinability. This achieved to reduce the weight by approximately 28 g per connecting rod, which, including the crankshaft balance adjustment, achieved a total weight reduction for the main moving components of approximately 290 g in the new ACCORD V6 engine.

In addition, this high fatigue strength powder-forged connecting rod provides the same fatigue strength as high-strength hot-forged non-tempered lightweight connecting rods (fracture splitting type). This means that they can be designed with the same weight, and results in flexible production, suited to each production base, regardless of the manufacturing method involved.

6. Conclusion

Technology was established to increase fatigue strength without increasing the hardness of powder-forged connecting rods produced locally in North America.

New powder-forged materials obtained using this technology were used to reduce the connecting rod weight without lowering the machinability. These results are summarized below.

(1) Reducing the C content to reduce the pearlite, and increasing the Cu content to strengthen the ferrite solid solution is an effective means of increasing the fatigue strength while suppressing an increase in hardness.
(2) Porosity occurring in the surface layers of the connecting rod during forging can become a starting point for fatigue fractures. Reducing the C content lowers the deformation resistance, enabling to reduce this porosity and make the pores spherical in shape, which effectively increases the fatigue strength.
(3) The new powder-forged materials increase the fatigue strength by 30% or more without lowering machinability, compared to the conventional materials, and achieved to reduce the connecting rod weight.
(4) The new material provides the same performance as hot-forged non-tempered high-strength lightweight connecting rods (fracture splitting type). This provides interchangeability in high output, high load engines produced in both Japan and North America, and expands the local production range to which this new technology can be applied.

References

(1) Matsubara, T., Sato, Y., Kimura, K., Kawase, N., Ito, S.: Development of Free Machining Titanium Alloy for Connecting Rods, HONDA R&D Technical Review, Vol. 3, p. 12-26
(2) Matsubara, T., Sato, Y., Iida, Z., Taguchi, T.: Development of a High Fatigue Strength Free Machining Microalloyed Steel for Connecting Rods, HONDA R&D Technical Review, Vol. 4, p. 73-85
(3) Iida, Z., Takada, K., Suzuki, S., Sato, C.: Development of Lightweight Connecting Rod, Honda R&D Technical Review, Vol. 17, No. 2, p. 115-121
(4) Fukuda, S., Etou, H.: Development of Fracture Splitting Connecting Rod, JSAE Review, Vol. 23, No. 1, p. 101-104 (2002)
(5) Yamaguchi, M., Ookuma, S., Miyazawa, T., Yamada, Y.: Development of Fracture-Splitting Connecting Rod, NISSAN Technical Review, No. 56, p. 21-25 (2005)
(6) Ilia, E., O'Neill, M., Tutton, K., Lanni, G., Letourneau, S., Haehnel, M.: Benchmarking the Industry: Powder Forging Makes a Better Connecting Rod, SAE paper, No. 2005-01-0713, p. 1-13 (2005)
(7) Ilia, E., O'Neill, M., Tutton, K.: Higher Fatigue Strength Materials for Powder Metal Forged Connecting Rods, SAE paper, No. 2002-010611, p. 1-7 (2002)
(8) James, B. W., McDermott, M. J., Powell, R. A.: "Powder Forging" Metals Handbook, ASM International, Vol. 14, No. 9 (1988)
(9) Nihon Gakujyutsu Shinkoukai Seikou Dai19iinkai: Tekkou to Goukingenso (Jyou), Seibundo Shinkousya, p. 353-355(1966) (in Japanese)

Author


Kentaro TAKADA


Ryosuke KOGURE


Teruo KOBAYASHI

Development and Application for Identification of Sound Source Using Inverse Method for Road Noise

Fumihiko IDE* Hiroko TADA* Kazuhito MISAJI*
Theophane Courtois** Claudio Bertolini**

ABSTRACT

A method of analyzing the sound source identification has been studied in an attempt to enhance road noise performance. In order to reduce the cabin noise level originating in mid-frequency structure-borne noise, it is necessary to identify the sound radiating panels that contribute to the sound pressure level. The research discussed in this paper identified the sound sources using the interior cavity sound pressure levels under vehicle operational condition and the acoustic transfer functions with a loudness speaker placed on the each panel adjacent to the cavity on test bench. To prevent the accuracy of source identification from being affected by errors in measurements, the inverse matrices of acoustic transfer functions was not employed. As a result of the vehicle tests, it is verified that the method enable to predict the reconstruct cabin noise level from 100 to 600 Hz with a reliable accuracy.

1. Introduction

The enhancement of automotive interior cavity quietness is an important factor in increasing the commercial appeal of vehicles.

Simulations employing numerical computations have been recognized as an effective method of predicting interior cavity sound pressure level and applying countermeasures efficiently and accurately. In general, the finite element method (FEM) is used to analyze structure-borne noise frequencies below 200 Hz, and statistical energy analysis (SEA)[(1)] is used to analyze airborne noise frequencies above 500 Hz. On the other hand, in order to extend the range of application of simulations the frequency range to which FEM can be applied has now been expanded to above 200 Hz, and a hybrid of FEM and SEA that considers the contribution of structure-borne noise has been formularized[(2)]. As a result, these new methods have enabled the proposal of analytic methods that take in the mid-frequency range. However, it has been still challenging that the use of simulations by itself to study the 200-800 Hz range. Therefore, methods of analysis involving tests are generally employed for this frequency range.

Transfer path analysis[(3)] is an analytic method involving tests that has been employed generally. In this method, the vibration of the panels enclosing the cabin and the acoustic transfer function between the panels and measurement points in the cabin are measured. By synthesizing these vibrations and functions, it is enable to determine the sound pressure level at the measurement point. However, the measurement of panel vibration in a real vehicle analysis entails a considerable amount of time, and the removal and reinstallation of parts can affect the repeatability of data. Therefore, there are cases in which this method cannot be employed during the actual vehicle development process. For applying and determining the specification within a limited vehicle development period, the quick identification of contributing areas is demanded. Therefore, it is necessary that the development of analytical method not relying on panel vibration measurement.

In this research, with considering the characteristics of the conventional transfer path analysis method, an analytical method focusing on structure-borne road noise, in particular in the mid-frequency range (100–600 Hz) is discussed. This method did away with the requirement for direct measurement of panel vibration by using the inverse

* Automobile R&D Center
** RIETER Automotive Switzerland

matrix method to identify sound sources[4]. This paper will also discuss the verification of the accuracy of the method in identifying the main contributing sound sources using a real vehicle, in this case a 4-door sedan, and the achieved reduction in the cabin noise level through the use of an increased amount of sound insulator.

2. Method of Analysis

2.1. Range of Applicability of Method

In order to establish a method that could be effectively employed in the actual vehicle development process, the project target is set as the achievement of the ability to identify the sound sources that make the main contribution to cabin noise using a method of analysis that focuses on structure-borne road noise in the mid-frequency range (100–600 Hz) and the ability to predict the noise reduction level that would be achieved through the use of a sound proof package (sound insulator and asphalt sheet). In addition, the project set out to develop a method that would not require movement of the vehicle or removal of any parts for ensuring the repeatability of measurements, and that would enable the entire measurement procedure to be completed within five days.

2.2. Method Radiated Sound Sources Identification

In this section, the method of sources identification using the inverse method is discussed.

The square of the sound pressure level at any point i in the cabin, P_i^2(Pa^2), is determined as the sum of the panel contributions which enclose the cabin. When each panel contribution is determined as the product of the sound power radiated by panel j, W_j(W), and the sound power transfer function from panel j to the cabin measurement point i, G_{ij}(Pa^2/W), the relation between the parameters can be expressed as Eq.(1).

$$P_i^2 = \sum_j G_{ij} \cdot W_j \qquad (1)$$

The sound power radiated by the panel, W_j, is determined from the two-stage test measurements described below.

2.2.1. Measurement of cabin sound pressure level during vehicle operational condition

The cabin noise level, $\{P_i^2\}$, is measured with multiple microphones positioned inside the cabin on a chassis dynamometer under sweep condition (Fig. 1). The number of microphones used is larger than the number of panels enclosing the cabin. These noise levels are important for determining the radiated sound power from the panels using the inverse method, which is discussed later.

2.2.2. Measurement of the acoustic transfer function on a test bench

The panels enclosing the cabin are divided into smaller areas, and the acoustic transfer function matrix $[G_{ij}]$ from each panel j to the cabin measurement points i is measured on a test bench (Fig. 2).

The layout of the microphones was the same as that of on chasses dynamometer. Loudness speaker was mounted on each panel and the noise level close to the speaker and the vibration of the speaker cone were measured simultaneously with the sound power radiated by the speaker as the reference.

Based on the results of the test measurements conducted in the two stages discussed above, Eq. (2) can be expressed as a matrix based on Eq. (1), and the sound power radiated by the sound sources can be expressed as Eq. (3).

$$\left\{P_i^2\right\} = \left[G_{ij}\right] \cdot \left\{W_j\right\} \qquad (2)$$

$$\left\{W_j\right\} = \left[G_{ij}\right]^{-1} \cdot \left\{P_i^2\right\} \qquad (3)$$

2.3. Reconstruction of Noise Level and Prediction of Reduction of Noise Level

Using the radiated sound power from each panel determined in Eq. (3) and the acoustic transfer functions, the square of the reconstructed noise level at any point in the cabin, P_{calc}^2, can be expressed as Eq. (4).

$$P_{calc}^{\ 2} = \sum_j G_{ij} \cdot W_j \qquad (4)$$

The radiated sound power from the panels can be reduced by modifying the structure of the vehicle framework and the panels which reduces the speed of vibration of the surfaces of the panels, and by using the sound insulating materials which increases the insertion loss (IL) performance. However, if the level of vibration

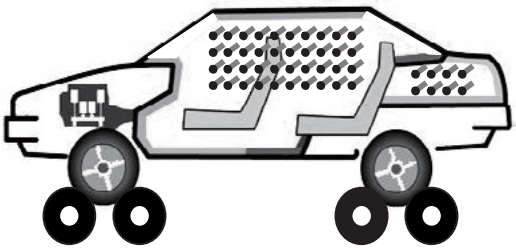


Fig. 1 Operational data under broad band excitation

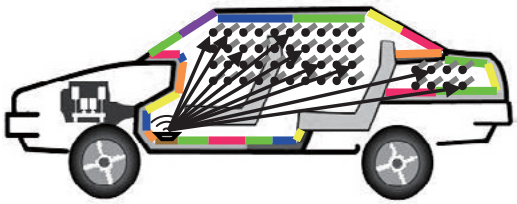


Fig. 2 Frequency response of acoustical power

of the panels is reduced by the vehicle framework and panels modification, the panel vibration has to be measured after the modification. In this method, therefore, the framework and panels modification is not be discussed. While, with regard to the use of sound insulating materials, if the properties of the sound insulation materials are known, then the IL performance following their use can be predicted without conducting measurements with the vehicle. The goal, therefore, was the establishment of the method which enables to predict the reduction of the cabin noise level that would be achieved by the employment of sound insulating materials after the sound source identification of the main contributor.

2.4. Method of Increasing Analytic Accuracy

As shown in Eq. (3), the radiated sound power from each panel is calculated using the inverse matrix of the acoustic transfer function matrix.

When the acoustic transfer function, $[G_{ij}]$, is the square matrix, the inverse matrix $[G_{ij}]^{-1}$ can be derived directly and the radiated sound power from the panel determined mathematically. However, when the noise levels at the measurement points contain errors due to the vehicle operational condition on the chasses dynamometer, the error in the determined radiated sound power from the panel can increase. The magnitude of this error is dependent on the size of the inverse matrix of the acoustic transfer function. Therefore, when measuring the multiple points in the cabin, the determination of the radiated sound power using the inverse matrices is not appropriate. It is necessary to determine the power robustly with regard to measurement errors.

For the determination, the non-negative least squares algorithm (NNLS)[7] was adopted instead of the inverse matrices. The NNLS can be expressed as Eq. (5).

Since the NNLS method uses iterative computation, the calculation time increases in comparison to the inverse matrices method. However, it possesses the advantages of not being too affected by measurement errors, and of increasing the number of measurement points easily against the number of sound sources.

$$\min_{W_j} \left\| G_{ij} \cdot W_j - P_i^2 \right\| \;;\; W_j \geq 0 \qquad (5)$$

In addition, by introducing the variations to the measured noise level data at each measurement point under vehicle operational condition, the error $\{p_i^2\}+\{\delta p_i^2\}$ was deliberately induced in the measured noise level, and the standard deviation for the radiated sound power from the panels is determined. Using the results of this standard deviation and the acoustic transfer functions, the variation in the reconstructed noise level is expressed as Eq. (6). Panels with a higher level of variation were judged as possessing lower reliability, therefore they were eliminated from consideration as areas for contribution analysis[6), (7)].

3. Verification of Method in Real Vehicle

In this section, it is discussed that the sound source identification result using a real vehicle, which is a 2L-class 4-door sedan (North American specifications). Moreover, the reduction in the cabin noise level achieved by the use of sound proof materials is discussed.

3.1. Results of Basic Verification Using Artificial Sound Sources

For verifying the effectiveness of the developed method, the identification of the main contributing sound sources using the loudness speakers as artificial sound sources is carried out. The position of the microphones and other aspects of the test set-up were identical to those employed in vehicle tests.

Loudness speakers were positioned on the front floor (FFL), rear floor (RFR), and parcel shelf (PSL). For designing to reproduce the artificial radiated sound source from panels (Fig. 3), the speaker outputs were set as a different level of sound pressure power. The acoustic transfer functions matrix from each area to the measurement points was measured, and the radiated sound power from each area was identified. Figure 4 shows the identified radiated sound power from each area. The FFL and the PSL displayed the highest level of radiated sound power, which indicated that test results could be reproduced. By contrast, the radiated sound power of the RFR could not be distinguished from that of other areas

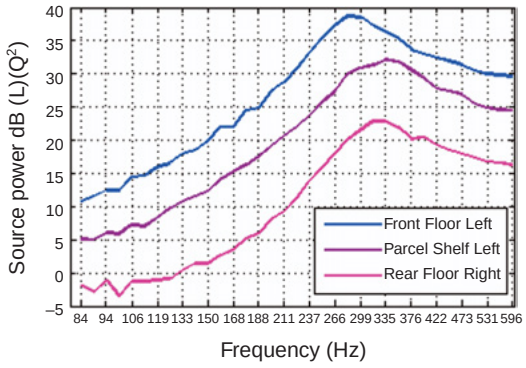


Fig. 3 Artificial excitation: actual loudspeaker power

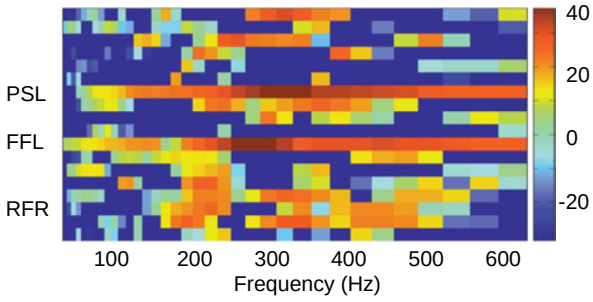


Fig. 4 Identified power radiation of each panel

not being excited by speakers. It was believed an effect of background noise during the identification of radiated power. Therefore, when the radiated power level is low, the care needs to be exercised in the analyses.

3.2. Overview of Vehicle Measurements

For cabin noise measurements during vehicle operational condition, the vehicle was placed in a semi-anechoic room. For reproducing the cabin noise and spectrum under a normal road surface driving condition, a roller bench with a roller surface reproduced on road surfaces was used. The vehicle was operated in idle and in neutral gear, and the vehicle speed was set to vary ±6 km/h to counteract the effect of the rotation order of the chassis rollers. During verification tests, two different road surfaces (smooth and rough) and two vehicle speeds (50 km/h ± 6 km/h and 60 km/h ± 6 km/h) were employed.

Measurements of the acoustic transfer functions were conducted on the bench with the engine turned off. Because the sound power radiated from the loudness speakers (the source of excitation) was used as a reference for the acoustic transfer functions, accelerometer and microphone were mounted on the speakers (Fig. 5).

3.3. Definition of Microphones and Areas for Analysis

The microphones had to be positioned for obtaining optimum sound data from anywhere in the cabin, and the positioning had to be shared between vehicle tests and bench excitation tests. For these reasons and completing each measurement at one time, a number of microphones were selected (Fig. 6).

These rules were followed in positioning the microphones in the cabin:

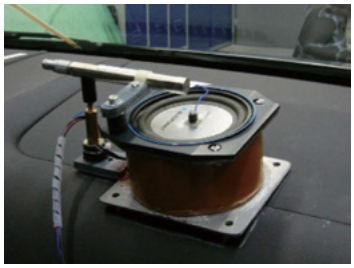


Fig. 5 Definition of loudspeaker setup

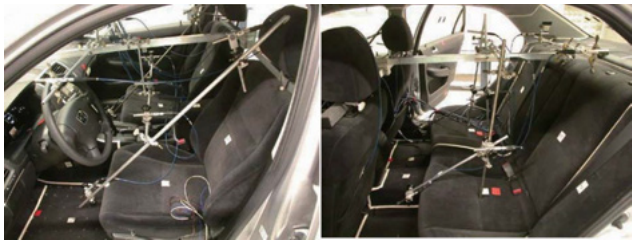


Fig. 6 Definition of microphone setup

Table 1 Definition of areas in passenger compartment for measurement

	ID	Surface
1	FDL	Front Door Left
2	FDR	Front Door Right
3	RDL	Rear Door Left
4	RDR	Rear Door Right
5	WSFL	Windscreen Front Left
6	WSFR	Windscreen Front Right
7	PSL	Parcel Shelf Left
8	PSR	Parcel Shelf Right
9	IPL	Instrument Panel Left
10	IPR	Instrument Panel Right
11	FFL	Front Floor Left (+Dash lower left)
12	FFR	Front Floor Right (+Dash lower right)
13	HLFT	Head Liner Front
14	HLRR	Head Liner Rear
15	RFL	Rear Floor Left (+Under Front Seat Left)
16	RFR	Rear Floor Right (+Under Front Seat Right)
17	RSL	Rear Seat Left
18	RSR	Rear Seat Right

(1) To the extent possible, the microphones should be positioned at uniform intervals in the cabin.
(2) There should be a distance of at least 30 cm between neighboring microphones.
(3) The microphones should be positioned at least 30 cm from the nearest loudness speaker.
(4) The microphones should be positioned at least 20 cm from the panels in the cabin.
(5) The microphones should be positioned facing the nearest panel.

In this verification, nineteen microphones were positioned in the vehicle cabin following these rules.

The definition of the areas constituted by the panels enclosing the cabin is determined by the vehicle dimensions and the analyzed frequencies. In addition, if the areas are small, the upper limit of the analyzed frequency range becomes higher. However, by dividing the cabin up into small areas, the result will be affected from the phase relationship between the area and contiguous areas. In this method, since all values are expressed using energy, this contribution of phase would decrease the analytic accuracy. Therefore, the size of the area is maintained as large as possible. Table 1 shows the areas after division of the cabin.

By using a sufficient number of microphones to complete data measurements at one time with maintaining the accuracy of the data, the entire process, from set-up to measurement, was conducted in two days.

3.4. Results of Reconstruction of Cabin Sound Pressure

The sound power radiated by each area was identified using the sound pressure levels at the measurement points

under vehicle operation and the acoustic transfer function to each measurement point when the vehicle was on the bench. The sound pressure level at the measurement points was reconstructed using the identified radiated sound power from the panels and the acoustic transfer functions. Figures 7 and 8 show a comparison of measured and reconstructed sound pressure level measurement point at the driver's ear. Under both analytic conditions, the sound pressure level is predicted with accuracy within ±3 dB above 100 Hz. In addition, both measured and reconstructed sound pressure levels display a peak at 237 Hz. Hereafter, an additional analysis was carried out on this frequency.

3.5. Results of Identification of Main Contributing Areas

In the identification of the contributing areas, each area contribution to the sound pressure level of any microphone at specific frequencies was determined. Figure 9 shows the results of the contribution analysis (Analyzed frequency: 237 Hz; Measurement point: Driver's seat; Vehicle speed: 44-56 km/h). In the figure, "Recomposition" indicates the sound pressure level reconstructed from all the areas, and "Main contribution" indicates the sound pressure level reconstructed from areas contributing mainly, which levels are down to 20 dB from the "Recomposition".

The variation in reconstructed sound pressure determined using Eq. (6) is also indicated in the each are contribution in Fig. 9. The areas indicated by hatching display a low level of variation in sound pressure, and these represent reliable analytic results. Only these areas will be employed for detailed analysis to reduce sound pressure in the cabin.

Figure 10 shows the results from Fig. 9 compiled for different vehicle speeds and different road surfaces. Under all test conditions, the parcel shelf area, both right and

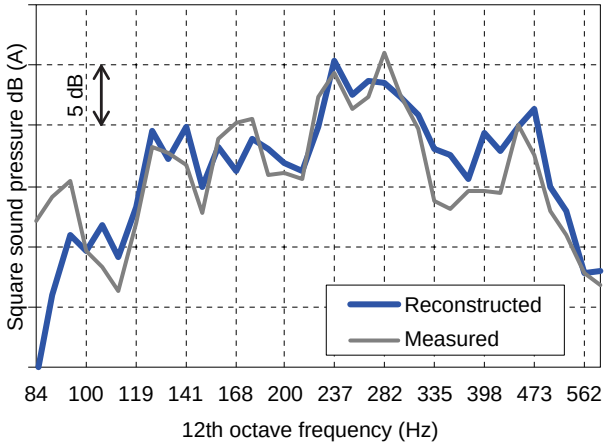


Fig. 7 Comparison of reconstruction and measurement (Rough rollers 44-56 km/h)

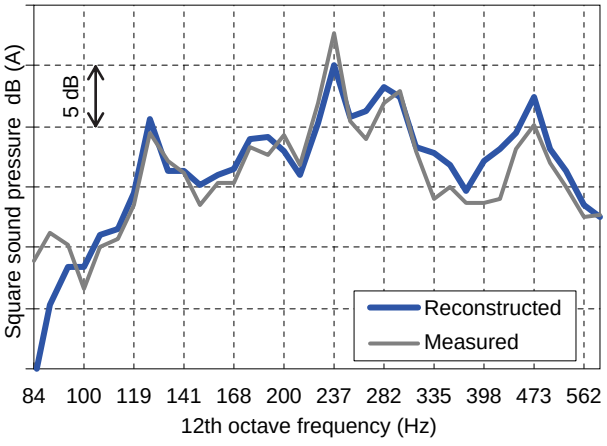


Fig. 8 Comparison of reconstruction and measurement (Smooth rollers 54-66 km/h)

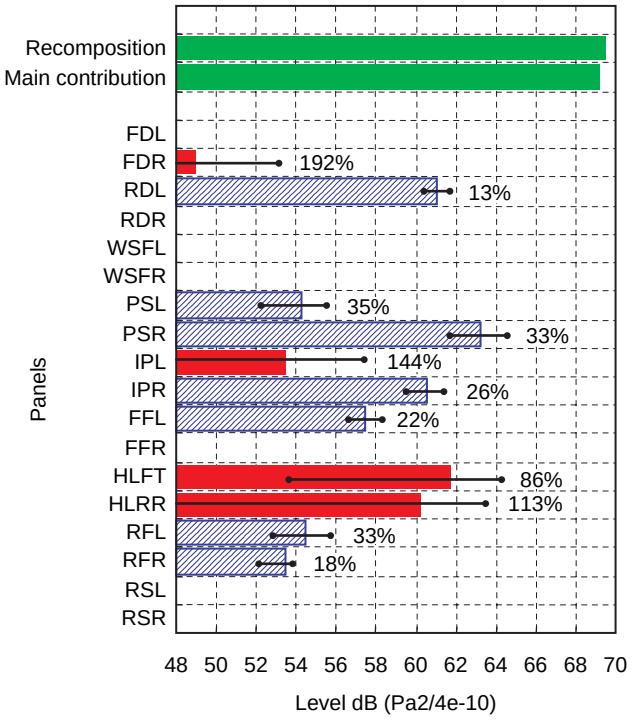


Fig. 9 Contribution of each area to sound pressure at frequency band 237 Hz

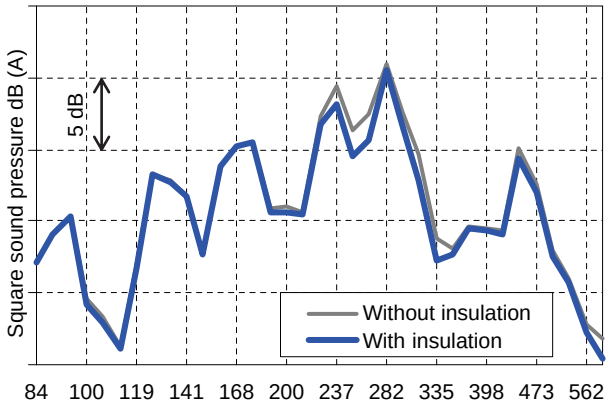
Running condition		Main contributions (Ranking)			
Roughness	Speed				
Smooth	44-56 km/h	PSR	IPL		
	54-66 km/h	PSR	IPL		
Rough	44-56 km/h	PSR	HLF	RDL	IPR
	54-66 km/h	PSL	IPR	RDL	IPL

Fig. 10 Summary of area contribution at frequency band 237 Hz

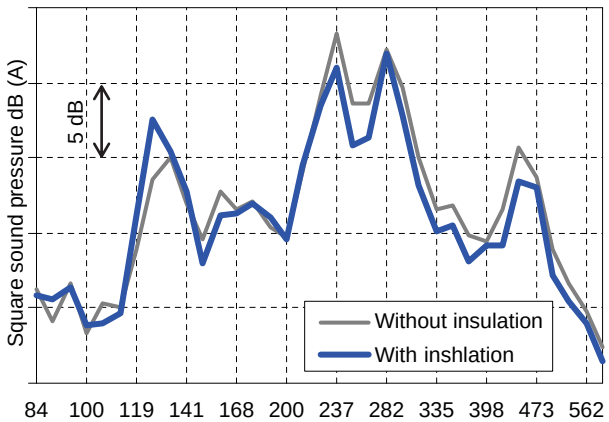
left, displayed the highest contribution at the measurement point at driver's ear. The instrument panel area also displayed a high contribution, but standard deviation was higher for different test conditions, therefore the reliability was judged as low. This area was not made the subject of countermeasures to reduce sound pressure levels.

3.6. Results of Verification of Sound Pressure Reduction Achieved by Employment of Sound Insulating Materials on Main Contributing Areas

The reduction in cabin noise achieved by employing sound insulating materials on areas that had been found as the main contribution was studied. According to the result shown in Fig. 10 indicated that the parcel shelf area made the higher contribution, sound insulating materials were employed on this area. Figure 11 shows the comparison between the results of cabin noise levels measured under vehicle operational condition and predicted cabin noise levels were compared, which condition is on the rough rollers at vehicle speeds of 44-56 km/h. The prediction results displayed a good level of accuracy, centering on 237 Hz.



(a) Prediction



(b) Measurement

Fig. 11 Comparison of sound pressure with and without insulation (Rough rollers - 50 km/h)

3.7. Verification of Effect on Cabin Noise under Driving Condition on Road Surfaces

The effect of the countermeasures applied in this project under driving condition on a road was verified. Figure 12 shows the reduction in sound pressure at the driver's ear achieved by the employment of sound insulating materials on the parcel shelf area. The sound pressure level at 237 Hz has been reduced as well as on the chassis roller.

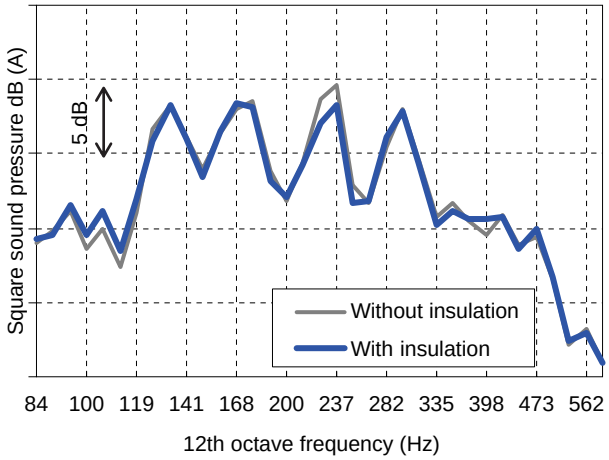


Fig. 12 Comparison of sound pressure with and without insulation (on road - 50 km/h)

4. Conclusion

Based on the transfer path analysis using the inverse matrix method, a method focusing on medium-frequency structure-borne road noise enabling identification of the main sound sources and reduction of cabin noise levels has been developed.

The use of the non-negative least squares method, which is not affected by issues of measurement accuracy, has increased the accuracy of sound source identification, and a method of area identification as sound sources using stochastic variables and standard deviation with reliable evaluation has been developed.

Tests in a real vehicle indicated that the reconstructed sound pressure level could be predicted with high accuracy within ±3 dB against measurements. The main contributing areas can be also identified, and the effect of employment of sound insulating materials predicted.

By doing away with the requirement for panel excitation tests and minimizing the measurement set-up, the new method has enabled the procedure to be completed, from set-up to sound pressure reconstruction analysis, in two days.

References

(1) Misaji, K., Tada, H., Yamashita, T., Nakamura, M., Tanaka, H., Kokabu, S., Morie, D.: Testing Uniqueness of Hybrid SEA Modeling Solution for a Passenger Car, 2003 SAE Noise & Vibration Conference & Exhibition, 2003-01-1408 (2003)
(2) Shorter, P. J., Langley, R. S.: Vibro-acoustic analysis of complex systems, Journal of Sound and Vibration, Vol. 288 (2005)
(3) LMS International, “Transfer Path Analysis:” The Qualification and Quantification of Vibro-Acoustic Transfer Paths, LMS International, Application Notes (1995)
(4) Orefice, G., Dutto, D., Gottardi, S., Avenati-Bassi, F., Cifelli, P., Prando, F., Tinti, F.: Rolling Noise Characterization and Optimization: a Two-Step Methodological Approach for Integrating Structural and Passive Treatment Countermeasures, RIETER Conference 2003
(5) Verheij, J. W.: Inverse and reciprocity methods for machinery noise source characterization and sound path quantification, International Journal of Acoustics and Vibration, Vol. 2 (1997)
(6) Guasch, O., Magrans, F. X., Rodríguez, P. V.: An inversion modeling method to obtain the acoustic power of the noise sources in a large factory, Applied Acoustics, Vol. 63, No. 4 (2002)
(7) Magrans, F. X., Rodríguez, P. V.: An innovative approach for the noise reconstruction and analysis at the medium-high frequencies, Proceedings of Euro-Noise, Vol. 1 (1998)

Author


Fumihiko IDE


Hiroko TADA


Kazuhito MISAJI


Theophane Courtois


Claudio Bertolini

Calibration of Tooth Profile Measurement and Uncertainty Analysis Based on Ball Artifact Method

Kenta UMETSU* Wataru ISHIDO** Kinya FUJIWARA*

ABSTRACT

Tooth profile measurements were calibrated using a double ball artifact that is traceable to a national standard of length. From the calibrated results, an evaluation technology that quantifies the uncertainty of tooth profile measurement in a 1-to-1 correspondence with a tooth profile of arbitrary specifications was established. In this evaluation technology, the work of calibrating the measuring machine has been minimized, and measurement simulations have been made feasible by modeling the statistical properties, as well as algebraic calculation from the model during tooth profile measurement, enabling the reliability of tooth profile measurement to be statistically evaluated. As a result, during tooth profile inspections on the manufacturing floor, practical inspection accuracy is now guaranteed.

1. Introduction

Many of the functions of a gear, such as quietness, rely on the accuracy of the 3-dimensional curved form.

For example, there is a report[1] to the effect that the profile accuracy for satisfying quiet driving is approximately 1 μm, and advances are being made concerning gear manufacturing accuracy. Gear measuring machines are widely used to measure and inspect gear tooth accuracy. In order to cope with the increasingly high level of gear accuracy, however, highly accurate measuring technology and a high level of calibration technology for measuring the appropriateness and reliability of measuring accuracy are being demanded. For example, 1 μm is demanded for class 0 (highest) accuracy under ISO 1328-1 and JIS B 1702-1 gear accuracy standards.

Previously, in order to calibrate a gear measuring machine, a highly machined and evaluated gear was used as a calibration standard (hereafter called “artifact”). However, when using a gear artifact and aiming for high accuracy as a standard thereto, the following issues exist at present.

(1) There is a limit to the level of accuracy to which a gear can be machined.

(2) There is no method of measuring a gear to high accuracy and guaranteeing it.

Also, when a gear is used as an artifact, an artifact consisting of a single specification gear is not very appropriate for enabling an accuracy guarantee to be rigorously performed on gears of numerous specifications, as the object of inspection. Consequently, to establish a method that can cope with the increasing accuracy of gears and practically guarantee the inspection accuracy in the inspection on the production line is not an easy task. In light of this situation, in recent years a method of calibration for tooth profile measurement using a double ball artifact (DBA) has been proposed in ISO/TR 10064-5. In the double ball artifact method, a steel ball having a high degree of sphericity and highly accurate surface properties, and is treated as a pseudo-involute gear, is measured, and the deviation between the measurement results and the ideal profile is quantified. Here, the deviation is defined as the tooth profile measurement deviation.

In addition to the conventional purpose of DBA use, the calibration method reported in this paper aims to quantify multiple kinematic errors from the calibration data, such as the positioning errors of the guide and rotary table, which constitute the kinematic mechanism of the

* Automobile R&D Center

** Forum Engineering Inc.

Table 1 Specification of DBA

Name	Material	Thermal expansion coefficient [/K]	Size [mm]
Base plate	Clearceram-Z	0.8×10^{-7}	ϕ 130
Steel ball	Bearing steel	11.6×10^{-6}	S ϕ 25.4

gear measuring machine, and determine the extent to which the kinematic error contributes to the tooth profile measurement deviation. This is because the kinematic error of the mechanism has systematic repetition, and it is expected that the accuracy of the tooth profile measurement deviation can be enhanced by numerically correcting the systematic error. In addition, reference was made to the tooth profile measurement deviation, which was quantified by calibration, and evaluation technology for quantifying the uncertainty of measurement in a 1-to-1 correspondence with a tooth profile of arbitrary specifications was established.

As a result of this evaluation technology, the difference in the measurement accuracy prior to performing a profile inspection can be quantitatively predicted, using gear measuring machines that have mutually different performance, and a traceability system, which is being viewed with importance in recent years, has been constructed. Because DBAs are calibrated by a national measuring organization, a gear measuring machine that is calibrated by a DBA is also traceable to a national standard. In this paper, the method of quantifying the uncertainty of measurement of the abovementioned tooth profile of arbitrary specifications is described in the sequence below.

(1) Making a geometrical model of measurement using DBAs, and making a formula for obtaining a solution
(2) Uncertainty analysis of the tooth profile measurement deviation obtained by calibration
(3) Method of tooth profile measurement uncertainty simulation using the results of uncertainty analysis of tooth profile measurement deviation

2. Principle of Calibration Using a Double Ball Artifact

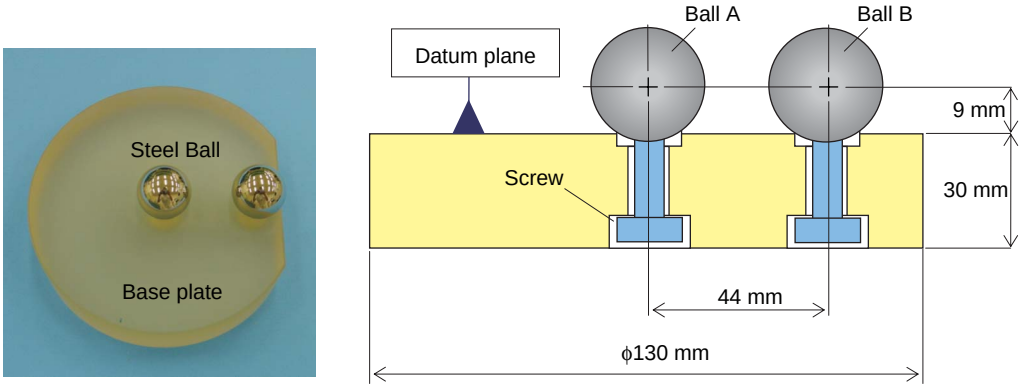
2.1. Design of a Double Ball Artifact

Figure 1 shows a schematic diagram of a DBA. In the datum plane of the DBA, the two balls are located as shown in Fig. 1(b). During measurement, balls A and B are considered to be a shaft center perpendicular to the datum plane, and an involute gear profile, respectively, and are made to function accordingly. For this reason, the distance between the centers of balls A and B should be determined with high accuracy.

Table 1 shows the basic specifications of the fabricated DBA. The base plate uses extremely low expansion material Clearceram to minimize the thermal deformation of the center distance between A and B, which depends on the measurement environment. Balls are used because precision machining is easy, a highly accurate profile can be easily obtained, and calibration that is traceable to a national standard has been realized.

2.2. Making a Model of the Principle of Calibration, and Method of Obtaining a Solution

Figure 2 shows a schematic diagram of a model obtained when a DBA is installed on a gear measuring



(a) Picture of DBA (b) Cross section of DBA

Fig. 1 Schematic of produced DBA

machine, and Fig. 3 is a photograph of the actual layout. The layout is such that the center position of the rotary table of the gear measuring machine coincides with the position of the center o of ball A of the DBA, and minute layout errors are numerically corrected. Based on this layout, when the center of ball B moves from position a, where it used to be, prior to the start of the measurement, to position c with rolling angle ε, the probe scans line l_1, which touches the base circle radius r_b, parallel to the y axis. However, in actual fact, the x axis has a positioning error e_x, so the probe moves along line l_2.

At this time, the y coordinate of the probe position of which the rolling angle e is a function is expressed by Eq. (1), where the y coordinate of center point c of ball B is y_c, and the y component from point c to the center position of the probe touching ball B is ΔY.

In the case where it is assumed that there is no error in the positioning of the measuring machine and the form of the probe, and the probe scans line l_1 while touching the ideal involute, if the radius of the probe is r_p, the y coordinate of the center of the probe is expressed by Eq. (2).

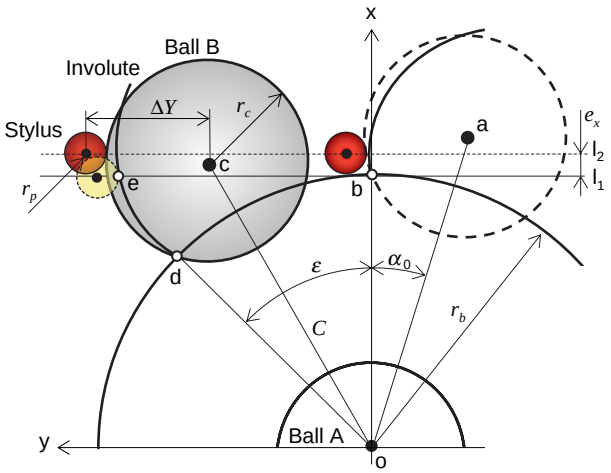


Fig. 2 Schematic model of DBA alignment on gear measuring machine

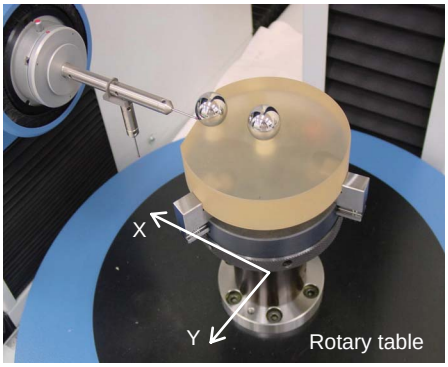


Fig. 3 Picture of DBA alignment on gear measuring machine

From Eqs. (1) and (2), the difference Δf between Ys and Y_1 is defined as the deviation between the arc of the ball and the involute form, as shown in Eq. (3).

$$\begin{aligned} Y_S &= f(\varepsilon) \\ &= Y_c + \Delta Y \\ Y_c &= C\,Sin\,(\varepsilon - \alpha_0), \\ \Delta Y &= \sqrt{(r_c + r_p)^2 - (r_b + e_x - C\,Cos\,(\varepsilon - \alpha_0))^2} \end{aligned} \quad , \quad (1)$$

Where,
C: Master ball center distance
α_0: Initial angle of rotary table
ε: Rolling angle
e_x: x axis positioning error
r_c: Master ball radius
r_p: Probe radius
r_b: Base circle radius

$$Y_I = r_b \cdot \varepsilon + r_p \quad (2)$$

$$\Delta f = Y_S - Y_I \quad (3)$$

In this model, the initial angle of the rotary table is used as a parameter, hence compared to the Kondo model[2], it is stated simply, and is advantageous in that the parameter estimation calculation process and uncertainty analysis can be simplified.

In Eq. (1), the initial angle α_0 and x axis positioning error e_x have errors with respect to a nominal value determined from the design value of the mechanism, hence they are used as parameters that perform calibration simultaneously. The theoretical value vector and the observed value vector of the form deviation of Eq. (3) acquired with respect to the continuously changing rolling angle ε are $\Delta \boldsymbol{f}_{Theo}$ and $\Delta \boldsymbol{f}_{obs}$, respectively. If the difference between these vectors is defined as vector $\boldsymbol{Y}_{obs}$ in Eq. (4), it will be feasible to arrange simultaneous equations concerning the unknown parameter p to be estimated. If the Jacobian matrix comprising the partial differential coefficient of $\boldsymbol{p}$ in Eq. (4) is defined as $\boldsymbol{A}$[3], a design value will be assigned to $\boldsymbol{p}$ as the initial value, and a convergence value of $\boldsymbol{p}$ will be obtained from the non-linear least squares method (Gauss-Newton method), which updates the value as $\boldsymbol{p}^+$ according to Eq. (5). Here, the suffix t of the matrix indicates a transposition, and $\boldsymbol{S}$ indicates the error matrix of $\boldsymbol{Y}_{obs}$. In this analysis, the error propagation to the parameter estimation of the measurement is not taken into account, so $\boldsymbol{S}$ is a unit matrix.

$$\boldsymbol{Y}_{obs} = \Delta \boldsymbol{f}_{obs} - \Delta \boldsymbol{f}_{Theo},\ \boldsymbol{Y}_{obs} = f(\boldsymbol{p}),\ \boldsymbol{p} = \begin{pmatrix} \alpha_0 \\ e_x \end{pmatrix} \quad (4)$$

$$\boldsymbol{p}^+ = (\boldsymbol{A}^t \boldsymbol{S}^{-1} \boldsymbol{A})^{-1} \boldsymbol{A}^t \boldsymbol{S}^{-1} \boldsymbol{Y}_{obs},\ \boldsymbol{p} = \boldsymbol{p} + \boldsymbol{p}^+ \quad (5)$$

Table 2 Setting condition for DBA measurement parameters

Parameter	Set value	Estimated value	Unit
Module	7.7639	—	mm
Number of teeth	12	—	—
Radius of base circle	43.7741	—	mm
α_0	16.63802	16.63799	deg
e_x	0	0.4	μm

In the parameter that is to be evaluated as a kinematic error in the gear measuring machine, there exists a systematic positioning error e_y of the y axis. Here, in order to calibrate $\boldsymbol{p}$ and e_y simultaneously, e_y was modeled according to Eq. (6) from an approximation polynomial, using the rolling angle e, which is based on the rotary table. In Eq. (6), $\boldsymbol{B}$ and β are a basis function matrix, based on a Legender function[4], and its coefficient vector, respectively.

At this time, the observed value $\boldsymbol{Y}_{ey}$ consisting of $\boldsymbol{Y}_{obs}$ from which the effect of estimation value $\boldsymbol{p}$ has been removed is equivalent to the positioning error on the y axis, so this relationship is shown in Eq. (7). Note that e_y can be estimated using the least squares method from Eq. (7).

$$e_y = \boldsymbol{B}\boldsymbol{\beta},\ \boldsymbol{B} = (B_0(\varepsilon)\ \cdots\ B_n(\varepsilon)),\ \boldsymbol{\beta} = \begin{pmatrix} \beta_0 \\ \vdots \\ \beta_n \end{pmatrix} \tag{6}$$

$$\begin{aligned} \boldsymbol{Y}_{ey} &= \boldsymbol{Y}_{obs} - \boldsymbol{A}\boldsymbol{p} \\ &= \boldsymbol{B}\boldsymbol{\beta} \end{aligned} \tag{7}$$

2.3. Result of Estimating the Tooth Profile Measurement Deviation and Measuring Machine Kinematic Error

To acquire data for the purpose of estimating the tooth profile measurement deviation, a DBA having Table 1 specifications was used to set the initial values used in the gear specifications and unknown parameter estimation $\boldsymbol{p}$, as shown in Table 2. Figure 4 shows the theoretical curve Δf_{Theo} and measured curve Δf_{obs} in the settings of Table 2. In the results of Fig. 4, data obtained by suitably translating Δf_{obs} so that it coincides with Δf_{Theo} is used, and the result of calculating p from Eq. (5) is as shown in Table 2. It can be confirmed that there is a minute error in the positioning of the x axis and the rotary table. Also, the estimated value of $e_{y,}$ calculated from Eq. (7), is as shown in Fig. 5, and the observed data Y_{ey} is approximated with good accuracy.

With this method, multiple kinematic errors, such as the translation and rotating components of the mechanism of the measuring machine, can be simultaneously estimated from a single observed result, and it is also easy to statistically describe the effect that the error $\boldsymbol{S}$ in the observed value in Eq. (5) has on the reliability of the calculated kinematic error. On the other hand, the construction of a model and the calculation process tends to become complicated.

Compared to this method, the conventional method[5], which successively estimates each kinematic error value from multiple measurement methods permits a model to be simply constructed; however, the cost of each kinematic error measurement is high and explaining the statistical mutual relationship of the estimated kinematic

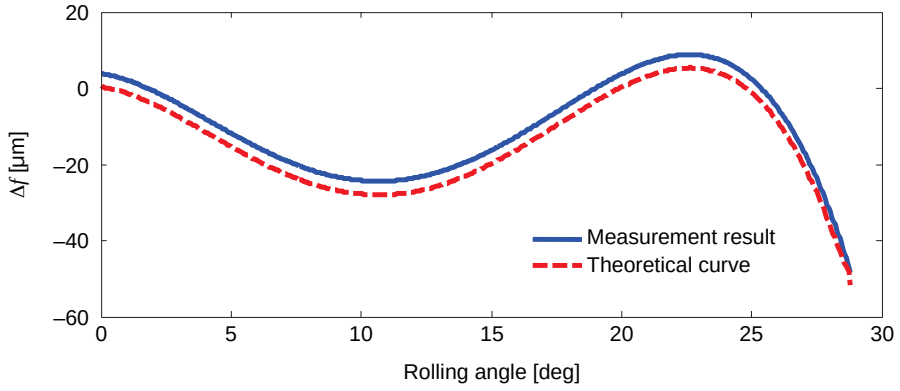


Fig. 4 Example of calibration measurement results

errors from multiple measurement data is challenging. The tooth profile measurement deviation means that the modeled parameters $\boldsymbol{p}$ and e_y simultaneously contribute to the measurement, so Fig. 6, which indicates the simultaneous contribution of $\boldsymbol{p}$ and e_y, is defined as the tooth profile measurement deviation f_{ref}. If e_y and f_{ref} in the figure are compared with each other, a difference in the absolute values can be confirmed.

In the calibration using DBA, the kinematic error in the mechanism of the measuring machine was deemed to be estimable, so the tooth profile measurement deviation and its mutual relationship were clarified quantitatively.

3. Quantification of the Uncertainty of the Tooth Profile Measurement Calibration Results

3.1. Double Ball Artifact Uncertainty Evaluation

Using the tooth profile measurement deviation estimated from calibration, the construction of a method of evaluating uncertainty of the tooth profile measurement of a gear that has arbitrary specifications satisfying the following is studied.

(1) The calibration results should be traceable to a national standard.

(2) A method that minimizes the necessity for a preparatory test for making an uncertainty evaluation, and uses numerical calculations that can be easily developed on the production line. In this sub-section, the uncertainty that contributes to tooth profile measurement deviation that depends upon the double ball artifact is quantified.

The combined uncertainty of Δf in Eq. (3) is derived according to GUM[6] guidelines. Here, it is necessary that the combined standard uncertainty of Y_S and Y_1 be both known. Because Y_1 is a nominal value, only the combined standard uncertainty of Y_S in Eq. (1) is quantified.

The combined uncertainty of Y_S can be expressed as shown in Eq. (8), in which the uncertainty of the random component that depends upon the gear measuring machine is u_M and the uncertainty of the random component that depends upon the DBA is u_{DBA}. The standard uncertainty of parameter p is expressed as $u(p)$.

Here, because r_b is the nominal value of the base circle radius, it is not considered a source of uncertainty. Also, the uncertainty of temperature dependency is not taken into account in $U_{DBA.}$ This is because, even if the temperature change during measurement is assumed to be an excessive value of 1 K with respect to the DBA coefficient of linear expansion, 0.8 x 10^{-7}/K, the thermal deformation with respect to the evaluated ball distance of

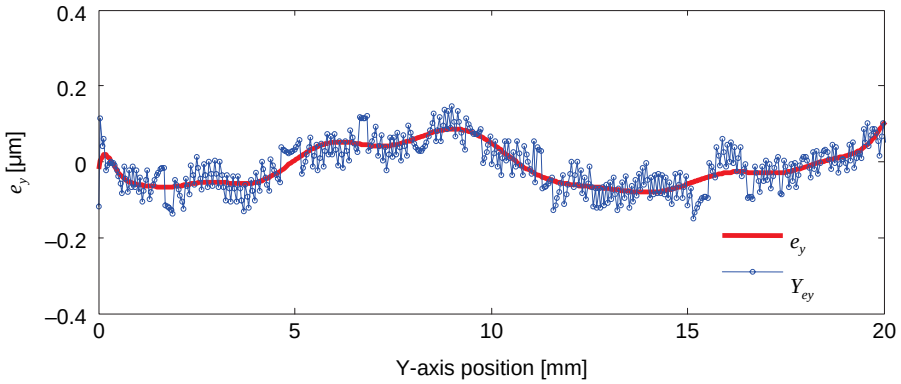


Fig. 5 Estimation result of Y-axis positioning error

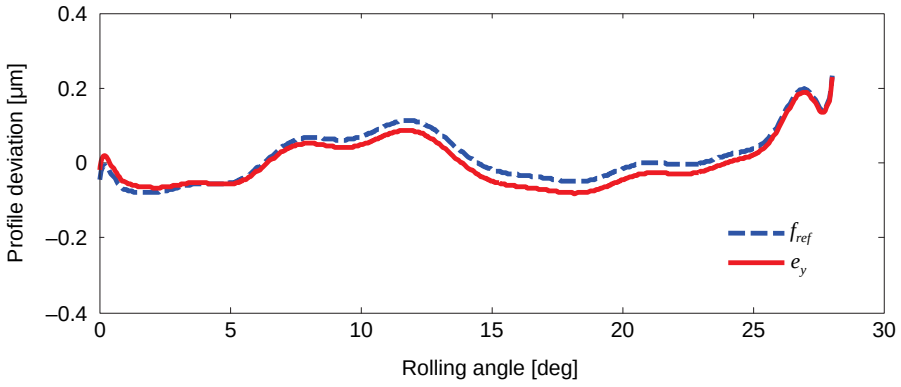


Fig. 6 Estimation result of tooth profile deviation

Table 3 Sources of DBA uncertainty

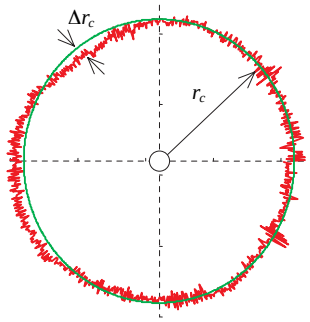
Uncertainty sources	Symbol	Standard uncertainty	Type of distribution	Type
Length between two master spheres	C	0.13 μm	Normal	B
Radius of master sphere	r_c	60 nm	Normal	B
Thermal coefficient of DBA	α_{DBA}	0.1×10^{-7}/K	Rectangular	B
Temperature of DBA during measurement	t_{DBA}	1 K	Rectangular	A

44 mm is 4 x 10^{-3} μm, which is so small that it can be ignored.

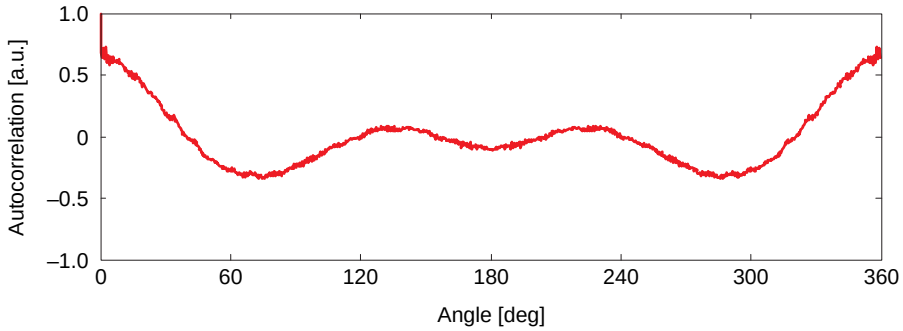
$$
\begin{aligned}
u^2(Y_s) &= u_M^2 + u_{DBA}^2 \\
u_M^2 &= \left(\frac{\partial Y_s}{\partial e_x}\right)^2 u^2(e_x) + \left(\frac{\partial Y_s}{\partial e_y}\right)^2 u^2(e_y) + \left(\frac{\partial Y_s}{\partial r_p}\right)^2 u^2(r_p) + \left(\frac{\partial Y_s}{\partial \varepsilon}\right)^2 u^2(\varepsilon) \\
u_{DBA}^2 &= \left(\frac{\partial Y_s}{\partial r_c}\right)^2 u^2(r_c) + \left(\frac{\partial Y_s}{\partial C}\right)^2 u^2(C)
\end{aligned}
\tag{8}
$$

Concerning Eq. (8), the uncertainty source of DBA and its standard uncertainty are summarized in Table 3. The accuracy of the radius r_c in the red path of the master ball was made 60 nm, based on the results of research[7] involving measurement of the roundness of a ball of the same size and grade as that of the ball used.

Figure 7(a) shows the form of the ball's red path acquired using a coordinate measuring machine that had a measurement accuracy of u = 0.6 + L/1000 μm and L: Evaluation length mm. Also, if the form data and its residual from the least squares circle with respect to the form data is defined as Δr_c, the autocorrelation with respect to the Δr_c angle becomes that shown in Fig. 7 (b), and periodic correlation with respect to the phase in which it anticipates the machining history can be seen on the surface of the ball. However, because the measuring accuracy of the ball surface form using a coordinate measuring machine is insufficient for an evaluation accuracy of the roundness of a 60 nm ball, and because the existence or otherwise of surface form correlation does not contribute very much to u_{DBA}, correlation is ignored in this analysis.



(a) Form deviation of master ball



(b) Autocorrelation of master ball form deviation

Fig. 7 Form deviation and autocorrelation of master ball on DBA

Taking the foregoing into consideration, when the combined standard uncertainty u_{DBA} (k = 1, k: coverage factor) that conforms to Eq. (8) is calculated, the result becomes that shown in Fig. 8(a). From Fig. 8(a), the reliability range due to u_{DBA} of curve Δf is as shown in Fig. 8(b). The maximum contribution to the uncertainty of u_{DBA} corresponds to the center distance of the ball, and the center distance is evaluated by a laser interferometer. Consequently, regarding Δf of Eq. (3), a profile standard that is traceable to the length is realized.

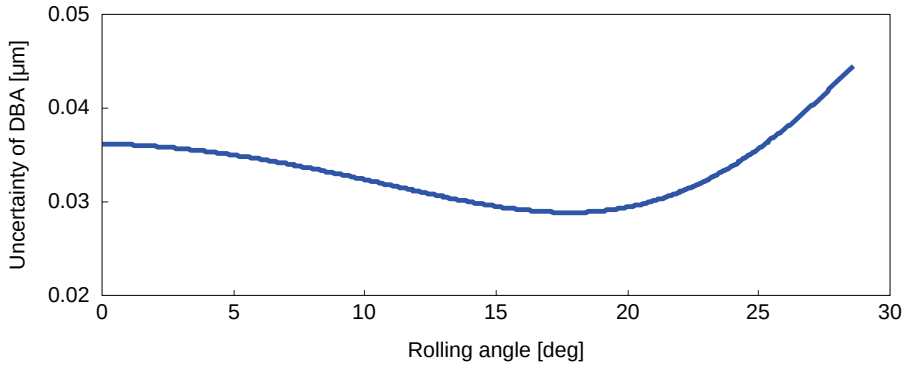
3.2. Evaluation of Uncertainty of Gear Measuring Machine

The uncertainty sources that are dependent on the gear measuring machine are e_x, e_y, r_p, and ε from the tooth profile measurement model in Eq. (1). If the standard uncertainty in these parameters can be determined, the uncertainty of tooth profile measurement by the measuring machine can be evaluated from Eq. (8) based on the error propagation rule.

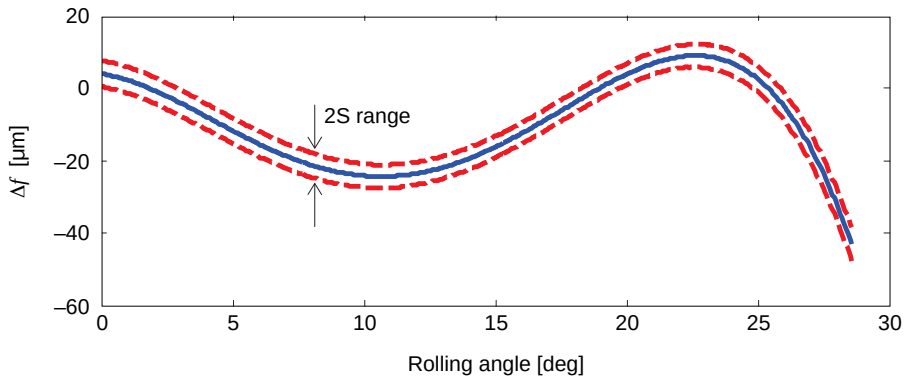
As an evaluation method that does not rely on the error propagation rule, a method that estimates the final measurement uncertainty by means of simulation that simultaneously generates suitable random numbers for each of the model uncertainty sources is also being developed[8].

Regarding the abovementioned simulation method, it is necessary to evaluate such uncertainty sources as the positioning error of the guide and the positioning error of the rotary table in advance, by means of an external measuring machine such as a laser interferometer, and there are cases in which the uncertainty of the evaluation machine is added to the uncertainty of each factor, resulting in an excessively high evaluation. Also, it is impractical for the user to perform this type of evaluation work because of cost limitations.

Here, because simple, repetitive measurement of DBAs can be performed in a short time, the uncertainty acquired from DBAs is estimated as the uncertainty item u_M of the random component that depends upon the gear measuring machine in Eq. (8). u_M has a variation that depends upon the rolling angle as shown in Fig. 9, and has an average uncertainty $u_{M(Ave)}$ of 0.035 μm. Because the absolute value of u_M is minute, and because it has no marked systematicity with respect to phase, DBA uncertainty, u_{DBA}, and the combined standard uncertainty of u_M, that is, the uncertainty u_{com} of the tooth profile measurement deviation, are constant regardless of the angle of rotation, and are defined in Eq. (9). Here, u_{com} is an uncertainty of approximately 0.05 μm (k = 1) as shown in Fig. 9.



(a) Uncertainty of DBA depending on rolling angle



(b) Theoretical curve and uncertainty resulting from DBA

Fig. 8 Uncertainty of DBA estimated from calibration certification of NMIJ (National Metrology Institute of Japan)

$$u_{com} = \sqrt{u_{M(Ave)}^2 + u_{DBA}^2} \quad (9)$$

3.3. Monte Carlo Simulation of Tooth Profile Measurement Deviation

Using the uncertainty u_{com} of the quantified tooth profile measurement deviation, the reproduction by means of a Monte Carlo simulation of the repetitiveness with respect to the tooth profile measurement deviation f_{ref} estimated as shown in Fig. 6 has been studied. An outline of the principle of the simulation is as shown in Fig. 10, and consists of the following items. In this sub-section, stages (2) to (4) are formulated.

(1) The tooth profile measurement deviation f_{ref} estimated from measurement performed using a DBA is taken as a reference value.

(2) A uncertainty matrix of the tooth profile measurement deviation that bears a 1-to-1 correspondence to the phase of the reference value f_{ref} is constructed.

(3) Measurement random errors are generated by singular value decomposition of the uncertainty matrix.

(4) Data of the tooth profile measurement deviation obtained by combining the reference value f_{ref} and the random measurement errors is reproduced.

In the case where the number of data components of the reference value f_{ref} is defined as n, if the n x n unit matrix is defined as $\boldsymbol{I}$, the calibration uncertainty matrix Σ is expressed as Eq. (10) from Eqs. (8) and (9).

If $\boldsymbol{U}$ and $\boldsymbol{V}$ are defined as orthogonal matrices, the result of a singular value decomposition of the uncertainty matrix Σ becomes as shown in Eq. (11). The diagonal elements of matrix $\boldsymbol{D}$ are the square of the respective singular values s, and have properties that correspond to the uncertainty of the mutually uncorrelated normal distributions.

If each column element of matrix $\boldsymbol{V}$ is defined as $\boldsymbol{V}_i$ (i: 1 to n), one set of measurement random errors in a 1-to-1 correspondence with the phase of the reference value f_{ref} can be generated by performing one trial of Eq. (12). Here, the Monte Carlo simulation indicates the process

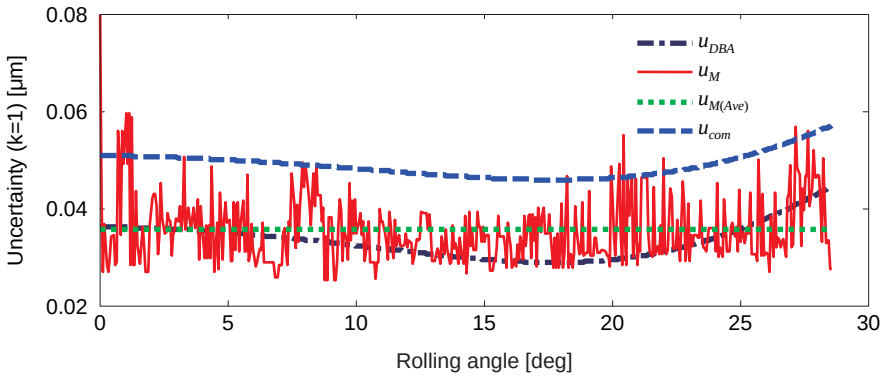


Fig. 9 Combined standard uncertainty of tooth profile measurement

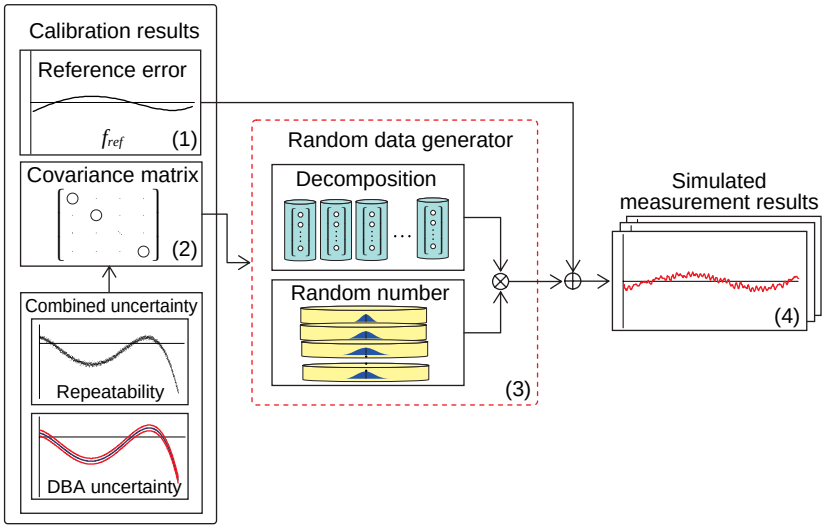


Fig. 10 Statistic simulation method for evaluating uncertainty of tooth profile calibration

that generates normal random numbers at standard deviation 1 independently, for each probability variable $\boldsymbol{X} = (x_1 \ \cdots \ x_n)$ of the expected value of zero. Note that there is no limit to the number of simulation trials.

$$\boldsymbol{\Sigma} = (u_M^2 + u_{DBA}^2)\,\boldsymbol{I} \approx u_{com}^2\,\boldsymbol{I} \tag{10}$$

$$\boldsymbol{\Sigma} = \boldsymbol{U}\boldsymbol{D}\boldsymbol{V}^t,\ \boldsymbol{D} = \begin{pmatrix} s_1^{\,2} & & \\ & \ddots & \\ & & s_n^{\,2} \end{pmatrix} \tag{11}$$

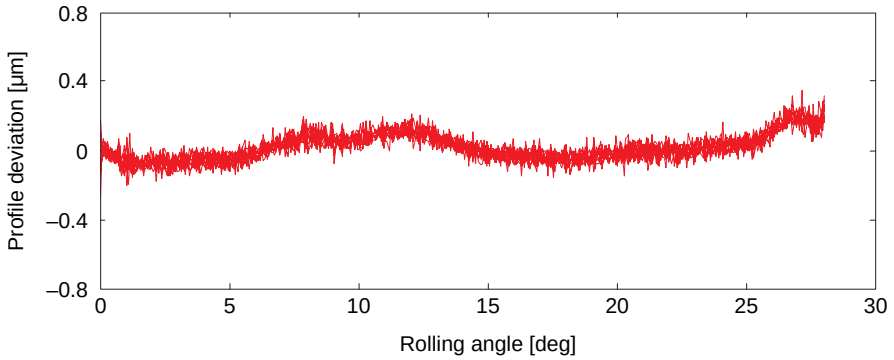
$$\boldsymbol{f}_{ran} = s_1 \cdot x_1 \boldsymbol{V}_1 + s_2 \cdot x_2 \boldsymbol{V}_2 + \cdots + s_n \cdot x_n \boldsymbol{V}_n,\ \boldsymbol{V} = (\boldsymbol{V}_1 \boldsymbol{V}_2 \cdots \boldsymbol{V}_n) \tag{12}$$

As an example of a simulation trial, Fig. 11 shows 10 sets of pseudo tooth profile measurement deviation data generated by combination due to 10 trials of f_{ran} and reference value f_{ref}. Compared to the results of 10 cycles of measurement shown in Fig. 11(a), the pseudo tooth profile measurement deviation data of Fig. 11(b) also exhibits a tendency to be systematic, however, because DBA uncertainty is added, the behavior of the random component is large, and all of the uncertainty of the uncertainty sources occurs simultaneously.

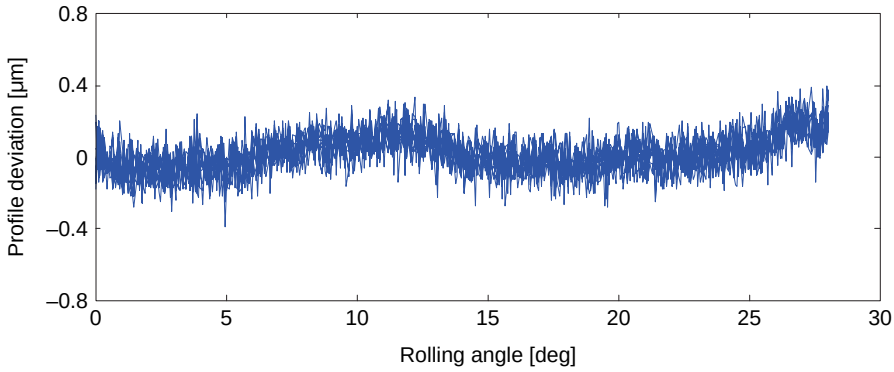
The uncertainty of the evaluation of the DBA ball distance used was 0.13 µm (k = 1), however it has been reported[7] that when publicly known technology is used, a ball distance of 0.01 µm (k = 1) is achieved. If the ball distance is evaluated at 0.01 µm, it is feasible to estimate that the uncertainty of the pseudo tooth profile measurement deviation of Fig. 11(b) is several percent on the low side.

4. Tooth Profile Measurement Uncertainty Analysis

The tooth profile measurement simulation results and the tooth profile measurement with respect to arbitrary specifications that can be estimated from these results are converted into uncertainty values. The minimum to maximum shift range y_{min} to y_{max} of guide y, evaluated by calibration of the measuring machine from the DBA specification of Table 3, extends from approximately 0 to 25 mm. If module m used for the gear is made $0.5 \le m \le 3$ mm in steps of 0.5, for example, and the pitch circle diameter D_0 is made $20 \le D_0 \le 120$ mm in steps of 20, the shift range of the y axis needed for performing these inspections becomes as shown in Fig. 12. The range of gear specifications that satisfies y_{max} is $D_0 \le 80$ mm and



(a) Profile deviation repeatability observed by DBA



(b) Profile deviation repeatability generated by simulation

Fig. 11 Comparison of tooth profile deviation between observation and simulation

$m \le 2.5$ mm. Consequently, here the uncertainty of gear measurement that simultaneously satisfies $20 \le D_0 \le 80$ mm and $0.5 \le m \le 3.0$ mm is quantified.

When the combination of an arbitrary m and D_0 is determined, the rolling angle range ε_{range} and shift range Y_{range} of the guide y necessary for scanning the probe from the dedendum to the addendum are determined as Eqs. (13) and (14), and the shift range of the guide y equivalent to the inspection range of the profile conforming to JIS B1702-1 and ISO 1328-1 is determined.

$$\varepsilon_{range} = \sqrt{\left(\frac{r_t}{r_b}\right)^2 - 1},\ r_b = r_0 Cos(\alpha) \tag{13}$$

Where,
r_b: Base circle radius
r_t: Addendum circle radius
r_0: Pitch circle diameter
α: Pressure angle

$$Y_{range} = r_b \cdot \varepsilon_{range} \tag{14}$$

Figure 13 shows the results of referring to the tooth profile measurement deviation f_{ref}, which corresponds to the shift range of guide y, and performing a tooth profile measurement simulation. Here, five trials were performed, and for each simulation trial, the least squares straight line of the mean profile and parameters of the profile deviation, the total profile deviation F_α, profile form deviation $f_{f\alpha}$, and the profile angle deviation $f_{H\alpha}$, all of which were standardized by ISO 1328-1, were calculated, then the standard deviation corresponding to the number of trials was calculated. The uncertainty is as shown in Eq. (15) where the average value of the total profile deviation, for example, is $\overline{F}_\alpha$, and the standard deviation is $\sigma(F_\alpha)$.

$$u(F_\alpha) = \overline{F}_\alpha + 2\sigma(F_\alpha) \quad (k=2) \tag{15}$$

As an example of the analysis results, Fig. 14 indicates F_α, $f_{f\alpha}$, and $f_{H\alpha}$. It can be confirmed that F_α and $f_{f\alpha}$ have linearity with respect to the pitch circle diameter, module, and uncertainty.

The merits of this uncertainty evaluation, based on tooth profile measurement calibration and calibration simulation, are as follows.

(1) The necessary preparatory test and calibration work for evaluating the uncertainty of the measuring machine were minimized, and it was feasible to simulate tooth profile measurement by utilizing an algebraic model of the statistical nature of measurement in the tooth profile measurement deviation evaluation, and by calculation, thus eliminating the work of statistical evaluation by measurement work.

(2) The necessary accuracy with respect to a profile of arbitrary specifications could be determined in advance, by simulating tooth profile measurement, and the uncertainty for each inspection result could also be guaranteed.

(3) The DBA uncertainty is taken into consideration in the

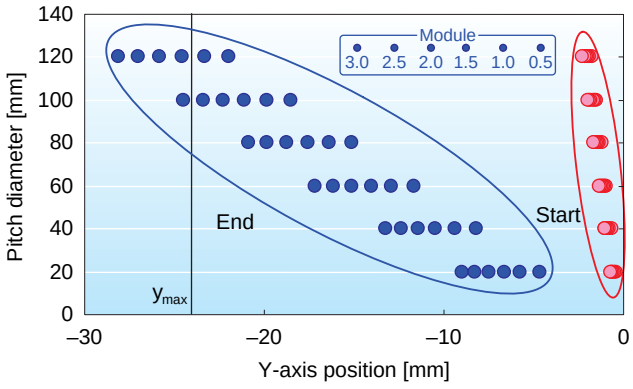


Fig. 12 Range of Y-axis movement for tooth profile measurements

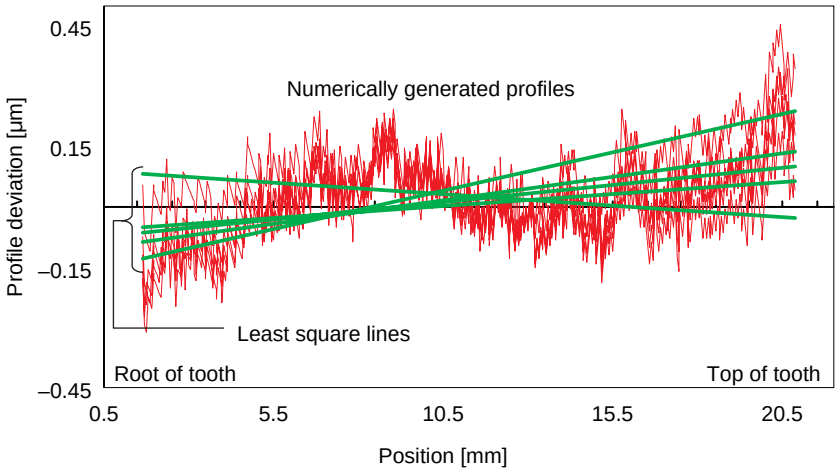
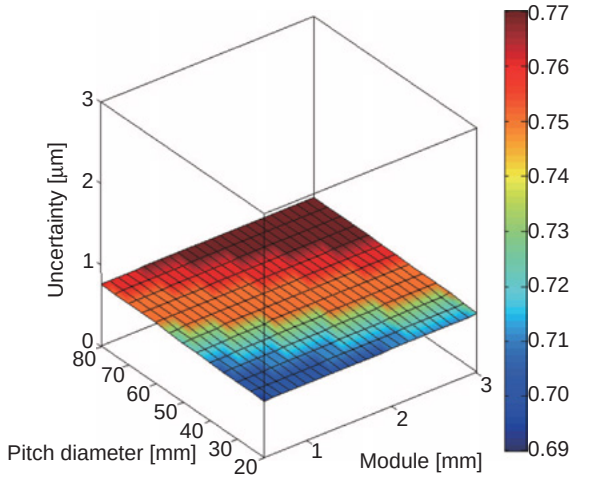
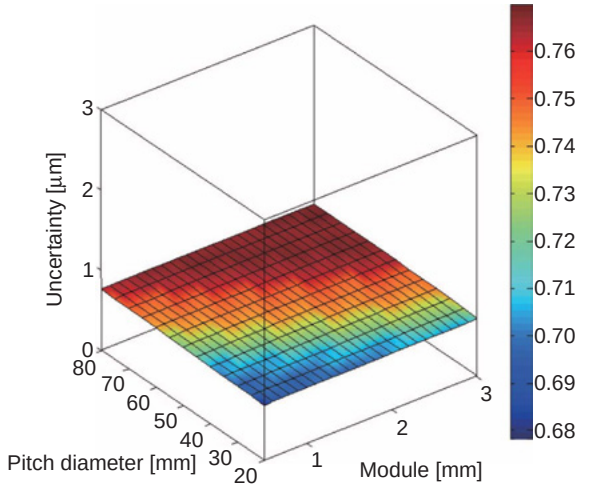


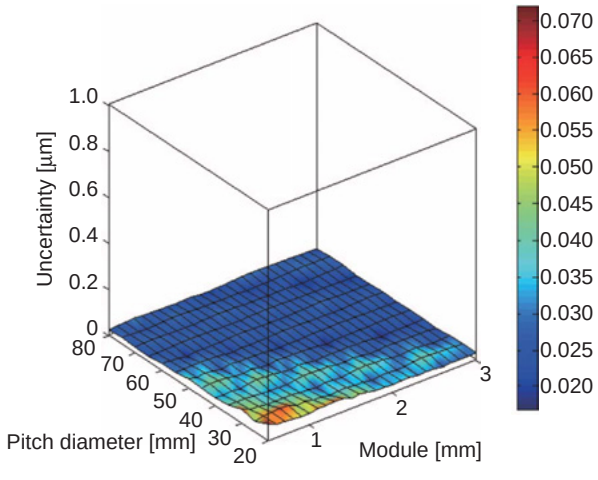
Fig. 13 Generated tooth profile deviation and average tooth profiles by simulation



(a) Uncertainty evaluation for F_α



(b) Uncertainty evaluation for $f_{f\alpha}$



(c) Uncertainty evaluation for $f_{H\alpha}$

Fig. 14 Examples of uncertainty evaluation (k=2)

uncertainty of the analyzed profile deviation parameter, which is traceable to a national standard, so the difference in accuracy between multiple measuring machines is uniformly evaluated.

5. Conclusion

Calibration of tooth profile measurement was performed using DBAs. From the calibrated results, evaluation technology that quantifies the uncertainty of tooth profile measurement in a 1-to-1 correspondence with a tooth profile of arbitrary specifications was established. The conclusions obtained are as follows.

(1) Modeling of calibration using DBAs and a method of estimating the kinematic error in the mechanism of a measuring machine were formulated. The quantitative mutual relationship between the profile measurement deviation and kinematic error were clarified by means of this method.

(2) The uncertainty of tooth profile measurement was algebraically modeled, and singular value decomposition was used to formulate a method of simulating a tooth profile measurement that has traceability, from the computed results.

(3) From the simulation, a method of evaluating the uncertainty of the tooth profile deviation parameter in the measurement of a tooth profile of arbitrary specifications was derived.

References

(1) Kubo, A., Komori, M.: Kyoukitansin, No. 3 p. 1-2 (2004) (in Japanese)

(2) Kondo, K.: A new proposal of primary artifact for calibration of gear measuring machines and calibration method, The Japan Society of Mechanical Engineers Bibliography, Vol. 8, p. 508-515 (2005)

(3) Nakagawa, T., Koyanagi, Y.: Saisho Jijyou Hou niyoru Jikken Deeta Kaiseki, Toukyou Daigaku Shuppan, p. 35 (1982) (in Japanese)

(4) Shinozaki, H., Matsushita, Y.: Ouyou Suuchi Keisanhou Nyuumon (Jyou), Korona Sha, p. 175 (1976) (in Japanese)

(5) Zhang, G.: A Displacement Method for Machine Geometry Calibration, Annals of the CIRP, Vol. 37, No. 1, p. 515-517 (1998)

(6) BIPM, IEC, IFCC, ISO, IUPAC, IUPAP, OIML: Guide to the expression of uncertainty in measurement, ISO, First edition (1993)

(7) Kondo, Y., Noguchi, S., Kondo, K., Osawa, S., Naoi, K., Takatsuji, T., Kurosawa, T.: Tooth Form Evaluation Using Ball Artifact: Development of a Measuring Instrument of Ball Center Distance Traceable to National Standard of Length, Journal of the Japan Society for Precision Engineering, Vol. 71, No. 10, p. 1260-1265 (2005)

(8) Tanaka, H., Shimojo, M., Kajitani, M., Sato, T., Takeda, R., Kojima, M., Yuzaki, M., Kato, S., Shibuya, Y., Kondo, T.: Evaluation of measurement uncertainty in gear measuring instruments by the Monte Carlo simulation, The American Society for Precision Engineering, Proceedings of the Eighteen Annual Meeting, p. 395-398 (2003)

■ Author ■


Kenta UMETSU


Wataru ISHIDO


Kinya FUJIWARA

Development of Moment Assist and System Weight Compensation Control for Wearable Walking Assist System

Yasushi IKEUCHI*

ABSTRACT

With the aim of realizing a “user-friendly walking assist system” to support the lifestyles of elderly persons, a new assist control method was developed that combines assist functionality for the user with system weight compensation.

Different computational processing models were developed for the user and the unit. A processing method was proposed in which inverse dynamics analysis is used to calculate the assist moment from user processing and the system weight compensation from unit processing. A floor reaction force for the system weight compensation processing method was established to allow system weight compensation control. A high degree of stability in the vector orientation of the floor reaction force for system weight compensation was shown in tests. In addition, this method enables estimation of the user’s floor reaction force vector by applying the user’s dynamics model. Thus, it was shown that there are good prospects for the realization of a user-friendly walking assist system that does not employ floor reaction force sensors in the system.

1. Introduction

It is predicted that the aging of Japanese society will continue to increase in pace in the future. The elderly tend to withdraw from participation in society when they begin to lose confidence in their health or physical strength[1]. Taking this social background into consideration, Honda is seeking to contribute to supporting the lives of the elderly by conducting research on a wearable walking assist system that reduces the load on the body during movement. Prioritizing the comfort of the user, the goal of the research is to realize a “user-friendly walking assist system.” Research to date has focused on enabling the motion of the system to follow the user’s intentions, and has sketched an outline of a system using a proposed joint moment assist method that estimates joint moment as the user is moving and provides assist power depending on the estimated joint moment[2].

In an attempt to increase the user-friendliness of the system, the goal of the research discussed in this paper was to help prevent the user from having to support the weight of the system, through the development of a new control method that enables the weight of the system to be compensated at the same time as assist is provided to the user.

2. Conventional Methods and Associated Issues

The use of inverse dynamics analysis[2, 3] and the use of measurements of the electromyography (EMG) of the joints[4] are the two standard control methods used in joint moment assist. The method using inverse dynamics analysis[5] roughly models the user using a rigid body link model. Based on this model, the method uses translation motion Eq. (1) to calculate the force on the distal end of the user’s legs (i.e. the floor reaction force) and the reaction forces on the user’s ankle, knee, and hip joints, in that order. Using these joint reaction forces, the method employs a rotational motion equation to calculate the moment of the user’s ankle, knee, and hip joints. Assist is provided to the joints based on these joint moments.

* Fundamental Technology Research Center

$$\mathbf{F}_{foot_distal} = \mathbf{Frf}$$
$$\mathbf{F}_{n_proximal} = m_n(\ddot{\mathbf{u}}_{n_G} + \mathbf{G}) - \mathbf{F}_{n_distal} \quad (1)$$
$$\mathrm{F}_{n+1+_distal} = -\mathbf{F}_{n_proximal}$$

F: Force vector on ends of links
Frf: Floor reaction force vector
$\mathbf{u}_G$: Vector at position of center of gravity
G: Vector of acceleration due to gravity
m: Mass
n: Link number
distal: Distal end (Link end furthest from hips)
proximal: Proximal end (Link end closest to hips)

This method requires multiple sensors to determine the floor reaction force vector and the direction of the center of gravity to be used in Eq. (1). These sensors should be positioned in the user's shoes and on the system body. A number of issues should therefore be addressed before this method can be used in practice, including optimization of the shape of the sensors, and their miniaturization, to attempt to help prevent them from causing discomfort to the user.

The other method, which measures the electromyography of the user's muscles, estimates muscular tension from electromyography and provides joint assist on that basis. This method requires EMG sensors to be directly applied to the user's skin, and the issues here are to develop EMG sensors that place a minimal burden on the user, and to determine an appropriate method of placing the sensors.

Whichever method is used, to further reduce the burden on the user, it is important to attempt to help prevent the user from having to support the weight of the unit. A control method that has been developed to reduce the burden on the user when shifting loads from place to place[6] represents one example of the use of control for system weight compensation. This system switches between a dynamic mode, when supporting one leg (single support), and a static mode, when supporting both legs (double support). The issues in this system are to achieve continuity when switching between modes, and to enable compensation for dynamic motion, even when the system is providing double support.

3. A User-friendly Assist Method

Figure 1 shows the relationship between joint moment assist and the user. When the user moves, the nerves in his or her brain and spinal cord send signals causing the

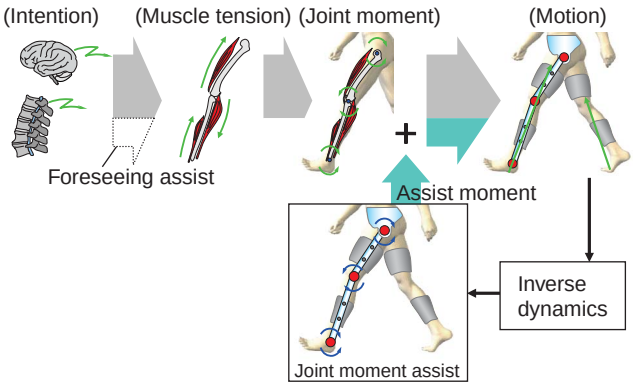


Fig. 1 Human intention and moment assist

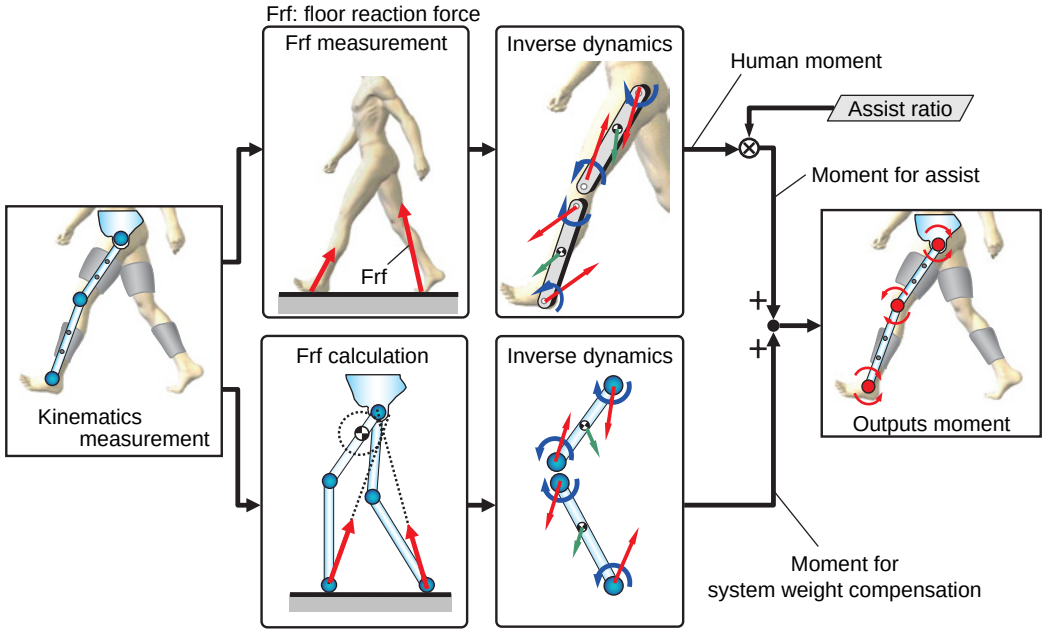


Fig. 2 Assist and system weight compensation

muscles to contract. This force of contraction generates a rotational moment around the axis of the joint, and the joint moves. The joint moment is considered to reflect the intention of the user. If this joint moment could be determined by inverse dynamics analysis, and assist moment provided on this basis, it would enable the system to move as the user intended. Furthermore, balancing this joint moment assist with system weight compensation would produce a user-friendly assist system.

One potential method of achieving this would be to regard the user and the system as an integrated whole, and to apply inverse dynamics analysis using a dynamics model incorporating physical properties, including the mass and moment of inertia of the thigh and shin, in order to calculate actuator output values that include compensation for the weight of the unit. However, when the physical characteristics of the system and the user (position of center of gravity of joints, etc.) differ in this integrated dynamics model, assist and system weight compensation cannot be accurately controlled. Given this, in order to realize a form of system weight compensation control suited to a walking assist system, this research proposes a method in which the user and the system are considered separately, separate dynamics models are defined, and inverse dynamics analyses conducted for each.

The flow of this control method is shown in Fig. 2. There are two flows: The "user-side" calculation that determines the assist moment to be provided to the user, and the "system-side" calculation that determines the moment for system weight compensation. In order to estimate the user's joint moment, in the user-side, flow sensors are first used to determine the floor reaction force received by the user's leg from the ground, and inverse dynamics analysis is conducted using this floor reaction force and motion data (the angle of the user's joints, etc.). The joint moment obtained from this calculation is multiplied by a proportion between 0 and 1 to determine the assist moment.

To calculate the moment required for system weight compensation, the system-side flow first determines the floor reaction force for system weight compensation received by the leg section of the system from the floor, and conducts inverse dynamics analysis using this floor reaction force and motion data (the angle of the joints in the unit, etc.).

The addition of the assist moment and the system weight compensation moment determined in this way gives the target value for the actuator output moment.

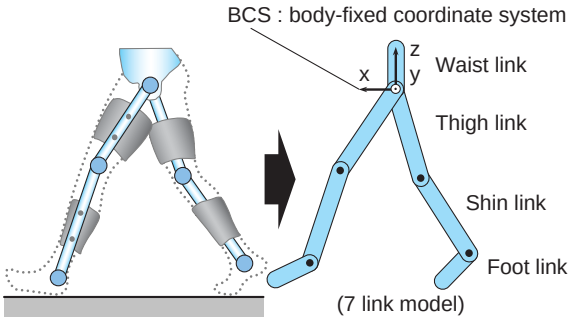


Fig. 3 Link modeling of system

4. Calculations for System Weight Compensation

4.1. Dynamics Model and Coordinate System

For dynamics calculations, the system is considered to be made up of rigid body links. As Fig. 3 shows, calculations use a seven-link model considered separately from the user, consisting of hip, right thigh, left thigh, right shin, left shin, right foot, and left foot links.

A body-fixed coordinate system (BCS) centered on the system is employed in the calculations. The point of origin of this coordinate system is the center point of the hip joints of the system. The z axis is extended in the proximal direction of the hip link, the y axis is extended to the right, and the x axis is extended in the direction of the cross product of the z and y axes. The BCS is a non-inertial coordinate system[7] capable of rotational and translational motion, and uses the equation of motion shown as Eq. (2) for rotational motion. Equation (3) is used for translational motion. The coriolis and centrifugal forces generated by the rotation of the coordinate system are low, compared to the translational inertia in this translational motion equation, and these forces are therefore not considered.

$$I \times \dot{\omega} = M - I \times \dot{\omega}_o \quad (2)$$

$$m \times \ddot{u}_G = F - m \times acc_o \quad (3)$$

I: Moment of inertia
m: Mass
M: Moment
F: Translational force
ω: Angular velocity
ω_0: Angular velocity of coordinate system
acc_0: Acceleration of point of origin of coordinate system

Absolute coordinate systems were not used for any of the equations in this research; all equations were defined in terms of non-inertial coordinate systems.

This makes data on angles from the vertical unnecessary, and enables a system to be constructed without the use of sensors to measure the direction of the force of gravity.

4.2. Calculation of System Floor Reaction Force required for System Weight Compensation

4.2.1. Concept of system weight compensation floor reaction force

System weight compensation should not require any

force from the user, and should function under static and dynamic operating conditions. The floor reaction force required for this type of operation is termed the system weight compensation floor reaction force.

When only one leg is being supported, a unique floor reaction force can be determined dynamically, if data on the movement of the system as a whole is available. However, as three examples in Fig. 4 show, when two legs are being supported, while the resultant force remains the same, there are an infinite number of combinations of the floor reaction force between the left and right legs. Given this, it was decided that new constraint conditions for the floor reaction force should be set.

4.2.2. Issues in previous method of calculation of floor reaction force

As Fig. 5 shows, in the initial method of calculation of floor reaction force[2], the floor reaction force vector during single support was calculated from acceleration data for the entire system. A constraint condition was applied during double support, in which the floor reaction force vector was considered to be moving in the direction of the center of gravity of the entire unit. However, when the entire unit is displaying angular acceleration motion around the center of gravity, the floor reaction force vector should have a moment arm in relation to the center of gravity, and therefore the direction of the floor reaction force vector during double support was inaccurate.

In addition, because of this inaccuracy, the direction of the floor reaction force vector was discontinuous when the system switched between single and double support. It was possible, as a result, that the system would not be able to compensate for its weight, and that the user would experience a feeling of discontinuity.

The direction of the floor reaction force vector also fluctuated during single support. This is conjectured to have been because variations in the results of the second-order differential equations, used to determine the acceleration of each link position, affected the acceleration data for the system as a whole, resulting in instability in the direction of the floor reaction force vector.

4.2.3. Constraint condition for floor reaction force vector that considers angular acceleration motion

In order to address the issues relating to the constraint condition in the previous calculation method, a constraint condition was proposed in which the system weight compensation floor reaction force vector had a moment

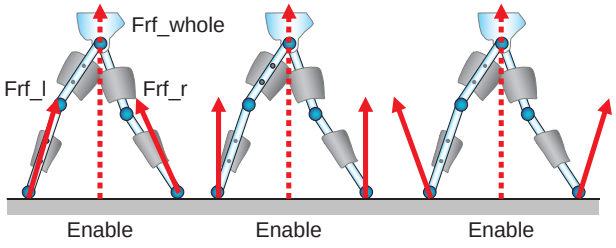


Fig. 4 Three examples of numberless floor reaction force patterns

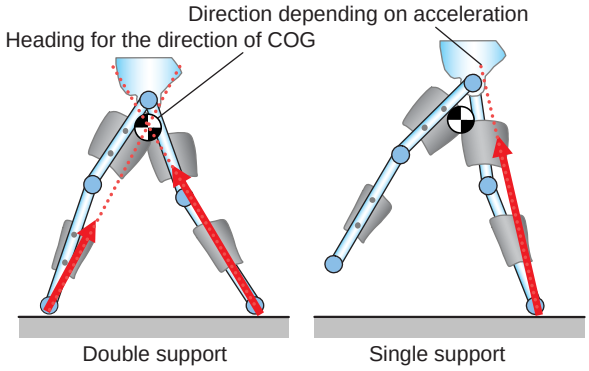


Fig. 5 Previous calculation method

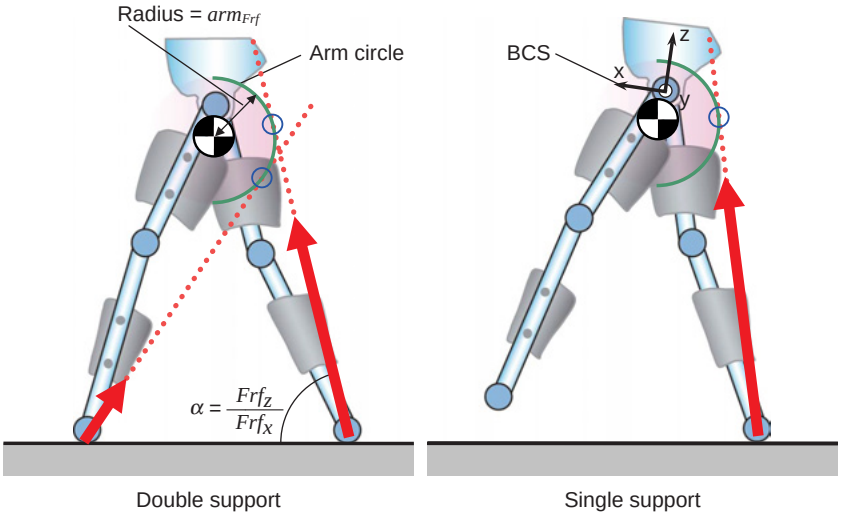


Fig. 6 Constraint of floor reaction force vector

arm in relation to the center of gravity. As Fig. 6 shows, the constraint condition operates within a two-dimensional plane extending from the x and y axes of the BCS. The constraint condition applied is contact between the system weight compensation floor reaction force vector and an arm circle within this plane, with the center of gravity of the system as its center and the moment arm as its radius. When angular acceleration motion is moving forward, the vector contacts the rear of the arm circle; when angular acceleration motion is moving backwards, the vector contacts the front of the arm circle. The moment arm is calculated from Eq. (4), which is based on the principle that a change in the degree of angular momentum is equivalent to the impulse moment during the change, and Eq. (5), based on the law of inertia.

$$\frac{d^{BCS}L_{whole}}{dt} = arm_{Frf} \cdot \left| {}^{BCS}\mathbf{Frf}_{whole} \right| \quad (4)$$

$${}^{BCS}\mathbf{Frf}_{whole} = m_{whole} \cdot \left({}^{BCS}\ddot{\mathbf{u}}_{whole_G} + {}^{BCS}\mathbf{acc}_{BCS_o} \right) \quad (5)$$

L_{whole}: degree of angular motion of system around system center of gravity
arm_{Frf}: Moment arm of floor reaction force vector in relation to system center of gravity
${}^{BCS}\mathbf{Frf}_{whole}$: Comprehensive reaction force vector from perspective of BCS

Application of this constraint condition to both single and double support would make the floor reaction force vector continuous when switching between the modes. In addition, it also possesses the benefit of making the floor reaction force vector during single support stable.

4.2.4. Calculation of moment arm for floor reaction force vector

As Eq. (6) indicates, the change over time in the degree of angular motion around the center of gravity of the system is expressed as the sum of the rotational inertia force generated by the rotation of the links, and the rotational inertia force generated by the revolution of the links around the system center of gravity.

$$\frac{d^{BCS}L_{whole}}{dt} = \sum_n \left\{ I_n \cdot \left({}^{BCS}\dot{\omega}_n + {}^{BCS}\dot{\omega}_{BCS} \right)_y \right\} + \sum_n \left\{ m_n \cdot arm_{n_acc} \cdot \left| {}^{BCS}\ddot{\mathbf{u}}_{n_G} - {}^{BCS}\ddot{\mathbf{u}}_{whole_G} \right| \right\} \quad (6)$$

${}^{BCS}\dot{\omega}_n$: Angular acceleration vector of nth link from perspective of BCS
${}^{BCS}\dot{\omega}_{BCS}$: BCS angular acceleration vector
arm_{n_acc}: Moment arm of acceleration vector of nth link in relation to system center of gravity
${}^{BCS}\ddot{\mathbf{u}}_{n_G}$: Acceleration vector of nth link from perspective of BCS
${}^{BCS}\ddot{\mathbf{u}}_{whole_G}$: Acceleration vector of system center of gravity from perspective of BCS

As Fig. 7 shows, arm_{n_acc} in Eq. (6) is the moment arm of the acceleration vector of the center of gravity of link n around the center of gravity of the system. The parallelogram shown in Fig. 7 is formed from the vector of the position of the center of gravity of the link, from the perspective of the center of gravity of the system and the acceleration vector of the position of the center of gravity of the link from the perspective of the center of gravity of the system. Because the acceleration vector moment arm corresponds to the height of the parallelogram when the acceleration vector is taken as its base, arm_{n_acc} can be calculated from Eq. (7).

$$arm_{n_acc} = \frac{\left| \left({}^{BCS}\mathbf{u}_{n_G} - {}^{BCS}\mathbf{u}_{whole_G} \right) \times \left({}^{BCS}\ddot{\mathbf{u}}_{n_G} - {}^{BCS}\ddot{\mathbf{u}}_{whole_G} \right) \right|}{\left| {}^{BCS}\ddot{\mathbf{u}}_{n_G} - {}^{BCS}\ddot{\mathbf{u}}_{whole_G} \right|} \quad (7)$$

Inputting arm_{n_acc} determined in this way for all the links in Eq. (6) and inputting the result and the comprehensive floor reaction force vector calculated in Eq. (5) in Eq. (4) gives the floor reaction force vector moment arm, arm_{Frf}.

4.2.5. Formularization of floor reaction force vector

During single support, the floor reaction force vector contacts the arm circle discussed above, and the magnitude of the vector is assumed to be the magnitude of the comprehensive floor reaction force vector, ${}^{BCS}\mathbf{Frf}_{whole}$. Equation (8), which enables calculation of floor reaction force during right leg support, can be obtained based on these conditions. A similar equation is used for left leg support.

$$\begin{aligned} {}^{BCS}Frf_{R_x} &= \left| {}^{BCS}\mathbf{Frf}_{whole} \right| \cdot \cos\left(\tan^{-1}\alpha_R \right) \\ {}^{BCS}Frf_{R_z} &= \left| {}^{BCS}\mathbf{Frf}_{whole} \right| \cdot \sin\left(\tan^{-1}\alpha_R \right) \\ {}^{BCS}Frf_{L_x} &= 0 \\ {}^{BCS}Frf_{L_z} &= 0 \end{aligned} \quad (8)$$

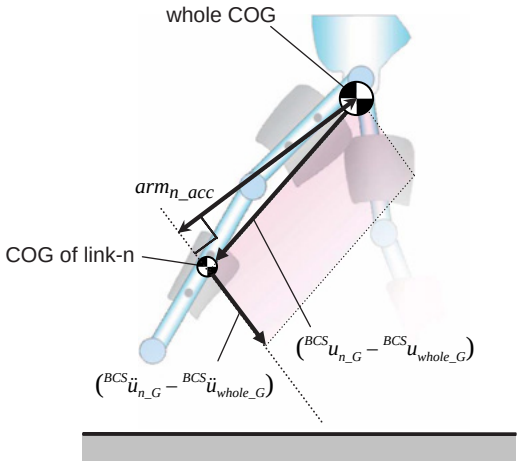


Fig. 7 Moment arm of link acceleration

${}^{BCS}Frf_{R_x}$: x component of floor reaction force vector for right leg

α_R: Inclination of floor reaction force vector (Frf_z/Frf_x) (See Fig. 6)

In the same way, during double support, both the right and left floor reaction force vectors contact the arm circle, and the sum of the x components of the right and left floor reaction force vectors and the sum of the z components of the right and left reaction force vectors are equivalent to each component of the respective comprehensive floor reaction forces (${}^{BCS}\boldsymbol{Frf}_{whole}$). Equation (9), which enables calculation of each component of the floor reaction force vector, can be obtained from this condition.

$$
\begin{aligned}
{}^{BCS}Frf_{R_x} &= \frac{{}^{BCS}Frf_{whole_z} - \alpha_L \cdot {}^{BCS}Frf_{whole_x}}{\alpha_R - \alpha_L} \\
{}^{BCS}Frf_{R_z} &= \frac{\alpha_R \cdot {}^{BCS}Frf_{whole_z} - \alpha_R \cdot \alpha_L \cdot {}^{BCS}Frf_{whole_x}}{\alpha_R - \alpha_L} \\
{}^{BCS}Frf_{L_x} &= \frac{{}^{BCS}Frf_{whole_z} - \alpha_R \cdot {}^{BCS}Frf_{whole_x}}{-\alpha_R + \alpha_L} \\
{}^{BCS}Frf_{L_z} &= \frac{\alpha_L \cdot {}^{BCS}Frf_{whole_z} - \alpha_R \cdot \alpha_L \cdot {}^{BCS}Frf_{whole_x}}{-\alpha_R + \alpha_L}
\end{aligned}
\qquad (9)
$$

The y component of the floor reaction force vector is calculated in the same way, using a two-dimensional plane extending from the y and z axes of the BCS.

4.2.6. Results of calculation of system weight compensation floor reaction force

Figure 8 shows the results of calculations of the system weight compensation floor reaction force for an experimental system fitted with acceleration and angular velocity sensors at the hips. The horizontal axis shows time, and the vertical axis shows the angle of inclination of the floor reaction force vector. Using the previous system (results shown as the fine line in the graph), in which the direction of the system weight compensation floor reaction force vector was determined from acceleration data, fluctuations can be observed during single support, and there is discontinuity when the system switches between single and double support. By contrast, the results obtained using the method developed in this research (bold line in the graph), which considers the moment arm of the system weight compensation floor reaction force vector, are stable and do not display fluctuations. In addition, the direction of the vector is continuous when switching between single and double support. This demonstrates that the method possesses sufficient performance as a method of calculating the floor reaction force for system weight compensation.

In addition, the application of the method to a dynamics model of the user enables calculation of the floor reaction force vector for the user. This makes a floor reaction force sensor, as employed in the previous assist method, unnecessary and thus brings the realization of a user-friendly walking assist system closer.

5. Conclusion

A control logic that balances the provision of assist for walking and system weight compensation has been developed in order to realize a user-friendly walking assist system that will contribute to the lives of the elderly. The main details of this development can be summarized as follows:

(1) A calculation method has been proposed in which the user and the system are considered separately and separate inverse dynamics analyses are used to calculate the assist moment for the user and the system weight compensation moment for the system.

(2) A method of calculating the floor reaction force required for system weight compensation has been developed. This method enables system weight compensation for both rotational and translational motion. Tests showed that the direction of the system weight compensation floor reaction force that is generated by the calculation method is highly stable. The application of the method enables the floor reaction force vector, received by the user's

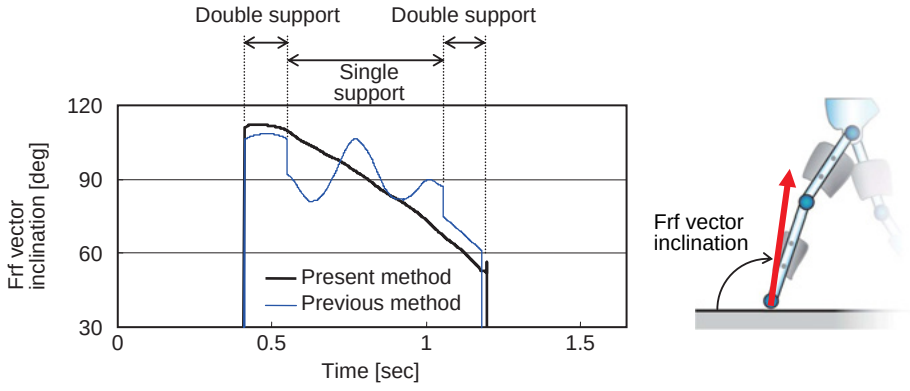


Fig. 8 Result of floor reaction force calculation

leg, to be estimated, thus eliminating the requirement for a floor reaction force sensor, bringing the realization of a user-friendly walking assist system closer to reality.

6. Afterword

Prioritizing user comfort, Honda is attempting to develop a user-friendly walking assist system. The research discussed in this paper has proposed a method that enables the system both to provide assistance and compensate for its own weight. By refining the calculation methods employed, this research has attempted to further reduce the burden on the user.

The author is committed to continuing research on a walking assist system that prioritizes user comfort, in an attempt to make it easier for the elderly and others in need of assistance to participate in society.

References

(1) http://www8.cao.go.jp/kourei/whitepaper/w-2006/zenbun/18index.html
(2) Katoh, H., Hirata, T.: The concept of a walking assistance suit, D&D2001 Symposium on Welfare Engineering, W418 (2001)
(3) Nakamura, T., Saito, K., Kosuge, K.: Control of Wearable Walking Support System Based on Human-Model and GRF, Proceedings of the 2005 IEEE International Conference on Robotics and Automation, p.4405-4410 (2005)
(4) JP, 2005-95561, A (2005)
(5) Tsuchiya, K.: Chapter 5 Integrated analysis, Introduction to clinical walking analysis, Ishiyaku Publishers, Inc., p. 110-115 (1994)
(6) Kazerooni, H., Racine, J. L., Huang, L., Steger, R.: On the Control of the Berkeley Lower Extremity Exoskeleton (BLEEX), Proceedings of the 2005 IEEE International Conference on Robotics and Automation, p. 4364-4371 (2005)
(7) Yamamoto, K.: Chapter 9 Kinematics in Noninertial system, Dynamics, Gakujutsu Tosho Shuppan-sha Co., Ltd., p. 78-85 (1995)

Author



Yasushi IKEUCHI

